Dayglow Emissions on Mars and Venus

Thesis submitted to
Cochin University of Science and Technology

In partial fulfillment of the requirements
for the award of

Doctor of Philosophy
in
Physics

UNDER THE FACULTY OF SCIENCES

by
Sonal Kumar Jain

Space Physics Laboratory
Vikram Sarabhai Space Centre
Indian Space Research Organisation
Thiruvananthapuram
INDIA

January 2013

dedicated to

my dear grandmother
(Late Smt. Savitri Devi)

Declaration

This is to declare that the work presented in this thesis is original and no part of it has been submitted for the award of any degree or diploma of any other university or institution.

January 2013 **Sonal Kumar Jain**

भारत सरकार
अंतरिक्ष विभाग
विक्रम साराभाई अंतरिक्ष केन्द्र
तिरुवनन्तपुरम-695 022
केरल, भारत
फोन : (0471) 2562330
फैक्स : (0471) 2706535
e-mail: Bhardwaj_spl@yahoo.com

सत्यमेव जयते

Government of India
Department of Space
Vikram Sarabhai Space Centre
Thiruvananthapuram-695 022
Kerala, INDIA
Telephone : (0471) 2562330
Fax : (0471) 2706535
e-mail: Anil_Bhardwaj@vssc.gov.in

SPACE PHYSICS LABORATORY

Dr. Anil Bhardwaj, FNA, FASc
Scientist G & Head, Planetary Science Branch

CERTIFICATE

Certified that the thesis entitled "**Dayglow Emissions on Mars and Venus**" submitted by Mr. Sonal Kumar Jain, to Cochin University of Science and Technology, Cochin, embodies the original results of the investigations carried out at the Space Physics Laboratory, Vikram Sarabhai Space Centre, Thiruvananthapuram, under my guidance. The work presented in this thesis has not been submitted for the award of any other degree or diploma to any other university or institution.

January 2013

Dr. Anil Bhardwaj
Thesis Supervisor

Dr. K. Krishnamoorthy
Director
Space Physics Laboratory

Acknowledgments

No creation in this world is a solo effort. Neither is my Ph.D. thesis...
Undertaking this Ph.D. has been a life-changing experience for me. I knew that path would have been difficult without the support of many people, who have walked along with me and helped me choose the right direction during my Ph.D. tenure. Though it will not be enough to express my gratitude in words to all those people who helped me, I would still like to give my many, many thanks to all these people.

First and foremost, I am indebted to my supervisor, Dr. Anil Bhardwaj, Head, Planetary Science Branch, Space Physics Laboratory, who introduce me to the planetary sciences and provided constant support throughout my tenure here in Space Physics Laboratory. It is difficult to overstate my gratitude and appreciation for his great enthusiasm, and constant effort to explain things in much simpler and clearer way. Thank you Sir, for constructive criticisms, numerous suggestions, and providing guidance whenever needed.

I am extremely grateful to Dr. K. Krishnamoorthy, Director, Space Physics Laboratory, for his constant encouragement and for providing me with excellent facilities to pursue my work. I also thank him for critically evaluating my thesis work as a member of the research committee.

My sincere thanks are due to Prof. R. Sridharan, Former Director of Space Physics Laboratory for his support and valuable suggestions.

I also appreciate the advice of the academic committee members (Dr. K. Parameswaran, Dr. M. Mohan, Dr. K. Rajeev, Dr. Prabha R. Nair, Dr. Geetha Ramkumar, Dr. Tarun Pant, Dr. R. K. Choudhary, Dr. Suresh Raju, Dr. K. Kishore Kumar Dr. S.Suresh Babu, Dr. Sunil Kumar, Dr. D. B.Subramanyam, Dr. Satheesh Thampi, Dr. G. Manju, Dr. N. V. P. Kiran Kumar, Dr. Siji Kumar and Dr. S. S. Das) and my sincere thanks to them for their critical comments, which enabled me to make the necessary improvements in my work.

Special thanks to members of research committee (Prof. Anatharaman, Dr. K. Mohan Kumar, Prof. K. R. Santosh, Prof. Ramesh Babu T) for their support, criticism, encouragement, and scholarly advice.

I also acknowledge Dr. Sandhya, Dr. Vipin, Dr. Mukunda, Dr. M. M. Hossain, Dr. Vineeth, Dr. Vijayakumar, Dr. Nizy, Dr. P. Hegde, Dr. Uma, T. P. Das, Neha, Manoj Mishra, Imran, Sobhan, K. Subrahmanyam, Supriya, and Mridula for the motivation and support provided.

Thanks are also due to all office staff of Space Physics Laboratory (Ms. P. R. Suseela, Ms. Shishira, Ms. Shalini, Mr. Watson, Mr. Ashokan, Mr. T. K. Vijayan, Mr. Jihas, Ms. Prameela, to mention a few). I acknowledge Mrs. C. Geetha for taking care of all non-scientific works. I also thank the administrative staff of Cochin University of Science and Technology for their whole hearted support.

This research work was supported by Department of Space, Government of India. I would like to acknowledge the financial assistance provided by the Indian Space Research Organization (ISRO) through the research fellowship. Thanks are due to the staff at the VSSC Library for their assistance.

It is my pleasure to express my heartfelt thanks to Dhanya and Raghuram, for long scientific discussions *(though sometimes irritating). I owe them a lot for the many enlightening conversations, enthusiasm and fun we had together in SPL. Thank you guys for your friendship and support.*

I thank my batch mates, Lijo, Veena, and Liji for their support, humour, and affectionate company at SPL. It is also my pleasure to acknowledge all my current and previous colleagues at SPL, Dr. Smitha Thampi, Dr. Rani, Dr. Susan, Dr. Denny, Dr. Marina, Dr. Bijoy, Dr. Meenu, Dr. Naseema, Dr. Sreeja and Dr. Swain, Anish, Prijith, Sumod, Sherine, Ambili, Anu, Asha, Tinu, Arun, Abhinaw, Arya, Manoj, Madhav, Renju, Neethu, Ajesh, Ashok, Lakshmi, and Sreedevi.

I would like to extend a warm thanks to all the people, with whom I celebrated most of festivals here in God's own country and feel at home away from home (special Thanks for all the delicious treats and parties and please keep it up). To mention a few, Sidharth and Uma, Mukunda and Mitali Bhabhi, Mr. Manoj Mishra and Nidhi Bhabhi, Yogesh. My hearty thanks to Dr. Korak and Shalini Bhabhi for their love and affection.

A good support system is important to survive and staying sane during Ph.D. tenure. I was lucky to have the same, when I talk about my dear friend Jai Prakash Chaubey, (not only we share an apartment but coincidently birth date also). Thank you mate for being with me in ups and downs of life during last six years and also for being the most encouraging and helpful friend I ever had.

Now, I thank the people who mean world to me, my Maa (Smt. Saroj Jain) and Papa (Shri Santosh Jain), for their love and blessings, Bade Bhaiya (Saurabh) and Bhabhi (Seema), Didi (Smita) and Jijaji (Manish) for their support and affection.

Finally, I must thank my wife Shilpa for her understanding, love, and support during the past few years. Enjoying a wonderful life with you dear, I am looking forward to many more happy and exciting years together.

For any errors or inadequacies that may remain in this work, of course, the responsibility is entirely my own.

Sonal Kumar Jain

Contents

Thesis advisor
Anil Bhardwaj

Author
Sonal Kumar Jain

Dayglow Emissions on Mars and Venus

Preface

Since the beginning of space era, the quest for understanding the atmospheres of Earth's two neighbours Mars and Venus fascinated planetary scientists. The upper atmospheric studies of Mars and Venus have been carrying out since sixties. At present, atmospheres of Mars and Venus are being investigated by Mars Express and Venus Express, respectively. SPICAM aboard Mars Express observations have provided wealth of information on Martian upper atmosphere and enhanced our understanding regarding the energetics of upper atmosphere of Mars. SPICAM observations span more than a Martian years. These measurements have been very informative and have helped us understand the effect of dust storms, seasonal variations, solar zenith angles etc., on Martian dayglow emissions. SPICAM has also observed for the first time ultraviolet emissions of N_2 on Mars. Very recently, first observations of CO Cameron band and CO_2^+ ultraviolet doublet emissions on Venus using the SPICAV instrument have been reported. Since the atmospheres of both Mars and Venus is predominantly CO_2, the dayglow emissions are expected to be governed by similar processes. However, there are considerable differences in terms of solar energy input and atmospheric density. Recent measurements on Mars and Venus have shown that dayglow emissions on the two planets have similar features. However, it is important to understand the underlying physics and chemistry of the processes governing the dayglow emissions on Mars and Venus.

An attempt has been made in this thesis to model some of the emissions observed by SPICAM and SPICAV on Mars and Venus, respectively, viz., CO Cameron band, CO_2^+ ultraviolet doublet, N_2 triplet bands, atomic oxygen green (5577 Å), red doublet (6300, 6364 Å), and ultraviolet (2972 Å) emissions. One of major sources of these emissions is photoelectron impact ionization/excitation. In this thesis, an electron degradation model based on Monte Carlo technique has been developed to calculate the production/excitation rates of above mentioned emissions due to electron impact.

The limb brightness profiles of emissions are calculated and compared with the observations wherever available. The effect of various model input parameters on dayglow emissions intensities is also evaluated.

A brief introduction of the work carried out in this thesis is provided in Chapter 1. The details of input parameters, viz., photon and electron impact cross sections and solar flux models are provided in Chapter 2. In Chapter 3, development of an electron degradation model in a CO_2 dominated atmosphere is discussed. Chapters 4, 5, and 6 present the modelling of above mentioned emissions in the atmospheres of Mars and Venus. A summary of the results presented in the thesis is presented in Chapter 7 along with the future scope of the studies reported herein.

Referred Publications:

1. Anil Bhardwaj and **Sonal Kumar Jain** (2009), Monte Carlo Model for electron degradation in a CO_2 atmosphere, *Journal of Geophysical Research*, *114*, A11309, pp. 1–14, doi:10.1029/2009JA014298.

2. **Sonal Kumar Jain** and Anil Bhardwaj (2011), Model calculation of N_2 Vegard-Kaplan band emissions in Martian dayglow, *Journal of Geophysical Research, 116*, E07005, pp. 1–11, doi:10.1029/2010JE003778.

3. Anil Bhardwaj and **Sonal Kumar Jain** (2012), Calculations of N_2 triplet states vibrational populations and band emissions in venusian dayglow, *Icarus*, *217*, 752–758, doi:10.1016/j.icarus.2011.05.026.

4. **Sonal Kumar Jain** and Anil Bhardwaj (2012), Impact of solar EUV flux on CO Cameron band and CO_2^+ UV doublet emissions in the dayglow of Mars, *Planetary and Space Science*, *63-64*, 110–122, doi:10.1016/j.pss.2011.08.010.

5. Anil Bhardwaj and **Sonal Kumar Jain** (2012), Production of N_2 Vegard-Kaplan and other triplet band emissions in the dayglow of Titan, *Icarus*, *218*, 989 – 1005, doi:10.1016/j.icarus.2012.01.019.

6. Anil Bhardwaj and **Sonal Kumar Jain** (2012), CO Cameron and CO_2^+ UV doublet band emissions in the dayglow of Venus: Role of CO in Cameron band production, *Journal of Geophysical Research*, revised submitted.

7. **Sonal Kumar Jain** and Anil Bhardwaj (2012), Atomic oxygen red, green, and ultraviolet line emissions in the dayglow of Mars, *Journal of Geophysical Research*, under preparation.

Conference Presentations:

1. **Jain, S. K.**, and A. Bhardwaj, Model Calculation of CO and CO_2 Dayglow emission on Mars, National Space Science Symposium (NSSS), Saurashtra University, Rajkot, India, Feb. 24–27, 2010.

2. **Jain, S. K.**, and A. Bhardwaj, Model for ultraviolet dayglow emissions on Mars, 7th annual meeting of Asia Oceania Geosciences Society (AOGS), Hyderabad, India, July 4–9, 2010.

3. **Jain, S. K.**, and A. Bhardwaj, Model for ultraviolet dayglow emissions on Mars, International workshop on Advances in Planetary Atmospheres and Exploration, Physical Research Laboratory, Ahmedabad, India, July 12–13, 2010.

4. A. Bhardwaj and **S. K. Jain**, Nitrogen triplet band emission in the dayglow of Mars, 8th annual meeting of Asia Oceania Geosciences Society (AOGS) Taipai, Taiwan, August 8–12, 2011.

5. **Jain, S. K.**, and A. Bhardwaj, Study of N_2 Vegard-Kaplan band emission in the dayglow of Mars, Venus, and Titan, National Space Science Symposium (NSSS), S. V. University, Tirupati, India, February 14–17, 2012.

6. **Jain, S. K.**, and A. Bhardwaj, Effect of solar EUV flux on the ultraviolet dayglow emissions of Mars, National Space Science Symposium (NSSS) at S. V. University, Tirupati, India, February 14–17, 2012.
7. A. Bhardwaj and **S. K. Jain**, Forbidden atomic oxygen line emissions in the dayglow of Mars, 39th meeting of COSPAR, Mysore, India, July 14–22, 2012.
8. **Jain, S. K.**, and A. Bhardwaj (2012), Effect of solar EUV flux on CO Cameron band and CO_2^+ UV doublet dayglow emissions of Mars, 39th meeting of COSPAR, Mysore, India, July 14–22, 2012.
9. **Jain, S. K.**, and A. Bhardwaj (2012), N_2 triplet band emissions in the dayglow of Venus, Mars, and Titan, 39th meeting of COSPAR, Mysore, India, July 14–22, 2012.

Acronyms

AE-E Atmospheric Explorer-E.
AYS Analytical Yield Spectra.

CSDA Continuous Slowing Down Approximation.

DCS Differential Elastic Scattering Cross Section.
DR Dissociative Recombination.
DSMC Direct Simulation Monte Carlo.

ESA European Space Agency.
EUV Extreme Ultraviolet.
EUVAC EUV flux model for Aeronomic Calculation.

F10.7 10.7-cm radio flux.
FISM Flare Irradiance Spectral Model.
FUSE Far Ultraviolet Spectroscopic Explorer.
FUV Far Ultraviolet.

HUT Hopkins Ultraviolet Telescope.

IR Infra-red.

MarMCET Mars Monte Carlo Electron Transport.
MEx Mars Express.
MTGCM Mars Thermospheric General Circulation Model.

PD Photodissociation.
PVO Pioneer Venus Orbiter.
PVOUVS Pioneer Venus Orbiter Ultraviolet Spectrometer.

S2K SOLAR2000.
SEE Solar EUV Experiment.
SPICAM SPectroscopy for the Investigation of the Characteristics of the Atmosphere of Mars.
SPICAV SPectroscopy for the Investigation of the Characteristics of the Atmosphere of Venus.
SZA Solar Zenith Angle.

TCS Total Scattering Cross Section.
TIMED Thermospheric Ionospheric Mesospheric Energy and Dynamics.

UV Ultraviolet.
UVIS Ultraviolet Imaging Spectrograph.
UVS Ultraviolet Spectrometer.

VEx Venus Express.
VIMS Visual and Infrared Mapping Spectrometer.
VK Vegard-Kaplan.
VTGCM Venus Thermospheric General Circulation Model.

XUV soft X-rays.

Chapter 1

Introduction

Venus, Earth, and Mars—the three terrestrial planets with atmospheres–have many features in common. Earth and Venus, in particular, are nearly the same size and seem to have been quite similar atmospheric composition when they formed and cooled, probably with large inventories of CO_2 and water vapour. Martian atmosphere is subjected to large diurnal and seasonal changes due to its rotational period and axial tilt, respectively, which are similar to that of Earth. Table 1.1 shows some important physical properties of three terrestrial planets.

Table 1.1: Major physical properties of Venus and Mars in comparison with Earth.

Parameter	Venus	Earth	Mars
Distance from Sun (AU)	0.72	1	1.38-1.66
Diameter	0.95	1	0.5
Mass	0.8	1	0.1
Obliquity to orbit (deg)	177.3	23.45	25.19
Density (g/cm^3)	5.2	5.5	3.9
Acc. due to gravity (m/s^2)	8.6	9.8	3.7
Escape velocity (km/s)	10.36	11.19	5.02
Major atmospheric composition	CO_2, N_2	N_2, O_2	CO_2, N_2
Scale height (km)	14.9	8.4	10.6
Solar Constant	1.9	1	0.52–0.36
Length of day	243	1	1.03
Pressure (bar)	90	1	7E-3
T (Mean surface temperature) (K)	740	288	220
T (exosphere) (K)	100–300	700–1000	150–300

The atmospheres of Mars and Venus are predominantly composed of CO_2 with a small amount (2.5–4.5%) of N_2. However, compared to Venus, the atmospheric pressure on Martian surface is about four orders of magnitude smaller. The composition of lower thermosphere, which is located at approximately 120 km on Mars and 135 km on Venus, is nearly the same as that of the bulk atmosphere [*Fox and Dalgarno*, 1979a; *Fox and Bougher*, 1991; *Fox and Sung*, 2001]. Above the homopause, photodissociation and diffusion in the gravitational field cause the products of CO_2 photolysis (CO and O) to become relatively more abundant. Figure 1.1 shows the image of Martian atmosphere taken by Viking 1 orbiter. Atmospheres of both Mars and Venus have been studied extensively by several space missions. The information gathered by these missions have helped in better understanding of energetic of upper atmospheres of the two planets.

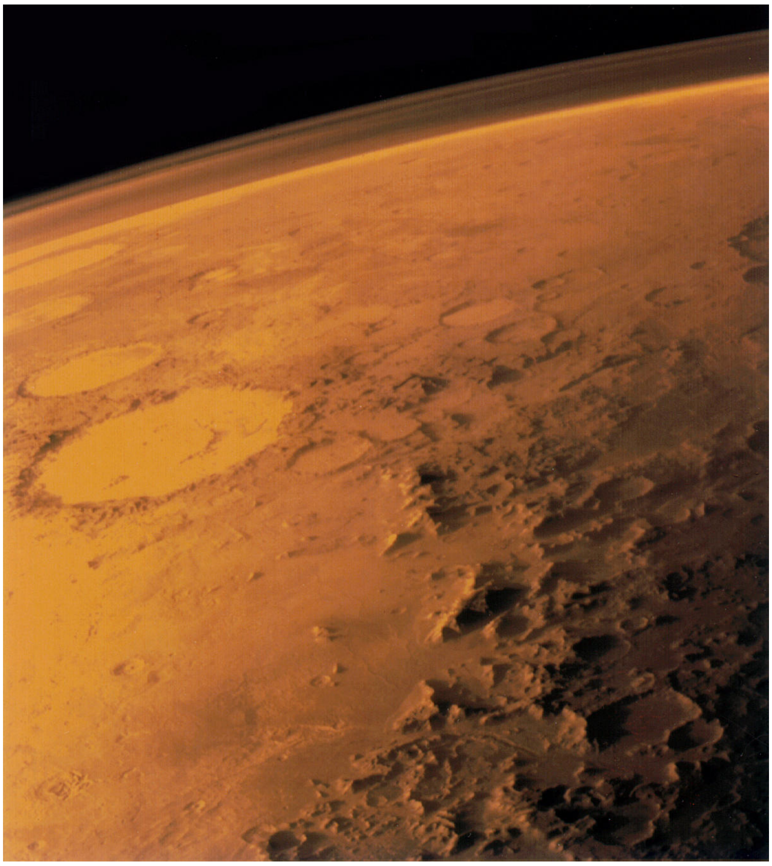

Figure 1.1: The image taken by the Viking 1 orbiter shows the thin atmosphere of Mars. Image credit JPL-NASA.

The present thesis is aimed at understanding some of the physical processes that are governed by the interaction of solar radiation with the upper atmospheres of Mars and Venus. Absorption of solar radiation in the atmosphere of a planet results in excitation, dissociation, ionization, and heating of the atmosphere constituents, and many other aeronomical processes which then follow. The photoionization produces photoelectrons, which lose their energy through a variety of collisions causing further excitation, ionization, dissociation, and heating of the upper atmosphere. The emissions that originate due to excitation processes in the atmosphere of the planets are generally classified as dayglow, nightglow, and aurora. Dayglow is the luminosity of the dayside atmosphere that is mainly due to the interaction of solar radiation with atmospheric gases. Dayglow emissions are the most common feature of any planetary atmosphere. These emissions are the perfect tracer for the processes occurring in the emitting region of atmosphere. Dayglow provides basic information about atmospheric composition and its structure, and can be used to study energy deposition processes, dynamics, and chemistry of the atmosphere. Thus, dayglow emissions constitute an important diagnostic tool to study the atmospheric regions, which are otherwise difficult to study. There are variety of processes—involving atomic, molecular, neutral, and ionic species—governing the dayglow emissions in a planetary atmosphere.

The research presented in this thesis concerns the various ultraviolet and visible dayglow emissions emanating from the atmospheres of Mars and Venus. The study focuses mainly on CO Cameron band, CO_2^+ ultraviolet doublet, N_2 triplet band, and atomic oxygen 2972, 5577 Å, and red doublet (6300, 6364 Å) line emissions from sunlit atmospheres of Mars and Venus. This thesis addresses the modelling of these emissions in the light of updated reaction rates and cross sections, and recent observations by Mars Express (MEx) and Venus Express (VEx) on Mars and Venus, respectively. This chapter provides a short introduction to the various processes responsible for dayglow emissions in atmospheres of Mars and Venus. A brief review of dayglow observations and theoretical modelling studies on Mars and Venus is also given in this chapter. Finally, an overview of the entire work carried out in the thesis is presented.

1.1 Dayglow emission

Emissions originating from a sunlit atmosphere span a wide range of electromagnetic spectrum from Ultraviolet (UV) to Infra-red (IR). The wavelength of emitting photon depends on the type of transition involved—electronic, vibrational, and rotational. A schematic of various transition and associated emitted photon wavelength regime is shown in Figure 1.2. Photons emitted in electronic, vibrational, and rotational transitions have wavelengths in UV/visible, IR, and sub millimetre, respectively. Depending on the application, information required, and observation conditions, emissions at different wavelengths provide useful information of the emitting medium.

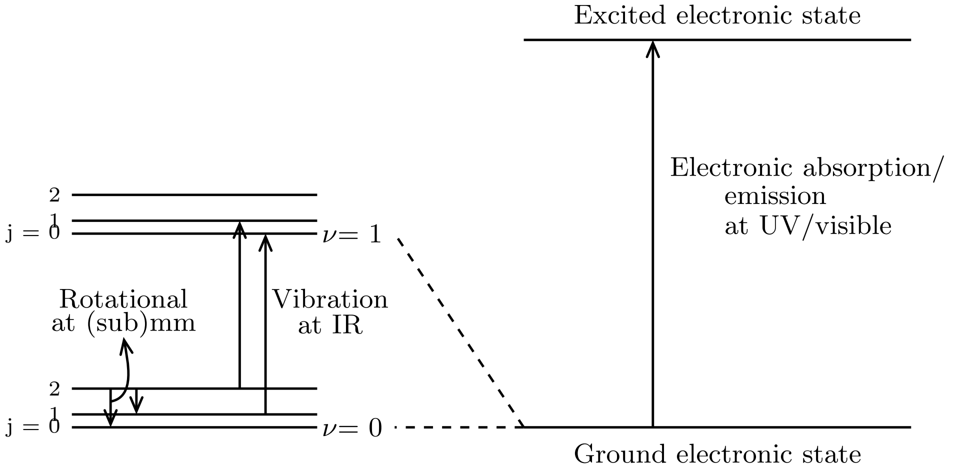

Figure 1.2: Schematic diagram depicting transitions in electronic, vibration, and rotational levels. Adapted from lecture notes of E. F. van Dishoeck.

In the present work, the focus is mainly on the dayglow features in ultraviolet and visible wavelength region. Planetary ultraviolet spectroscopy is not only meant for inferring the composition of an atmosphere, it can tell us about the energy inputs into that atmosphere, trace the dynamics, and also allow us to use the planetary atmosphere as a natural laboratory for the determination of cross sections, lifetimes, and excitation processes. The advantage of ultraviolet emissions is that most of radiative transport problems in UV are quite straight forward, being decoupled from the planetary radiation field [see reviews of *Meier*, 1991; *Paxton and Anderson*, 1992]. The observations below 3000 Å—so called "solar blind"—are simple and easily distinguishable from background radiation. This minimal background is due to the absorption of the ultraviolet solar radiation below the 3000 Å in and below the thermosphere that prevents the scattering of radiation from planetary surface. In IR and visible, emission features are seen against the background which is both absorbing and emitting and also illuminated by the planetary surface from below. Most of the resonance emission lines of the atomic and molecular components of the thermosphere (major or trace species) are mostly in the ultraviolet region of the dayglow spectrum. Consequently, remote sensing of UV spectral regime provide a useful diagnostic tool to infer the composition of minor species also in the upper atmosphere. Limb profiling of an emission provide attractive approach to infer altitudinal distribution of emitting species, scale height, and temperature information at that altitude. Many important discoveries regarding the composition, energetic, and dynamics of planetary upper atmosphere have been made using ultraviolet observations.

1.2 Physics of dayglow emission

Sun, the dominant source of energy for the planetary atmospheres, continuously emits electromagnetic radiation and corpuscular radiation known as 'solar wind.' The energy that is deposited in the planetary upper atmosphere by solar electromagnetic radiation is dissipated mainly through radiative decay processes, giving rise to airglow. The term airglow has been conventionally adopted as a convenient designation for the non-thermal radiation emitted by the upper atmosphere other than due to aurora. Airglow is further categorized as (i) dayglow, that occur when the atmosphere is directly illuminated by the Sun, (ii) twilight glow, is the emission emanating from day-night terminator of a planetary atmosphere, and (iii) nightglow, which is the night-time luminosity generated by the release of the energy stored in dissociation or ionization products, produced during the daytime or transported from the dayside. Scattering of stellar/interplanetary radiation by atmospheric species could also be a source of nightglow. Emissions from the planetary atmosphere on the dayside spectrum can be from a number of sources:

1.2.1 Photon impact

Solar photons incident on the planetary atmosphere can excite the species of the atmosphere through a variety of scattering processes, viz., resonant, fluorescence, Rayleigh, Mie, and Raman scattering. Resonant and fluorescence scattering are limited to transitions that are dipole allowed or optically allowed. Interstellar photons, whose importance relative to the solar photon flux increases with increasing heliocentric distance, can also excite the atmosphere in the same manner as the solar photons [e.g., *Yelle and Sandel*, 1986]. In addition to the scattering processes the photons can excite the atmospheric medium directly in the three more ways, viz., the photon impact ionization excitation, photodissociative excitation, and photodissociative ionization excitation. Of these, some important processes are depicted in Figure 1.3 and are discussed below:

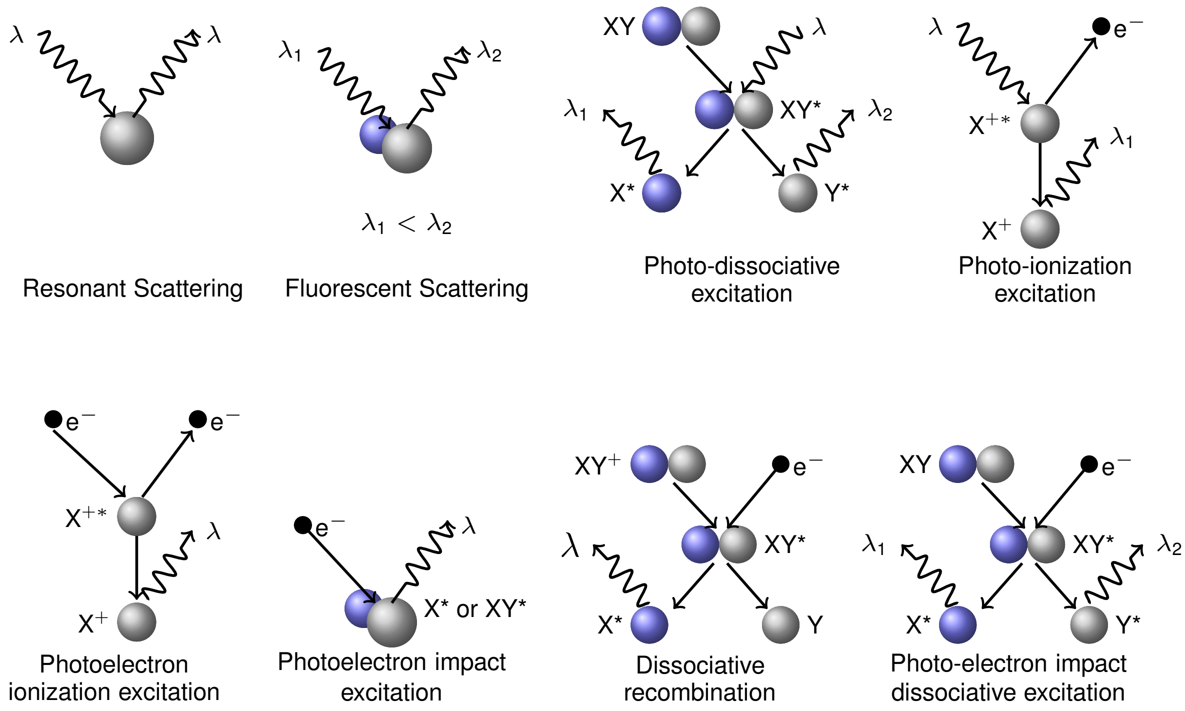

Figure 1.3: Various processes responsible for dayglow emission in a planetary atmosphere. [adapted from *Leblanc et al.*, 2006].

Resonance Scattering

$$\mathrm{X} + \mathrm{h}\nu \rightarrow \mathrm{X}^* \rightarrow \mathrm{X} + \mathrm{h}\nu$$

Resonance scattering occurs when the incident photon and emergent photon are almost exactly equal in energy (the difference is due to the uncertainty principle which leads to "natural broadening" of the line and the Doppler shift of the emitting photon which leads to "Doppler Broadening" of the line). Resonance scattering is usually important for optically allowed transitions. An important example of this process is the atomic hydrogen line seen in planetary coronae at 1216 Å [*Chaufray et al.*, 2008a, b; *Hedelt et al.*, 2010].

Fluorescence Scattering

$$\mathrm{XY + h\nu_1 \rightarrow XY^* \rightarrow XY + h\nu_2}$$

In fluorescent scattering a molecule is electronically excited by an incident radiation, which then remits at a longer wavelength. Emissions arising due to resonance-fluorescence scattering of solar photon give information about the atmospheric constituents and their abundance even when they are very minor constituents. Resonant and fluorescent scattering are limited to transition that are dipole or optically allowed. An important example of this in the atmosphere of Mars and Venus is the CO Fourth Positive group [*Fox and Dalgarno*, 1979a; *Fox and Bougher*, 1991].

Photo-ionization excitation

$$\mathrm{X + h\nu \rightarrow X^{+*} + e}$$

$$\mathrm{X^{+*} \rightarrow X^{+} + h\nu'}$$

If photon energy is sufficiently large, it can ionize the molecule/atom. The ionized species can be in excited state (see Figure 1.3). Apart from that photon can dissociate the parent molecule and one or both of the daughter species can be in ionize state. This process is responsible for CO_2^+ UV doublet emission in the atmospheres of Mars and Venus [*Fox and Dalgarno*, 1979a; *Fox and Bougher*, 1991; *Shematovich et al.*, 2008; *Simon et al.*, 2009; *Cox et al.*, 2010; *Chaufray et al.*, 2012].

Photodissociative excitation

$$\mathrm{XY + h\nu \rightarrow X^* + Y^*}$$

$$\mathrm{X^* \rightarrow X + h\nu'}$$

$$\mathrm{Y^* \rightarrow Y + h\nu''}$$

Solar photon can dissociate the molecules, and the daughter species can be excited states. This process can also give rise to various excited species in a planetary atmosphere. It is one of the important sources of CO($a^3\Pi$) and O(^1S) and O(^1D) in the atmospheres of Mars and Venus [*Barth et al.*, 1971; *Stewart*, 1972; *Leblanc et al.*, 2006; *Chaufray et al.*, 2012].

1.2.2 Photoelectron impact

Solar photons having sufficient energy can ionize the atom or molecule creating energetic electron called "photoelectron". These photoelectrons are the major source of producing radiation from optically forbidden transitions. These photoelectrons can be observed directly by in-situ techniques [e.g., *Coates et al.*, 2010]. The possible ways a photoelectron can excite the atmosphere are: (i) impact excitation, (ii) impact dissociative excitation, (iii) impact ionization excitation, and (iv) impact dissociative ionization excitation.

To study the photoelectron impact excitation in the atmosphere one requires a technique to model the degradation of electrons in the medium. Using the model (whose input includes a model atmosphere, solar flux, photoabsorption and photoionization cross sections, and electron impact cross sections) the photoelectron energy spectrum is first calculated and subsequently the steady state photoelectron flux. These photoelectron fluxes are then employed with the desired altitude distribution of neutral gas density and the relevant electron impact excitation/emission cross section to obtain the volume excitation/emission rate, and finally the intensity of a particular emission. There are many techniques used to calculate the photoelectron flux in the planetary atmospheres. A brief description of various electron degradation techniques is given in Chapter 3. Some of the important electron impact excitation processes are shown in Figure 1.3 and are discussed below:

Photoelectron impact excitation

$$\mathrm{XY + e^* \rightarrow XY^* \rightarrow XY + h\nu}$$

or

$$\mathrm{X + e^* \rightarrow X^* \rightarrow X + h\nu}$$

Photoelectron impact excitation is often the most efficient means for exciting optically forbidden transition in atoms or in molecules. Photoelectron impact is the primary production source of N_2 triplet states in the atmosphere of Earth as well as on Mars [*Meier*, 1991; *Broadfoot et al.*, 1997; *Leblanc et al.*, 2006, 2007].

Photoelectron impact dissociative excitation

$$\mathrm{XY + e^* \rightarrow X^* + Y^* + e}$$

$$\mathrm{X^* \rightarrow X + h\nu}$$

$$\mathrm{Y^* \rightarrow Y + h\nu}$$

The CO Cameron bands ($a^3\Pi - X^1\Sigma^+$) are prominent emission in the dayglow of Mars and Venus between 1800 and 2500 Å and photoelectrons impact excitation is one of the sources of CO(a$^3\Pi$) [*Barth et al.*, 1971; *Fox*, 1992; *Leblanc et al.*, 2006; *Jain and Bhardwaj*, 2012; *Gronoff et al.*, 2012a; *Chaufray et al.*, 2012].

Photoelectron impact ionization excitation

Apart from that photoelectron impact ionization excitation and photoelectron impact dissociative ionization excitation are also important sources of dayglow.

$$\mathrm{X + e^* \rightarrow X^{+*} + e + e}$$

or

$$\mathrm{XY + e^* \rightarrow X^{+*} + Y + e + e}$$

$$\mathrm{X^* \rightarrow X + h\nu}$$

Electron impact ionization is one of sources of CO_2^+ UV emission on Mars and Venus [*Barth et al.*, 1971; *Fox*, 1992; *Leblanc et al.*, 2006; *Jain and Bhardwaj*, 2012; *Gronoff et al.*, 2012a; *Chaufray et al.*, 2012].

1.2.3 Neutral and ion impact

Excitation of the atmospheric constituents by the precipitating ring current particles (ions and neutrals) can be an important source of emissions, particularly during the magnetic substorms. Ring current ions generally precipitate at around mid-high-latitudes (since ions follow the magnetic field trajectory), but precipitation of neutrals occurs preferably at low latitudes. Energetic neutrals are created by charge exchange collisions of energetic (keV-MeV range) ring current ions with the ambient planetary neutral gas corona. Most of these resulting fast neutrals are lost to the space, but a fraction precipitate into the atmosphere, and thereby be a source of emissions [*Bhardwaj*, 1997]. Energetic neutrals escaping the planetary magnetospheres have been observed on Earth [e.g., *Roelof et al.*, 1985; *Henderson*, 1997], and on Jupiter, Saturn, and Uranus [e.g., *Cheng*, 1986; *Krimigis*, 1988; *Carbary et al.*, 2009]. Both Mars and Venus do not have any intrinsic magnetic field and hence are subjected to direct solar wind interaction with their upper atmosphere. Energetic neutrals are created in the vicinity of Mars and Venus due to charge exchange process [*Holmström and Kallio*, 2004; *Futaana et al.*, 2012].

1.2.4 Chemical reactions

The reactions between the species of the atmosphere (ion, electron, atom, and molecule) can result in the production of emissions via recombination and chemiluminescence processes. Chemiluminescence is a type of luminescence produced as a result of the generation of electronically excited products of a chemical reaction which subsequently emit photons. Recombination is a process of reunion (neutralization) of an electron and an ion which may result in the excited neutral species that subsequently decays producing radiation. There are two types of recombination: the one occurring in atomic species is known as 'radiative recombination', and the other occurring in molecular species is known as 'dissociative recombination'. Both chemiluminescence and recombination processes are major source of nightglow.

Dissociative Recombination (DR) is the primary mechanism for electron loss in ionized, low-pressure molecular gases and plasmas, such as planetary ionospheres [*Mitchell and Guberman*, 1989].

$$\mathrm{XY^+ + e \rightarrow X + Y + \Delta E}$$

or

$$\mathrm{XY^+ + e \rightarrow X^* + Y^*}$$

$$\mathrm{X^* \rightarrow X + h\nu}$$

For a diatomic molecular ion XY^+, atomic fragment products are X and Y, and kinetic energy release ΔE. Because the initial potential energy of the ion is usually 4 to 9 eV above the lowest dissociation limit of the neutral XY molecule, ample energy is available to leave some or all of the products X and Y in electronically excited states (or in rotationally or vibrationally excited states if they are molecules instead of atoms). Hot oxygen atoms in the exosphere of Mars and Venus results from the DR of O_2^+ [e.g., *Fox and Hac*, 2009].

1.3 Overview on dayglow emissions on Mars and Venus

1.3.1 Observations

Airglow spectra of Mars and Venus resemble each other as a consequence of the similar chemical composition of the atmosphere of the two planets. However, the intensities and the spatial distribution of the emissions reflect differences in distance from the Sun, total atmospheric pressure, N_2/CO_2 and O/CO_2 ratios, and dynamical processes [*Fox*, 1992]. Since, the atmospheres of Mars and Venus is CO_2 dominated, the dayglow emanating from the upper atmosphere of these two planets is mostly due to the CO_2 and its dissociated products. Experiments designed to measure airglow intensities on Mars and Venus using spacecraft have been carried out since 1967. Table 1.2 shows the list of spacecraft airglow experiments carried out on Mars and Venus. The dayglow measurements on Mars and Venus have also been made by several space-borne telescopes [*Feldman et al.*, 2000; *Krasnopolsky*, 2007; *Hubert et al.*, 2010, 2012]. A brief review of dayglow observations on Mars and Venus is given below.

Mars

First spacecraft to visit Mars was Mariner 4 in July 1965. Since then, several spacecraft have visited Mars. Figure 1.4 shows the various planetary missions to Mars, along

Table 1.2: Airglow Experiments on missions to Mars and Venus.

Spacecraft	Date	Instrument	Reference
		Mars	
Mariner 6 and 7	July–Aug. 1969	Ebert-Fastie scanning spectrometer Range: 1100–2100 Å 1900–4300 Å (20 Å resolution)	*Pearce et al.* [1971]
Mariner 9	Nov. 1971– Oct. 1972	Ebert-Fastie scanning spectrometer Range: 1100–3500 Å	*Hord et al.* [1970]
Mars 2 and 3	Dec. 1971– Mar. 1972	3-channel filter photometers 1050–1340 Å and 1225–1340 Å	*Dement'eva et al.* [1972]
Mars 5	Feb.–Mar. 1974	Filter photometer (1050–1340 Å) With H and D Cells	*Bertaux et al.* [1975]
		Visible spectrometer (3000–8000 Å)	*Krasnopolsky and Krys'ko* [1976]
Mars Express	Dec. 2003– present	UV and IR spectrometer (SPICAM) 1180–3200 Å and 12000–48000 Å 10000–17000 Å (Nadir looking)	*Bertaux et al.* [2000]
		Venus	
Mariner 5	Oct. 1967	3-channel filter photometer 1050–2200 Å, 1250–2200 Å, and 1350–2200 Å	*Barth et al.* [1967]
Venera 4	Oct. 1967	3-channel filter photometer 1050–1340 Å and 1225–1340 Å	*Kurt et al.* [1968]
Mariner 10	Feb. 1974	Multi-channel UV spectrometer 200–1700 Å	*Broadfoot et al.* [1977]
Venera 9 and 10	Oct. 1975	Visible Spectrometer (3000–8000 Å)	*Krasnopolsky et al.* [1976]
		Lyman alpha filter photometer with H and D Cells	
Venera 11 and 12	Dec. 1978	Multi-channel UV spectrometer 300–1700 Å, 12 Å passband	*Kurt et al.* [1980]
Pioneer Venus	Dec. 1978– 1992	UV spectrometer 1100–1800 Å 1600–3300 Å; (13 Å resolution)	*Stewart* [1980]
Venus Express	Apr. 2006– present	UV and IR spectrometer (SPICAV) 1180–3200 Å; 22000–44000 Å; 7000–17000 Å	*Bertaux et al.* [2007]

with level of solar activity (in terms of sunspot numbers) at the time they encountered Mars. The Mariner 4 (1965), Mariner 6 and 7 (1969), Mariner 9 (1971–72), and Viking 1 and 2 (1976–80) missions provided the first quantitative knowledge about the structure, energetics, and dynamics of the Mars atmosphere [*Kloire et al.*, 1965; *Barth et al.*, 1969, 1971, 1972; *Nier and McElroy*, 1976; *Stewart et al.*, 1972; *Stewart*, 1972].

Mariner 6 and 7 flybys provided the first measurements of UV airglow emissions on Mars. This was followed by Mariner 9 orbiter observations. The Mariners 6, 7, and 9 ultraviolet spectrometers covered a range of 1200–4000 Å. Mariner 6 and 7 instruments measured the dayglow spectra in the wavelength range 1100–2100 Å with 10 Å resolution and from 1900 to 4300 Å with 20 Å resolution [*Pearce et al.*, 1971]. Mariner 9 ultraviolet

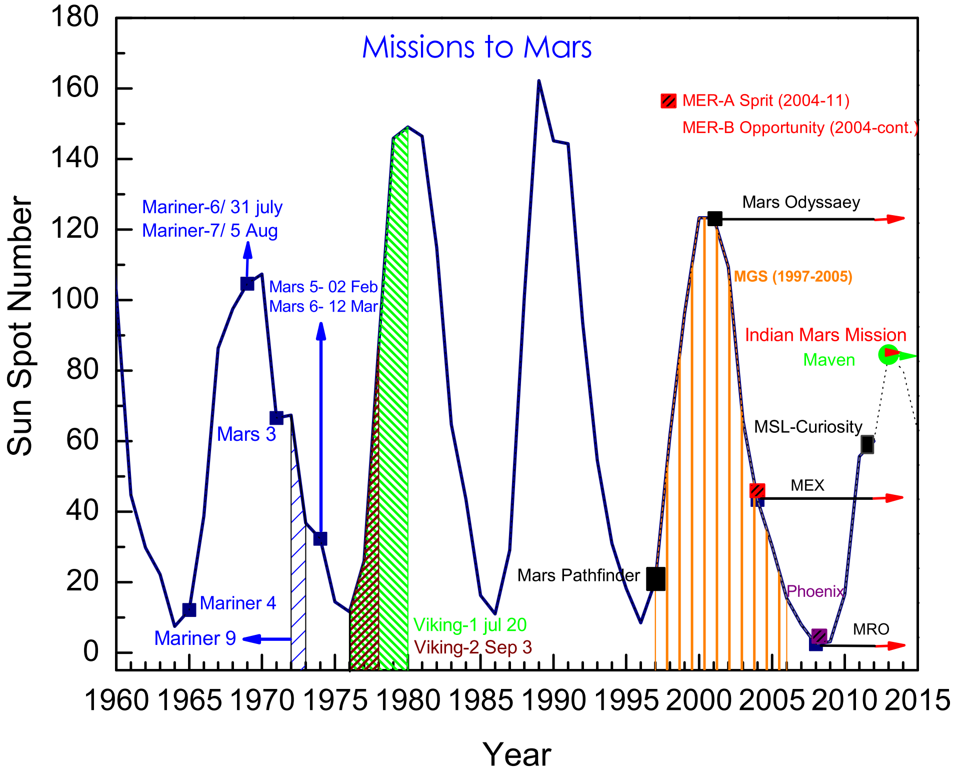

Figure 1.4: Yearly mean sunspot numbers for the period 1960–2012 and the various planetary missions to Mars. Sunspot numbers for years 2013-2015 (dotted curve) are taken from `http://www.swpc.noaa.gov/ftpdir/weekly/Predict.txt`.

spectrometer (which was similar to that flown on Mariner 6 and 7) recorded the Martian dayglow spectra between 1100 and 3500 Å at 15 Å resolution for 120 days. Figures 1.5 and 1.6 show the spectra recorded by Mariner 6 and 7, and Figures 1.7 and 1.8 show the Mariner 9 observations. Data on the thermal structure and composition of the upper atmosphere and their variations were obtained [*Barth et al.*, 1971, 1972; *Stewart*, 1972; *Stewart et al.*, 1972; *Anderson*, 1974; *Stewart et al.*, 1992], and abundances of CO_2, O, CO, and H in the thermosphere and O_3 in the lower atmosphere were measured. The best quality UV spectra of Mars were obtained by using the Hopkins Ultraviolet Telescope (HUT) [*Feldman et al.*, 2000] and Far Ultraviolet Spectroscopic Explorer (FUSE) [*Krasnopolsky and Feldman*, 2002] Earth-orbiting observatories. However, these spectra were not spatially resolved. Table 1.3 shows the major emission features observed by various instruments on Mars.

The emission features observed by Mariner 6, 7, and 9 were: H Lyman-α at 1216 Å, OI 1304 and 1356 Å, CI 1561 and 1657 Å, the fourth positive ($A^1\Pi - X^1\Sigma^+$) and Cameron bands ($a^3\Pi - X^1\Sigma^+$) of CO, and ultraviolet doublet ($B^2\Sigma^+ - X^2\Pi$) and Fox-Duffendack-Barker ($A^2\Pi - X^2\Pi$) bands of CO_2^+ [*Stewart*, 1972; *Barth et al.*, 1972]. Soviet orbiters Mars 2 and 3 measured H Lyman-α and OI 1304 Å emissions between 1971 and 1972 [*Dement'eva et al.*, 1972]. After the Mariner and Mars series of spacecraft,

Table 1.3: Major dayglow emission features observed on Mars and Venus

Species	Transition	Band System	Observed		References
		(Wavelength)	Mars	Venus	
CO_2^+	$B^2\Sigma_u^+ \rightarrow X^2\Pi_g$	UV doublet (2883, 2896 Å)	Yes	Yes	*Stewart* [1972] *Leblanc et al.* [2006]; *Chaufray et al.* [2012]
	$A^2\Pi_u \rightarrow X^2\Pi_g$	Fox-Duffendack-Barker (2800–5000 Å)	Yes	No	*Stewart* [1972] *Leblanc et al.* [2006]
CO	$a^3\Pi \rightarrow X^1\Sigma^+$	Cameron bands (1900–2700 Å)	Yes	Yes	*Stewart* [1972] *Leblanc et al.* [2006]; *Chaufray et al.* [2012]
	$A^1\Pi \rightarrow X^1\Sigma^+$	Fourth Positive Bands (1200–2800 Å)	Yes	Yes	*Leblanc et al.* [2006] *Feldman et al.* [2000]; *Krasnopolsky and Feldman* [2002]
	$C^1\Sigma^+ \rightarrow X^1\Sigma^+$	Hopfield Birge bands ((0,0) at 1088 Å)	Yes	Yes	*Feldman et al.* [2000] *Feldman et al.* [2000]
	$B^1\Sigma^+ \rightarrow X^1\Sigma^+$	Hopfield Birge bands ((0,0) at 1152 Å)	Yes	Yes	*Feldman et al.* [2000]
CO^+	$B^2\Sigma^+ \rightarrow X^2\Sigma^+$	First Negative (2100–2700 Å)	Yes	No	*Stewart et al.* [1972]
N_2	$A^3\Sigma_u^+ \rightarrow X^1\Sigma_g^+$	Vegard-Kaplan (1500–6500 Å)	Yes	No	*Leblanc et al.* [2006] *Leblanc et al.* [2007]
H	2p → 1s	Lyman$-\alpha$ (1216 Å)	Yes	Yes	*Leblanc et al.* [2006] *Chaufray et al.* [2012]
OI	$^1S \rightarrow {}^3P$	(2972 Å)	Yes	Yes	*Stewart* [1972] *Leblanc et al.* [2006]; *LeCompte et al.* [1989]
	$^3S \rightarrow {}^3P$	(1302, 1304, 1306 Å)	Yes	Yes	*Leblanc et al.* [2006]; *Feldman et al.* [2000]
	$^5S \rightarrow {}^3P$	(1356, 1358 Å)	Yes	Yes	*Leblanc et al.* [2006]; *Feldman et al.* [2000]; *Krasnopolsky and Feldman* [2002]
	$^3P \rightarrow {}^3D^0$	(989 Å)	Yes	Yes	*Feldman et al.* [2000]; *Krasnopolsky and Feldman* [2002]; *Gérard et al.* [2011a]
	$^3P^0 \rightarrow {}^3S^0$	(1040 Å)	Yes	Yes	*Feldman et al.* [2000]; *Gérard et al.* [2011a]
	$^1D \rightarrow {}^1D^0$	(1152 Å)	Yes†	Yes†	*Feldman et al.* [2000]; *Gérard et al.* [2011a]
OII	$^4S \rightarrow {}^4P$	(834 Å)	Yes	Yes	*Feldman et al.* [2000]; *Gérard et al.* [2011a]

Note– Apart from above mentioned emissions, HeI, HeII, CI, NI, and OI lines have been observed on Mars and Venus [*Broadfoot et al.*, 1974; *Kurt et al.*, 1980; *Feldman et al.*, 2000; *Krasnopolsky and Feldman*, 2002; *Leblanc et al.*, 2006; *Hubert et al.*, 2012].

†Includes blended CO B–X (0-0) emission.

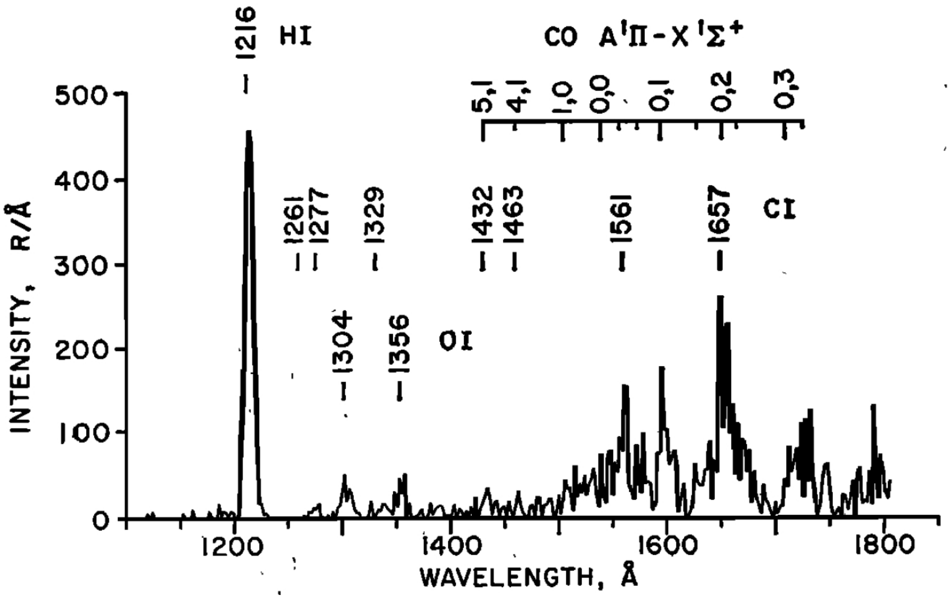

Figure 1.5: The spectrum of Mars from 1100 to 1800 Å at 10 Å resolution. The data are the average of four limb profiles obtained by Mariner 6 and 7 and binned over the tangent point altitude range 160 to 180 km [*Barth et al.*, 1971].

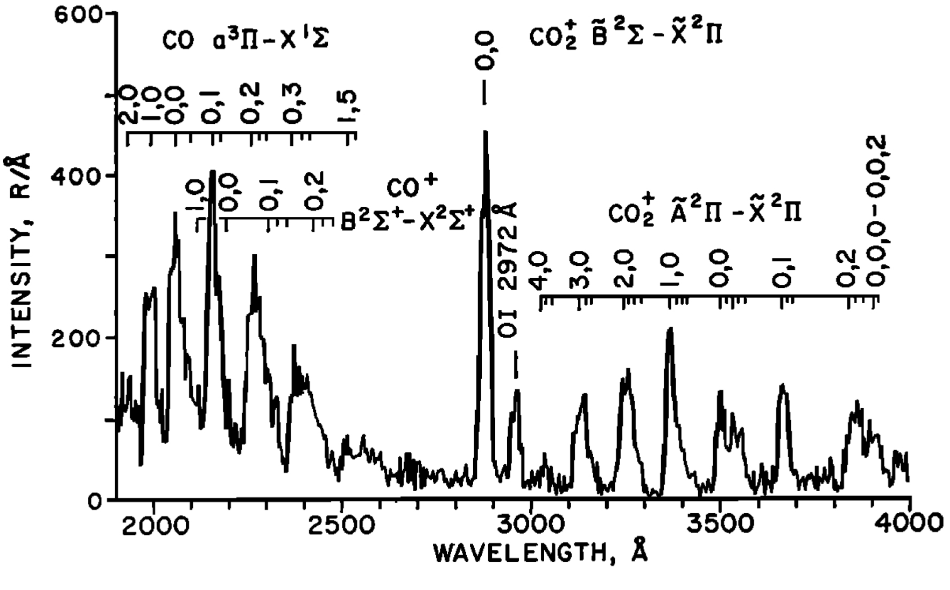

Figure 1.6: Same as Figure 1.5. The spectrum of Mars from 1900 to 4000 Å at 20 Å resolution [*Barth et al.*, 1971].

the next set of airglow observations are carried out more than three decades later by Mars Express (MEx). MEx, the first planetary mission attempted by European Space Agency (ESA), provided continuous airglow measurements of Mars [*Bertaux et al.*, 2006; *Leblanc et al.*, 2006; *Shematovich et al.*, 2008; *Simon et al.*, 2009; *Cox et al.*, 2010; *Gronoff et al.*, 2012a]. MEx carried a dedicated instrument SPectroscopy for the Investigation of the Characteristics of the Atmosphere of Mars (SPICAM) for airglow measurements. SPICAM has broaden our understanding about Martian dayglow. Dayglow emissions observed by SPICAM in UV wavelengths include H Lyman-α, atomic oxygen emissions

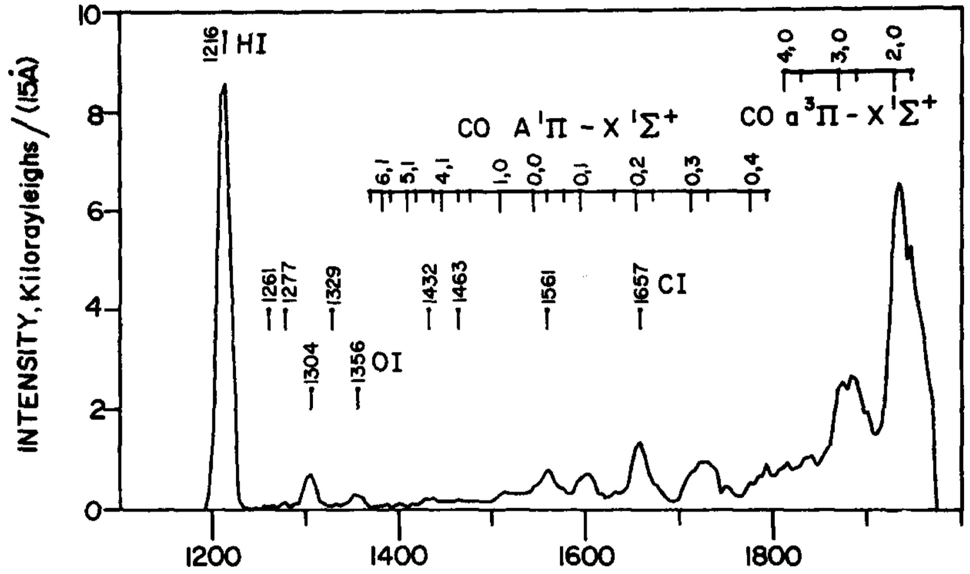

Figure 1.7: The spectrum of Mars from 1100 to 2000 Å at 15 Å resolution obtained by Mariner 9. The spectrum is the result of averaging 120 individual limb observations for a tangent altitude range of 100 to 150 km [*Barth et al.*, 1972].

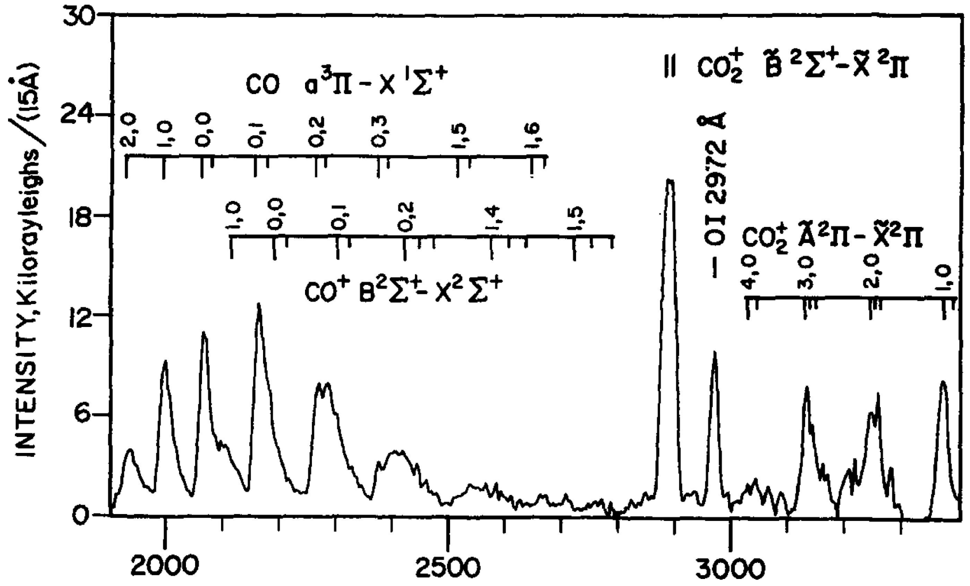

Figure 1.8: Same as Figure 1.7. The spectrum of Mars from 2000 to 3400 Å at 15 Å resolution obtained by Mariner 9 [*Barth et al.*, 1972].

at 1304 and 2972 Å, Cameron and Fourth Positive bands of CO, CO_2^+ ultraviolet doublet $(B - X)$, and several CI lines emissions [cf. *Leblanc et al.*, 2006; *Chaufray et al.*, 2008b]. Figure 1.9 shows the Martian dayglow spectra from 1200–3000 Å recorded by SPICAM. These emission features are similar to those observed by Mariner 6, 7, and 9 but with better sensitivity, and spatial and temporal coverage. Though first negative bands of CO^+ are shown in Figures 1.6 and 1.8, these features were missing in the synthetic spectra constructed by *Conway* [1981]. The observations recorded by SPICAM/MEx have not shown any emission features of CO^+ first negative band.

SPICAM has observed dayglow emissions on Mars throughout the Martian year and

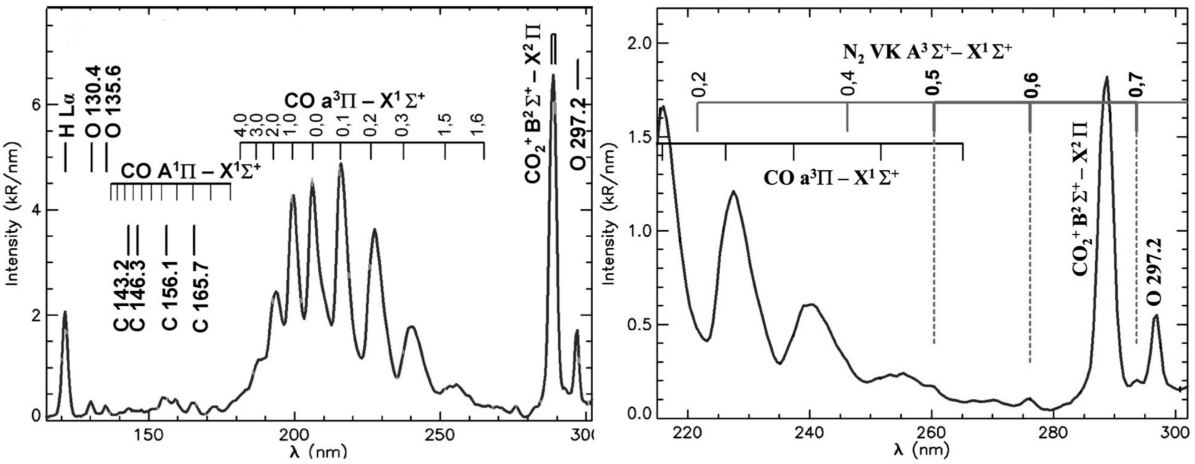

Figure 1.9: The spectrum of Mars from 1200 to 3000 Å obtained by SPICAM onboard Mars Express. The right panel shows the N_2 VK bands in the dayglow of Mars. This spectra is taken from *Leblanc et al.* [2006].

showed the effect of Solar Zenith Angle (SZA) and seasonal variation on emission features [*Leblanc et al.*, 2006, 2007; *Shematovich et al.*, 2008; *Simon et al.*, 2009; *Cox et al.*, 2010]. SPICAM also provided first observation of N_2 UV emissions in Martian dayglow [*Leblanc et al.*, 2006, 2007]. N_2 Vegard-Kaplan (VK) (0, 5) and (0, 6) band emissions at 2604 and 2762 Å, respectively, have been observed; N_2 VK (0, 7) emission at 2937 Å has also been reported, but it has large uncertainty [*Leblanc et al.*, 2007]. Figure 1.9 (right panel) shows the N_2 VK bands in Martian dayglow measured by SPICAM. The effect of dust storm on dayglow emission intensities on Mars has been observed by both Mariner 9 and MEx [*Stewart et al.*, 1972; *Cox et al.*, 2010]. A planetwide dust storm on Mars can heat the lower atmosphere and raise the altitude of the atmosphere [*Forget et al.*, 2009; *Bougher*, 1995], the effect of which can be seen in the scale height of dayglow emission features.

Venus

Several spacecraft, viz., Mariner 5 (3-channel photometer: 1050–2200 Å, 1250–2200 Å, 1350–2200 Å); Venera 4 (1050–1340 Å, 1225–1340 Å); Mariner 10 (200–1700 Å); Venera 9 and 10 (visible spectrometers 3000–8000 Å and Lyman α filter photometer); Venera 11 and 12 (300–1700 Å); Pioneer Venus Orbiter (PVO) (1100–1800 Å and 1600–3300 Å); Cassini (561–1182 Å and 1155–1913 Å) have visited Venus so far. Figure 1.10 shows the various planetary missions to Venus, along with level of solar activity (in terms of sunspot numbers) during which they encountered Venus.

Currently, the VEx is orbiting Venus which has an experiment SPectroscopy for the Investigation of the Characteristics of the Atmosphere of Venus (SPICAV) (1100–3100 Å, 7000–17000 Å, 23000–42000 Å) for aeronomical studies of Venusian atmosphere. The major emission detected in the dayglow of Venus includes HeI 584 Å and HeII 304 Å

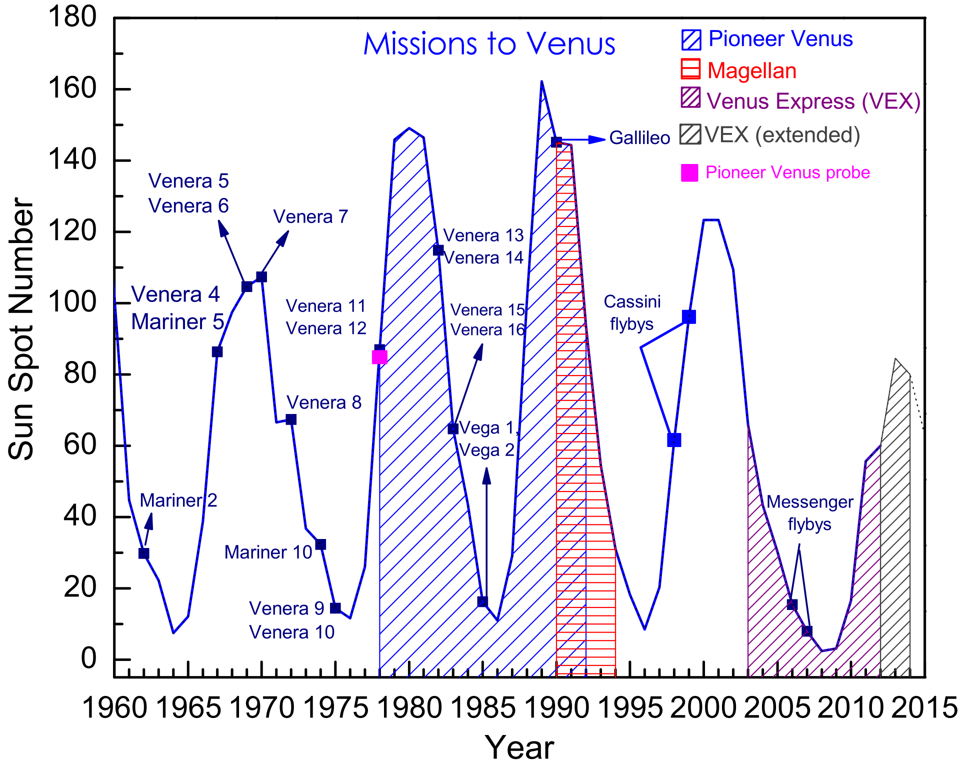

Figure 1.10: Yearly mean sunspot numbers for the period 1960–2012 and the various planetary missions to Venus. Sunspot numbers for years 2013-2015 (dotted curve) are taken from `http://`www.swpc.noaa.gov/ftpdir/weekly/Predict.txt.

lines; OI 989 Å, OI 1304 Å triplet, OI 1356 Å, OI 2972 Å; OII 834 Å; CI 1561 and 1657 Å; H Lyman-α; Cameron, Fourth Positive and Hopfield–Birge bands of CO; and CO_2^+ UV doublet [e.g., *Kurt et al.*, 1968; *Barth et al.*, 1967; *Broadfoot et al.*, 1974, 1977; *Bertaux et al.*, 1981; *LeCompte et al.*, 1989; *Gérard et al.*, 2011a, b; *Hubert et al.*, 2012; *Chaufray et al.*, 2012]. These missions have made remote and global in-situ measurements of the composition, airglow, and temperature, giving insight into the energetics and dynamics of the thermosphere of the Venus. A review of past observations of Venus missions is given by *Fox and Bougher* [1991]. Table 1.3 shows few major dayglow emissions on Venus.

Rottman and Moos [1973] measured the first spectrum of the Venus ultraviolet dayglow in the 1200–1900 Å range using a moderate resolution spectrometer flown on a rocket. They identified H Lyman-α, OI 1304 and 1356 Å features, CO Fourth Positive bands and CI 1561 Å and 1657 Å line emissions. Mariner 10 carried out a multichannel spectrometer observations in February, 1974 and measured emission features in 200–1700 Å range [*Broadfoot et al.*, 1977]. Venera 11 and 12 flyby spacecraft also carried spectrometers similar to that mounted on Mariner 10, but more sensitive than the Mariner 10 instrument [*Bertaux et al.*, 1981]. The features detected by Mariner 10 and Venera 11 and 12 were He 584 Å, H Lyman-α (1216 Å), OI 1304 Å triplet, CI 1657 Å, and CO Fourth Positive bands in a wavelength range around 1500 Å [*Broadfoot*

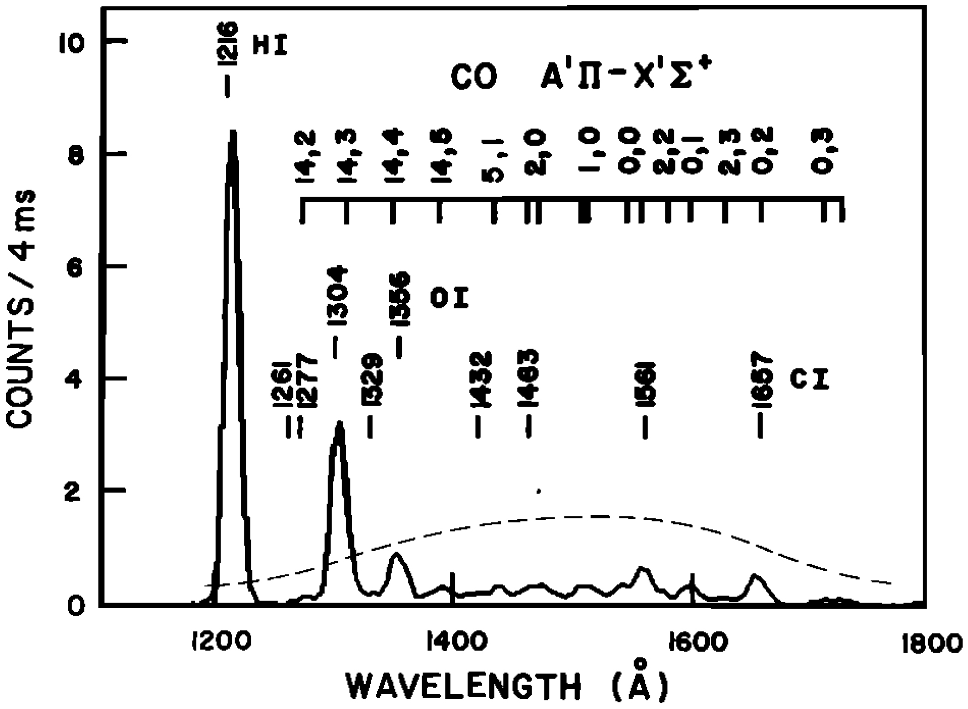

Figure 1.11: Dayglow spectrum of Venus in the range 1100–1800 Å recorded by Pioneer Venus Orbiter Ultraviolet Spectrometer. From *Durrance* [1981].

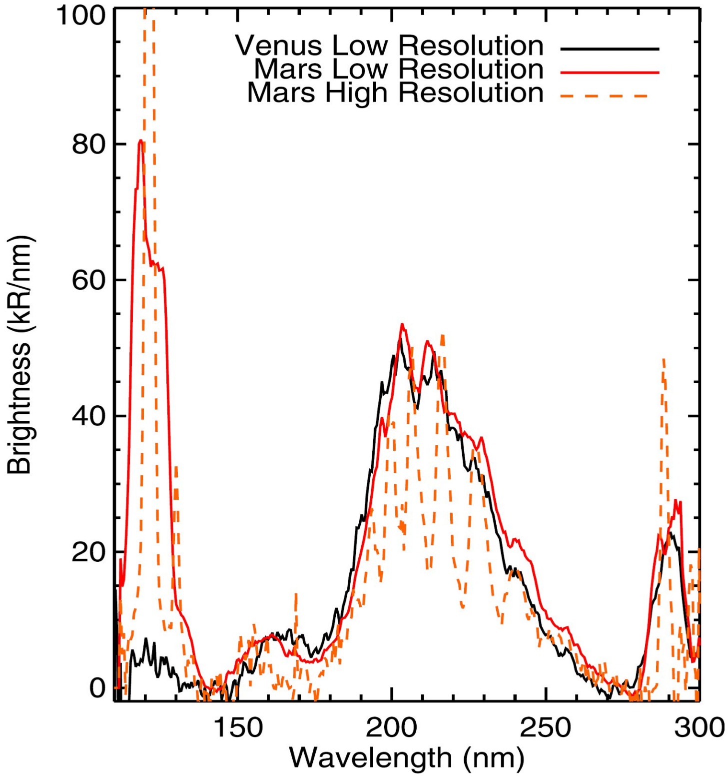

Figure 1.12: Venusian dayglow profile obtained by SPICAV/Venus Express (black curve) at 10 nm spectral resolution. Martian dayglow observed by SPICAM/MEx between 160–180 km is also shown at the 10 nm spectral resolution (solid red line) and 1.5 nm spectral resolution (dashed orange line). Martian dayglow profiles are multiplied by a factor of 120. This figure is taken from *Chaufray et al.* [2012].

et al., 1974; *Kurt et al.*, 1980; *Fox and Bougher*, 1991]. Venera 11 and Venera 12 also detected HeII 304 Å line emission [*Kurt et al.*, 1980]. The Pioneer Venus Orbiter (PVO) was one of the most successful planetary missions till date. Pioneer Venus Orbiter Ultraviolet Spectrometer (PVOUVS) recorded Venusian dayglow and nightglow spectra during 1978–1992. Figure 1.11 shows the dayglow spectrum of Venus in the range 1100–1800 Å recorded by PVOUVS. *LeCompte et al.* [1989] have reported observation of OI 2972 Å emission by PVOUVS in the dayglow of Venus. Cassini UVIS spectrometer made observations during the Venus flyby in June 1999 covering the EUV (56.3-118.2 nm) and FUV (111.51–91.2 nm) spectral range at 0.37 nm resolution [*Gérard et al.*, 2011a; *Hubert et al.*, 2010, 2012]. Several new lines were identified associated to HI (97.3 nm, 102.6 nm), OI (98.9 nm, 104 nm), NI (91.9 nm, 109.7, 113.4, 119.2, 120.0 nm), CI(111.4 nm, 115.8 nm, 126.1 nm, 127.7 nm), CII (133.5 nm) and CO (108.8, 115.2, 159.7 nm and possibly 107.6 nm) [*Gérard et al.*, 2011a; *Hubert et al.*, 2010, 2012]. Despite year round observations by PVO from the orbit around Venus, CO Cameron band and CO_2^+ UV doublet emission were never observed by PVOUVS [*Fox and Dalgarno*, 1981; *Fox and Bougher*, 1991]. *Stewart et al.* [1979] identified a possible CO Cameron band emission at 206.8 nm in the nightglow of Venus, but full band was not observed on Venus by PVO as observed on Mars by Mariner spacecraft (and later by SPICAM/MEx). Very recently, *Chaufray et al.* [2012] have reported the first observation of CO Cameron band and CO_2^+ UV doublet emissions in the dayglow of Venus. Figure 1.12 shows the dayglow spectrum of Venus observed by SPICAV [*Chaufray et al.*, 2012]. A low and high resolution dayglow spectra of Mars obtained by SPICAM is also shown in Figure 1.12, indicating similarity in dayglow emission features on the two planets as expected due to similar composition of their upper atmospheres. More information on CO Cameron band and CO_2^+ UV doublet emissions on Mars and Venus is provided in Chapter 4.

1.3.2 Modelling studies

Several theoretical studies have been made for the production of excited species in the upper atmospheres of Mars. On the basis of laboratory experiments and observed spectrum, *Barth et al.* [1971] have proposed possible excitation mechanisms for various dayglow emission features observed on Mars by Mariner 6 and 7. They concluded that with the exception of HI 1216 Å, OI 1304 Å lines and a part of the CO_2^+ $(A-X)$ bands, all the emissions in the Martian atmosphere may be produced by the action of solar photons and photoelectrons on CO_2. *Conway* [1981] analysed the Mars airglow spectra obtained by ultraviolet spectrometer on board Mariner 9 spacecraft by using the high-resolution synthesis of observed emissions. They found that the shape of CO Cameron band can not be characterized by a single rotational temperature but two temperatures: 1600°K for lower values of J (rotational quantum number) and 10000°K for higher J values. Based on the comparison of theoretical zenith intensity of Cameron bands with the Mariner 9 observation, *Conway* [1981] suggested a $CO(a^3\Pi)$ cross section value of 7×10^{-17} cm^2 for electron impact dissociation of CO_2 (see Chapter 4 for more details).

Theoretical calculations of the different ultraviolet dayglow emissions on Mars for the conditions of Viking 1 measurements (low solar activity) were made by *Mantas and*

Hanson [1979] and *Fox and Dalgarno* [1979a]. *Fox and Dalgarno* [1979a] also made a detailed assessments of heating of neutral and ionized component of atmosphere arising due to the absorption of solar ultraviolet radiation. The emissions considered in their study include Cameron and fourth positive bands of CO, Fox-Duffendack-Barker ($A-X$) and ultraviolet double ($B-X$) of CO_2^+, OI (2972, 5577, and 6300 Å), and CI (1329, 1657, and 1561 Å), and CII 1335 Å line emissions. *Fox and Dalgarno* [1979a] also calculated emissions from N_2 triplet bands. Ultraviolet emission from one of the triplet states (N_2 Vegard-Kaplan band) have been observed in the Martian dayglow [cf. *Leblanc et al.*, 2006, 2007] more than two decades later since *Fox and Dalgarno*' study. A detailed review of airglow and aurora in the atmosphere of Mars and Venus is given in *Fox* [1992].

Recently, theoretical calculations have been carried by several groups [*Shematovich et al.*, 2008; *Simon et al.*, 2009; *Cox et al.*, 2010; *Huestis et al.*, 2010; *Gronoff et al.*, 2012a], to explain the recent measurements obtained by using SPICAM. *Shematovich et al.* [2008] have used Monte Carlo model to solve the Boltzmann equation and calculated the electron transport in the atmosphere of Mars. They have used Mars Thermospheric General Circulation Model (MTGCM) for the conditions similar to that of SPICAM observations. *Shematovich et al.* [2008] have calculated brightness profiles of CO Cameron band and CO_2^+ doublet emission and compared their results with the SPICAM observation. They also predicted seasonal variations of CO Cameron band and CO_2^+ UV doublet emissions on Mars.

Simon et al. [2009] have used numerical one-dimensional kinetic model Trans-Mars to calculate photoelectron flux in the Martian atmosphere. They compared their model calculated brightness profiles of CO Cameron band and CO_2^+ doublet emissions with the SPICAM observation for low solar activity condition. The shape of brightness profiles and altitude of emission peak calculated by *Simon et al.* [2009] is in good agreement with the SPICAM observation, when the Viking CO_2 density is divided by a factor of 3. However, intensities of CO Cameron band and CO_2^+ doublet emissions calculated by *Simon et al.* [2009] are about 25% and 15%, respectively, higher than the SPICAM-observed intensities. *Simon et al.* [2009] have attributed this discrepancy in calculation and observation to geometrical factors and limitation of their one dimensional model.

Cox et al. [2010] have used the airglow model of *Shematovich et al.* [2008] to study the Martian dayglow for one specific season ($Ls = 90°$ to $180°$). Their model calculations overestimate the CO Cameron band and CO_2^+ doublet brightness intensity by a factor of 1.74 and 1.41, respectively. According to *Cox et al.* [2010], these discrepancies may be due to the uncertainties in the electron impact cross section of $CO(a^3\Pi)$ and photon impact excitation cross section of $CO_2^+(B^2\Sigma_u^+)$ production. Their model was also unable to simulate the measured altitude peak of CO Cameron band and CO_2^+ UV doublet emissions for Ls values between 90° and 135°, due to the difference in actual CO_2 density and the profile used in their model calculation.

Recently, *Gronoff et al.* [2012a, b] have calculated the production of excited species and brightness profiles of CO Cameron band, CO_2^+ UV doublet, and OI 2972 Å emissions on Mars. They have used Aeroplanet model for dayglow calculation on Mars. Aeroplanet model is restructured and enhanced version of the Trans-* model series (e.g., Trans-Mars, Trans-Venus) [*Lummerzheim and Lilensten*, 1994], which have been used by Gronoff and Co-workers to calculate the excited species production in the atmospheres of Mars and Venus [*Gronoff et al.*, 2008; *Simon et al.*, 2009; *Nicholson et al.*, 2009]. *Gronoff et al.* have used Monte Carlo model to calculate the model uncertainties due to different model input parameters in calculating the excited species production in the atmosphere of Mars. *Gronoff et al.* [2012a] have calculated the brightness profiles of OI 2972 Å, CO Cameron band, and $CO_2^+(B^2\Sigma_u^+)$ doublet emissions and compared their results with the SPICAM observation.

Modelling studies of emissions from sunlit atmosphere of Venus have been made since seventies onward. *Cravens et al.* [1978] calculated the emission rates of major dayglow features on Venus to predict the emission intensities that PVO would be able to observe. They have used two stream technique [*Nagy and Banks*, 1970] for electron precipitation in the atmosphere of Venus. They calculated brightness profiles of Cameron and Fourth Positive bands of CO, CO^+ First Negative band, and CO_2^+ $A-X$ and $B-X$, emissions at SZA = 60°. *Fox and Dalgarno* [1981] presented a detailed model calculation of dayglow emissions on Venus based on PVO data. This model was very similar to the one that *Fox and Dalgarno* [1979a] developed for Mars. *Fox* [1982] calculated the production of metastable species and subsequent emissions in the Venusian ionosphere. A detailed review of observations and models related to different dayglow emissions on Venus was given by *Fox and Bougher* [1991]. A model for Venus ionosphere for low (F10.7 = 80) and high (F10.7 = 200) solar activity conditions have been presented by *Fox and Sung* [2001]. Their calculations include production of several ions and metastable species in the ionosphere of Venus.

Gronoff et al. [2008] have used Trans-Venus model to calculate the production of ions and excited species in the atmosphere of Venus. Their model was proposed to calculated dayglow and nightglow emissions of the upper atmosphere of Venus. Using the Monte Carlo technique used by *Shematovich et al.* [2008] to model Mars dayglow, *Gérard et al.* [2008a] have modelled OI 1304 and OI 1356 Å emissions in the Venusian dayglow and aurora. They compared their model calculated intensities with the PVOUVS and HUT observations. This group used this numerical model to explain the Far Ultraviolet (FUV) observations of Venus made by Ultraviolet Imaging Spectrograph (UVIS) on board Cassini [*Hubert et al.*, 2010, 2012; *Gérard et al.*, 2011a].

1.4 Model for dayglow emissions

Modelling of dayglow emissions, aided by laboratory studies and observations, are essential tool to understand the underlying chemical and physical processes occurring in the upper atmosphere of a planet. Figure 1.13 shows the synopsis of model for dayglow emissions. The initial input of the model is the solar Extreme Ultraviolet (EUV) and FUV photon flux which ionizes, dissociates, or excites the atom and molecules present in the upper atmosphere. The solar flux and altitudinal distribution of atmospheric constituents are required to calculate the photo excitation rates and photoelectron production rate. The details of solar flux, photoabsorption and photoionization cross section, and electron impact cross sections are provided in Chapter 2. Photoelectrons, generated due to photoionization, start losing their energy in collisions with atmospheric constituents. To study the electron energy degradation in an atmosphere, a technique to simulate the degradation of energy of the electron is required. The inputs of such a technique include the model atmosphere, photoelectron production rate, and electron impact cross sections. Several different techniques are used to degrade the energy of electrons in a gaseous medium. In the present study, the Analytical Yield Spectra (AYS) method, which is based on the output of Monte Carlo model, is used. With the help of AYS, the photoelectron flux is calculated in the atmospheres of Mars and Venus, which is subsequently employed to calculate electron impact excitation/emission rates. Both the photoelectron impact excitation rates and photon impact excitation rates are used

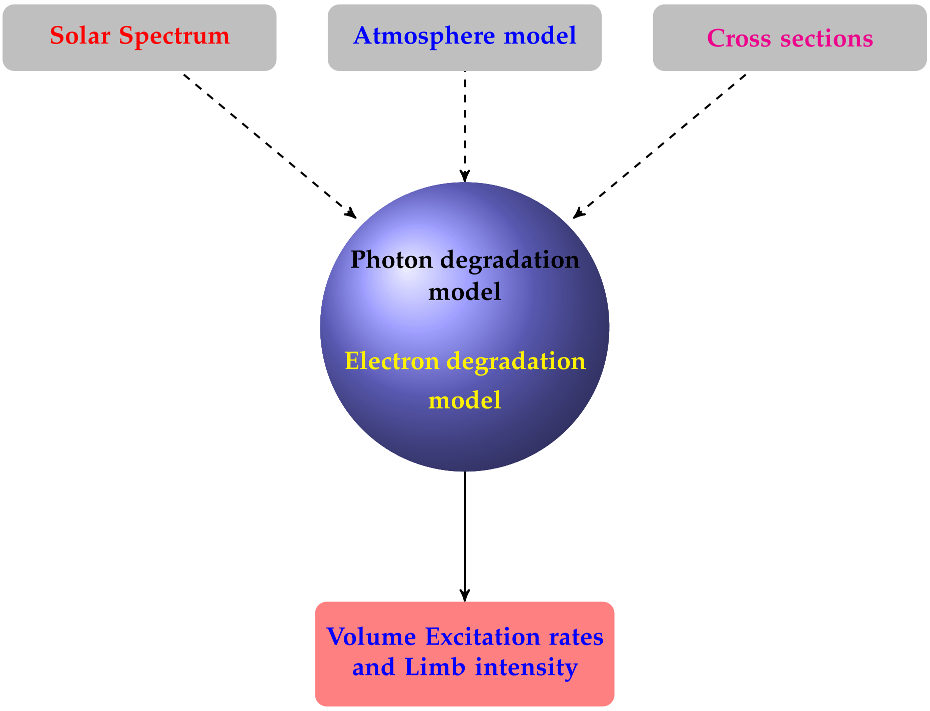

Figure 1.13: Synopsis of model for calculating dayglow emissions.

to obtain the total excitation rate. The volume excitation/emission rates (for optically thin emissions) can be integrated along the line of sight to calculate the limb intensity, which can be compared with the observation. By comparing model calculations with observations, the model input parameters can be constrained.

1.5 Motivations of this study

It is clearly depicted in Figure 1.12 that the emission features on Mars and Venus are similar, which is due to the similar composition of atmospheres of the two planets. The earlier observations by Mariner 6, 7, and 9, Mars 2, 3, and 5, and Viking 1 and 2 provided basic understanding of Martian upper atmosphere. Most of the earlier modelling calculations of airglow emissions on Mars were carried out using the available input parameters and model atmospheres. Since then, there has been a significant enhancement in our understanding of Martian atmospheric parameters with the help of recent planetary missions to Mars. Also atomic and molecular parameters, viz., cross sections, Einstein coefficients, and Frank-Condon factors have been updated. With the current continuous measurements of dayglow emissions by SPICAM on Mars and by SPICAV on Venus—first set of observations on Venus being reported very recently by *Chaufray et al.* [2012]—new modelling studies of emission features in the atmosphere of Mars and Venus are an essential requirement. Although, the atmospheres of Mars and Venus are dominated by CO_2, there are differences in the mixing ratio of upper atmospheric constituents and neutral density on the two planet. Also due to small (0.72 AU) heliocentric distance, Venus receives about 5 times more solar flux than Mars. One of the motivations of the present work is to make a quantitative assessment of contributions of difference processes in the dayglow emissions on Mars and Venus. As discussed in Section 1.4, model calculated emission intensities directly depend on input parameters such as solar EUV flux, model atmosphere, and cross sections. Evaluation of the effect of various input parameters on emission intensities is also one of the aim of the present study.

1.6 Thesis structure

The work carried out in this thesis is useful for current dayglow observations on Mars and Venus, which are being carried out by Mars Express and Venus Express, respectively, and will be helpful for future planetary missions, e.g., MAVEN and Indian Mars orbiter missions. As seen in Table 1.3, there are several atomic and molecular emissions observed on Mars and Venus. In this thesis, the following emission features on Mars and Venus are studied: CO Cameron band, CO_2^+ UV doublet, N_2 VK and other triplet band, OI 2972 Å and visible green (5577 Å) and red doublet (6300, and 6364 Å) lines.

The details of photoabsorption and photoionization cross sections, electron impact inelastic cross sections, and input solar EUV-FUV flux used in the present study are provided in Chapter 2.

- **Chapter 3: Monte Carlo Model**
  The development of Monte Carlo model for degradation of electrons in a CO_2 atmosphere is described in Chapter 3. The output of Monte Carlo simulation is used to generate the "yield spectra", which embodied all the information related to electron degradation process, and can be used to calculate the "yield" or (population) for any inelastic process. The numerical yield spectra have been fitted analytically resulting in an Analytical Yield Spectra (AYS). Mean energy per ion pair and efficiencies for inelastic processes have been calculated in this chapter using AYS, which compares well with those obtained by using numerical yield spectra. The AYS presented in this chapter is used to calculate steady state photoelectron fluxes in the atmospheres of Mars and Venus in the subsequent chapters.

  Each of the subsequent three chapters addresses a detailed calculation of emissions (UV/visible) emanating from the upper atmospheres of Mars and Venus and also addresses the issue regarding the effect of input parameters on the emission intensities.

- **Chapter 4: CO Cameron band and CO_2^+ UV doublet emissions**
  Chapter 4 focuses on the modelling of CO Cameron band and CO_2^+ UV doublet emissions in the dayglow of Mars and Venus during low, moderate, and high solar activity conditions. The CO Cameron band and CO_2^+ UV doublet emissions are the brightest UV emissions features in the dayglow of Mars and Venus. This chapter also demonstrates the utility and efficiency of the AYS in the atmospheric application. The AYS developed in Chapter 3 is employed to calculate the photoelectron fluxes in the atmospheres of Mars and Venus. These fluxes are then used to obtain the volume excitation/emission rates. The calculated brightness profiles of CO Cameron band and CO_2^+ doublet emissions are compared with observed profiles by SPICAM and SPICAV on Mars and Venus, respectively. The effect of solar EUV flux models on the intensities of CO Cameron band and CO_2^+ doublet emissions is also studied. The present study shows that a change in solar EUV flux due to use of different solar flux models can result in 20–40% variation in the calculated UV dayglow emission intensity in the atmospheres of Mars and Venus.

- **Chapter 5: N_2 Triplet band emissions**
  A model for N_2 triplet band emissions in the dayglow of Mars and Venus is developed in Chapter 5. Recently, for the first time, the N_2 Vegard-Kaplan band emission have been observed on Mars. The modelling of these emissions helps in

understanding the processes governing these emissions on Mars and Venus. On Mars, the present calculations show that a reduction in the N_2 density by a factor of 3 in the Mars Thermospheric General Circulation Model is required to obtain an agreement between calculated limb profiles of VK (0-6) emission and SPICAM observation. The calculated intensities on Venus are about a factor of 10 higher than those on Mars. During high solar activity the overhead intensity of N_2 triplet emission on Mars and Venus is $\sim$2 to 3 times higher than that during low solar activity condition. As a case study, the N_2 triplet band calculation model is applied to Titan to explain the recent Cassini UVIS observations. The model calculated limb intensity of N_2 VK emission in the 150–190 nm wavelength region on Titan is in good agreement with the Cassini UVIS–observed limb profile.

- **Chapter 6: OI UV (2972 Å), and visible (5577, 6300 Å) emissions**
  A detailed model of atomic oxygen UV 2972 Å $O(^1S \rightarrow {}^3P)$ and visible (green and red lines) emissions is presented in Chapter 6. The OI 2972 Å emission has been observed on both Mars and Venus [*Leblanc et al.*, 2006; *LeCompte et al.*, 1989]. The OI 2972 Å emission originate from ^1S state of atomic oxygen. Only 10% of $O(^1S)$ atoms decay by emitting photons at 2972 Å wavelength and the remaining 90% decays through $O(^1S \rightarrow {}^1D)$ channel by emitting photons at green (5577 Å) wavelength. The transition from $O(^1D)$ to ground $O(^3P)$ state gives rise to red doublet (6300, 6364 Å) emission. Thus, the presence of OI 2972 Å emission in Martian and Venusian dayglow indicates that atomic oxygen visible emissions should be present on these planets. The recommended yields of $O(^1S)$ and $O(^1D)$ in photodissociation of CO_2 are presented in this chapter. Below 120 km, on Mars and Venus, the main production source of $O(^1D)$ is photodissociation of CO_2, while at higher altitudes dissociative recombination of O_2^+, $O(^1S)$ radiative decay, and photodissociation of CO_2 are the major sources. On Mars, during both solar minimum and maximum conditions, the main production mechanism of $O(^1S)$ is photodissociation of CO_2, while on Venus photodissociation of CO_2 is the major source of $O(^1S)$ production below 160 km only. Above that altitude, the contributions of dissociative recombination of O_2^+ and electron impact on O increase significantly. The present calculations show that the major loss process for $O(^1S)$ is radiative decay, while for $O(^1D)$, its quenching by CO_2. The effect of $O_2^+(\nu)$ vibrational distribution on $O(^1S)$ and $O(^1D)$ production is found to be negligible. On Mars, the calculated OI 2972 Å emission profiles are in agreement with the Mariner and Mars Express observations.

A summary of entire work carried out in this thesis along with some future projections is presented in Chapter 7.

Chapter 2

Electron and photon impact cross sections and solar flux models

2.1 Introduction

The regions of the solar spectrum that are absorbed in the thermospheres and upper mesospheres of the planets are generally characterized by wavelengths less than 2000 Å. Modelling of dayglow emissions requires a sophisticated input solar soft X-rays (XUV) and Extreme Ultraviolet (EUV)-Far Ultraviolet (FUV) flux. Solar flux is a fundamental parameter needed to model physics, chemistry and dynamics of the upper atmosphere of planets. Since observations of solar EUV irradiance are not frequent and generally not available simultaneously with the observation for the upper atmospheric studies, the solar EUV-FUV flux model become important for modelling of aeronomical quantities in planetary atmospheres. A brief description of solar EUV-Ultraviolet (UV) flux models used in the study of various dayglow emissions in atmospheres of Mars and Venus is presented in Section 2.2.

Solar photons in the wavelength range 10–1000 Å are mainly responsible for the ionization of most of gases that are present in the atmosphere. Hence, the generation of photoelectron and its energy depends on the incoming solar radiation and its interaction with the atmospheric constituents. Thus, it is important to have the knowledge of photoabsorption and photoionization cross sections of species under consideration to model the attenuation of solar radiation as its traverse through atmosphere. The brief description of photoabsorption and photoionization cross sections of major atmospheric gases in the atmospheres of Mars and Venus is given in the Section 2.3.

The ionization process creates secondary electron which carries excess energy of the photon that has ionized the species. Photoelectrons, generated due to photoionization process, can have enough kinetic energy to ionize the atmospheric constituents and produce secondary electrons. Similarly, energetic electrons precipitating along the magnetic field lines into the auroral atmosphere of planets can ionize the medium producing secondary electrons. Besides ionization, the electron energy is lost in excitation, dissociation, attachment, and heating. Hence, the study of electron energy deposition in atmosphere is an important aspect in understanding processes like aurora, dayglow, and nightglow.

The study of electron energy deposition in CO_2 gas is of particular interest to the atmosphere of Mars and Venus, which are dominated by the CO_2 (95%), and to the other CO_2-containing atmospheres, e.g., comets. To study the degradation of electrons in a gaseous medium two important tasks have to be accomplished. First compilation of various elastic and inelastic cross sections, and second, use of an apportionment method to degrade electron and distribute its energy in various loss channels. In this Chapter a detailed review of the literature on electron impact cross sections of CO_2 is presented (see Section 2.4). Besides CO_2, a brief description of electron impact cross sections for other gases (viz., N_2, CO, O, O_2) present in the atmospheres of Mars and Venus is presented in Section 2.5. The second task, i.e., the electron energy apportionment method, will be discussed in Chapter 3.

2.2 Solar flux models

Since the solar EUV radiation initiates and controls the majority of chemical, dynamical, and radiative processes observed in the planetary upper atmosphere, the variation in this radiation is responsible for much of the variability observed in atmospheric processes in planetary thermosphere. The solar XUV-EUV flux is very small (about 5 orders of magnitude) compared to the visible part of the solar spectrum, but the solar cycle variability of this wavelength region is much greater than the rest of the spectrum. Characterization of the solar EUV flux for use in aeronomical and ionospheric studies was developed during seventies based on the Atmospheric Explorer-E (AE-E) data [*Hinteregger*, 1976; *Hinteregger et al.*, 1981; *Torr and Torr*, 1985]. Two AE-E reference spectra SC#21REF and F79050N have been published by *Torr and Torr* [1985] at 37 wavelength bins for solar minimum and maximum conditions, respectively. Many models still use the binning of the spectrum that was first proposed by *Torr et al.* [1979]. The success of this approach has to do with its simplicity and the existence of a set of absorption and ionization cross sections for each wavelength bin. A detailed discussion on the development of solar EUV flux models is provided by *Lean* [1990], *Richards et al.* [1994], *Woods et al.* [2005], *Lilensten et al.* [2008], and *Lean et al.* [2011].

Different solar EUV flux models have been used to study the interaction of solar radiation with planetary upper atmosphere, and their effects on atmospheric processes have been studied by several authors. *Fox et al.* [1996] have studied the effect of different solar EUV flux models on calculated electron densities on Mars for low and high solar activity conditions. They have used 85315 and 79050 solar fluxes of *Tobiska* [1991] and SC#21REF and F79050N AE-E reference solar spectra of Hinteregger [*Torr et al.*, 1979] for low and high solar activity conditions, respectively. *Fox et al.* [1996] found that due to smaller fluxes at short wavelength range (18–200 Å) in Hinteregger spectra, lower peak in electron density profile is significantly reduced (30–35%) compared to that calculated using solar flux of *Tobiska* [1991]. *Buonsanto et al.* [1995] calculated ionospheric electron density on Earth using EUV flux model for Aeronomic Calculation (EUVAC) model of *Richards et al.* [1994] and EUV94X solar flux model of *Tobiska* [1994]. They found that photoionization rate in F2 region calculated by using EUV94X model is larger than that calculated using EUVAC model due to the large EUV fluxes in 300–1050 Å wavelength range in EUV94X solar flux model.

For a given solar activity there are significant differences between the EUV fluxes reproduced by different solar flux models. These models are based on the different input parameters and proxies, e.g., 10.7-cm radio flux (F10.7), Mg II, and Ly-α are used as indices for solar activity, and used for parametrization of solar EUV flux models [*Richards et al.*, 1994; *Tobiska and Barth*, 1990; *Lilensten et al.*, 2008]. Recently, Solar EUV Experiment (SEE) on the Thermospheric Ionospheric Mesospheric Energy and Dynamics (TIMED) spacecraft provided calibrated database of solar EUV irradiance. This data have been used to constrain six solar proxies (Mg II, F10.7, and 0–4, 30.5, 121.5, and 35 nm irradiances) in Flare Irradiance Spectral Model (FISM) [*Chamberlin et al.*, 2009]. *Richards et al.* [2006] have constructed a high resolution version of EUVAC (HEUVAC) based on F10.7 solar proxy. The TIMED SEE data has also been included in the SOLAR2000 (S2K) model [*Tobiska*, 2004] to improve model accuracy in the XUV-EUV spectral region [*Tobiska and Bouwer*, 2006]. These indices only partly describe the multiple facets of solar activity and none of them is truly representative of the variability of the EUV spectrum at all wavelengths [*Dudok de Wit et al.*, 2007]. Therefore, accurate forecasting cannot depend on any of these models, regardless of their (numerous) qualities. In spite of all these limitation solar EUV flux models are very important tool to model aeronomical processes due to non availability of actual solar EUV flux simultaneously with the aeronomical observations.

Presently, S2K model [*Tobiska et al.*, 2000; *Tobiska*, 2004] and EUVAC model of *Richards et al.* [1994] are commonly used solar EUV flux models in aeronomical studies of Mars and Venus; *e.g.*, *Simon et al.* [2009] and *Huestis et al.* [2010] have used EUVAC model, while *Shematovich et al.* [2008], *Gronoff et al.* [2008], and *Cox et al.* [2010] have used S2K model for the dayglow calculations on Mars and Venus, respectively. In the present study, the EUVAC model of *Richards et al.* [1994] and S2K v.2.36 solar EUV model of *Tobiska* [2004] are used.

2.2.1 EUVAC

EUVAC model of *Richards et al.* [1994] is based on solar F10.7 and its 81-day average and also on the F74113 reference spectra. F74113 reference spectra is obtained from a rocket experiment flown on April 23, 1974, and it is revised using the measurement of solar spectrum (in wavelength range 140–1850 Å) by AE-E satellite [*Heroux and Hinteregger*, 1978]. Based on the measured photoelectron flux, *Richards et al.* [1994] have increased the short wavelength fluxes in F74113 flux; flux below 250 Å, and below 150 Å, are doubled and tripled, respectively, to reproduced the measured photoelectron flux spectrum. The solar EUV fluxes using EUVAC model are calculated using F10.7 and F10.7A (81-days average F10.7 solar proxy) and by scaling the F74113 at wavelength bin i as

$$F_i = F74113_i[1 + A_i(P - 80)] \tag{2.1}$$

Where, $F74113_i$ is the modified reference spectra, A_i is the scaling factor, and $P = (F10.7 + F10.7A)/2$ is a proxy [*Richards et al.*, 1994]. The values of $F74113_i$ and A_i is given in Table 2.1.

2.2.2 SOLAR2000

S2K irradiance model of *Tobiska* [2004] has been developed using measured solar irradiance with wavelength range extending from the X-rays to infrared, i.e., 1 to 1000000 nm. In the EUVAC model, F74111 is used as a reference spectra, while reference spectra in S2K model is based on different inputs for various spectral regions of solar flux. Between 0.1 and 121 nm, two models can be used, i.e. S2K EUV [*Tobiska et al.*, 2000] or VUV2002 model [*Woods and Rottman*, 2002]. Apart from that HI Lyman-α spectra irradiance also has been used in S2K as one of the proxies. From 122 to 240 nm, the VUV2000 model is used, while above 420 nm, the ASTM E-490 reference spectrum is used [*Tobiska and Bouwer*, 2006]. In later versions, all satellite, rocket, and reference data sets used in the S2K model derivation have been scaled to absolute level of SEE data in each 0.1 nm wavelength bin on the SC21REF21 format [cf. *Tobiska and Bouwer*, 2006, for more details]. Figure 2.1 shows the composite reference spectra used in S2K model.

S2K uses various proxies for different region of solar spectrum, e.g., in XUV (1–10 nm) region, F10.7 and coronal image are used as proxies; in EUV (10–120 nm) region, F10.7, H Lyman-α, Mg II c/w, He I 10830 EW, Ca II K images are used as proxies; and in FUV (120–200 nm) region, proxies are F10.7, H Lyman-α, Mg II c/w, He I 10830 EW, Ca K 1 Å, Ca II K [cf. *Tobiska*, 2004]. S2K irradiance is available at 1 nm bins (1-1000000 nm), 37 bins (1.86–105 nm), 867 bins (1.862–120.52 nm), and 1664 bin (1.862–200 nm) and can be downloaded from `http://www.SpaceWx.com` for a given date of year.

In Chapters 4 and 5 the solar EUV flux at 37 wavelength bin is used, which is taken from EUVAC and S2K models. The 37 wavelength bin solar EUV flux does not include the flux higher than 1150 Å, which is mainly responsible for dissociation of parent molecule. In the Chapter 6, where modelling of atomic oxygen dayglow emission

Table 2.1: Parameters for the EUVAC solar flux model. .

bin	λ Å	F74113	Ai
1*	50–100	1.200	1.0017E-02
2	100–150	0.450	7.1250E-03
3*	150–200	4.800	1.3375E-02
4*	200–250	3.100	1.9450E-02
5	256.32	0.460	2.7750E-03
6*	284.15	0.210	1.3768E-01
7*	250–300	1.679	2.6467E-02
8*	303.31	0.800	2.5000E-02
9	303.78	6.900	3.3333E-03
10*	300–350	0.965	2.2450E-02
11*	368.07	0.650	6.5917E-03
12*	350–400	0.314	3.6542E-02
13*	400–450	0.383	7.4083E-03
14*	465.22	0.290	7.4917E-03
15*	450–500	0.285	2.0225E-02
16	500–550	0.452	8.7583E-03
17	554.37	0.720	3.2667E-03
18	584.33	1.270	5.1583E-03
19	550–600	0.357	3.6583E-03
20*	609.76	0.530	1.6175E-02
21	629.73	1.590	3.3250E-03
22	600–650	0.342	1.1800E-02
23	650–700	0.230	4.2667E-03
24	703.36	0.360	3.0417E-03
25	700–750	0.141	4.7500E-03
26	765.15	0.170	3.8500E-03
27*	770.41	0.260	1.2808E-02
28	789.36	0.702	3.2750E-03
29	750–800	0.758	4.7667E-03
30	800–850	1.625	4.8167E-03
31	850–900	3.537	5.6750E-03
32	900–950	3.000	4.9833E-03
33	977.02	4.400	3.9417E-03
34	950–1000	1.475	4.4167E-03
35	1025.72	3.500	5.1833E-03
36	1031.91	2.100	5.2833E-03
37	1000–1050	2.467	4.3750E-03

*Bin dominated by coronal fluxes.

F74113 reference flux unit is 10^9 photon cm^{-2} s^{-1}.

Read 1.0017E-02 as 1.0017×10^{-2}.

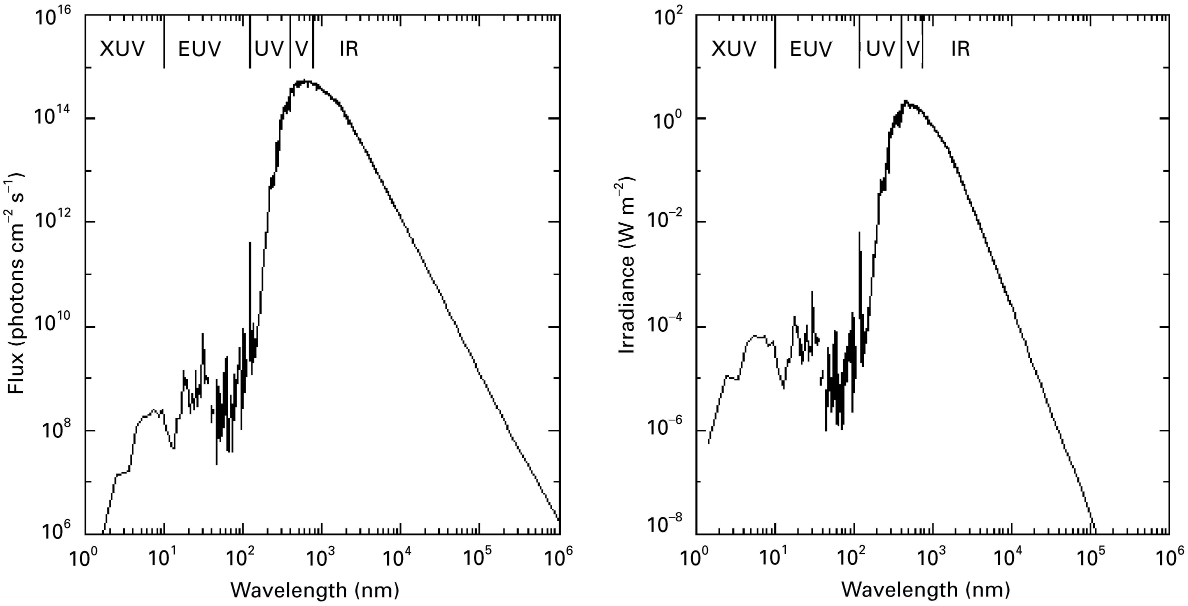

Figure 2.1: Solar irradiance format for SOLAR2000 from the X-rays to the infrared taken from *Tobiska et al.* [2000]. The total integrated irradiance in this spectrum is 1367.28±0.02 W m^{-2} including EUV variability [*Tobiska et al.*, 2000]. Left panel shows solar flux in units of photons cm^{-2} s^{-1}, whereas right panel shows solar flux in units of total irradiance (W/m^{-2}).

requires photodissociation of CO_2, CO, and O_2 molecules, the solar EUV-FUV flux is taken up to 1800 Å, at 10 Å bin interval from S2K model.

2.3 Photoabsorption and photoionization cross section

The production of photoelectrons directly depends on the attenuation of solar EUV flux in an atmosphere. The attenuation of solar radiation in an atmosphere can be calculated using Lambert-Beer equation, which requires photoabsorption cross sections of the gases present in the atmosphere. The electron production rate in photoionization depends upon the photoionization cross section of species present in the atmosphere and flux of ionizing photon. Hence, a brief description of photoionization and photoabsorption cross sections of major gases in the atmospheres of Mars and Venus are presented here.

The CO_2, being the major gas in the atmosphere of Mars and Venus, plays an important role in the attenuation of solar radiation and determines the production and energy of photoelectrons in Martian and Venusian atmospheres. The photoabsorption cross section of CO_2 is reported by *Nakata et al.* [1965], *Cook et al.* [1966], *Lewis and Carver* [1983], *Chan et al.* [1993], and *Shaw et al.* [1995]. *Berkowitz* [2002] has determined the photoabsorption cross sections of CO_2 based on the earlier measurements. Recently, *Sakamoto et al.* [2010] have recommended the photoabsorption cross section of

Table 2.2: Photoabsorption, photoionization, and dissociative photoionization cross sections (in units of 10^{-18} cm^2) of CO_2.

bin	λ Å	$CO_2^{Abs.}$	$CO_2^{+\,Ion.}$	CO_2^+	CO^+	O^+	C^+	CO_2^{++}
1	50–100	1.550	1.551	0.447	0.163	0.626	0.306	0.009
2	100–150	4.616	4.616	2.083	0.510	1.320	0.658	0.045
3	150–200	9.089	9.089	4.960	1.052	1.929	1.033	0.115
4	200–250	14.361	14.320	8.515	1.618	2.622	1.433	0.132
5	256.32	16.505	16.114	11.113	1.467	2.260	1.168	0.106
6	284.15	19.016	18.601	13.004	1.640	2.572	1.287	0.098
7	250–300	17.518	17.141	11.906	1.539	2.382	1.219	0.095
8	303.31	21.492	21.387	14.390	1.959	3.271	1.706	0.061
9	303.78	21.594	21.435	14.414	1.968	3.280	1.715	0.058
10	300–350	23.574	23.629	15.954	2.442	3.426	1.794	0.013
11	368.07	25.269	25.558	18.271	3.040	3.128	1.104	0.015
12	350–400	24.871	25.517	17.982	2.995	3.224	1.310	0.006
13	400-450	28.271	27.172	21.082	3.369	2.597	0.124	0.000
14	465.22	29.526	28.755	24.378	2.247	2.130	0.000	0.000
15	450–500	30.254	30.578	27.163	1.504	1.911	0.000	0.000
16	500–550	31.491	32.594	30.138	0.820	1.636	0.000	0.000
17	554.37	33.202	33.211	31.451	0.409	1.351	0.000	0.000
18	584.33	34.200	33.857	32.382	0.305	1.170	0.000	0.000
19	550–600	34.913	34.959	33.482	0.306	1.171	0.000	0.000
20	609.76	35.303	35.303	34.318	0.135	0.850	0.000	0.000
21	629.73	34.300	34.300	33.795	0.037	0.468	0.000	0.000
22	600–650	34.447	34.573	34.003	0.043	0.527	0.000	0.000
23	650–700	33.699	32.287	32.287	0.000	0.000	0.000	0.000
24	703.36	23.518	20.856	20.856	0.000	0.000	0.000	0.000
25	700–750	32.832	27.490	27.490	0.000	0.000	0.000	0.000
26	765.15	93.839	86.317	86.317	0.000	0.000	0.000	0.000
27	770.41	61.939	51.765	51.765	0.000	0.000	0.000	0.000
28	789.36	26.493	21.676	21.676	0.000	0.000	0.000	0.000
29	750–800	39.831	34.094	34.094	0.000	0.000	0.000	0.000
30	800–850	13.980	10.930	10.930	0.000	0.000	0.000	0.000
31	850–900	44.673	7.135	7.135	0.000	0.000	0.000	0.000
32	900–950	52.081	0.000	0.000	0.000	0.000	0.000	0.000
33	977.02	42.869	0.000	0.000	0.000	0.000	0.000	0.000
34	950–1000	50.311	0.000	0.000	0.000	0.000	0.000	0.000
35	1025.72	15.100	0.000	0.000	0.000	0.000	0.000	0.000
36	1031.91	14.200	0.000	0.000	0.000	0.000	0.000	0.000
37	1000–1050	18.241	0.000	0.000	0.000	0.000	0.000	0.000

$CO_2^{Abs.}$ and $CO_2^{+\,Ion.}$ denote the total absorption cross sections and sum of all ionization cross section, respectively.

Table 2.3: Photoabsorption, photoionization, and dissociative photoionization cross sections (in units of 10^{-18} cm^2) of N_2 and O_2.

bin	λ Å	$N_2^{\mathrm{Abs.}}$	$N_2^{+\,\mathrm{Ion.}}$	N_2^+	N^+	$O_2^{\mathrm{Abs.}}$	$O_2^{+\,\mathrm{Ion.}}$	O_2^+	O^+
1	50–100	0.720	0.720	0.443	0.277	1.316	1.316	1.316	0.000
2	100–150	2.261	2.261	1.479	0.782	3.806	3.806	2.346	1.460
3	150–200	4.958	4.958	3.153	1.805	7.509	7.507	4.139	3.368
4	200–250	8.392	8.392	5.226	3.166	10.900	10.900	6.619	4.281
5	256.32	10.210	10.201	6.781	3.420	13.370	13.370	8.460	4.910
6	284.15	10.900	10.900	8.100	2.800	15.790	15.790	9.890	5.900
7	250–300	10.493	10.492	7.347	3.145	14.387	14.388	9.056	5.332
8	303.31	11.670	11.670	9.180	2.490	16.800	16.800	10.860	5.940
9	303.78	11.700	11.700	9.210	2.490	16.810	16.810	10.880	5.930
10	300–350	13.857	13.857	11.600	2.257	17.438	17.441	12.229	5.212
11	368.07	16.910	16.910	15.350	1.560	18.320	18.320	13.760	4.560
12	350–400	16.395	16.395	14.669	1.726	18.118	18.121	13.418	4.703
13	400–450	21.675	21.674	20.692	0.982	20.310	20.308	15.490	4.818
14	465.22	23.160	23.160	22.100	1.060	21.910	21.910	16.970	4.940
15	450–500	23.471	23.471	22.772	0.699	23.101	23.101	17.754	5.347
16	500–550	24.501	24.501	24.468	0.033	24.606	24.608	19.469	5.139
17	554.37	24.130	24.130	24.130	0.000	26.040	26.040	21.600	4.440
18	584.33	22.400	22.400	22.400	0.000	22.720	22.720	18.840	3.880
19	550–600	22.787	22.787	22.787	0.000	26.610	26.613	22.789	3.824
20	609.76	22.790	22.790	22.790	0.000	28.070	26.390	24.540	1.850
21	629.73	23.370	23.370	23.370	0.000	32.060	31.100	30.070	1.030
22	600–650	23.339	23.339	23.339	0.000	26.017	24.936	23.974	0.962
23	650–700	31.755	29.235	29.235	0.000	21.919	21.306	21.116	0.190
24	703.36	26.540	25.480	25.480	0.000	27.440	23.750	23.750	0.000
25	700–750	24.662	15.060	15.060	0.000	28.535	23.805	23.805	0.000
26	765.15	120.490	65.800	65.800	0.000	20.800	11.720	11.720	0.000
27	770.41	14.180	8.500	8.500	0.000	18.910	8.470	8.470	0.000
28	789.36	16.487	8.860	8.860	0.000	26.668	10.191	10.191	0.000
29	750–800	33.578	14.274	14.274	0.000	22.145	10.597	10.597	0.000
30	800–850	16.992	0.000	0.000	0.000	16.631	6.413	6.413	0.000
31	850–900	20.239	0.000	0.000	0.000	8.562	5.494	5.494	0.000
32	900–950	9.680	0.000	0.000	0.000	12.817	9.374	9.374	0.000
33	977.02	2.240	0.000	0.000	0.000	18.730	15.540	15.540	0.000
34	950–1000	50.988	0.000	0.000	0.000	21.708	13.940	13.940	0.000
35	1025.72	0.000	0.000	0.000	0.000	1.630	0.000	0.000	0.000
36	1031.91	0.000	0.000	0.000	0.000	0.000	0.000	0.000	0.000
37	1000–1050	0.000	0.000	0.000	0.000	1.346	0.259	0.259	0.000

$N_2^{\mathrm{Abs.}}$ and $N_2^{+\,\mathrm{Ion.}}$ denote the total absorption cross sections and sum of all ionization cross section, respectively. Same for $O_2^{\mathrm{Abs.}}$ and $O_2^{+\,\mathrm{Ion.}}$.

Table 2.4: Photoabsorption, photoionization, and dissociative photoionization cross sections (in units of 10^{-18} cm^2) of CO and O.

bin	λ Å	$CO^{Abs.}$	$CO^{+\,Ion.}$	CO^+	C^+	O^+	C^{++}	$O^{Abs.}$	$O^{+\,Ion.}$
1	50–100	0.866	0.866	0.291	0.282	0.247	0.046	0.730	0.729
2	100–150	2.391	2.391	1.074	0.672	0.600	0.045	1.839	1.839
3	150–200	4.671	4.671	2.459	1.156	1.029	0.027	3.732	3.732
4	200–250	7.011	7.011	4.082	1.514	1.411	0.004	5.202	5.201
5	256.32	8.614	8.614	5.449	1.593	1.572	0.000	6.050	6.050
6	284.15	10.541	10.541	7.713	1.141	1.687	0.000	7.080	7.080
7	250–300	9.424	9.424	6.361	1.502	1.561	0.000	6.461	6.461
8	303.31	11.867	11.867	9.209	1.076	1.582	0.000	7.680	7.680
9	303.78	11.900	11.900	9.246	1.073	1.581	0.000	7.700	7.700
10	300–350	13.441	13.441	11.532	0.963	0.946	0.000	8.693	8.693
11	368.07	15.259	15.259	13.980	0.771	0.509	0.000	9.840	9.840
12	350–400	14.956	14.956	13.609	0.814	0.533	0.000	9.687	9.687
13	400–450	17.956	17.956	16.876	0.962	0.118	0.000	11.496	11.496
14	465.22	20.173	20.173	19.085	1.029	0.058	0.000	11.930	11.930
15	450–500	20.574	20.574	19.669	0.895	0.009	0.000	12.127	12.127
16	500–550	21.085	21.085	20.454	0.631	0.000	0.000	12.059	12.059
17	554.37	21.624	21.624	21.565	0.060	0.000	0.000	12.590	12.590
18	584.33	22.000	22.000	22.000	0.000	0.000	0.000	13.090	13.090
19	550–600	21.910	21.895	21.895	0.000	0.000	0.000	13.024	13.024
20	609.76	22.100	21.918	21.918	0.000	0.000	0.000	13.400	13.400
21	629.73	22.025	22.025	22.025	0.000	0.000	0.000	13.400	13.400
22	600–650	21.915	21.845	21.845	0.000	0.000	0.000	13.365	13.365
23	650–700	21.036	20.097	20.097	0.000	0.000	0.000	17.245	17.245
24	703.36	23.853	22.115	22.115	0.000	0.000	0.000	11.460	11.460
25	700–750	25.501	21.084	21.084	0.000	0.000	0.000	10.736	10.736
26	765.15	26.276	13.033	13.033	0.000	0.000	0.000	4.000	4.000
27	770.41	15.262	9.884	9.884	0.000	0.000	0.000	3.890	3.890
28	789.36	33.132	17.350	17.350	0.000	0.000	0.000	3.749	3.749
29	750–800	20.535	11.375	11.375	0.000	0.000	0.000	5.091	5.091
30	800–850	22.608	17.559	17.559	0.000	0.000	0.000	3.498	3.498
31	850–900	36.976	11.701	11.701	0.000	0.000	0.000	4.554	4.554
32	900–950	50.318	0.000	0.000	0.000	0.000	0.000	1.315	1.315
33	977.02	28.500	0.000	0.000	0.000	0.000	0.000	0.000	0.000
34	950–1000	52.827	0.000	0.000	0.000	0.000	0.000	0.000	0.000
35	1025.72	1.388	0.000	0.000	0.000	0.000	0.000	0.000	0.000
36	1031.91	1.388	0.000	0.000	0.000	0.000	0.000	0.000	0.000
37	1000–1050	8.568	0.000	0.000	0.000	0.000	0.000	0.000	0.000

$CO^{Abs.}$ and $CO^{+\,Ion.}$ denote the total absorption cross sections and sum of all ionization cross section, respectively. Same for $O^{Abs.}$ and $O^{+\,Ion.}$.

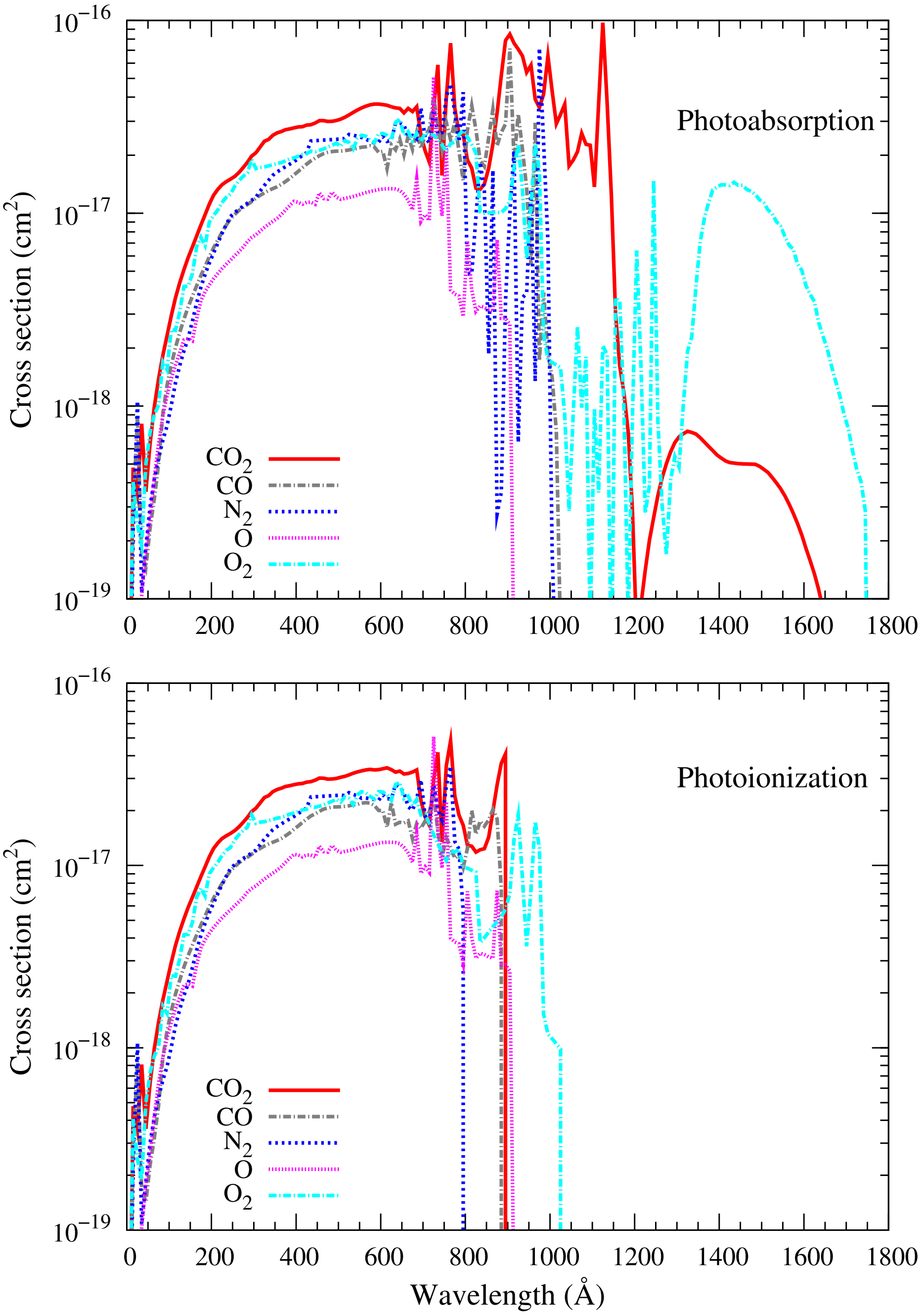

Figure 2.2: Photoabsorption and photoionization cross sections of CO_2, CO, N_2, O, and O_2.

CO_2 based on studies of *Chan et al.* [1993] and *Berkowitz* [2002]. The photoabsorption cross section of CO_2 recommended by *Sakamoto et al.* [2010] has been used in the present study. The cross sections of CO_2 for total photoionization and ionization in various dissociative states in present study is based on branching ratio from compiled database of *Huebner et al.* [1992] (`http://amop.space.swri.edu`). Photoabsorption and photoionization cross sections of CO, N_2 O, and O_2 are taken from photocross sections and rate coefficients database (`http://amop.space.swri.edu`) [*Huebner et al.*, 1992].

As stated earlier, calculations in Chapters 3, 4, and 5 are carried using solar EUV flux at 37 wavelength bin intervals. *Schunk and Nagy* [2000] have recommended the photoabsorption and photoionization cross sections at 37 bins, which are in good agreement with CO_2 cross section of *Sakamoto et al.* [2010] when averaged at 37 wavelength bins. *Schunk and Nagy* [2000] have also provided photoabsorption and photoionization cross sections for CO, N_2, O_2, and O at 37 wavelength intervals, which are in are in agreement with those given from *Huebner et al.* [1992], when averaged at 37 wavelength bins. The photoabsorption and photoionization cross sections recommended by *Schunk and Nagy* [2000] have been used in the present study. The photoabsorption and photoionization cross sections of CO_2, CO, N_2, O and O_2 at 37 wavelength bins are given in Tables 2.2–2.4. The photoabsorption and photoionization cross sections are also presented graphically in Figure 2.2. Below 1100 Å, photoabsorption cross sections of CO_2, CO, N_2, and O_2 are roughly same, while that of O is around factor of 2 lower compared to other gases. Above 1200 Å, photoabsorption cross sections of CO_2 and O_2 dominant. Since the CO_2 density on Mars' and Venus' upper atmosphere is more than 3 orders of magnitude higher than that of O_2, most of the solar photon absorption above 1200 Å is due to the CO_2.

2.4 Cross sections for electron impact on CO_2

In the following sections a detailed review of electron impact cross sections for CO_2 is given, which includes cross sections of elastic and various inelastic processes, and the total scattering cross section.

2.4.1 Total

The laboratory measured Total Scattering Cross Section (TCS) is available between 0.1 eV and 5000 eV. The TCS for e-CO_2 collision has been measured by several authors in different energy ranges: *Ferch et al.* [1981] in the energy range 0.007–4.5 eV, *Buckman et al.* [1987] 0.1–5 eV, *Szmytkowski et al.* [1987] 0.5–3000 eV, *Kimura et al.* [1997] 0.8–500 eV, *Kwan et al.* [1983] 1–500 eV, and *Garcia and Manero* [1996] 400-5000 eV. At low energies, the TCS of *Szmytkowski et al.* [1987], *Buckman et al.* [1987], and *Ferch et al.* [1981] are in agreement to within 10%. *Zecca et al.* [2002] have determined the best value of TCS. In the lowest energy range (<1 eV) *Zecca et al.* [2002] adopted the experimental data of *Ferch et al.* [1981] and *Buckman et al.* [1987], which are in good agreement with each other. In the 1–1000 eV energy range, *Zecca et al.* [2002] averaged the cross sections obtained by *Szmytkowski et al.* [1987], *Kimura et al.* [1997] and *Kwan et al.* [1983], with equal weight, to obtain the recommended values, which are in good agreement with *Garcia and Manero* [1996] at higher (>400 eV) energies. In his review, *Itikawa* [2002] has recommended the TCS of *Zecca et al.* [2002]. The TCS reaches a maximum value of 60×10^{-16} cm^2 at 0.1 eV [*Ferch et al.*, 1981; *Buckman et al.*, 1987],

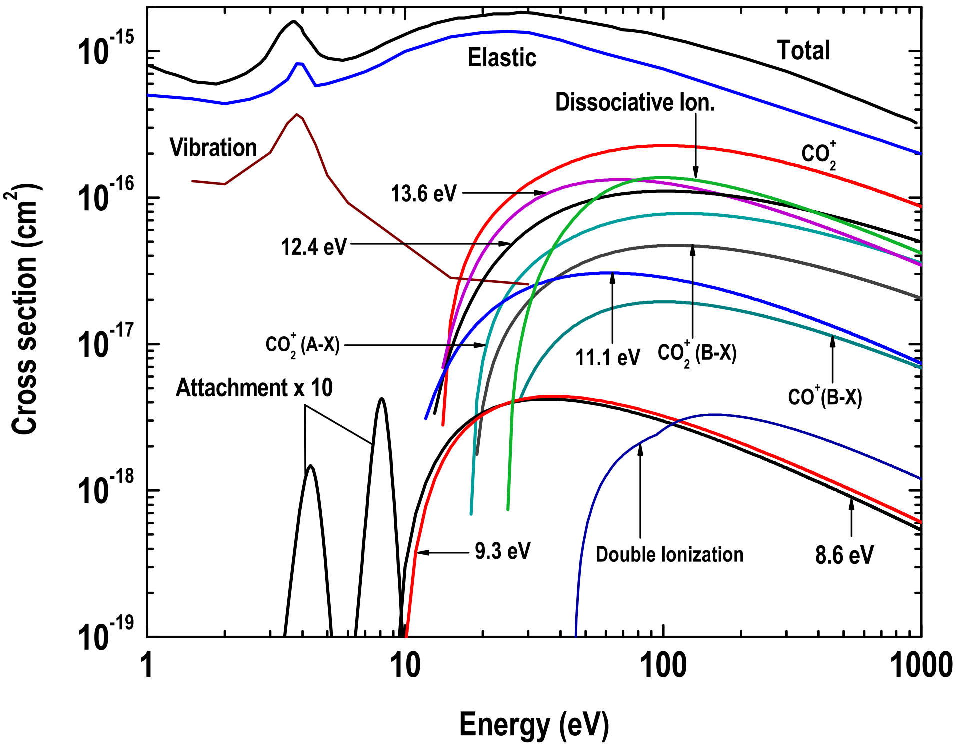

Figure 2.3: The electron impact cross sections of CO_2 for elastic, major inelastic processes, along with the total cross section.

it then goes through a minimum of 5.5×10^{-16} cm^2 at 1.9 eV [*Szmytkowski et al.*, 1987]. At lower energies a resonant structure is present ∼3.8 eV, where the cross section shows a peak with a value of 1.6×10^{-15} cm^2. The total e-CO_2 collision cross section profile is shown in Figure 2.3.

2.4.2 Elastic

2.4.2.1 Differential elastic

The Differential Elastic Scattering Cross Section (DCS) for e-CO_2 collision has been measured by many authors [cf. review by *Itikawa*, 2002; *Karwasz et al.*, 2001].

In the 1–4 eV energy, the DCS values of *Gibson et al.* [1999] and *Tanaka et al.* [1998] are in good agreement at forward angles ($\leq 50°$), however at larger angles they differ by 20–30%. Overall, at most of the energies there is a good agreement in shape between these two DCS. At 30, 40, and 50 eV, the DCS measurements of *Gibson et al.* [1999], *Kanik et al.* [1989], and *Tanaka et al.* [1998] are in reasonable accord, within the uncertainties of each measurement, and at 50 eV the DCS of *Gibson et al.* [1999] and *Register et al.* [1980] are consistent. At 100 eV, the measured DCS values of *Iga et al.* [1999] are in good agreement with *Kanik et al.* [1989] and *Tanaka et al.* [1998].

In the present study, the DCS values are taken from *Tanaka et al.* [1998] in the 1-100 eV range, however values at 40, 50, 70, 80, and 90 eV are taken from *Kanik et al.* [1989] which agree well with the cross section of *Tanaka et al.* [1998] in the entire energy

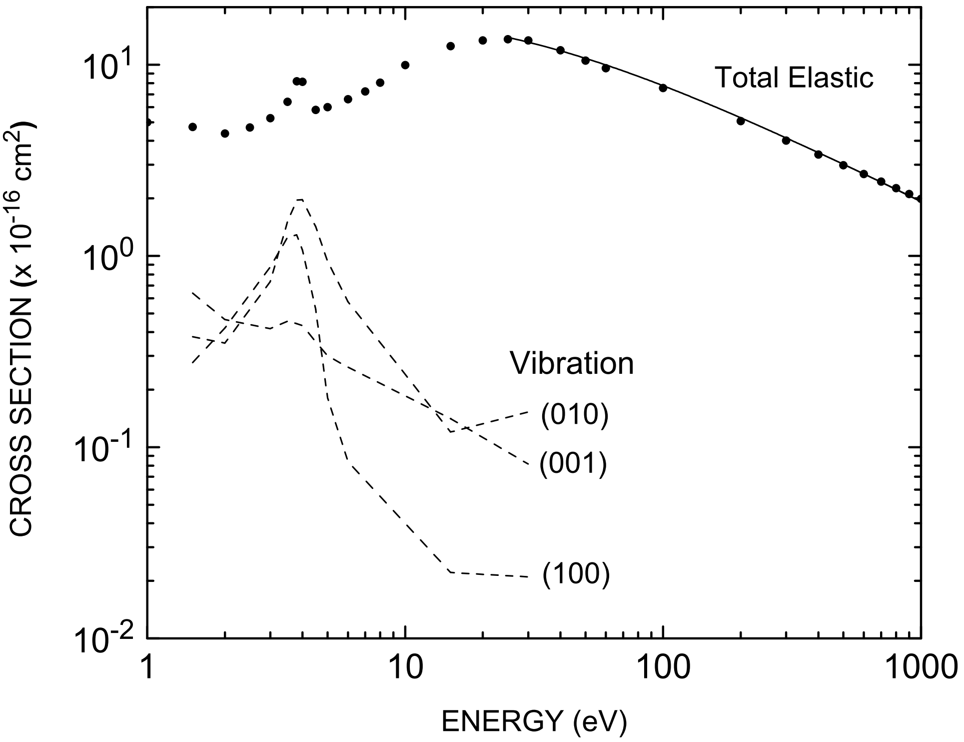

Figure 2.4: The e-CO_2 total elastic cross section and vibrational excitation cross sections for three modes. For elastic cross section, symbol represents the cross section values of *Itikawa* [2002], and solid curve represents the analytical fit using Eq. 2.2. Dashed curve represents the vibrational excitation cross sections taken from *Itikawa* [2002].

range. The DCS values in 200-400 eV range are taken from *Iga et al.* [1999], and those in 500-1000 eV are taken from *Iga et al.* [1984]. The DCS values used in this work. are shown in tabular format in Table 2.5.

2.4.2.2 Total elastic

Based on the DCS measured by *Register et al.* [1980], *Tanaka et al.* [1998] and *Gibson et al.* [1999], *Buckman et al.* [2002] have determined the total elastic cross section in 1–100 eV range with an estimated uncertainty of ±30%. *Shirai et al.* [2001] have reported the recommended elastic cross section up to 1000 eV by considering the beam data of *Iga et al.* [1999]. *Itikawa* [2002] has recommended the elastic cross section of *Buckman et al.* [2002] in the energy range 1–60 eV, and *Shirai et al.* [2001] in the energy range 100–1000 eV. The two data sets merge smoothly.

In the present study, total elastic cross section is taken from *Itikawa* [2002]. The total elastic cross section is fitted using the semi-empirical formula [*Bhardwaj and Michael*, 1999a]:

$$\sigma(E) = \frac{1}{A_1 + B_1 E} + \frac{1}{A_2 + B_2 E} + \frac{2}{E} \frac{\sqrt{A_1 A_2}}{A_2 B_1 - A_1 B_2} \ln \frac{(1 + B_1 E/A_1)}{(1 + B_2 E/A_2)}, \tag{2.2}$$

where A_1, B_1, A_2, and B_2 are the fitting parameters, whose values are 8.09×10^{-16} Å^{-2}, 2.184×10^{-2} Å^{-2} keV, 0.92 Å^{-2}, and 5.0×10^{-4} Å^{-2} keV, respectively, and E is the

Table 2.5: Elastic differential cross section for electron impact on CO_2 (in units of 10^{-16} cm^2 sr^{-1})

Energy	Angle (degree)									
(eV)	0	5	10	15	20	30	40	50	60	70
1.5	(1.350)*	(1.252)	(1.154)	(1.056)	0.9580	0.7620	0.5410	0.4050	0.3289	0.2957
2.0	(1.157)	(1.055)	(0.954)	(0.852)	0.7505	0.5472	0.3896	0.2455	0.2368	0.2489
3.0	(1.174)	(1.060)	(0.945)	(0.831)	0.7160	0.4868	0.3069	0.3118	0.3386	0.3779
3.8	(2.295)	(2.059)	(1.824)	(1.589)	1.3536	0.8831	0.6294	0.5897	0.5715	0.5367
4.0	(2.007)	(1.844)	(1.681)	(1.517)	1.3536	1.0269	0.7770	0.6857	0.6472	0.5834
5.0	(0.250)	(0.333)	(0.416)	(0.499)	0.5824	0.7486	0.8076	0.8994	0.8079	0.7272
6.0	(0.501)	(0.546)	(0.592)	(0.637)	0.6823	0.7730	0.8244	0.8383	0.8373	0.7644
6.5	(0.933)	(0.914)	(0.896)	(0.878)	0.8599	0.8236	0.9132	0.9286	0.8950	0.6978
7.0	(0.986)	(0.960)	(0.934)	(0.909)	0.8828	0.8313	0.9039	0.9391	0.8025	0.7558
8.0	(16.88)	(12.95)	(9.02)	5.0890	1.1590	1.0020	0.9640	0.8542	0.7214	0.6755
9.0	(24.24)	(18.56)	(12.87)	7.1830	1.4960	1.5880	1.0870	0.9487	0.8375	0.6622
10.0	(39.19)	(29.96)	(20.74)	11.520	2.2977	1.5342	1.2136	0.9926	0.7430	0.6260
15.0	(31.84)	(24.84)	(17.84)	10.843	3.8430	2.7180	1.7789	1.1756	0.7997	0.5777
20.0	(13.80)	(11.77)	(9.743)	7.7149	5.6871	3.2623	1.8542	1.2248	0.7475	0.4324
30.0	(19.89)	(17.10)	(14.31)	(11.52)	8.7310	3.1540	1.4363	0.7430	0.4678	0.3060
40.0	(15.70)	(13.51)	(11.31)	(9.115)	6.9200	2.5300	1.0400	0.5300	0.3100	0.1800
50.0	14.820	12.690	10.560	8.4300	6.3000	2.0400	0.8100	0.4000	0.2100	0.1440
60.0	(13.44)	(11.50)	(9.556)	(7.614)	5.6710	1.7860	0.6597	0.3412	0.1683	0.1109
70.0	(10.61)	(9.055)	(7.50)	(5.945)	4.3900	1.2800	0.5200	0.2500	0.1420	0.1130
80.0	(9.79)	(8.35)	(6.91)	(5.470)	4.0300	1.1500	0.4700	0.2200	0.1360	0.1090
90.0	(8.50)	(7.24)	(5.98)	(4.72)	3.4600	0.9400	0.3800	0.2000	0.1450	0.1120
100.0	(9.273)	(7.893)	(6.514)	(5.134)	3.7543	0.9950	0.3969	0.2026	0.1502	0.1124
200.0	(31.75)	(22.68)	13.610	4.5390	2.4170	0.6160	0.3380	0.2230	0.1270	0.0952
300.0	(19.35)	(13.86)	8.3720	2.8850	1.2350	0.3880	0.2670	0.1290	0.0716	0.0539
400.0	(16.82)	(12.00)	7.1900	2.3770	1.0400	0.4550	0.2150	0.0968	0.0624	0.0523
500.0	(132.80)	77.22	21.600	6.6100	2.7800	1.5600	0.7130	0.3140	0.2190	0.1620
800.0	(138.20)	75.020	11.810	4.1800	2.6500	0.9050	0.3280	0.1900	0.0920	0.0673
1000.0	(113.0)	62.100	11.200	3.5500	2.3500	0.6600	0.2820	0.1430	0.0925	0.0640

*Value inside the bracket indicates a linearly extrapolated value.

Table continues to next page.

Table 2.5: Contd.

Energy	Angle (degree)									
(eV)	80	90	100	110	120	130	135	150	165	180
1.5	0.2700	0.2405	0.3080	0.3040	0.3567	0.3650	(0.3629)	(0.3816)	(0.3941)	(0.4065)
2.0	0.2765	0.2845	0.3021	0.3276	0.3776	0.3992	(0.4100)	(0.4424)	(0.4748)	(0.5072)
3.0	0.3876	0.3937	0.3950	0.4380	0.4830	0.5173	(0.5345)	(0.5859)	(0.6374)	(0.6888)
3.8	0.5539	0.5739	0.5096	0.5187	0.5280	0.5475	(0.5573)	(0.5865)	(0.6158)	(0.6450)
4.0	0.5595	0.5037	0.4431	0.4217	0.4258	0.4803	(0.5076)	(0.5893)	(0.6711)	(0.7528)
5.0	0.6026	0.4794	0.3910	0.2647	0.2523	0.2853	(0.3018)	(0.3513)	(0.4008)	(0.4503)
6.0	0.6422	0.5258	0.4518	0.3476	0.3136	0.3798	(0.4129)	(0.5122)	(0.6115)	(0.7108)
6.5	0.6616	0.5300	0.4252	0.3390	0.3201	0.3520	(0.3680)	(0.4158)	(0.4637)	(0.5115)
7.0	0.6258	0.5273	0.4333	0.3766	0.3798	0.3724	(0.3687)	(0.3576)	(0.3465)	(0.3354)
8.0	0.6761	0.5343	0.4596	0.4263	0.4058	0.5183	(0.5746)	(0.7433)	(0.9121)	(1.0810)
9.0	0.5799	0.5394	0.4811	0.4381	0.4816	0.6006	(0.6601)	(0.8386)	(1.0170)	(1.1960)
10.0	0.5468	0.4856	0.4478	0.4319	0.5304	0.7077	(0.7964)	(1.0620)	(1.3280)	(1.5940)
15.0	0.4471	0.3596	0.3673	0.4046	0.5445	0.7832	(0.9026)	(1.2610)	(1.6190)	(1.9770)
20.0	0.3516	0.3041	0.3071	0.3887	0.5493	0.6738	(0.7361)	(0.9228)	(1.1100)	(1.2960)
30.0	0.1896	0.1882	0.2391	0.2536	0.3195	0.4441	(0.5064)	(0.6933)	(0.8802)	(1.0670)
40.0	0.1330	0.1190	0.1130	0.1500	0.2400	(0.330)	(0.3750)	(0.5100)	(0.6450)	(0.7800)
50.0	0.1180	0.0920	0.0810	0.1300	0.2500	(0.370)	(0.4300)	(0.6100)	(0.7900)	(0.9700)
60.0	0.0936	0.0911	0.0812	0.01175	0.1805	0.2748	(0.3220)	(0.4634)	(0.6049)	(0.7463)
70.0	0.1040	0.0850	0.0910	0.1400	0.2100	(0.280)	(0.3150)	(0.4200)	(0.5250)	(0.6300)
80.0	0.0900	0.0850	0.0900	0.1200	0.1800	(0.240)	(0.2700)	(0.3600)	(0.4500)	(0.5400)
90.0	0.0804	0.0890	0.0920	0.1200	0.1600	(0.200)	(0.2200)	(0.2800)	(0.3400)	(0.4000)
100.0	0.0840	0.0697	0.0754	0.0880	0.1076	0.1373	(0.1522)	(0.1967)	(0.2413)	(0.2858)
200.0	0.0756	0.0646	0.0709	0.0770	0.0804	0.0878	(0.0944)	(0.1142)	(0.1340)	(0.1538)
300.0	0.0505	0.0376	0.0337	0.0314	0.0272	0.0233	(0.0217)	(0.0169)	(0.0121)	(0.0073)
400.0	0.0376	0.0305	0.0256	0.0255	0.0236	0.0223	(0.0202)	(0.0139)	(0.0076)	(0.0013)
500.0	0.1080	0.0843	0.0752	0.0658	0.0548	(0.0438)	(0.0383)	(0.0218)	(0.0053)	(0.00001)
800.0	0.0523	0.0319	0.0283	0.0238	0.0221	(0.0204)	(0.0195)	(0.0170)	(0.0145)	(0.0119)
1000.0	0.0360	0.0275	0.0220	0.0165	0.0149	(0.0133)	(0.0125)	(0.0101)	(0.0077)	(0.0053)

*Value inside the bracket indicates a linearly extrapolated value.

energy of the electron in eV. The lower limit of fit is 30 eV, and fitted cross section is shown in Figure 2.4. At energies below 30 eV it is difficult to fit the cross section using above equation due to resonance structure present at low energies (∼4 eV), and hence these values are fed numerically in the model calculations.

2.4.3 Dissociative electron attachment

The dissociative attachment process in e-CO_2 collisions, which mainly occurs at energies <12 eV, leads to the formation of negative ions O^-, O_2^-, and C^-. *Rapp and*

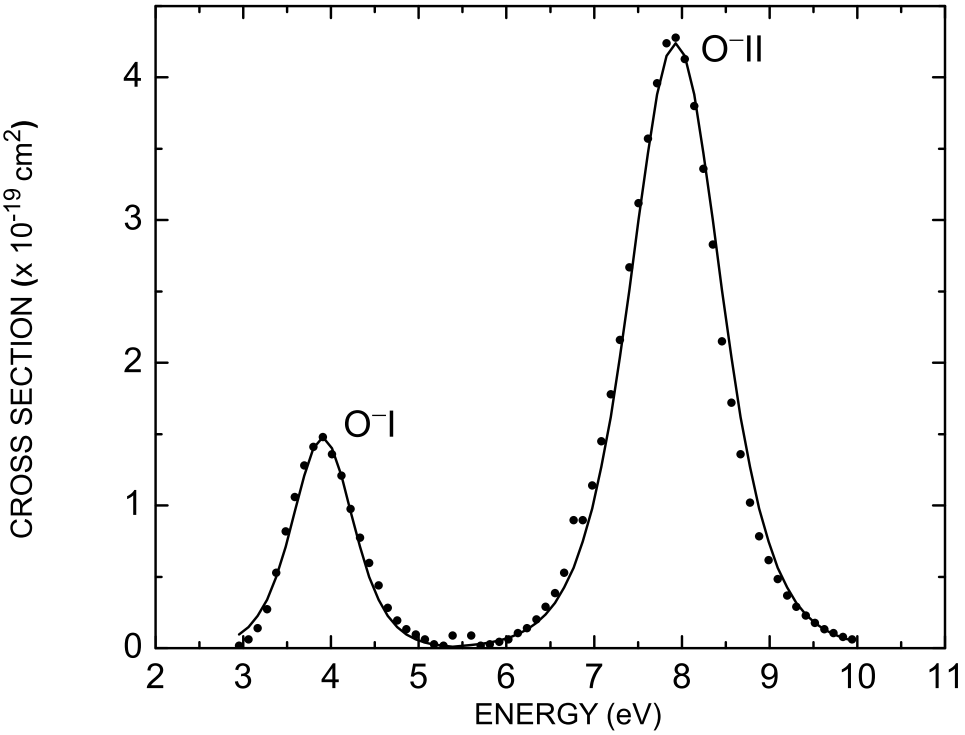

Figure 2.5: Dissociative electron attachment cross section of CO_2 for the formation of O^- ion. Symbol represents the values of *Itikawa* [2002] based on *Rapp and Englander-Golden* [1965]; solid curve represents analytical fit of O^- cross section using Eq. 2.3. I and II denotes the first and second peak, respectively.

Briglia [1965] measured absolute values of the total cross section for the production of negative ions from CO_2. *Orient and Srivastava* [1983] obtained the cross section for the production of O^- ions and showed that it is the dominant anion. Their values are in agreement with those of *Rapp and Briglia* [1965] within the uncertainty of the cross sections (±20%) and the energy scale (±0.1 eV). *Spence and Schulz* [1974] measured the cross sections for the production of C^- and O_2^- ions. The cross section for O_2^- production has two peaks of the order of 10^{-24} cm^2 at 11.3 and 12.9 eV, while cross section for C^- production has three peaks with the largest value of $\sim 2 \times 10^{-21}$ cm^2. The cross sections for O_2^- and C^- are small compared to that of O^-, and hence are not considered in our study. We have adopted the cross section values of *Rapp and Briglia* [1965] for the production of O^- ions from CO_2. The cross section shows a double-peak structure – peaks at 4.1 and 8.3 eV, with the later peak value (4.28×10^{-19} cm^2) about 2.5 times the value of the former peak. The cross section for each peak has been fitted with the following analytical form [*Bhardwaj and Michael*, 1999a]:

$$\sigma(E) = \frac{Ae^t/U}{(1+e^t)^2}, \tag{2.3}$$

Here $t = (E - W_p)/U$, where W_p is the energy at the peak. The values of the overall normalization parameter A and the effective width parameter U for each of the peaks

Table 2.6: Parameters for electron attachment process of CO_2.

	W_P	A	U	W_{th}
O^-I	4.3	0.0013×10^{-16}	0.22	3.4
O^-II	8.1	0.0056×10^{-16}	0.33	5.9

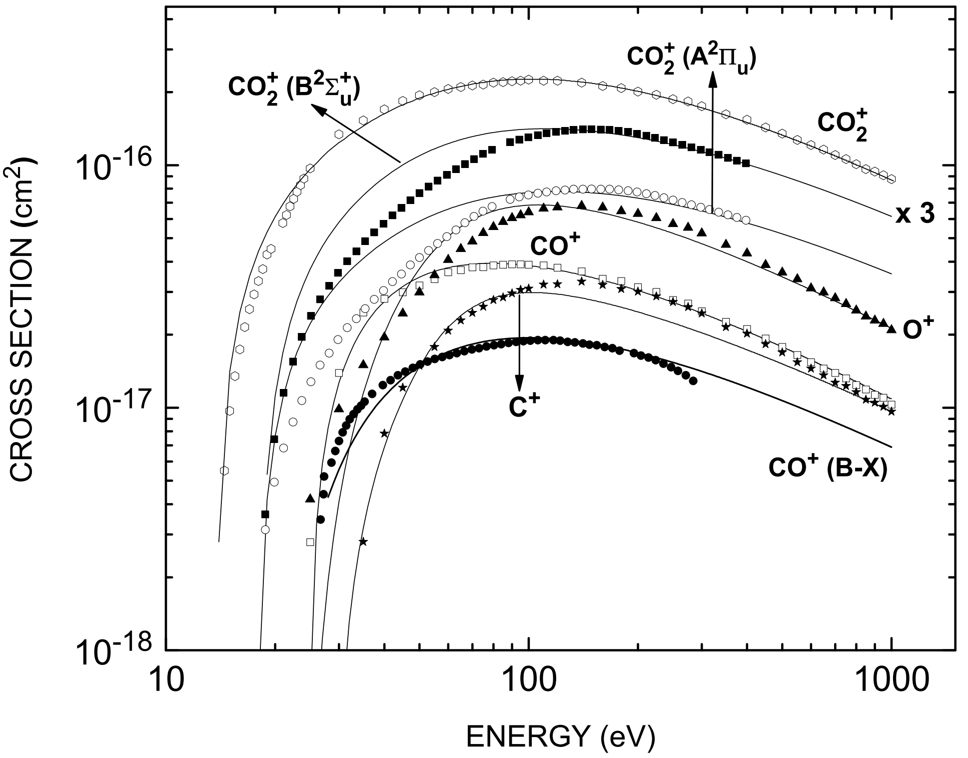

Figure 2.6: Ionization and emission cross sections of CO_2. Symbol represents the values of *Itikawa* [2002], and solid curve represents the analytical fits using Eq. 2.4 except for CO^+(B-X) state, which is fitted using Eq. 2.5. Note that the cross section for $CO_2^+(B^2\Sigma_u^+)$ state has been plotted after multiplying by a factor of 3.

along with the parameter W_p and the threshold energy W_{th} are presented in Table 2.6. The fitted cross sections along with laboratory measurements are given in Figure 2.5.

2.4.4 Ionization

The ionization and dissociative ionization of CO_2 by electron impact produce singly and doubly ionized ions (CO_2^+, CO^+, C^+, O^+, C^{++}, O^{++}, and CO_2^{++}). The cross sections for these processes have been reported by *Rapp and Englander-Golden* [1965], *Shyn and Sharp* [1979], *Orient and Srivastava* [1987], *Tian and Vidal* [1998], and *Straub et al.* [1996]. *McConkey et al.* [2008] have reviewed the electron impact dissociation cross sections for CO_2. For the total ionization cross section, measurements of *Orient and Srivastava* [1987], *Tian and Vidal* [1998], and *Straub et al.* [1996] are within the error limits with the values of *Rapp and Englander-Golden* [1965] up to 1000 eV, and with the data of *Shyn and Sharp* [1979] in the energy range 50-400 eV. *Tian and Vidal* [1998] have

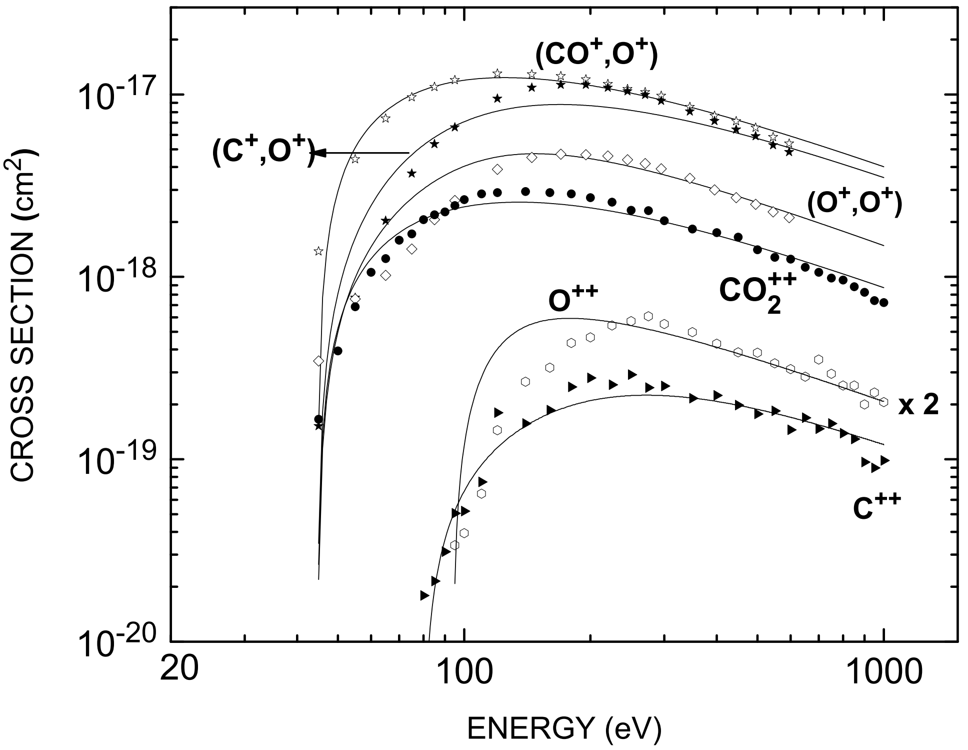

Figure 2.7: Cross sections for electron impact double ionization of CO_2. Symbol represents the measured cross section values and solid curve represents the analytical fit using Eq. 2.4. Cross sections for (CO^+,O^+), (C^+,O^+), and (O^+,O^+) have been taken from *Tian and Vidal* [1998], and that for CO_2^{++}, O^{++}, and C^{++} from *Itikawa* [2002]. Cross section for O^{++} has been plotted after multiplying by a factor of 2.

also measured the cross sections for double and triple ionization of CO_2 due to electron impact. After a survey of the available experimental data, *Lindsay and Mangan* [2002] suggested recommended values of ionization cross section. Their partial cross sections are based on the measurement of *Straub et al.* [1996]. For total ionization cross section below 25 eV, *Lindsay and Mangan* [2002] adopted the values of *Rapp and Englander-Golden* [1965]. At energies above 25 eV, they reported uncertainties of 5% for the partial cross sections for the production of CO_2^+, CO^+, C^+, O^+, and the total ionization cross section. The cross sections at energies below 25 eV have uncertainties of 7%. There are also uncertainties in appearance energies of fragmented ions CO^+, C^+, O^+, C^{++}, and O^{++}. The appearance energies for the fragmented ions are taken from *Itikawa* [2002] in this study.

The dissociative and direct ionization cross sections recommended by *Lindsay and Mangan* [2002] [cf. *Itikawa*, 2002; *McConkey et al.*, 2008] are used in the present work. The CO_2^+ ion can be produced in four excited states, viz., $X^2\Pi_g$, $A^2\Pi_u$, $B^2\Sigma_u^+$, and $C^2\Sigma_g^+$. Cross sections for $A^2\Pi_u$ and $B^2\Sigma_u^+$ states have been taken from *Itikawa* [2002], while the cross sections for $X^2\Pi_g$ and $C^2\Sigma_g^+$ states have been taken from *Jackman et al.* [1977]. For double ionization, cross sections of (CO^+,O^+), (C^+,O^+), and (O^+,O^+) production have been taken from *Tian and Vidal* [1998] up to 600 eV; these cross sections have not been added in the total ionization cross section because they are already accounted in the cross sections for the formation of CO^+, C^+, and O^+ ions. All these cross sections have been fitted using the analytical expression [*Jackman et al.*, 1977; *Bhardwaj and Michael*, 1999a].

$$\sigma(E) = A\Gamma\left[arctan\frac{(T_M - T_0)}{\Gamma} + arctan\left(\frac{T_0}{\Gamma}\right)\right], \tag{2.4}$$

where

$$A(E) = \left[\frac{K}{E + K_B}\right] \ln\left[\frac{E}{J} + J_B + \frac{J_C}{E}\right];\ \Gamma(E) = \Gamma_S\left[\frac{E}{E + \Gamma_B}\right];$$

$$T_0(E) = T_S - \left[\frac{T_A}{E + T_B}\right];\ T_M = \frac{E - I}{2}.$$

Here E is the incident energy in eV, I is the fitting ionization potential in the eV, which is generally close to the threshold potential (W_{th}), and σ is in units of 10^{-16} cm^2. This form gives the asymptotic behaviour $\sigma(E) \propto E^{-1} \ln E$ at high energies, which is expected from the Born approximation. The fitting parameters are presented in the Table 2.7. The fitted cross sections for single and double ionization are shown in Figures 2.6 and 2.7, respectively.

2.4.5 Excitation cross sections

2.4.5.1 Vibrational excitation

CO_2 is a linear triatomic molecule, which has three normal modes of vibration, viz., a bending mode (0 n 0), a symmetric stretching mode (n 0 0), and an asymmetric stretching mode (0 0 n), with excitation energy 83 meV, 172 meV, and 291 meV, respectively [*Kochem et al.*, 1985]. Infrared active (010) bending and (001) asymmetric stretching modes in the near-to-threshold region follow the Born approximation. Moreover, the structure near the threshold of vibration excitation in CO_2 has been investigated by *Kochem et al.* [1985], vibrationally inelastic DCS above 4 eV impact energies have been measured by *Register et al.* [1980] for scattering angles $10° - 140°$ and impact energies of 4, 10, 20, and 50 eV, and by *Johnstone et al.* [1995] for only one scattering angle (20°) in the energy region 1 to 7.5 eV. *Nakamura* [1995] determined the vibrational cross section using swarm experiment. *Kitajima et al.* [2001] made measurements of DCS for the electron impact excitation of CO_2 for (010), (100), (001), and (020) vibrational modes over the scattering angles $20° - 130°$ and energy range 1.5-30 eV (except at 4 eV, where the smallest angle was extended up to 10°), and assigned an uncertainty of 30% to their measurements. Their DCS is consistent with the results of previous beam-type measurements. *Itikawa* [2002] has extrapolated the DCS of *Kitajima et al.* [2001] to obtain the total vibration cross sections for three modes, which are presented in Figure 2.4.

Table 2.7: Parameters for various ionization processes in electron impact on CO_2.

	W_{th}	I	K	K_B	J	J_B	Γ_S	Γ_B	T_S	T_A	T_B
CO_2^+(Total)	13.76	13.76	9.83	0.0	40.59	1.050	18.61	-13.23	-0.847	875	44.52
$CO_2^+(X^2\Pi_g)$	13.76	13.76	3.480	0.0	4.099	-2.35	11.11	-13.26	-0.847	1000	27.52
$CO_2^+(A^2\Pi_u)$	17.8	17.8	8.632	6.0	86.36	1.004	12.00	-18.80	-1.996	550	10.20
$CO_2^+(B^2\Sigma_u^+)$	18.1	18.1	4.632	5.0	85.36	1.004	12.00	-18.5	-0.978	450	10.20
$CO_2^+(C^2\Sigma_g^+)$	19.4	19.4	0.580	0.0	21.19	1.270	10.98	-19.00	-0.887	1000	38.80
CO^+	24.76	24.76	1.347	15.00	6.650	1.256	9.556	-24.0	1.887	800	25.52
O^+	24.5	24.5	2.399	40.00	11.34	-1.10	13.42	-24.0	-0.587	0.0	0.0
C^+	29.5	29.5	1.659	0.0	53.54	0.625	10.62	-29.0	2.800	21.8	44.00
C^{++}	79.94	79.94	0.0012	25.00	0.100	0.656	79.11	0.0	0.8473	0.0	0.0
O^{++}	94	94	0.0055	10.00	1.700	-3.156	20.11	0.0	-0.8473	0.0	0.0
CO_2^{++}	37.6	44.75	0.0583	1.20	0.250	0.0	11.57	35.26	1.548	800	30.52
(CO^+,O^+)	44.7	44.7	0.285	1.200	0.550	0.0	11.97	35.26	1.547	650	30.52
(C^+,O^+)	44.7	44.7	0.288	1.200	0.550	0.0	10.40	45.00	1.547	750	0.0
(O^+,O^+)	44.7	44.7	0.158	1.200	0.450	0.0	5.400	15.00	5.547	750	0.0

For all states the value of $J_c = 0.0$.

In this study, the cross sections for the three fundamental vibrational modes (010), (100), and (001) are taken from *Itikawa* [2002]. There are other modes also but their cross sections are small compare to these three fundamental modes.

2.4.5.2 Electronic excitation

There are several features in the optical and electron scattering spectrum of CO_2 in the energy loss range between 7 and 11 eV [*Herzberg*, 1966; *Rabalais et al.*, 1971; *Hall et al.*, 1973]. Except for Rydberg states, there is still no definite consensus about structure and assignment of the excited electronic states of CO_2. In the energy loss spectra of CO_2, *Green et al.* [2002] have found four clearly distinct peaks at 10.98, 11.05, 11.16, and 11.40 eV, with an uncertainty of 30% in their results. *Itikawa* [2002] in his review paper has recommended the DCS of *Green et al.* [2002], for the excitation of the 10.8-11.5 eV energy loss states. Recently, *Kawahara et al.* [2008] have given the integral cross section for electronic states $^1\Sigma_u^+$ and $^1\Pi_u$ of CO_2, based on the DCS measurement of *Green et al.* [2002] in the energy range 20-200 eV.

Theoretical calculations of electronic structure have also been made by several authors [*Nakatsuji*, 1983; *Spielfiedel et al.*, 1992; *Buenker et al.*, 2000; *Lee et al.*, 1999]. Using distorted-wave method, *Lee and McKoy* [1983] calculated the cross section for the excitation of eight low lying-states. But there is not much agreement among these calculations. In summary, there is still a need for a detailed study of excitation of electronic states of CO_2 by electron impact.

The empirical cross sections calculated by *Jackman et al.* [1977] for the electronic states of CO_2 are used in the present study. These cross sections have been obtained using equation:

$$\sigma(E) = \frac{(q_0 F)}{W^2}\left[1-\left(\frac{W}{E}\right)^{\alpha}\right]^{\beta}\left[\frac{W}{E}\right]^{\Omega} \tag{2.5}$$

where $q_0 = 4\pi a_0 R^2$ and has the value 6.512×10^{-14} $\mathrm{eV^2\ cm^2}$. The fitting parameter are given in Table 2.8. Sum of cross sections for two states 12.4 and 13.6 eV corresponds to CO Cameron band [cf. *Sawada et al.*, 1972]. A further discussion on the CO($a^3\Pi$) cross section is given in Chapter 4.

2.4.6 Emissions

Electron impact dissociation and ionization of CO_2 can result in the production of excited fragments of CO, O, and CO_2 in the neutral and ionized states, resulting in the emissions in the ultraviolet region. The strong band systems observed on Mars are Fox-Duffendack-Barker bands ($A^2\Pi_u \rightarrow X^2\Pi_g$) and ultraviolet doublet ($B^2\Sigma_u^+ \rightarrow X^2\Pi_g$) of CO_2^+, and Cameron bands ($a^3\Pi \rightarrow X^1\Sigma^+$) of CO [*Ajello*, 1971a; *Barth et al.*, 1971; *Bertaux et al.*, 2006; *Leblanc et al.*, 2006]. *Ajello* [1971a] measured the emission cross sections for the $A^2\Pi_u \rightarrow X^2\Pi_g$ and $B^2\Sigma_u^+ \rightarrow X^2\Pi_g$ bands of CO_2^+ from threshold to

Table 2.8: Parameters for various excitation and emission processes in electron impact on CO_2.

Excitation states	$W^{\dagger}$	α	β	$W_J{}^{\ddagger}$	Ω	F	$A.F.$
[Vibration, (010)]*	0.080	2.750	1.000	0.080	0.750	0.000060	0.0
[Vibration, (100)]	0.180	1.070	1.000	0.180	0.750	0.000031	0.0
[Vibration, (001)]	0.290	2.910	0.500	0.300	0.810	0.000445	0.0
8.6 eV state	8.600	0.556	2.000	8.600	0.936	0.060600	0.0
9.3 eV state	9.300	0.603	2.000	9.300	0.909	0.064000	0.0
11.1 eV state	7.760	0.246	3.000	11.100	1.110	4.420000	0.0
[12.4 eV state]	9.610	0.338	3.000	12.400	0.830	6.700000	0.0
[13.6 eV state]	10.50	0.625	3.000	13.600	0.849	3.350000	0.0
15.5 eV state	15.50	0.739	2.000	15.500	0.793	0.139000	0.750
16.3 eV state	12.30	0.605	3.000	16.300	0.911	0.716000	0.750
17.0 eV state	13.00	0.649	3.000	17.000	0.878	0.114000	0.750
17.8 eV state	14.00	0.977	3.000	17.800	0.725	0.051100	0.750
OI (1304)	20.10	0.599	3.000	22.000	1.000	0.127000	0.750
OI (1356)	16.40	0.600	3.000	20.400	0.944	0.168000	0.500
CI (1279)	15.70	1.000	3.000	26.200	0.643	0.010400	0.500
CI (1329)	21.80	1.000	3.000	20.900	1.040	0.020200	0.500
CI (1561)	22.40	1.000	3.000	24.500	0.982	0.053800	0.500
CI (1657)	21.10	1.000	3.000	24.100	0.947	0.872000	0.500
[CO^+(first negative)]	18.13	0.656	2.54	25.11	0.804	1.055	0.0

*Parameters are taken from *Jackman et al.* [1977], except for the states which are inside the square brackets whose parameters have been modified.

†Value is for fitting threshold.

‡Value is actual threshold.

300 eV. He also measured cross sections for the excitation of the fourth positive system of CO ($A^1\Pi \rightarrow X^1\Sigma^+$), the first negative system of CO^+ ($B^2\Sigma^+ \rightarrow X^2\Sigma^+$) and several atomic multipletes of carbon and oxygen produced from dissociative excitation of CO_2.

2.4.6.1 Emissions from CO_2^+

McConkey et al. [1968], *Ajello* [1971a], and *Tsurubuchi and Iwai* [1974] have detected emissions corresponding to the following transitions:

$$A^2\Pi_u \rightarrow X^2\Pi_g \quad \text{at } 293.6 - 438.4 \text{ nm}$$

and

$$B^2\Sigma_u^+ \rightarrow X^2\Pi_g \quad \text{at } 218.9 - 226.8 \text{ nm}$$

The peak value of cross sections measured by the three groups for the above transitions are in good agreement with each other. These emissions are well known in the Mars upper atmosphere. Both the ground and excited states of CO_2^+ are known to be linear [*Herzberg*, 1966]. The cross section of *Ajello* [1971a] has too steep an energy dependence near threshold compared to *McConkey et al.* [1968] and *Tsurubuchi and Iwai* [1974]. In his review, *Itikawa* [2002] recommended the cross sections of *Tsurubuchi and Iwai* [1974], for which the peak values are $(8.0 \pm 2.0) \times 10^{-17}$ cm^2 at 160 eV for the $A - X$ transition, and $(4.7 \pm 1.2) \times 10^{-17}$ cm^2 for the $B - X$ transition. We have taken the cross sections for $A - X$ and $B - X$ emissions of CO_2^+ from *Itikawa* [2002]. These cross sections have been fitted using Eq. 2.4. The fitting parameters are given in Table 2.7, and fitted cross sections in Figure 2.6.

2.4.6.2 Emissions from CO$^+$

Only *Ajello* [1971a] has measured the cross section for the emission of first negative system ($B^2\Sigma^+ \rightarrow X^2\Sigma^+$) of CO^+. The cross section exhibits an appearance potential of 25.11 eV, and the peak value of cross section is 1.9×10^{-18} cm^2 around 100 eV. The cross section for the excitation of the first negative system of CO^+ from electron impact on CO_2 is about a factor of 25 less than for excitation of the same system from CO [*Ajello*, 1971a]. We have adopted the cross section of *Ajello* [1971a], which has been fitted analytically using Eq. 2.5; the fitting parameters are given in Table 2.8. Figure 2.6 shows the fitted cross section along with experimental cross section.

2.4.6.3 Emissions from CO

Cross sections for the production of Cameron band system ($a^3\Pi \rightarrow X^1\Sigma^+$) and fourth positive system ($A^1\Pi \rightarrow X^1\Sigma^+$) of CO have been measured by *Ajello* [1971a]. The emission cross section for the fourth positive system is very weak and Ajello could not measure the cross section near threshold (13.48 eV). For the Cameron band system, *Ajello* [1971a] reported relative magnitudes of the cross section for the (0, 1) band at 215.8 nm. The upper state ($a^3\Pi$) of Cameron emission is metastable and has a radiative lifetime of ∼3 ms [*Gilijamse et al.*, 2007], and kinetic energies of the CO($a^3\Pi$) fragments are in the range of 0–1.2 eV [*Freund*, 1971]. *Erdman and Zipf* [1983] measured the total cross section for CO ($a^3\Pi \rightarrow X^1\Sigma^+$) electronic transition. They estimated the absolute magnitude of total Cameron band emission cross section of 2.4×10^{-16} cm^2 at 80 eV. A detailed discussion on CO(a$^3\Pi$) production in electron impact on CO is provided in Chapter 4. The Cameron band is the brightest emission feature in the UV dayglow of both Mars and Venus as well as an important emission in CO_2-containing atmospheres, e.g., comets [*Bhardwaj and Raghuram*, 2011, 2012]. The loss channels at 12.4 and 13.6 eV corresponds to CO Cameron cross section [*Sawada et al.*, 1972]. The parameters given by *Jackman et al.* [1977] at 12.4 and 13.6 eV have been modified in the present study to get the total value of 2.4×10^{-16} cm^2 at 80 eV. The modified parameters are given in Table 2.8.

2.4.6.4 Emissions from O and C

Both *Ajello* [1971a] and *Mumma et al.* [1972] have reported cross section for the emission of the O 130.4 nm triplet from electron impact on CO_2, but the measurements are not consistent with each other. There are many other atomic emissions produced in e-CO_2 collisions, but they have very small cross sections [cf. *van der Burgt et al.*, 1989]. *Kanik et al.* [1993] have reported the emission cross sections for O, O^+, C, C^+, CO, and CO^+ in the wavelength region 40–125 nm. All the cross sections of *Kanik et al.* [1993] are less than 10^{-18} cm^2. The OI and CI production cross sections are taken from *Jackman et al.* [1977] in the present study, for which the fitting parameters are given Table 2.8.

2.5 Electron impact cross sections of CO, N_2, O, and O_2

The electron impact cross sections for CO, N_2, O, and O_2 are taken from work of *Jackman et al.* [1977], which are semi-empirical cross sections. The parameters for different cross sections are given in Tables 2.9–2.12. The total ionization and excitation cross sections of CO, N_2, O, and O_2 are shown in Figure 2.8 along with the total and elastic cross sections. Total and elastic cross sections of CO, N_2, O_2, and O are from *Shirai et al.* [2001], *Itikawa et al.* [1989], *Itikawa* [2006], and *Itikawa and Ichimura* [1990], respectively.

2.6 Summary

The solar EUV flux is a very fundamental input parameter in the modelling of energetic and dynamics of planetary upper atmosphere and cometary coma. A brief description of solar EUV flux models used in the model calculations of various dayglow emissions on Mars and Venus is presented in this chapter. The applications of these solar flux models to study the various emission features on Mars and Venus are presented in Chapters 4, 5, and 6.

A brief description of photoabsorption and photoionization cross sections of CO_2, CO, N_2, O, and O_2 have been given the Chapter which are shown in graphical form in Figure 2.2 and also presented in tabular form in Tables 2.2, 2.3, and 2.4.

In this chapter a review of e-CO_2 cross sections is presented. The inelastic processes include, ionization, dissociative ionization excitation, dissociative excitation, and electron attachment process. A comprehensive set of electron impact cross sections of CO_2 based on recent laboratory measurements is presented. Figure 2.3 shows the summary

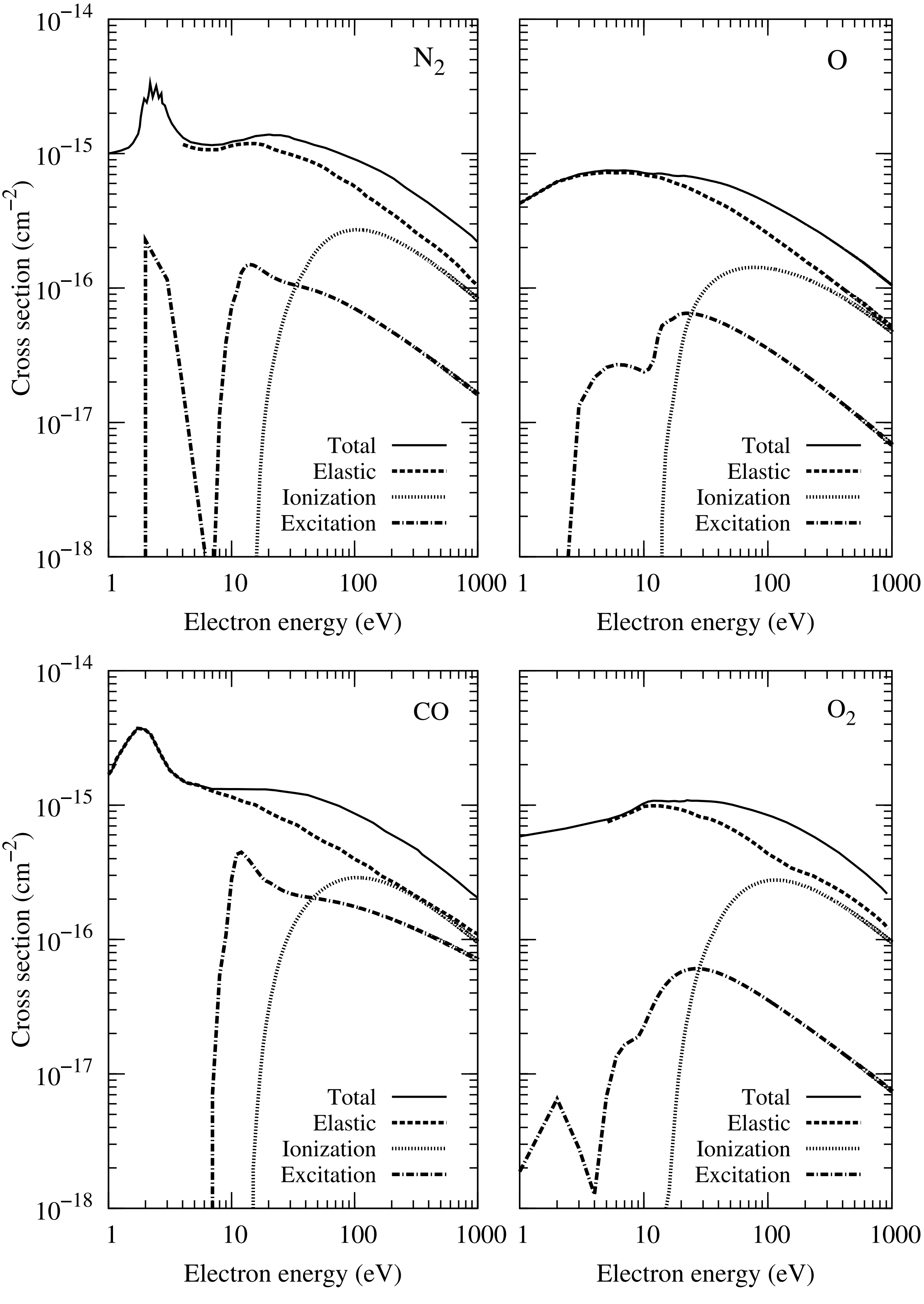

Figure 2.8: The total electron impact cross sections of CO, N$_2$, O, and O$_2$ along with cross sections for total ionization, excitation, and elastic processes.

Table 2.9: Parameters for various excitation and ionization processes in electron impact on Carbon monoxide (CO).

	Excited states	W*	α	β	$\bar{W_j}^\dagger$	Ω	F$_i$	A.F
1	A$^1\Pi$	7.900	0.125	1.000	8.510	0.750	0.749000	0.000
2	B$^1\Sigma^+$ (n=3)	9.580	0.125	1.000	10.780	0.750	0.067100	0.000
3	C$^1\Sigma^+$ (n=3)	10.700	0.125	1.000	10.400	0.750	0.553000	0.000
4	E$^1\Pi$ (n=3)	10.800	0.125	1.000	11.520	0.750	0.325000	0.000
5	F$^1\Pi$ (n=3)	11.700	0.125	1.000	12.370	0.750	0.069500	0.000
6	B$^1\Sigma^+$ (n=4)	11.400	0.125	1.000	12.590	0.750	0.168000	0.000
7	C$^1\Sigma^+$ (n=4)	12.100	0.125	1.000	12.800	0.750	0.369000	0.000
8	E$^1\Pi$ (n=4)	12.100	0.125	1.000	12.820	0.750	0.217000	0.000
9	F$^1\Pi$ (n=4)	12.400	0.125	1.000	13.110	0.750	0.046400	0.000
10	13.5 ev state	12.700	0.125	1.000	13.500	0.750	1.630000	0.000
11	a$^3\Pi$ (1)	6.450	1.000	3.000	6.220	5.020	13.60000	0.000
12	a$^3\Pi$ (2)	6.220	1.000	3.000	6.220	0.750	0.076000	0.000
13	b$^3\Sigma^+$ (1)	10.400	1.000	3.000	10.400	6.950	6.010000	0.000
14	b$^3\Sigma^+$ (2)	10.400	1.000	3.000	10.400	0.750	0.013500	0.000
15	a$'^3\Sigma^+$	9.350	10.300	1.870	6.910	2.600	0.874000	0.000
16	c$^3\Pi$	18.600	14.700	1.550	11.400	2.590	0.116000	0.000
17	d$^3\Delta$	2.320	2.550	111.00	7.500	1.860	0.010600	0.000
18	j$^3\Sigma^+$	8.000	10.000	17.700	11.270	2.630	0.026400	0.000
19	D$^1\Delta$	5.150	0.714	3.000	8.070	1.000	0.032500	0.000
20	CO$^-$	9.400	3.000	1.000	9.620	17.400	0.004760	0.000
21	CO$^-$	21.300	2.000	1.000	22.000	0.955	0.003440	0.000
22	OI (1304)	32.400	0.384	1.000	20.630	0.750	0.023900	0.500
23	OI (8447)	36.000	0.400	1.000	22.000	0.886	0.087300	0.500
24	OI (1279)	21.400	0.114	1.000	21.000	0.687	0.084600	0.500

	Rydberg states	I$_i$	α	β	δ	Ω	F*	A.F. -n	A.F. -n	A.F. -n
1	B$^1\Sigma^+$	14.010	0.125	1.0	0.900	0.750	0.621	0.0 -5	0.0 -6	
2	C$^1\Sigma^+$	14.010	0.125	1.0	0.650	0.750	7.180	0.0 -5	0.0 -6	
3	E$^1\Pi$	14.010	0.125	1.0	0.620	0.750	4.390	0.0 -5	0.0 -6	
4	F$^1\Pi$	14.010	0.125	1.0	0.110	0.750	1.680	0.0 -5	0.0 -6	
5	(L1)	16.540	0.125	1.0	1.040	0.750	6.940	0.5 -3	0.5 -4	0.5 -5
6	Tanaka α	16.540	0.125	1.0	0.680	0.750	3.470	0.5 -3	0.5 -4	0.5 -5
7	(L2)	16.540	0.125	1.0	0.150	0.750	3.470	0.5 -3	0.5 -4	0.5 -5
8	Ogawa 3	19.680	0.125	1.0	0.940	0.750	0.694	0.5 -3	0.5 -4	0.5 -5
9	Tanaka sharp β	19.680	0.125	1.0	0.680	0.750	2.770	0.5 -3	0.5 -4	0.5 -5
10	Tanaka diffuse β	19.680	0.125	1.0	0.580	0.750	2.770	0.5 -3	0.5 -4	0.5 -5
11	Ogawa 4	19.680	0.125	1.0	0.200	0.750	0.694	0.5 -3	0.5 -4	0.5 -5

	Ion. states	I$_i$	K	K$_B$	J	J$_B$	J$_C$	Γ_S	Γ_B	T$_S$	T$_A$	T$_B$
1	X$^2\Sigma^+$	14.010	3.530	0.0	12.600	0.0	0.0	12.100	-13.500	2.090	1000.0	28.00
2	A$^2\Pi_u$	16.540	3.370	0.0	12.600	0.0	0.0	12.100	-13.500	2.090	1000.0	28.00
3	B$^2\Sigma^+$	19.680	1.640	0.0	12.600	0.0	0.0	12.100	-13.500	2.090	1000.0	28.00
4	Diss. Ion.‡	22.000	0.866	0.0	0.010	0.0	0.0	13.600	44.000	2.040	1000.0	44.00

*Value is for fitting threshold. †Value is actual threshold. ‡Dissociative Ionization.

of total e-CO$_2$ cross sections used in the study. The e-CO$_2$ cross sections are represented analytically and fitting parameters are provided in Tables 2.5–2.8. The electron impact analytical cross sections of CO, N$_2$, O, and O$_2$ are also used in the present study. The parameters for them have been given in Tables 2.9–2.12 and total, ionization, excitation, and elastic cross sections are shown in Figure 2.8.

Table 2.10: Parameters for various excitation and ionization processes in electron impact on molecular Nitrogen (N_2).

	Excited States	W*	α	β	$\bar{W}_j{}^\dagger$	C	F	A.F.
1	$^1\Pi_u$	12.500	1.240	3.660	12.800	0.056	0.666000	0.0
2	$^1\Sigma_u^+$	13.300	1.290	3.720	14.000	0.061	0.000046	0.0
						Ω		
3	vib. ν=1–3	1.850	1.000	1.000	0.570	7.000	0.273000	0.0
4	vib. ν=4–8	2.150	1.000	1.000	1.680	9.000	0.241000	0.0
5	$A^3\Sigma_u^+$ (VK)	8.000	1.000	1.000	6.170	3.000	0.226000	0.0
6	$B^3\Pi_g$ (1P)	8.500	3.000	1.000	7.350	3.000	0.178000	0.0
7	$C^3\Pi_u$ (2P)	11.050	3.000	1.000	11.030	3.000	0.280000	0.0
8	$E^3\Sigma_g^+$	11.900	3.000	1.000	11.900	3.000	0.048000	0.0
9	$a^1\Pi_g$ (LBH)	8.600	1.000	1.000	8.550	1.000	0.136000	0.0
10	$a''^1\Sigma_g^+$(BH)	12.250	2.300	1.000	12.250	1.000	0.027000	0.0

	Rydberg States	I_i	α	β	δ	C	F*	A.F.–n	A.F.–n	A.F.–n
1	$X^2\Sigma_g^+$	15.580	1.180	3.440	0.700	0.062	5.110	0.000-3	0.000-4	0.000-5
2	$A^2\Pi_u$	16.730	1.170	3.420	1.040	0.065	2.240	0.500-3	0.500-4	0.320-5
3	$B^2\Sigma_u^+$	18.750	1.160	3.360	0.870	0.075	1.160	0.500-3	0.500-4	0.320-5
4	$D^2\Pi_g^+$	22.000	1.150	3.320	1.530	0.083	0.784	0.500-3	0.500-4	0.320-5
5	$C^2\Sigma_u^+$	23.600	1.130	3.250	0.800	0.096	0.784	0.500-3	0.500-4	0.320-5
6	40 eV state	40.000	1.130	3.250	0.800	0.096	1.120	0.500-3	0.500-4	0.320-5

	Ionization States	I_i	K	K_B	J	J_B	J_C	Γ_S	Γ_B	T_S	T_A	T_B
1	$X^2\Sigma_g^+$	15.580	2.120	0.0	1.740	0.0	0.0	13.800	15.580	4.710	1.000	31.160
2	$A^2\Pi_u$	16.730	1.060	0.0	1.740	0.0	0.0	13.800	16.730	4.710	1.000	33.460
3	$B^2\Sigma_u^+$	18.750	0.551	0.0	1.740	0.0	0.0	13.800	18.750	4.710	1.000	37.500
4	$D^2\Pi_g^+$	22.000	0.371	0.0	1.740	0.0	0.0	13.800	22.000	4.710	1.000	44.000
5	$C^2\Sigma_u^+$	23.600	0.371	0.0	1.740	0.0	0.0	13.800	23.600	4.710	1.000	47.000
6	40 eV state	40.000	0.530	0.0	1.740	0.0	0.0	13.800	40.000	4.710	1.000	80.000

*Value is for fitting threshold. †Value is actual threshold.

Table 2.11: Parameters for various excitation and ionization processes in electron impact on atomic oxygen (O)

	Excited states	W*	α	β	$\bar{W_j}^\dagger$	C	F_i	A.F
1	$(^4S^0)$ 3s $^3S^0$	9.530	0.860	1.440	9.530	0.320	0.056000	0.000
2	$(^4S^0)$ 3d $^3D^0$	17.900	1.260	0.490	12.100	0.610	0.031000	0.000
3	$(^2D^0)$ 3s $^3D^0$	12.500	0.860	1.440	12.500	0.320	0.056000	0.000
4	$(^2D^0)$ 3d $^3S^0$	15.350	1.260	0.490	15.350	0.610	0.006500	0.500
5	$(^2D^0)$ 3d $^3P^0$	15.350	1.260	0.490	15.350	0.610	0.007700	1.000
6	$(^2D^0)$ 3d $^3D^0$	15.350	1.260	0.490	15.350	0.610	0.005200	0.500
7	$(^2P^0)$ 3s $^3P^0$	14.100	0.860	1.440	14.100	0.320	0.037000	0.700
8	$(^2P^0)$ 3d $^3P^0$	16.940	1.260	0.490	16.940	0.610	0.008000	0.300
9	$(^2P^0)$ 3d $^3D^0$	16.940	1.260	0.490	16.940	0.610	0.006000	0.500
10	$2P^5$ $^3P^0$	15.500	0.860	1.440	15.500	0.320	0.042300	0.300
						Ω		
11	$2P^4$ ^1D	1.960	1.000	2.000	1.850	1.000	0.010000	0.000
12	$2P^4$ ^1S	4.180	0.500	1.000	4.180	1.000	0.004200	0.000
13	$(^4S^o)$ 3s $^5S^0$	10.600	19.200	10.500	9.290	2.690	0.013000	0.000
14	$(^4S^o)$ 3p ^5P	10.740	1.170	0.755	10.740	1.600	0.023400	0.000
15	$(^4S^o)$ 3p ^3P	11.640	18.200	5.600	11.000	0.855	0.057800	0.000

.	Rydberg states	I_i	α	β	δ	Ω	F*	A.F. -n	A.F. -n	A.F. -n
1	$(^4S^0)$ nd $^3D^0$	13.60	1.26	0.490	0.01	0.610	0.820	0.00 -4	0.00 -5	
2	$(^4S^0)$ ns $^3S^0$	13.60	0.86	1.440	1.16	0.320	0.349	0.00 -4	0.00 -5	
3	$(^2D^0)$ ns $^3D^0$	16.90	0.86	1.440	1.21	0.320	0.321	1.00 -4	1.00 -5	
4	$(^2D^0)$ nd $^3SPD^0$	16.90	1.26	1.490	0.04	0.610	0.503	0.70 -4	1.00 -5	
5	$(^2P^0)$ ns $^3P^0$	18.50	0.86	1.440	1.25	0.320	0.198	1.00 -4	1.00 -5	
6	$(^2P^0)$ nd $^3PD^0$	18.50	1.26	0.490	0.05	0.610	0.360	0.75 -4	0.75 -5	
7	$(^4S^0)$ ns $^5S^0$	13.60	19.20	10.500	1.24	2.690	0.071	0.00 -4	0.00 -5	
8	$(^4S^0)$ np ^3P	13.60	18.20	5.600	0.69	0.855	0.713	0.00 -4	0.00 -5	
9	$(^4S^0)$ np $^5P^0$	13.60	1.17	0.753	0.81	1.600	0.246	0.00 -4	0.00 -5	
10	$(^4S^0)$ nd $^5D^0$	13.60	1.00	2.000	0.01	3.000	0.200	0.00 -3	0.00 -4	0.00 -5
11	$(^2D^0)$ ns $^1D^0$	16.90	1.00	2.000	1.18	3.000	0.200	0.00 -3	0.00 -4	0.00 -5
12	$(^2D^0)$ np $^3PDF^0$	16.90	2.00	1.000	0.84	1.000	0.100	0.00 -3	0.00 -4	0.00 -5
13	$(^2D^0)$ np $^1PDF^0$	16.90	1.00	1.000	0.83	3.000	0.040	0.00 -3	0.00 -4	0.00 -5
14	$(^2D^0)$ nd $^3FG^0$	16.90	2.00	1.000	0.04	1.000	0.100	0.00 -3	0.00 -4	0.00 -5
15	$(^2D^0)$ nd $^1SPDFG^0$	16.90	1.00	2.000	0.04	3.000	0.200	0.00 -3	0.00 -4	0.00 -5
16	$(^2P^0)$ ns $^1P^0$	18.50	1.00	2.000	1.19	3.000	0.200	0.00 -3	0.00 -4	0.00 -5
17	$(^2P^0)$ np ^3SPD	18.50	2.00	1.000	0.86	1.000	0.100	0.00 -3	0.00 -4	0.00 -5
18	$(^2P^0)$ np ^1SPD	18.50	1.00	1.000	0.85	3.000	0.040	0.00 -3	0.00 -4	0.00 -5
19	$(^2P^0)$ nd $^3F^0$	18.50	2.00	1.000	0.05	1.000	0.100	0.00 -3	0.00 -4	0.00 -5
20	$(^2P^0)$ nd $^2PDF^0$	18.50	1.00	2.000	0.05	3.000	0.200	0.00 -3	0.00 -4	0.00 -5

	Ionization states	I_i	K	K_B	J	J_B	J_C	Γ_S	Γ_B	T_S	T_A	T_B
1	$^2S^0$	13.60	1.030	0.0	1.810	0.0	0.0	13.0	-0.815	6.410	3450	162.00
2	$^2D^0$	16.90	0.780	0.0	1.790	0.0	0.0	13.0	-0.815	6.410	3450	162.00
3	$^2P^0$	18.50	1.310	0.0	1.780	0.0	0.0	13.0	-0.815	6.410	3450	162.00

*Value is for fitting threshold. †Value is actual threshold.

These analytical cross sections represent the measured values of cross sections at all energies and can be easily used in the Monte Carlo simulation and other electron degradation methods. The applications of these cross sections in the study of degradation of electrons using Monte Carlo technique are presented in Chapter 3 and further in the calculation of volume excitation/emission rates in Chapters 4, 5, and 6.

Table 2.12: Parameters for various excitation and ionization processes in electron impact on molecular Oxygen (O_2).

	Excited states	W*	α	β	$\bar{W}_j$†	C	F$_i$	A.F
1	$B^2\Sigma_u^-$	8.400	1.190	2.310	8.400	0.037	0.254000	0.0
2	9.9 eV Peak	9.900	1.380	3.440	9.900	0.622	0.028500	0.0
						Ω		
3	$b^1\Sigma_g^+$	1.640	3.000	1.000	1.640	3.000	0.000500	0.0
4	$a^1\Delta_g$	0.980	3.000	1.000	0.980	3.000	0.000500	0.0
5	$A^3\Sigma_u^+$	4.500	1.000	1.000	4.500	0.900	0.021000	0.0

	Rydberg states	I$_i$	α	β	δ	C	F*	A.F. -n	A.F. -n	A.F. -n
1	$X^2\Pi_g$	12.100	1.220	3.710	1.080	0.044	0.688	0.00 -3	0.00 -4	0.000 -5
2	$a^4\Pi_u$	16.100	1.180	3.440	1.000	0.062	1.634	0.50 -3	0.50 -4	0.320 -5
3	$A^2\Pi_u$	16.900	1.170	3.410	1.070	0.065	1.634	0.50 -3	0.50 -4	0.320 -5
4	$b^4\Sigma_g^-$	18.200	1.160	3.360	0.690	0.073	1.462	0.50 -3	0.50 -4	0.320 -5
5	$B^2\Sigma_g^-$	20.300	1.140	3.280	1.000	0.093	0.946	0.50 -3	0.50 -4	0.320 -5
6	$c^4\Sigma_u^-, {}^2\Pi(III)$	23.000	1.140	3.280	1.000	0.093	1.176	0.50 -3	0.50 -4	0.320 -5
7	37 eV state	37.000	1.140	3.280	1.000	0.093	0.860	0.50 -3	0.50 -4	0.320 -5

	Ionization states	I$_i$	K	K$_B$	J	J$_B$	J$_C$	Γ_S	Γ_B	T$_S$	T$_A$	T$_B$
1	$X^2\Pi_g$	12.100	0.475	0.0	3.760	0.0	0.0	18.500	12.100	1.860	1000.0	24.200
2	$a^4\Pi_u$	16.100	1.129	0.0	3.760	0.0	0.0	18.500	16.100	1.860	1000.0	32.200
3	$A^2\Pi_u$	16.900	1.129	0.0	3.760	0.0	0.0	18.500	16.900	1.860	1000.0	33.800
4	$b^4\Sigma_g^-$	18.200	1.010	0.0	3.760	0.0	0.0	18.500	18.200	1.860	1000.0	36.400
5	$B^2\Sigma_g^-$	20.300	0.653	0.0	3.760	0.0	0.0	18.500	20.300	1.860	1000.0	40.600
6	$c^4\Sigma_u^-, {}^2\Pi(III)$	23.000	0.950	0.0	3.760	0.0	0.0	18.500	23.000	1.860	1000.0	46.000
7	37 eV state	37.000	0.594	0.0	3.760	0.0	0.0	18.500	37.000	1.860	1000.0	74.000

*Value is for fitting threshold. †Value is actual threshold.

Chapter 3

Monte Carlo model for electron degradation in CO_2 gas

3.1 Introduction

Photoionization is the main source of electrons and ions in the dayside upper atmosphere of planets. Photoelectrons, generated due to photoionization process, can have enough kinetic energy to ionize the atmospheric constituents and produce secondary electrons. Similarly, energetic electrons precipitating along the magnetic field lines into the auroral atmosphere of planets can ionize the medium producing secondary electrons. Besides ionization, the electron loses its energy in excitation, attachment, and dissociation. Hence, the study of electron energy deposition in atmosphere is an important aspect in understanding processes like aurora, dayglow, nightglow. Apart from that a detail knowledge about the energy deposition of electrons in a gaseous medium is of fundamental interest to many fields of science, viz., physics, chemistry, biology, interaction of electron with matter, laboratory plasmas and lasers, and astrophysics. To model the electron energy degradation in an atmosphere one has to first compile cross sections for various loss processes, and then develop an electron energy apportionment method, which will distribute the electron energy among different loss channels. A model for energy apportionment of electrons in CO_2 gas (second task) is discussed in this Chapter. The first task, i.e., compilation of various electron impact cross sections, is already addressed in Chapter 2.

There are several different techniques to study the degradation of electron in a gaseous medium; some of these methods are discussed below. The diffusion transport method is based on diffusion theory, and determines the photoelectron flux by solving a set of coupled flux equation [e.g., *Nisbet*, 1968; *Swartz*, 1972]. The calculation of diffusion coefficient for electrons through the atmosphere which depends on the electron pitch angle distribution and on the collisional scattering details is essential in the diffusion transport theory. The two-stream method [e.g., *Banks and Nagy*, 1970; *Nagy and Banks*, 1970], which uses two stream continuity equations to describe the electron fluxes moving into and out of the atmosphere along the magnetic field lines. This method has been used by many workers in different planetary applications [e.g., *Waite et al.*, 1983; *Solomon et al.*, 1988; *Haider et al.*, 1992]. The main drawback of this method is the insufficient resolution due to only two direction. A multi-stream approach has been presented by *Oran and Strickland* [1978] to calculate photoelectron flux in the ionosphere by solving Boltzmann equations. Similar approach has been used by *Perry et al.* [1999] to calculate the chemistry of Jovian auroral ionosphere by calculating the energy degradation of high energy electron into the auroral region. *Mantas and Bowhill* [1975] used the low-energy electron thermalization and transport based on the Boltzmann equation [cf. *Mantas*, 1975]. A similar approach of photoelectron flux calculation on Mars has been used by *Mantas and Hanson* [1979]. *Walt et al.* [1969] used a Fokker-Planck diffusion equation to describe simultaneous electron energy degradation, electron angular scattering through collision with atmospheric gases, and the effect of converging magnetic field of Earth upon the pitch angle distribution.

The Continuous Slowing Down Approximation (CSDA) technique has been used by many workers to study the energy degradation of charged particle in a gaseous medium [*Green and Barth*, 1965, 1967; *Stolarski and Green*, 1967; *Singhal et al.*, 1992]. In this technique a charged particle is continuous degraded in a medium from their initial energy to the minimum threshold energy. According to *Heaps and Green* [1974] use of CSDA technique is advantageous because it is inexpensive to use and gives reliable results regarding total population of excited states. But it has a disadvantage of not giving an accurate physical picture of the spatial degradation of primary electrons of energy less then few hundred eV. The Monte Carlo method gives a good representation of energy degradation of primaries as well secondary electrons at all energy. The Monte Carlo results agrees well with the experiment for energy degradation in the keV energy range [*Heaps and Green*, 1974]. According *Peterson* [1969], the CSDA approach is erroneous when the energy losses are a substantial fraction of the primary energy. *Peterson* [1969] suggested a discrete bin method, in which the energy range between primary and threshold value is divided into bins. Then the degradation processes is assumed to commence in which the primary energy is fractionally redistributed into the lower bins. This process is continued as each energy bin is emptied. In this manner the mean total number of excitations of each state produced in the complete degradation of an electron from a given incident energy is obtained [*Green et al.*, 1977].

Due to its effectiveness in solving the stochastic process Monte Carlo technique has been used to calculate photoelectron fluxes in the atmosphere of Earth [*Cicerone and Bowhill*, 1970, 1971; *Cicerone et al.*, 1973] and in cometary atmospheres [e.g., *Ashihara*, 1978]. It has also been used in the degradation of auroral electron and related problems in Earth atmosphere [*Maeda*, 1965; *Berger et al.*, 1970; *Solomon*, 1993; *Sergienko and Ivanov*, 1993; *Onda et al.*, 1999]. *Singhal and Bhardwaj* [1991] and *Bhardwaj and*

Singhal [1993] have studied the energization of the photoelectron and low-energy protons, respectively, by parallel electric field using Monte Carlo model. The Monte Carlo method has also been used for the sputtering studies [*Pospieszalska and Johnson*, 1996; *Johnson et al.*, 2000] as well as for the energy deposition of ring current [*Schroeder and Proelss*, 1991; *Bhardwaj and Singhal*, 1993; *Noël*, 1997]. *Lillis et al.* [2008, 2009, 2011] have developed a Mars Monte Carlo Electron Transport (MarMCET) model to study the solar wind electron precipitation along the crustal magnetic field of Mars. With the help of this code they investigated the coupled effects of crustal magnetic field gradient and precipitating electron pitch angle distribution. Monte Carlo method has also been used to calculate the photoelectron flux in the Martian and Venusian atmospheres by solving the kinetic Boltzmann equation [*Shematovich et al.*, 2008; *Gérard et al.*, 2008b, 2011a; *Hubert et al.*, 2010; *Simon et al.*, 2009; *Gronoff et al.*, 2012a, b].

Green et al. [1977] have suggested a basic distribution function whose physical implications are more transparent than are the implications of the equilibrium flux or degradation spectra *Fano and Spencer* [1975]. *Green et al.* have coined a name "Yield Spectra" for the product of distribution spectra and the total inelastic cross section. The numerical yield spectra is represented analytically by *Green et al.* [1977] for various gases, viz., Ar, H_2, H_2O, O_2, N_2, CO, CO_2, and He. This analytical representation of numerical yield is called Analytical Yield Spectra (AYS). The AYS technique is further developed by many workers [see *Green and Sighal*, 1979; *Jackman and Green*, 1979; *Singhal et al.*, 1980; *Singhal and Green*, 1981; *Green et al.*, 1985; *Singhal and Bhardwaj*, 1991; *Bhardwaj and Singhal*, 1993; *Bhardwaj and Michael*, 1999a; *Bhardwaj and Jain*, 2009]. The yield spectra contain information regarding the degradation process and can be used to calculate the yield of any given excited state. The AYS is used in the calculation of photoelectron or auroral electron fluxes and volume excitation/emission rates in planetary atmosphere and cometary coma [e.g., *Haider and Singhal*, 1983; *Singhal and Haider*, 1984; *Singhal and Haider*, 1986; *Bhardwaj and Singhal*, 1990; *Bhardwaj et al.*, 1990, 1995, 1996; *Bhardwaj*, 1999, 2003; *Haider and Bhardwaj*, 1997, 2005; *Bhardwaj and Haider*, 1999; *Bhardwaj and Michael*, 1999a; *Bhardwaj and Raghuram*, 2011; *Jain and Bhardwaj*, 2011, 2012; *Bhardwaj and Raghuram*, 2012; *Bhardwaj and Jain*, 2012a, b]. The use of AYS reduces the computation time drastically compared to the Monte Carlo technique.

A Monte Carlo model for electron energy (1000 eV) degradation in CO_2 gas is developed in this Chapter. By definition, the Monte Carlo method would be the one that involves deliberate use of random number in a calculation that has the structure of stochastic process. In the Monte Carlo simulation, modelling of an inherently stochastic system is carried out by artificial random sampling. Monte Carlo technique is the solution by probabilistic methods of non-probabilistic problem, e.g., the transport of radiation is a natural stochastic process that is amenable to the Monte Carlo method due to its probabilistic nature. Due to its stochastic and discrete nature of the actual atomic loss process, the Monte Carlo is the most accurate technique for studying the energy degradation of particles provided sufficient sample size is taken. Though Monte Carlo methods are computational effective but expensive compared to other deterministic methods.

The development of Monte Carlo model is presented in Section 3.2. The generation of yield spectra from Monte Carlo model output and subsequent representation of AYS is presented in Section 3.3. The calculated mean energy per ion pair and secondary and tertiary electron energy distribution is given in Sections 3.4 and 3.5, respectively. The AYS is used to calculate the efficiencies of various inelastic processes which are presented in Section 3.6. Section 3.7 gives the summary of the chapter. The AYS calculated in this chapter is used to calculate the photoelectron fluxes in the atmospheres of Mars and Venus which are presented in subsequent chapters.

3.2 Monte Carlo model

In the present study a Monte Carlo model is developed to simulate the local degradation of 1–1000 eV electrons in an atmosphere of CO_2 gas. The energy bin size is taken as 1 eV throughout the energy range. In the simulation elastic scattering between electrons and neutral CO_2 molecules, and various inelastic processes, like ionization, excitation, attachment, dissociation, and vibrational excitation are considered; the cross sections for these processes are described in Chapter 2. Figure 3.1 illustrates how an individual electron is treated in the Monte Carlo simulation. The initial energy of electron is specified in the beginning of simulation and its direction of movement is selected randomly. The mean distance between two successive collisions are calculated using a random number. When a collision occurs a decision is made to determine the nature of collision, whether the collision is elastic or inelastic. If an elastic event has taken place then the event is recorded in that energy bin and angular scattering is calculated using differential elastic cross sections which are described in Chapter 2. For an inelastic collision a further choice is made for the type of inelastic process that has taken place. The process is then recorded in appropriate energy bin and the energy loss is subtracted from the initial energy of electron. If the nature of collision is ionization then the secondary electron thus produced is also treated in a similar manner as the primary electron. In this manner the discrete energy losses are modelled in the Monte Carlo simulation. The electron is traced from its initial energy in the atmosphere till its energy reaches below cut-off value, which is the minimum threshold of all the inelastic events.

The initial energy E_0 of the electron is fixed at the beginning of the simulation and the direction of movement of the electron (θ, ϕ) is decided with the help of two random numbers R_1 and R_2 [random numbers are uniformly distributed in the range (0, 1)] as

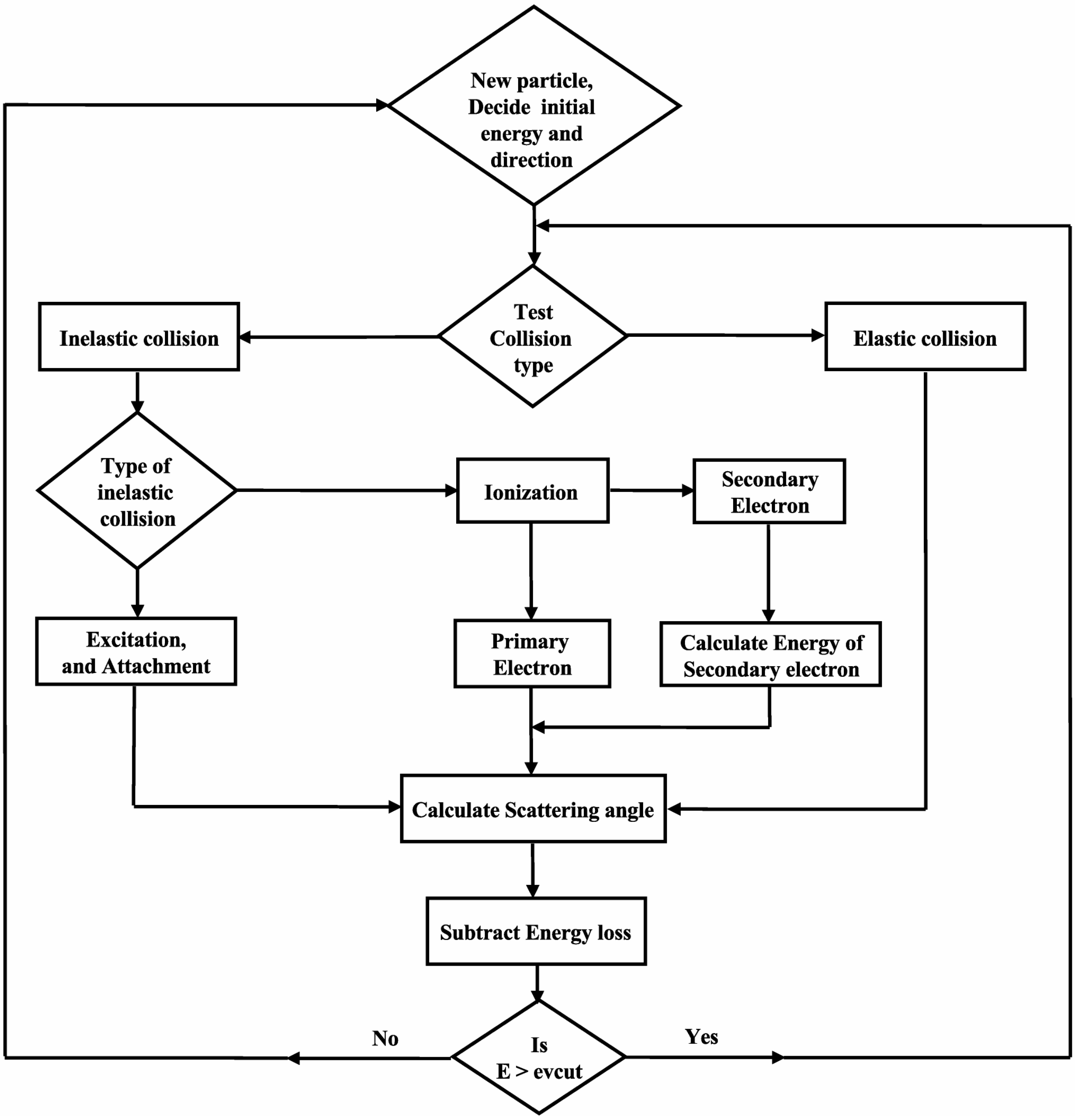

Figure 3.1: A simplified flow diagram of the Monte Carlo simulation. The diagram shows flow upto secondary electron, but tertiary and subsequent electrons are also treated in a similar manner in the simulation.

$$\theta = \cos^{-1}(1 - 2R_1) \tag{3.1}$$

$$\phi = 2\pi R_2. \tag{3.2}$$

The distance to next collision is calculated from

$$S = -\log(1 - R_3)/n\sigma_T \tag{3.3}$$

where R_3 is a random number, n is the number density of the neutral target species (taken as 1×10^{10} cm^{-3}), and σ_T is the total (elastic + inelastic) electron impact collision cross section. After generating a new random number R_4, the probability of elastic collision $P_{el} = \sigma_{el}/\sigma_T$ is calculated. if $P_{el} > R_4$, elastic collision takes place. if $P_{el} \leq R_4$, the inelastic event takes place, and in this case a further sampling is carried out for the type of inelastic event that has taken place with the help of another random number.

For elastic scattering the energy loss is calculated as

$$\begin{aligned} \triangle E &= \frac{m^2 v^2}{m+M} - \frac{m^2 v V_1 \cos\delta}{m+M}, \qquad (3.4) \\ V_1 &= v\left[\frac{m\cos\delta}{m+M} + \frac{[M^2 + m^2(\cos\delta - 1)]^{1/2}}{m+M}\right]. \end{aligned}$$

Here δ is the scattering angle in the laboratory frame, v and m are the velocity and mass, respectively, of the electron, and M is the mass of the target particle. Differential elastic cross sections (discussed in section 2.2.1) are used to obtain the scattering angle δ. Differential cross sections are fed numerically in the Monte Carlo model at 28 unequally spaced energy points (1.5, 2, 3, 3.8, 4, 5, 6, 6.5, 7, 8, 9, 10, 15, 20, 30, 40, 50, 60, 70, 80, 90, 100, 200, 300, 400, 500, 800, and 1000 eV) and at 20 scattering angles (0°, 5°, 10°, 15°, 20°, 30°, 40°, 50°, 60°, 70°, 80°, 90°, 100°, 110°, 120°, 130°, 135°, 150°, 165°, and 180°). At intermediate energies and angular points the values are obtained through linear interpolation. The energy $\triangle E$ is subtracted from the energy of the test particle. After the collision, the deflection angle relative to the direction (θ, ϕ) is obtained as

$$\begin{aligned} \cos\theta^{''} &= \cos\theta\cos\theta^{'} - \sin\theta\sin\theta^{'}\cos\phi^{'}, \\ \cos\phi^{''} &= (\cos\theta\cos\phi\sin\theta^{'}\sin\phi^{'} - \sin\phi\sin\theta^{'}\sin\phi^{'} + \sin\theta\cos\phi\cos\theta^{'})/\sin\theta^{''}, \qquad (3.5) \\ \sin\phi^{''} &= (\cos\theta\cos\phi\sin\theta^{'}\cos\phi^{'} - \cos\phi\sin\theta^{'}\sin\phi^{'} + \sin\theta\sin\phi\cos\theta^{'})/\sin\theta^{''}. \end{aligned}$$

Here $\theta^{'}$, $\phi^{'}$ are the scattering angles.

In the case of an inelastic collision, the next step is to find whether the event is ionization or any of the other type of inelastic collision. If the collision is an ionization event, a secondary electron is produced. The energy of the secondary electron T is calculated with the help of a random number R as [*Bhardwaj and Michael*, 1999a]

$$T = \frac{\Gamma_S\, E_v}{E_v + \Gamma_B}[\tan(RK_1 + (R-1)K_2)] + T_S - \left[\frac{T_A}{E_v + T_B}\right], \qquad (3.6)$$

where

$$\begin{aligned} K_1 &= \tan^{-1}\left\{\left[\frac{(E_v - I)}{2} - T_S + \frac{T_A}{(E_v + T_B)}\right] \Big/ \frac{\Gamma_S\, E_v}{(E_v + \Gamma_B)}\right\}, \\ K_2 &= \tan^{-1}\left\{\left[T_S - \frac{T_A}{(E_v + T_B)}\right] \Big/ \frac{\Gamma_S\, E_v}{(E_v + \Gamma_B)}\right\}. \end{aligned}$$

Here E_v is the energy of the incident primary electron before the ionization event. Γ_S, Γ_A, T_A, T_B, and T_S are the fitting parameters, and I is the ionization threshold. The values of these parameters are given in Table 2.7. If the energy of secondary electron, produced in the ionization event, is more than the lowest cut-off energy (which is 1 eV in the simulation) then it is also tracked in a same manner as the primary electron (cf. Figure 3.1). The secondary electrons can also cause ionization, producing tertiary electrons, which are treated in a similar way as secondary electrons. In the Monte Carlo simulation tertiary and subsequent electrons are also followed in similar manner as the primary. The number of secondary, tertiary, and subsequent electrons produced during the ionization events are stored in the appropriate energy bins. After the type of collision event has been decided, the appropriate energy is subtracted from the energy of the particle. All the collision events are recorded in the appropriate energy bins corresponding to the energy of the electron at the time of collision. The history (track view) of a particle with each interaction event is traced until the electron energy falls below an assigned cut-off value, which is 1 eV. The sample size in the present study is 10^6 particles for each simulation.

3.3 Yield spectra

When all the sampled electrons have been degraded, a two dimensional yield spectrum can be obtained, which is a function of the spectral energy E and incident primary electron energy E_0, defined as [*Green et al.*, 1977]:

$$U(E, E_0) = \frac{N(E)}{\triangle E}, \tag{3.7}$$

where $N(E)$ is the number of inelastic collision events for which the spectral energy of the electron is between E and $E + \triangle E$, where $\triangle E$ is the energy bin width, which is 1 eV in our model. This yield spectrum is related to the degradation spectrum or equilibrium flux $f(E, E_0)$ of *Spencer and Fano* [1954] by the equation

$$U(E, E_0) = \sigma_T(E) f(E, E_0), \tag{3.8}$$

where σ_T is the total inelastic collision cross section.

The analytical yield spectrum $U(E, E_0)$ embodies the non-spatial information of the degradation process. It represents the equilibrium number of electrons per unit energy at an energy E resulting from the local energy degradation of an incident electron of energy E_0, and can be used to calculate the yield J_j of any state j at energy E_0 with the help of following equation:

$$J_j(E_0) = \int_{W_{th}}^{E_0} U(E, E_0)\, P_j(E)\, dE \tag{3.9}$$

where $P_j(E) = \sigma_j(E)/\sigma_T(E)$ is the probability of occurrence of the jth process whose threshold potential is W_{th}. The yield for a particular process obtained by using the above equation is used to calculate the mean energy per ion pair and efficiencies for various loss processes. Except at very low energies, the yield spectrum $U(E, E_0)$ and

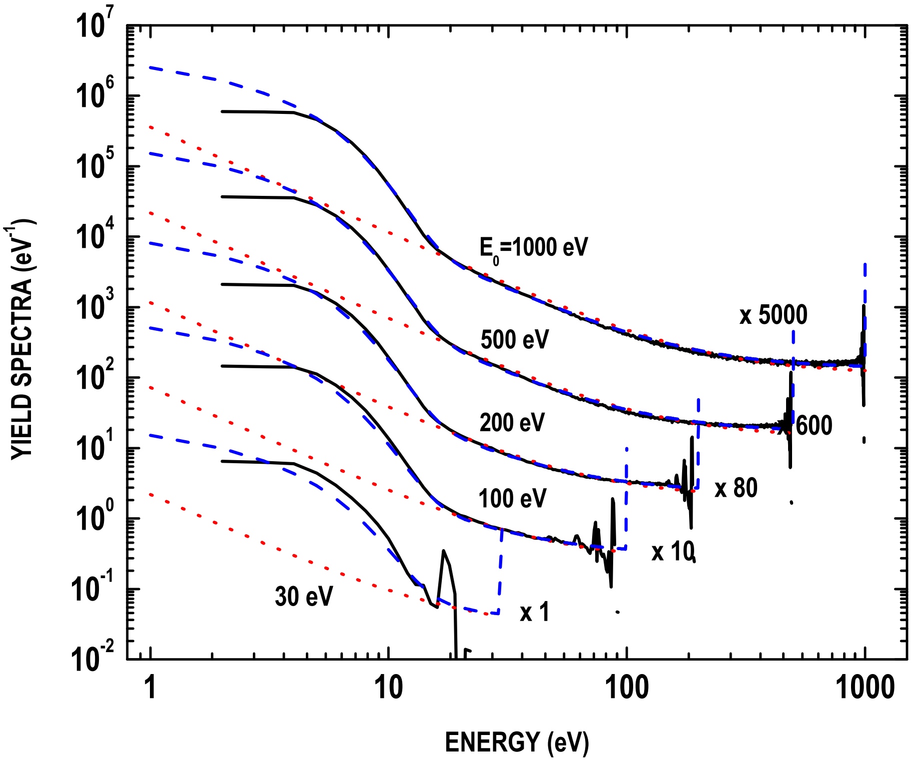

Figure 3.2: The numerical yield spectra from the Monte Carlo model (solid curve) and AYS using Eq. 3.11 (dotted curve) at incident energies (E_0) 30, 100, 200, 500, and 1000 eV. Dashed curve represents the improved AYS calculated by summing Eq. 3.11 and (3.14). The yield spectra at 100, 200, 500, and 1000 eV are plotted after multiplying by a factor of 10, 80, 600, and 5000, respectively.

the probability of excitation $P_j(E)$ both vary with E in a much simpler manner than do $f(E, E_0)$ and $\sigma_j(E)$.

For many application purposes the yield spectrum obtained by Eq. 3.7 is represented in the following form:

$$U(E, E_0) = U_a(E, E_0)\ H(E_0 - E - E_m) + \delta(E_0 - E). \tag{3.10}$$

Here H is the Heavyside function, with E_m being the minimum threshold of the processes considered, and $\delta(E_0 - E)$ is the Dirac delta function which allows for the contribution of the source itself. In atmospheric and astrophysical applications it is convenient to represent $U_a(E, E_0)$ in an analytical form [*Green et al.*, 1977]:

$$U_a(E, E_0) = A_1 \xi_0^s + A_2(\xi_0^{1-t}/\epsilon^{3/2+r}) \tag{3.11}$$

Here $\xi = E_0/1000$ and $\epsilon = E/I$ (I is equal to lowest ionization threshold). $A_1 = 0.027$, $A_2 = 1.20$, $t = 0$, $r = 0$, and $s = -0.0536$ are the best fit parameters.

Two other analytical forms given by *Singhal et al.* [1980] and *Green et al.* [1985] are also used in present calculation. The form given by *Singhal et al.* [1980] is:

$$U_a(E, E_0) = C_0 + C_1\,\chi + C_2\,\chi^2 \tag{3.12}$$

Here $\chi = E_0^{\Omega}/(E{+}L)$; where $\Omega = 0.585$ and $L = 1.0$ and E_0 is in keV, $C_0 = 0.0185$, $C_1 = 5.98$, and $C_2 = 210.4$ are fitted parameters. The analytical form given by *Green et al.* [1985] is:

$$U_a(E, E_0) = C_0 + C_1(E_k + K)/[(E - M)^2 + L^2]. \tag{3.13}$$

Here $E_k = E_0/1000$, and C_0, C_1, K, M, and L are the fitted parameters which are independent of the energy. The values of these constant parameters are $C_0 = 0.0299$, $C_1 = 430$, $K = 0.0041$ keV, $M = 0.31$ eV, and $L = 1.9$ eV.

In obtaining the analytical fits, the values of the yield spectra very close to E_0 is not include because in this regime yield spectra contain the rapid oscillations known as "Lewis effect" [cf. *Douthat*, 1975]. These oscillations are channels with a finite number of threshold energies, so that there are only certain energies near E_0 which an electron can acquire. Obviously, no electron can acquire an energy between E_0 and $E_0 - E_m$, and that is why the Heavyside function H is inserted in the first term on the right-hand side of Eq. 3.10. The numerical yield spectrum represented analytically using Eq. 3.11, 3.12, and 3.13 is the two-dimensional AYS. In present study, the AYS obtained using Eq. 3.11, which is presented in Figure 3.2 along with the numerical yield spectra obtained by using Eq. 3.10 is used. It is clear from Figure 3.2 that the analytical spectra represents quite well the numerical yield spectra above the ionization threshold; however, at lower energies (below 15 eV) the AYS departs from the numerical yield spectra. Similar behaviour is seen in the AYS of *Green et al.* [1977].

To overcome this deficiency an additional function is introduced to modify the lower energy part of the AYS:

$$U_b(E, E_0) = \frac{E_0 A_0 e^x / A_1}{(1 + e^x)^2}, \tag{3.14}$$

Here $x = (E - A_2)/A_1$, and A_0, A_1, and A_2 are the fitting parameters. The values of parameters are $A_0 = 10.095$, $A_1 = 5.5$, and $A_2 = 0.9$. Eq. 3.14 only affects the lower energy ($\leq$15 eV) part of the fit. The final AYS is the sum of Eq. 3.11 and 3.14 which is shown in Figure 3.2 at several incident energies: depicting a better fit at lower energies ($>$5 eV) as well as at higher energies.

Because of the simplicity of function and cost effective computational advantage, the AYS technique has been widely used in different planetary atmospheres for various aeronomical calculations, like steady state electron fluxes and volume production rates for any ionization or excitation state; the details of the computational technique are described in earlier papers [e.g., *Haider and Singhal*, 1983; *Singhal and Haider*, 1984; *Bhardwaj and Singhal*, 1993; *Singhal and Bhardwaj*, 1991; *Bhardwaj et al.*, 1990, 1996;

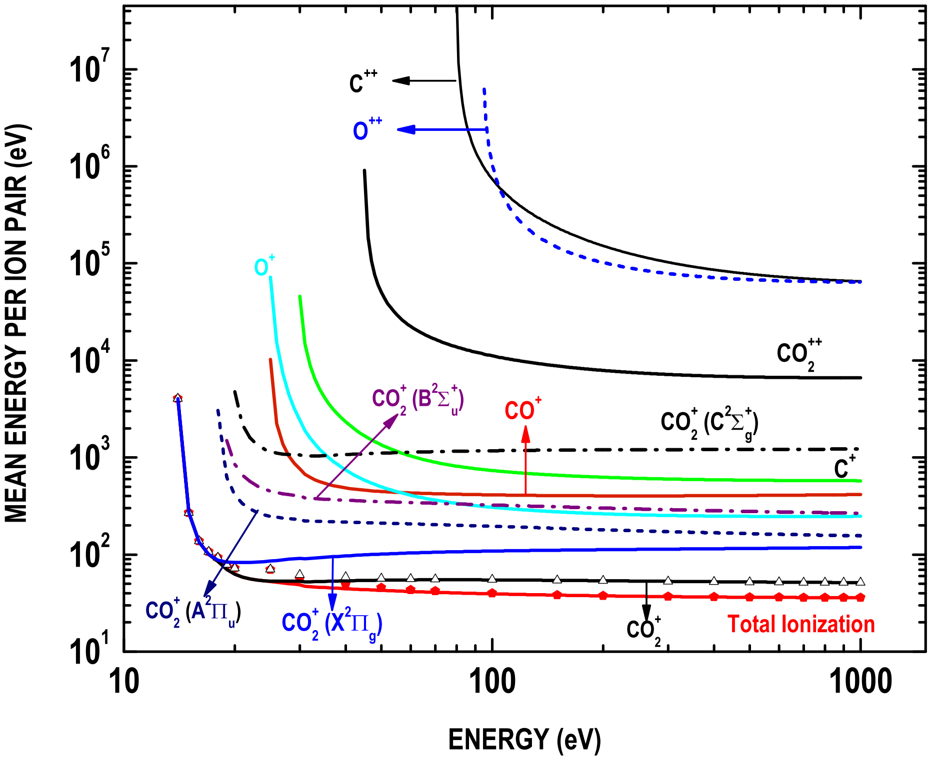

Figure 3.3: The mean energy per ion pair for ions CO_2^+ (CO_2^+ is the sum of four states $X^2\Pi_g$, $A^2\Pi_u$, $B^2\Sigma_u^+$, and $C^2\Sigma_g^+$), CO^+, O^+, C^+, CO_2^{++}, O^{++}, and C^{++}, and the neutral CO_2 gas (total). Symbol represents the μ calculated using numerical yield spectra for the CO_2^+ and neutral CO_2.

Bhardwaj, 1999, 2003; *Bhardwaj and Michael*, 1999a, b; *Bhardwaj and Haider*, 1999; *Michael and Bhardwaj*, 2000; *Haider and Bhardwaj*, 2005; *Bhardwaj and Raghuram*, 2011; *Jain and Bhardwaj*, 2011, 2012; *Bhardwaj and Raghuram*, 2012; *Bhardwaj and Jain*, 2012a, b].

3.4 Mean energy per ion pair

The mean energy per ion pair, μ_j, is defined as the incident energy E_0 divided by the number of ion pairs produced. It can be expressed as

$$\mu_j(E_0) = E_0/J_j(E_0), \tag{3.15}$$

where $J_j(E_0)$ is the population of the jth ionization process obtained by Eq. 3.9. The quantity mean energy per ion pair is known to approach a constant value at higher energies.

Figure 3.3 shows the mean energy per ion pair for the ions CO_2^+ (including the ground and excited states), CO^+, O^+, C^+, CO_2^{++}, O^{++} and C^{++} along with the mean energy per ion pair for neutral CO_2, solid symbol represents the mean energy per ion pair for neutral CO_2 obtained directly from the Monte Carlo simulation at few energy points.

Mean energy for all the ions decreases very rapidly above their threshold value, but after ~100 eV μ declines slowly and at higher energies it becomes almost constant. The values of μ for CO_2^+, CO^+, O^+, and C^+ at 200 (1000) eV are 53.6 (51.2), 403 (415), 263.1 (247.8), and 626.7 eV (576.2) eV, respectively. The mean energy per ion pair for neutral CO_2 gas is 37.5 (35.8) eV at 200 (1000) eV. *Fox and Dalgarno* [1979b] reported a value of 33.1 eV at 200 eV for the μ, while *Green et al.* [1977] obtained a value of 34.7 eV at 200 eV from their MDEB method. The measured value of the mean energy per ion pair in neutral CO_2 is 32.7 at high energies [*Klots*, 1968]. Mean energy per ion pair for $X^2\Pi_g$, $A^2\Pi_u$, $B^2\Sigma_u^+$, and $C^2\Sigma_g^+$ states of CO_2^+ at 200 (1000) eV are 112.3 (118.4), 180.3 (156), 301.5 (266.4), and 1999 (1222) eV, respectively.

3.5 Secondary electron energy distribution

During the degradation process, every time the electron undergoes an ionization collision event, a secondary electron is produced. The energy of the secondary electron produced is calculated using Eq. 3.6. The maximum energy of the secondary electron produced can be $(E - I)/2$, where E is the energy of the colliding electron and I is the ionization potential. As mentioned before, secondary and tertiary electrons are also treated in the same manner as the primary electrons in the Monte Carlo model. The energy distribution of secondary electrons is presented in Figure 3.4 at several incident energies showing the number of secondary electrons produced per incident primary electron. The energy distributions of tertiary and quaternary electrons, which are presented only at $E_0 = 1000$ eV, are much steeper than that of secondary electrons. Each incident electron of $E_0 = 1000$ eV at some point of its energy degradation process produces at least one secondary or tertiary or quaternary electron, whose energy is <7 eV.

3.6 Efficiency

As the electron collide with the atmospheric particles, they lose their energy and finally become thermalized. The energy of the colliding electron is divided among the various inelastic loss processes. Efficiency means the fraction of incident energy of the electron which is eventually deposited in a particular loss channel after the completion of the entire degradation process. The efficiency, $\eta_j(E_0)$, of the jth process at incident energy E_0 can be obtained as

$$\eta_j(E_0) = \frac{W_{th}}{E_0} J_j(E_0) \tag{3.16}$$

The efficiencies for all inelastic collisions have been calculated using numerical yield spectra obtained from Eq. 3.10 and the AYS [sum of Eq. 3.11 and 3.14].

Figure 3.5 presents efficiencies of various single ionization events producing CO_2^+, CO^+, O^+, and C^+. The CO_2^+ has the maximum efficiency throughout the energy region

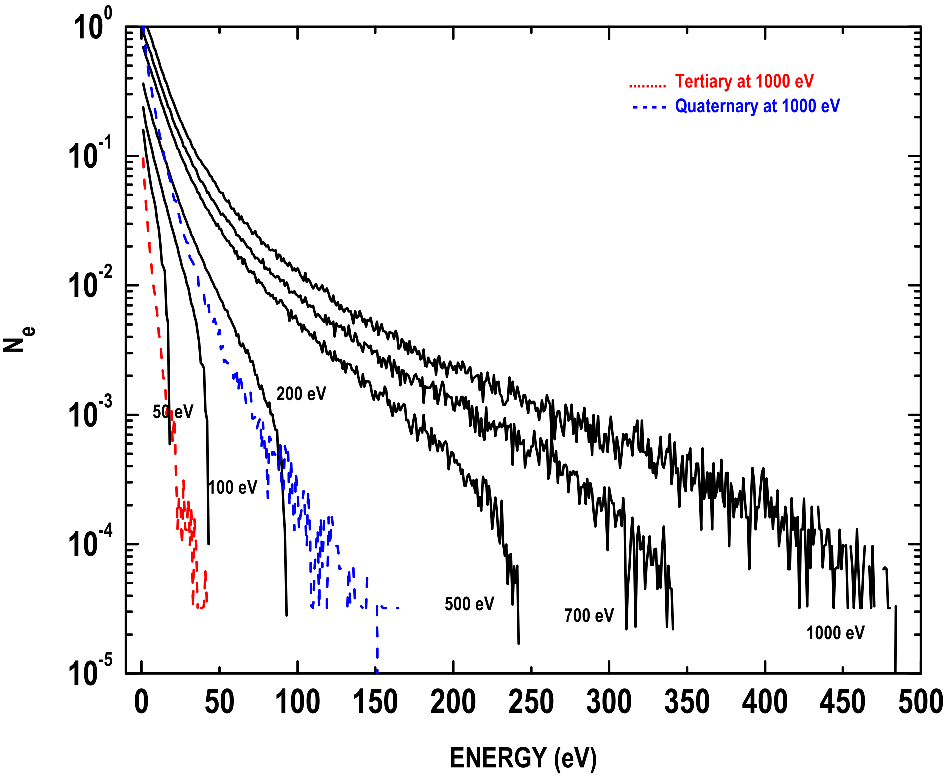

Figure 3.4: The energy distribution of secondary electrons in e-CO_2 collision at six incident energies (E_0): 50, 100, 200, 500, 700, and 1000 eV. N_e represents the number of secondary, tertiary, or quaternary electrons produced per incident primary electron. Red and blue curves represent energy distribution of tertiary and quaternary electrons, respectively at $E_0 = 1000$ eV.

due its higher ionization cross section. At 1000 eV, ~31% energy of the incident electron goes into CO_2^+ formation, while 5.9%, 9.8%, and 5% energy goes into the production of CO^+, O^+, and C^+, respectively. At higher energies (>100 eV), increase in the efficiencies for all ions is small, but near threshold it falls very rapidly. At threshold, efficiencies for CO_2^+, CO^+, O^+, and C^+ are 5.1%, 1.1%, 0.16% and 0.19%, respectively, while at 200 eV these are 29%, 6%, 9.2%, and 4.6%, respectively. Efficiencies for CO_2^+(A-X), CO_2^+(B-X), and first negative band of CO^+(B-X) are also shown in Figure 3.5. At 200 (1000) eV, 12.2 (11.6)% of incident electron energy goes in to the emission CO_2^+(A-X), while 9.8 (11.4)% and 3.0 (3.3)% goes in to the emissions CO_2^+(B-X) and CO^+(B-X), respectively.

Figure 3.6 shows the efficiencies for double ionization of CO_2. At 200 (1000) eV, efficiencies for CO_2^{++}, O^{++}, and C^{++} are 0.56 (0.67)%, 0.052 (0.12)%, and 0.092 (0.14)%, respectively. The efficiencies for (CO^+,O^+), (C^+,O^+), and (O^+,O^+) have also been calculated, based on cross sections of *Tian and Vidal* [1998], whose values are 2.7 (3.1)%, 1.8 (2.4)%, and 0.96 (1.1)% at 200 (1000) eV. It is clear from Figures 3.5 and 3.6, that efficiencies calculated from the model and those obtained by using AYS are in good agreement. Efficiencies for various excitation processes are presented in Figure 3.7.

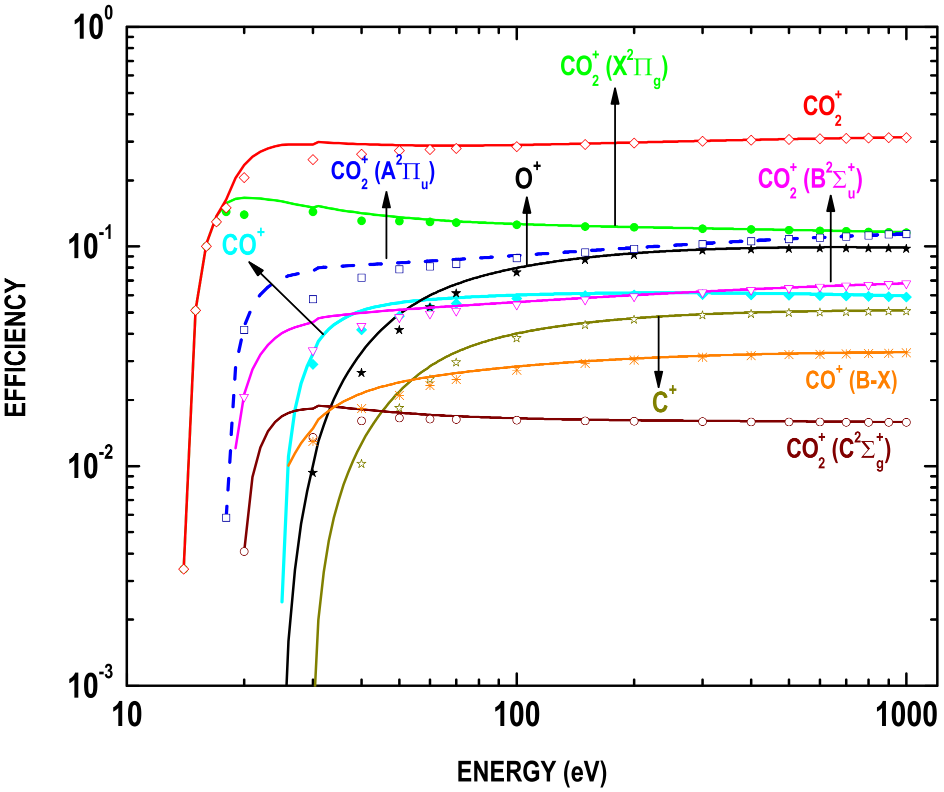

Figure 3.5: Efficiencies of various ionization and emission processes in e-CO_2 collision. Symbol represents the efficiency calculated by numerical yield spectra and curves represent the efficiency calculated by the AYS. $CO_2^+(A^2\Pi_u)$ and $CO_2^+(B^2\Sigma_u^+)$ represent FDB ($A^2\Pi_u \rightarrow X^2\Pi_g$) and ultraviolet doublet ($B^2\Sigma_u^+ \rightarrow X^2\Pi_g$) emissions, respectively, and CO^+(B-X) represents first negative band emission of CO^+ ion.

The 13.6, 12.4, and 11.1 eV states dominate the excitation events having efficiencies 16 (15)%, 12 (13)%, and 4.7 (4.2)% at 200 (1000) eV, respectively. Efficiencies of various line emissions of atomic oxygen and carbon are shown in Figure 3.8. Efficiencies for OI (1304), OI (1356), CI (1279), CI (1329), CI (1561), and CI (1657), are 0.12 (0.13)%, 0.27 (0.28)%, 0.084 (0.089)%, 0.035 (0.030)%, 0.10 (0.093)%, and 0.19 (0.18)%, respectively, at 200 (1000) eV. Overall efficiencies calculated from numerical yield spectra and AYS for various emission and excitation events are in good agreement.

In Figure 3.9, a summary picture of the electron energy distribution in CO_2 for all the loss processes grouped into important loss channels is presented. At higher (>50 eV) energies ionization is the dominant loss process with energy consumption of ∼50%. At lower energies (<15 eV), 11.1, 12.4, 8.6, and 9.3 eV loss channels are more important. At energies below 10 eV, vibration becomes the main loss channel. The efficiency for total attachment process is also shown , which produces negative ion O^-. The efficiency for anion O^- production peaks around 8 eV with a value of 0.8%, while it is 0.15 (0.13)% at 200 (1000) eV. The total efficiency for double ionization, which results in the production of CO_2^{++}, O^{++}, and C^{++} ions, is also depicted in the figure. The double

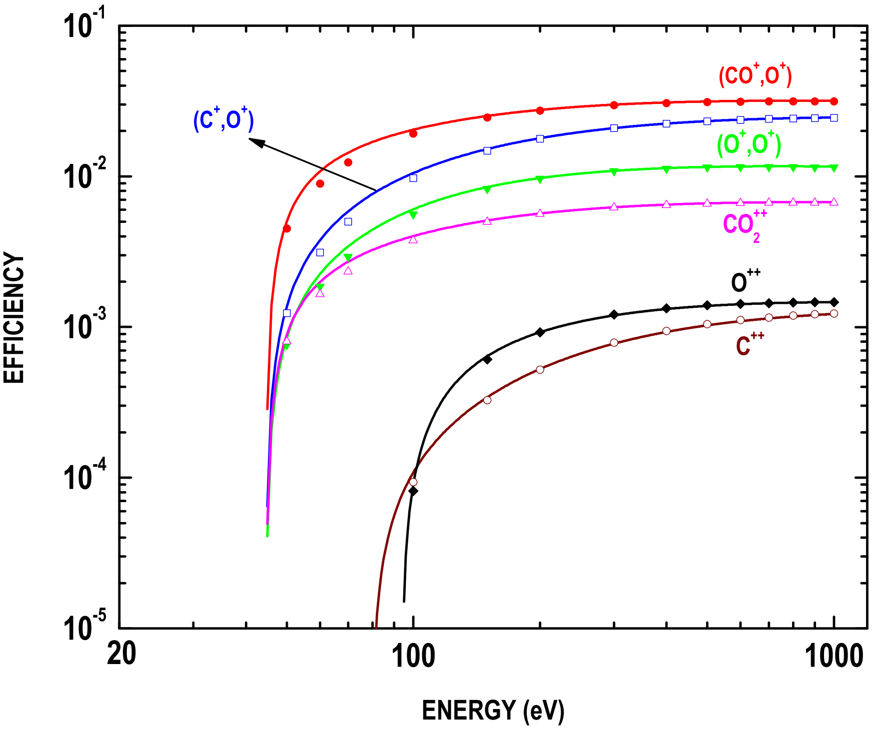

Figure 3.6: Efficiencies for double ionization of CO_2 due to electron impact. Symbol represents the efficiency calculated by numerical yield spectra and curves represent the efficiency calculated by the AYS.

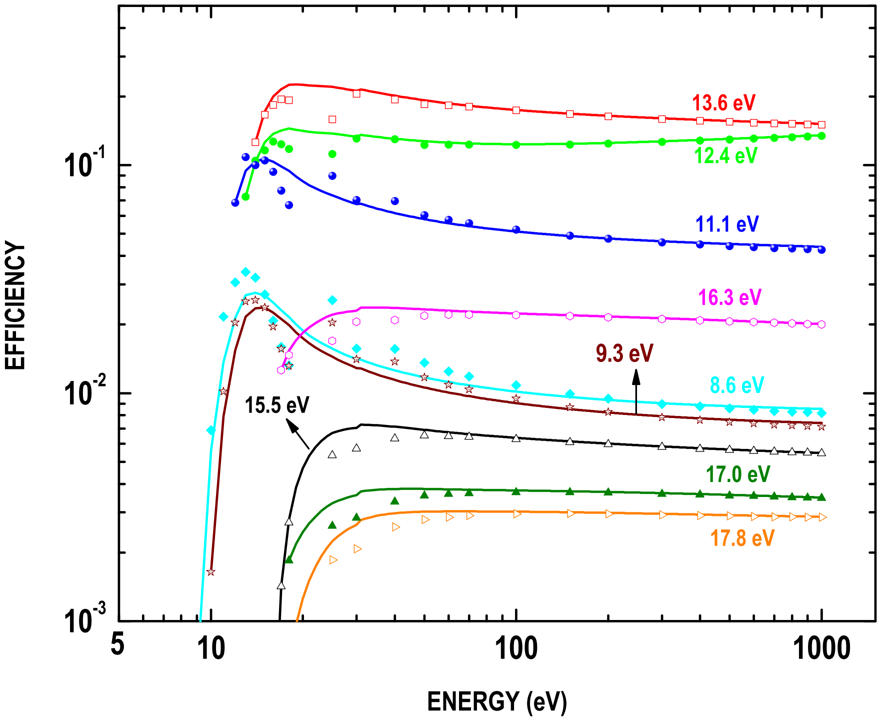

Figure 3.7: Efficiencies of various excited states in e-CO_2 collision. Symbol represents the efficiency calculated by numerical yield spectra and curves represent efficiency calculated by the AYS.

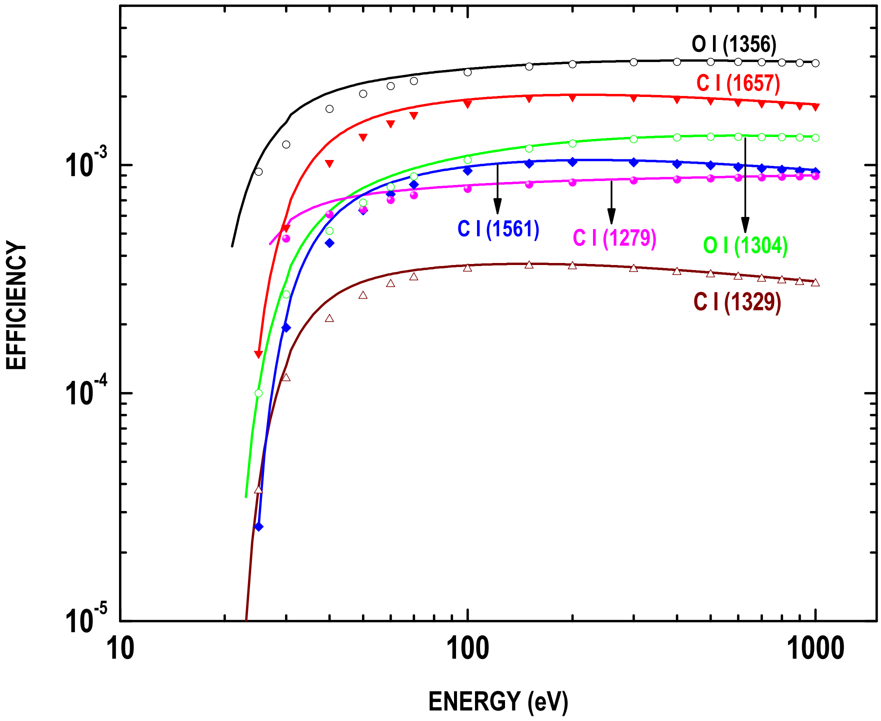

Figure 3.8: Efficiencies of various oxygen and carbon line emissions in e-CO_2 collision. Symbol represents the efficiency calculated by numerical yield spectra and curves represent the efficiency calculated by the AYS.

ionization efficiency raises sharply above 40 eV, having value of 0.4 (0.7)% at 100 (200) eV. Around 1000 eV, double ionization efficiency is 0.9%, which is higher than that of 8.6 and 9.3 eV excitation states. On the other hand, at energies >100 eV efficiency for dissociative ionization is higher than that of the 13.6 and 12.4 eV states.

3.7 Summary

In this Chapter a Monte Carlo model for ≤1000 eV electron degradation in CO_2 gas is presented. The output of the Monte Carlo model is used to calculate the numerical "yield spectra", which is represented by an analytical form. This AYS can be used in planetary atmospheres to determine various aeronomical quantities. In this study, the AYS given by *Green et al.* [1977] and *Singhal et al.* [1980] has been modified and improved by adding a term that provides a better analytical representation of yield spectra at lower (<15 eV) energies. The yield spectra is employed to compute the mean energy per ion pair and efficiency of various inelastic processes. The mean energy per ion pair for CO_2 is found to be 37.5 (35.8) at 200 (1000) eV. The energy distribution of secondary electrons produced per incident electron is presented at few incident energies.

Efficiency is an effective measure to know what fraction of the incoming particle energy goes into a particular loss channel. The efficiencies for various inelastic events are calculated by using the AYS as well as by using the numerical yield spectra obtained from

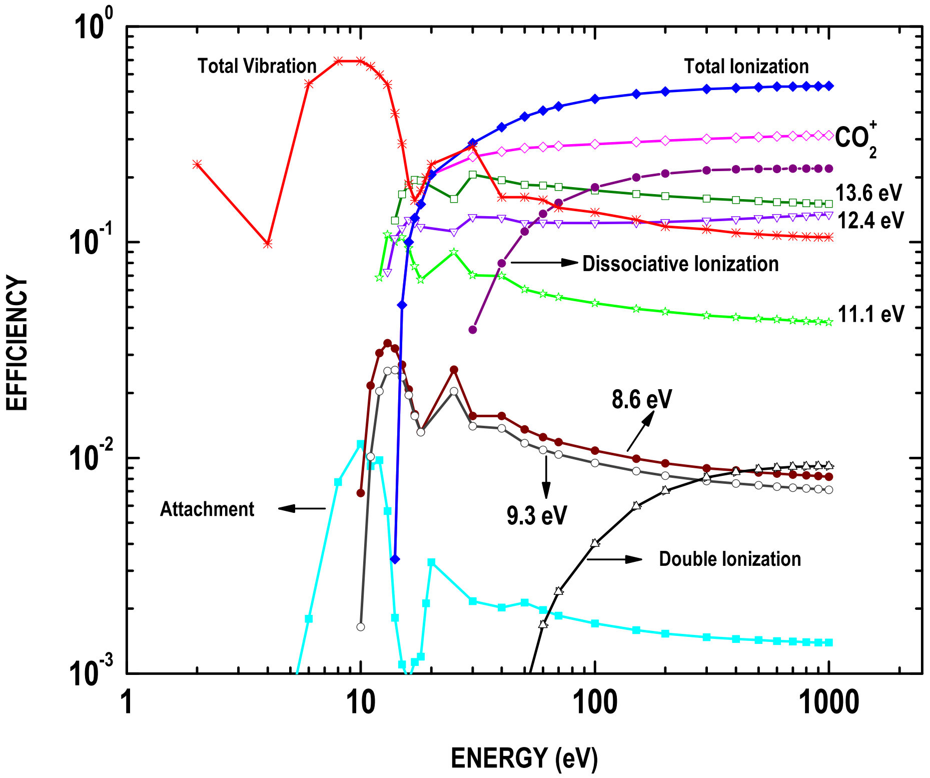

Figure 3.9: Efficiencies for various important loss channels in e-CO_2 collision calculated using numerical yield spectra. Dissociative ionization includes the production of O^+, C^+, and CO^+ ions; double ionization includes the production of CO_2^{++}, O^{++}, and C^{++} ions; and attachment denotes the production of O^- ion.

the Monte Carlo model. Efficiencies obtained by the two methods are in good agreement. In addition to major inelastic processes, efficiencies are presented for the formation of negative ions, double and dissociative double ionization of CO_2, and vibrational excitation in the (100), (010), and (001) states. Since the AYS do not represent well the numerical yield spectra at very low (<5 eV) energies, the yield for vibrational excitation and attachment processes calculated by the AYS would be approximate. Ionization is the dominant loss process; at higher energies, above 100 eV ∼50% energy goes into ionization. At energies around and below ionization threshold excitation processes become important, and at energy below 10 eV, vibration is the dominant loss channel consuming more than 70% energy. The 13.6 and 12.4 eV loss channels are also important, at 1000 eV, around 28% of incident particle energy goes in to these states. A part of these states represents the emissions of Cameron band system, which is an important emission in atmospheres of Mars and Venus as well as on comets.

Efficiencies presented in this chapter can be applied to planetary atmospheres by folding them with electron production rate and integrating over the energy. These results will be useful in the modelling of aeronomical processes in atmospheres of Mars, Venus, and CO_2-containing atmospheres.

Chapter 4

CO Cameron band and CO_2^+ UV doublet emissions

4.1 Introduction

First observations of CO Cameron band ($a^3\Pi$ – $X^1\Sigma^+$; 180 – 260 nm) and CO_2^+ ultraviolet doublet ($B^2\Sigma^+$ – $X^2\Pi$; 2883 and 2896 Å) emissions in the Martian dayglow were made by the Mariner 6 and 7 flybys in 1969–1970 [*Barth et al.*, 1971; *Stewart*, 1972]. These observations provided an opportunity to study the Martian upper atmosphere in a greater detail. Figure 4.1 shows the energy level diagram of CO. The CO Cameron band system arises due to the transition from the excited triplet $a^3\Pi$ state, the lowest of the triplet states, to the ground $X^1\Sigma^+$ state of CO. The transition from excited $CO_2^+(B^2\Sigma_u)$ to the ground $X^2\Pi$ state of CO_2^+ gives emission in ultraviolet wavelengths at 2883 and 2896 Å. Apart from these emissions, Fox-Duffenback-Berger band of CO_2^+ ($A^2\Pi_u$ – $X^2\Pi_g$), fourth positive band of CO, first negative band of CO^+ (B – X), and several atomic line emissions of carbon and oxygen atoms were also recorded by Mariner 6, 7, and 9 UV spectrometers [*Barth et al.*, 1971; *Stewart*, 1972; *Stewart et al.*, 1972]. Maximum intensity of CO Cameron band and CO_2^+ UV doublet emissions observed by Mariner 6 and 7 was 600 kR at ∼131 km and 35 kR at 148 km, respectively. With the help of theoretical calculations and laboratory measurements, *Barth et al.* [1971] proposed possible mechanisms for the observed dayglow emissions in the Martian atmosphere. They concluded that most of emissions observed on Mars is the result of photon and electron impact on CO_2 and its dissociative products.

The CO Cameron band and CO_2^+ UV doublet emissions were also observed in 1971–1972 by Mariner 9, the first spacecraft to orbit Mars. *Stewart et al.* [1972] observed a reduction in the intensity of CO Cameron band by a factor of 2.5 compared to Mariner 6 and 7 observations. They attributed this difference to the reduction in the solar activity and better calibration of Mariner 9 instrument. The observed maximum slant intensities of CO Cameron band were between 200 and 300 kR and averaged topside scale height for the same band was 17.5 km. *Stewart* [1972] also observed a good correlation between

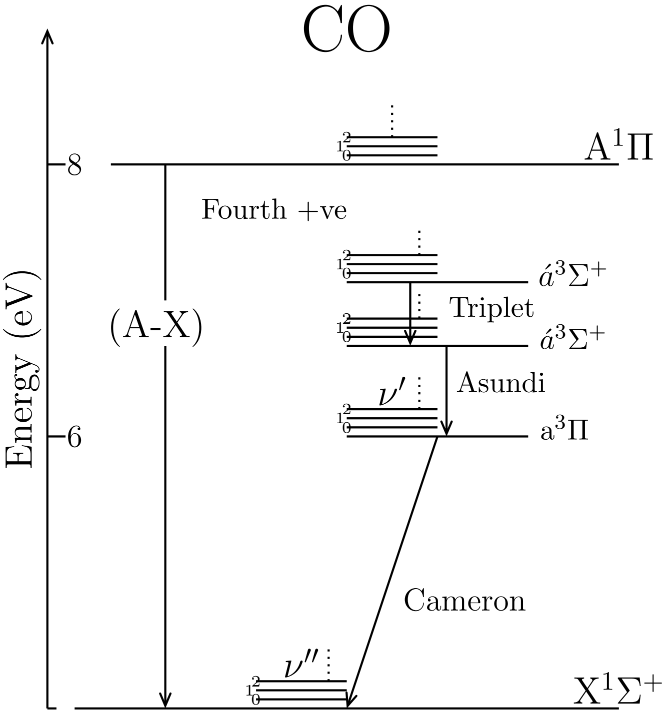

Figure 4.1: Schematic energy level diagram of Carbon Monoxide showing different spectroscopic transitions.

CO Cameron band intensity and solar F10.7 flux, which suggest that these emissions are controlled by the incident solar photon flux.

The SPectroscopy for the Investigation of the Characteristics of the Atmosphere of Mars (SPICAM) on-board Mars Express (MEx) have carried out airglow observations from Mars orbit more than three decade after the Mariner observations. Emissions observed by SPICAM in UV dayglow include H Lyman-α emission at 121.6 nm, the atomic oxygen emissions at 130.4 and 297.2 nm, the Cameron and fourth positive bands ($A^1\Pi - X^1\Sigma^+$) of CO, and CO_2^+ UV doublet emissions [cf. *Leblanc et al.*, 2006; *Chaufray et al.*, 2008b; *Gronoff et al.*, 2012a]. SPICAM has observed dayglow on Mars throughout the Martian year. The effect of Solar Zenith Angle (SZA), seasonal variation, and Martian dust storms on the dayglow emissions has been studied with the help of SPICAM-observations [cf. *Leblanc et al.*, 2006, 2007; *Shematovich et al.*, 2008; *Simon et al.*, 2009; *Forget et al.*, 2009; *Cox et al.*, 2010].

Several theoretical studies have been made for the dayglow emissions on Mars [*McConnell and McElroy*, 1970; *Barth et al.*, 1971; *Fox and Dalgarno*, 1979a; *Mantas and Hanson*, 1979; *Conway*, 1981; *Shematovich et al.*, 2008; *Simon et al.*, 2009; *Cox et al.*, 2010; *Gronoff et al.*, 2012a, b]. First detailed calculation of dayglow emission on Mars was carried out by *Fox and Dalgarno* [1979a]. Their calculated overhead intensities of CO Cameron band and CO_2^+ UV doublet emissions were 49 kR and 12 kR, respectively, for the low solar activity condition similar to Viking landing [*Fox and Dalgarno*, 1979a]. *Simon et al.* [2009] used Trans-Mars model to calculate limb intensities of CO Cameron band and CO_2^+ UV doublet emissions for low solar activity (condition similar to Viking landing) and compared them with SPICAM-observation. *Shematovich et al.* [2008] have used Direct Simulation Monte Carlo (DSMC) method for electron transport and calculated intensities of CO Cameron band and CO_2^+ UV doublet emissions in the Martian atmosphere. *Cox et al.* [2010] have presented a statistical analysis of Cameron band and UV doublet emissions, peak altitude of emissions, and ratio between UV doublet and Cameron band. They reported SPICAM-observations for one particular season, solar longitude (Ls) = 90 to 180°, and compared observational data with model calculations based on Monte Carlo method, which has also been used by *Shematovich et al.* [2008] for the Martian dayglow studies.

Recently, *Gronoff et al.* [2012a, b] have calculated the production of excited species and brightness profiles of CO Cameron band, CO_2^+ UV doublet, and OI 2972 Å emissions on Mars. They have used Aeroplanet model for dayglow calculation on Mars. Aeroplanet model is restructured and enhance version of the Trans-* model series (e.g., Trans-Mars, Trans-Venus) [*Lummerzheim and Lilensten*, 1994], which have been used by Gronoff and Co-workers to calculate the excited species production in the atmospheres of Mars and Venus [*Gronoff et al.*, 2008; *Simon et al.*, 2009; *Nicholson et al.*, 2009]. *Gronoff et al.* have used Monte Carlo model to calculate the model uncertainties due to different model input parameters in calculating the excited species production in the atmosphere of Mars.

Prior to Venus Express (VEx), Venus has been visited by several spacecraft (see Chapter 1), but none of them observed CO Cameron band and CO_2^+ UV doublet emissions in the dayglow of Venus. Very recently, the first observation of CO Cameron band and CO_2^+ UV doublet emissions made by SPectroscopy for the Investigation of the Characteristics of the Atmosphere of Venus (SPICAV) onboard VEx in the dayglow of Venus is reported by *Chaufray et al.* [2012]. The Cameron band brightness peaks at 137.5 ± 1.5 km with a peak brightness of 2000 ± 100 kR and the CO_2^+ doublet peaks at 135.5 ± 2.5 km with a peak brightness of 270 ± 20 kR [*Chaufray et al.*, 2012]. The spectral shape of the Cameron bands observed on Mars and Venus (see Figure 1.12) is very similar indicating that similar mechanisms are responsible for these emissions on the two planets. The above mentioned brightness of CO Cameron band and CO_2^+ UV doublet emissions on Venus is about 10 times higher than that reported on Mars for SZA <40° [*Leblanc et al.*, 2006].

This chapter provides a detailed calculation of various production sources of $CO(a^3\Pi)$ and $CO_2^+(B)$ in the dayglow of Venus and Mars. The study carried out in this chapter also aims to assess the impact of solar EUV flux models on CO Cameron band and CO_2^+ doublet emission intensities on Mars and Venus. Photoelectron flux, volume excitation rates, and overhead intensities are calculated on Mars and Venus using the two solar EUV flux models, viz., EUVAC [*Richards et al.*, 1994] and S2K [*Tobiska*, 2004], for low, moderate, and high solar activity conditions. Line of sight intensities for CO Cameron band and CO_2^+ doublet emissions are calculated and compared with the latest observations by SPICAM and SPICAV on Mars and Venus, respectively.

4.2 Development of the model

The neutral species considered in the model are CO_2, N_2, CO, O, and O_2. Model atmospheres for solar minimum and maximum conditions are taken from *Fox* [2004]. For the SPICAM observation conditions model atmosphere is taken from the Mars Thermospheric General Circulation Model (MTGCM) [*Bougher et al.*, 1999, 2000, 2004] as used in the study of *Shematovich et al.* [2008]. Model atmospheres for both low and high solar activity condition are shown in Figure 4.2 (top panel). Below 180 (200 km), CO_2 is the dominant gas in solar minimum (maximum) condition. Above this altitude atomic oxygen takes over CO_2 and becomes the dominant gas, which is similar to that in Earth's atmosphere where atomic oxygen becomes the dominant gas at higher altitudes (>250 km).

Neutral density (CO_2, N_2, CO, and O) profiles on Venus is taken from the VTS3 model of *Hedin et al.* [1983] for solar minimum (F10.7 = 60) and maximum (F10.7 = 200) conditions, for equatorial region and local time of 1500 hrs, which corresponds to SZA of around 45°. Density of O_2 is taken as 3×10^{-3} that of CO_2 based on the study of *Fox and Bougher* [1991]. Figure 4.2 (bottom panel) shows the model atmospheres of Venus for low and high solar activity conditions. Below 160 km (150 km in the case of high solar activity) CO_2 is the major species but above that altitude atomic oxygen becomes the dominant neutral in the atmosphere of Venus. Due to the higher gravity of Venus the fall in CO_2 density with altitude is much more rapid than that on Mars.

Production mechanisms for $CO(a^3\Pi)$ are photon and electron impact dissociative excitation of CO_2, electron dissociative recombination of CO_2^+, and electron impact excitation of CO. Since $X^1\Sigma^+ \rightarrow a^3\Pi$ is a forbidden transition, resonance fluorescence of CO is not an effective excitation mechanism. The $CO(a^3\Pi)$ is a metastable state; *Lawrence* [1972a] had measured its lifetime as 7.5 ± 1 ms, which is consistent with the the value of 9 ms measured by *Johnson* [1972]. Due to its long lifetime, cross section for the production of $CO(a^3\Pi)$ state due to electron impact dissociation of CO_2 (e-CO_2) is difficult to measure in the laboratory. *Ajello* [1971b] reported relative magnitudes of the cross section for the (0, 1) transition of CO Cameron band at 215.8 nm and reported a value of 7.1×10^{-17} cm^2 at 80 eV. This cross section value was later re-evaluated by *Erdman and Zipf* [1983]. Based on the radiative lifetime of 9 ms [*Johnson*, 1972], *Erdman and Zipf* [1983] evaluated the cross section given by *Ajello* [1971a] and reported a value of 9×10^{-17} cm^2 at 80 eV, which was subsequently multiplied by a factor of 2.7 to account for higher mean velocity of $CO(a^3\Pi)$ fragments, which might have escaped detection [*Wells et al.*, 1972]. Therefore, *Erdman and Zipf* [1983] have reported a value

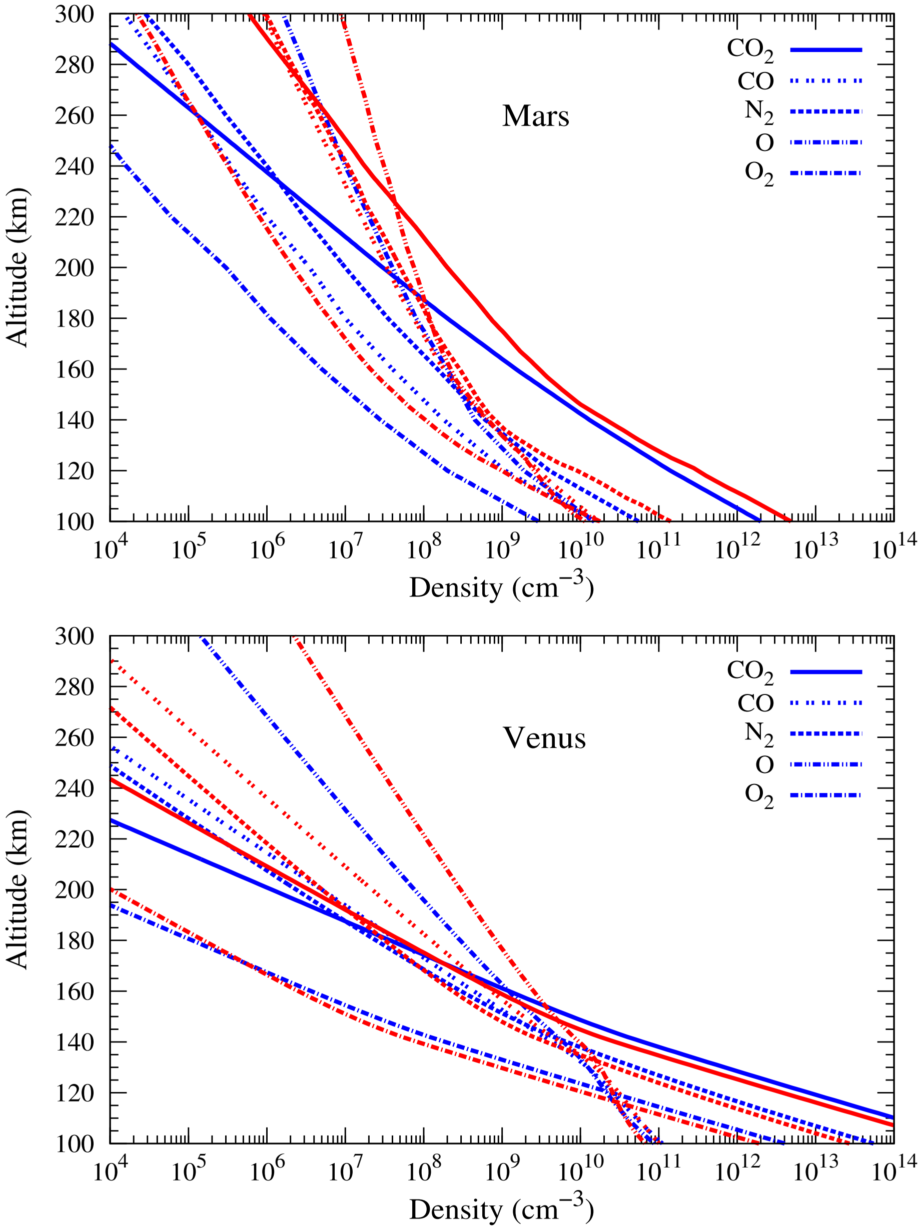

Figure 4.2: Model atmosphere of Mars (top panel) and Venus (bottom panel) for low (blue curves) and high solar activity (red curves) conditions.

of 2.4×10^{-16} cm^2 at 80 eV. *Avakyan et al.* [1998] have estimated the CO Cameron band cross section based on the cross section of *Ajello* [1971b] with the correction of *Erdman and Zipf* [1983]. *Bhardwaj and Jain* [2009] have analytically fitted the cross section of CO($a^3\Pi$) production due to electron impact on CO_2 using the suggested value of *Erdman and Zipf* [1983].

Based on theoretical and experimental work, *Gilijamse et al.* [2007] have re-analysed the radiative lifetime of CO($a^3\Pi$), and found a value of ∼3.16 ms, which is around 3 times less than the value of *Johnson* [1972]. *Conway* [1981] constructed a synthetic spectrum of Martian dayglow between 1800 and 2600 Å. Based on the comparison of theoretical zenith intensity of CO Cameron band with the Mariner observations, *Conway* [1981] suggested a peak cross section value of 7×10^{-17} cm^2 for electron impact dissociative excitation of CO_2. The value suggested by *Conway* [1981] is around a factor of 3 smaller than that of *Erdman and Zipf* [1983].

Recent comparison between calculations and observations of dayglow emission on Mars suggests a lower value of e-CO_2 cross section for the CO Cameron band production [*Simon et al.*, 2009; *Jain and Bhardwaj*, 2012; *Gronoff et al.*, 2012a]. *Jain and Bhardwaj* [2012] and *Gronoff et al.* [2012a] have shown that Cameron band cross sections of *Erdman and Zipf* [1983] should be reduced by a factor of 2 to 3, to bring the calculated CO Cameron band intensities in agreement with the Mars Express observation. In the present study the cross section for Cameron band production due to electron impact on CO_2 is taken from *Bhardwaj and Jain* [2009] after dividing it by a factor of 3, which is shown in Figure 4.3 along with the recommended cross section of *Avakyan et al.* [1998].

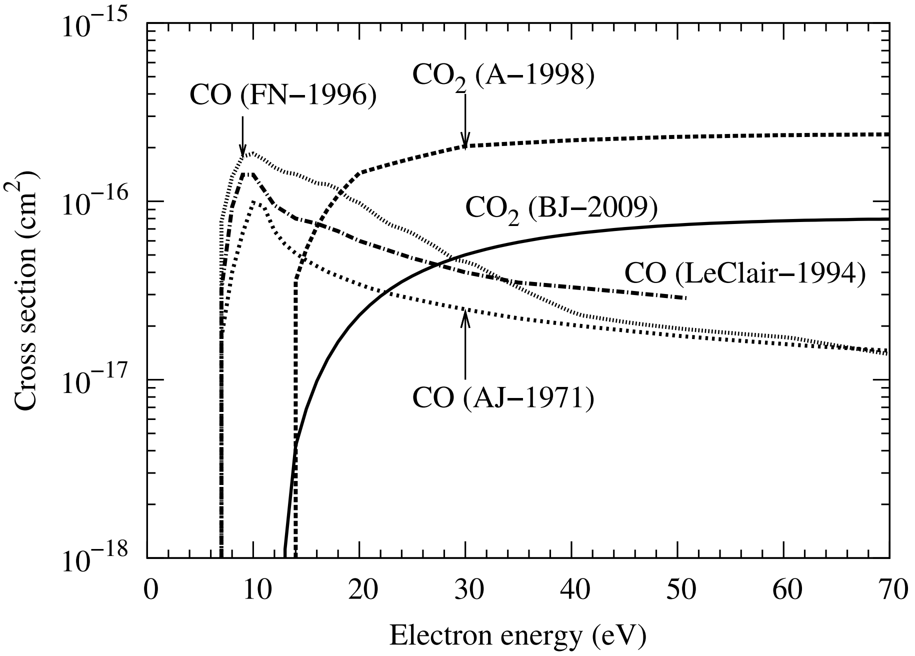

Figure 4.3: Cross sections for the production of CO($a^3\Pi$) due to electron impact on CO and CO_2. A-1998, BJ-2009, FN-1996, LeClair-1994 and AJ-1971 refer to *Avakyan et al.* [1998], *Bhardwaj and Jain* [2009], *Furlong and Newell* [1996], *LeClair et al.* [1994], and *Ajello* [1971b], respectively. BJ-2009 cross section is plotted after dividing it by a factor of 3.

Electron impact on CO (e-CO) is also a source of CO Cameron band. On Mars, due to less abundance of CO, it does not contribute significantly to the total Cameron band emission [*Fox and Dalgarno*, 1979a; *Simon et al.*, 2009; *Jain and Bhardwaj*, 2012; *Gronoff et al.*, 2012a]. However, on Venus, CO contribution can not be neglected due to its relatively larger abundance above 150 km (cf. Figure 4.2). In comets where the CO abundance is larger or equal to that of the CO_2, the major contribution to CO Cameron band emission comes from electron impact on CO [*Bhardwaj and Raghuram*, 2011; *Raghuram and Bhardwaj*, 2012]. *Ajello* [1971b] reported the Cameron band emission cross section following the electron impact on CO. *Ajello* used the (1,4) Cameron band at 2389 Å to normalize the entire band system cross section in electron impact excitation of CO. However, according to *Erdman and Zipf* [1983], the (1,4) Cameron band was contaminated by (6,16) CO fourth positive band. *Erdman and Zipf* [1983] repeated and re-analysed the *Ajello*'s experiment with higher sensitivity and concluded that total cross section value (1.1×10^{-16} cm^2 at 11 eV) measured by *Ajello* [1971b] should be reduced by a factor of 8 to an apparent value of 1.4×10^{-17} cm^2 at 11 eV. In addition to the contamination problem, *Ajello*'s total Cameron band emission cross section was based on the assumption of radiation lifetime of 1 ms for $a^3\Pi$ state. *Erdman and Zipf* [1983], used the radiative life of 9 ms [*Johnson*, 1972] and multiply the cross section (already corrected for contamination) by a factor of 9 and gave a cross section value of 1.5×10^{-16} cm^2 at 11 eV.

After accounting for corrections, the cross section value suggested by *Erdman and Zipf* [1983] is very close to the cross section of *Ajello* [1971b]. However, based on recent measurements on radiative lifetime of ∼3 ms [*Gilijamse et al.*, 2007], the Cameron band cross section in e-CO process should be reduced by a factor of 3. Similar correction is applied to Cameron band cross section in e-CO_2 process.

LeClair et al. [1994] have measured the e-CO cross section for CO($a^3\Pi$) production using solid xenon detector and time of flight (TOF) technique. *LeClair et al.* [1994] have given the integral cross section (ICS) of CO($a^3\Pi$)—that include cascading contributions from higher triplet states—by normalizing their excitation function to the maximum absolute cross section (1.5×10^{-16} cm^2 at 11 eV) obtained by *Erdman and Zipf* [1983]. The shape of normalized CO($a^3\Pi$) cross section measured by *LeClair et al.* [1994] is identical to the one recorded by *Ajello* [1971b]. However, maximum cross section is at 9.4 eV in *LeClair et al.* [1994] measurements compared to 11 eV in *Ajello* [1971b] experiment. *LeClair et al.* [1994] attributed this difference in peak position to the electron beam characteristic in the two experiment.

Furlong and Newell [1996] measured the absolute integral cross section for CO($a^3\Pi$) production in the e-CO collision by normalizing their measurements to maximum cross section value (1.698×10^{-16} cm^2 at 8.5 eV) of *Morgan and Tennyson* [1993]. Below 10 eV, their cross section is in good agreement with that of *LeClair et al.* [1994]. Above 10 eV, *Furlong and Newell* [1996] reported an increase in cross section due to the contribution from cascading into $a^3\Pi$ state. The cross sections obtained by *Furlong and Newell* [1996] are about a factor of 2 higher between 10 and 35 eV compared to that of *LeClair et al.* [1994].

The above mentioned discussion clearly points out the difference in the cross sections of CO($a^3\Pi$) in electron impact excitation of CO. In the present study, cross section of *Furlong and Newell* [1996] is used for CO($a^3\Pi$) production in e-CO collision. The cross section of *LeClair et al.* [1994] is also used to asses the effect of cross section in Cameron band intensity. The reason for using these two cross sections over the one measured by *Ajello* [1971b] is due to the fact that *Ajello*'s measured cross section have been shown to be flawed by *Erdman and Zipf* [1983]. However, the correction factor of radiative lifetime of 9 ms [*Johnson*, 1972] that *Erdman and Zipf* [1983] used to correct the $a^3\Pi$ state cross section in electron impact on CO_2 and CO is about a factor of 3 higher based on the recent radiative lifetime value of 3 ms. Since, *LeClair et al.* [1994] have normalized their measured cross section to maximum absolute cross section of CO($a^3\Pi$) obtained by *Erdman and Zipf* [1983], the cross section values given by *LeClair et al.* [1994] might be overestimated. The cross section measured by *Furlong and Newell* [1996] shows a broad shoulder above 10 eV, which they attributed to the cascade contribution from higher triplet states. The effect of the two set of CO($a^3\Pi$) cross section used in the present study will be discussed in later sections along with the importance of CO($a^3\Pi$) cross section in determining the role of CO in Cameron band production. Figure 4.3 depicts the CO($a^3\Pi$) cross sections for electron impact on CO used in the present study along with the cross section of *Ajello* [1971b].

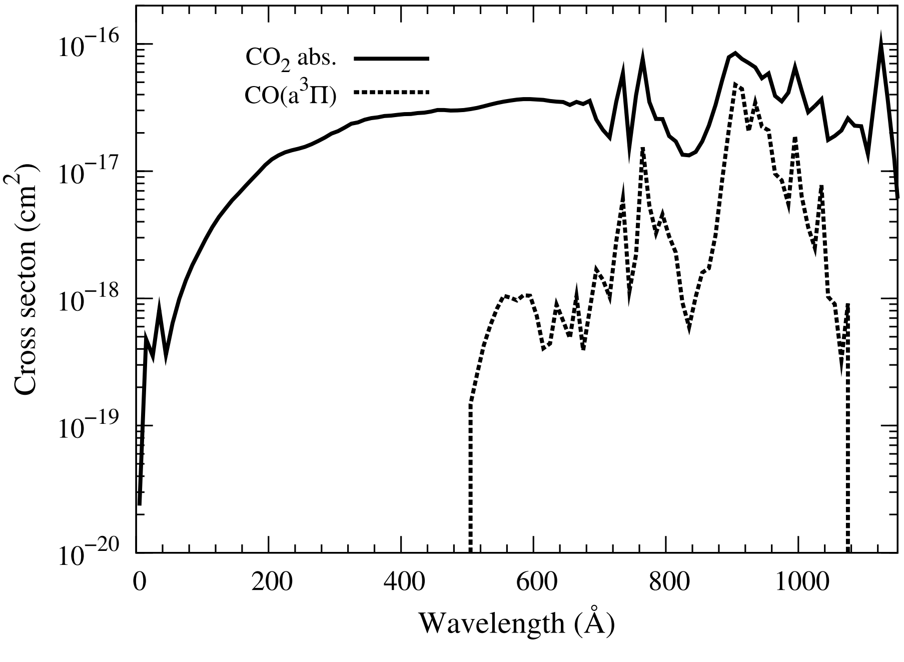

Figure 4.4: Cross section for the production of CO($a^3\Pi$) in the photodissociation of CO_2 taken from *Lawrence* [1972a]. Total photoabsorption cross section of CO_2 is also shown in the figure.

Cross section for photodissociation of CO_2 producing CO($a^3\Pi$) is taken from *Lawrence* [1972a], which is shown in Figure 4.4. The cross section is averaged at 37 wavelength bin according to solar flux input. A discussion on various photodissociative channels

Table 4.1: Major reactions for the production and loss of CO($a^3\Pi$).

Reaction	Rate (cm^3 s^{-1} or s^{-1})	Reference
$CO_2 + h\nu \rightarrow CO(a^3\Pi) + O(^3P)$	Model (K_1)	*Lawrence* [1972a]
$CO_2 + e^-_{ph} \rightarrow CO(a^3\Pi) + O + e^-$	Model (K_2)	*Present work*
$CO + e^-_{ph} \rightarrow CO(a^3\Pi) + e^-$	Model (K_3)	*Present work*
$CO_2^+ + e^- \rightarrow CO(a^3\Pi) + O$	$K_4^\dagger$	*Viggiano et al.* [2005]; *Rosati et al.* [2003]
$CO(a^3\Pi) + CO_2 \rightarrow CO + CO_2$	1.0×10^{-11}	*Skrzypkowski et al.* [1998]
$CO(a^3\Pi) + CO \rightarrow CO + CO$	5.7×10^{-11}	*Wysong* [2000]
$CO(a^3\Pi) \longrightarrow CO + h\nu$	$K_5 = 1.26 \times 10^2$	*Lawrence* [1971]

e^-_{ph} = photoelectron.

$^\dagger K_4 = 4.2 \times 10^{-7}(300/T_e)^{0.75} \times 0.29$ cm^3 s^{-1}; here, 0.29 is the yield of CO($a^3\Pi$) production.

K_1, K_2, K_3, K_4, and K_5 are described in Eq. 4.10.

of CO_2 is presented in Chapter 6. To calculate the production rate of CO($a^3\Pi$) due to dissociative electron recombination process, the densities of electron and major ions are calculated by including ion-neutral chemistry in the model. The coupled chemistry model is similar to that adopted in the studies of Bhardwaj and co-workers [*Bhardwaj et al.*, 1996; *Bhardwaj*, 1999; *Haider and Bhardwaj*, 2005]. Rate coefficients for ion-neutral reactions are taken from *Fox and Sung* [2001]. *Viggiano et al.* [2005] have measured rates for the electron-CO_2^+ recombination. They reported unit yield for the channel producing CO*, of which CO($a^3\Pi$) production yield is taken as 0.29 based on the measurements of *Skrzypkowski et al.* [1998] and *Rosati et al.* [2003]. Ion and electron temperatures are taken from *Fox* [2009]. Ion and electron densities are calculated under steady state photochemical equilibrium. To calculate the density of CO($a^3\Pi$) various sources of production and loss of CO($a^3\Pi$) is included in the model which are given in Table 4.1.

Major production sources of $CO_2^+(B^2\Sigma_u^+)$ are photon and electron impact ionization of CO_2. Cross section for the formation of $CO_2^+(B^2\Sigma_u^+)$ in electron impact ionization of CO_2 is taken from *Itikawa* [2002], and cross section for photoionization of CO_2 is based on the branching ratio given by *Avakyan et al.* [1998] (see Chapter 2). In the present study contribution of fluorescence scattering by CO_2^+ is included in the model calculation by taking g values of 5.3×10^{-3} and 1.2×10^{-3} for Venus and Mars, respectively, [*Dalgarno and Degges*, 1971]. While calculating the emission from B state of CO_2^+, we have taken the branching ratio of 0.5 from the CO_2^+(B) to (A) based on the study of *Fox and Dalgarno* [1979a].

The 37 bin EUVAC model of *Richards et al.* [1994] and S2K version 2.36 of *Tobiska* [2004] solar EUV flux are used in the study. In these models, bins consist of band of 50

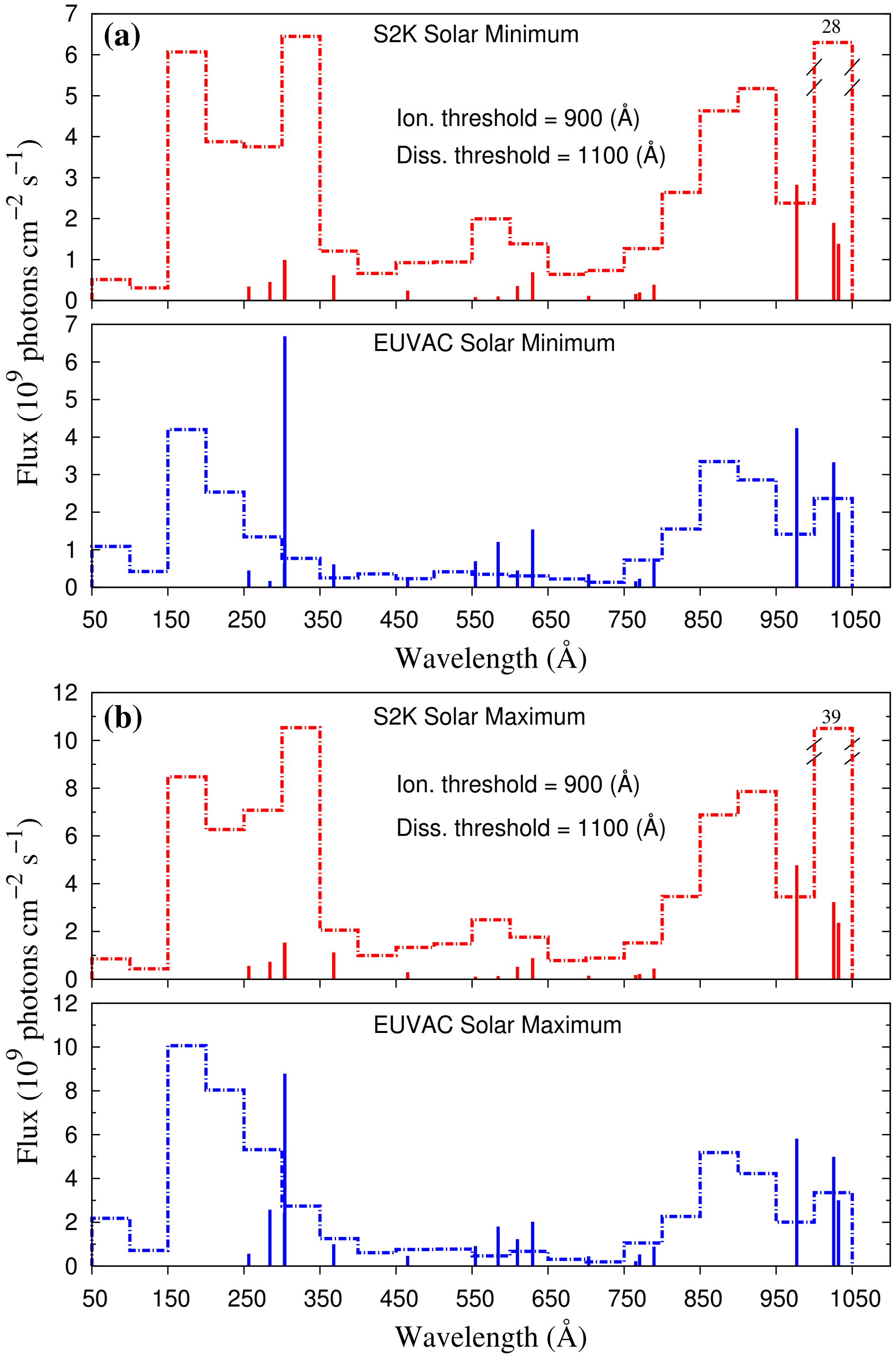

Figure 4.5: Solar photon flux at 1 AU, in bands and at lines, as a function of wavelength in EUVAC and S2K solar EUV flux models. (a) for the low solar activity condition on 20 July 1976 (similar to Viking landing, F10.7 = 70), and (b) for high solar activity condition on 2 August 1969 (similar to Mariner 6 and 7 observations period, F10.7 = 186).

Å width each and few prominent solar EUV lines, and are sufficient for the modelling of photoionization and photoelectron flux calculations [*Richards et al.*, 1994; *Simon et al.*, 2009]. Solar EUV flux has been taken at 1 AU and then scaled to the Sun-Mars (as seen from the Mars, taking the Sun-Earth-Mars angle into consideration) and Sun-Venus distances. Figure 4.5 shows the output of EUVAC and S2K solar EUV flux models for both solar minimum (20 July 1976) and solar maximum (2 August 1969) conditions at 1 AU. There are substantial differences in the solar EUV fluxes of EUVAC and S2K models; moreover, these differences are not similar in solar minimum and maximum conditions. In both, solar minimum and maximum conditions, the solar flux in bands is higher in S2K than in EUVAC, except for bins below 250 Å (150 Å for solar minimum condition), whereas the solar flux at lines is higher in EUVAC model at all wavelengths. A major difference between solar EUV fluxes of S2K and EUVAC models is the solar flux at bin containing 1026 Å H Ly-β line, which, in both solar minimum and maximum conditions, is about an order of magnitude higher in S2K compare to EUVAC solar flux model (cf. Figure 4.5). Flux at these wavelengths does not contribute to the photoionization, but are very important for dissociative excitation processes. The CO($a^3\Pi$) cross section in photodissociation of CO_2 lies in longer (700–1080 Å) wavelength regime [*Lawrence*, 1972a]. Hence, the excitation rate of CO in $a^3\Pi$ state followed by photodissociation of CO_2 would be larger when S2K solar EUV flux model is used.

Primary photoelectron production energy spectrum at altitude Z is calculated using

$$Q(Z,E) = \sum_l n_l(Z) \sum_{j,\lambda} \sigma_l^I(j,\lambda) I(Z,\lambda)\ \delta\left(\frac{hc}{\lambda} - E - W_{jl}\right) \tag{4.1}$$

$$I(Z,\lambda) = I(\infty,\lambda)\ exp[-\tau] \tag{4.2}$$

where,

$$\tau(\lambda, Z) = sec(\chi) \sum_l \sigma_l^A(\lambda) \int_Z^\infty n_l(Z')dZ', \tag{4.3}$$

is the optical depth at wavelength λ and altitude Z, σ_l^A and $\sigma_l^I(j,\lambda)$ are the total photoabsorption and photoionization cross sections of the jth ion state of the constituent l at wavelength λ, respectively; $I(\infty,\lambda)$ is the unattenuated solar flux at wavelength λ, $n_l(Z)$ is the neutral density of constituent l at altitude Z; χ is the SZA; $\delta(hc/\lambda - E - W_{jl})$ is the delta function, in which hc/λ is the incident photon energy, W_{jl} is the ionization potential of the jth ion state of the lth constituent, and E is the energy of ejected electron. The sec(χ) is used in model calculation in place of Chapman function ch(χ), which is valid for χ values upto 80°. The details of photoabsorption and photoionization cross sections used in the present study have been presented in Chapter 2.

In an atmosphere the absorption of photons maximizes where $\tau(\lambda, Z) = 1$. The altitude of unit optical depth is shown in Figure 4.6 for wavelengths from XUV to FUV for SZA = 45° in the atmospheres of Mars and Venus for low and high solar activity conditions. CO_2 is the main absorber of FUV and EUV photons on Mars and Venus, although at wavelengths less than 1000 Å, other species namely, N_2, CO, and O also attenuate incoming solar radiation (see absorption cross sections in Figure 2.2). High energy photons (<100 Å) deposit their maximum energy below 120 km on Mars.

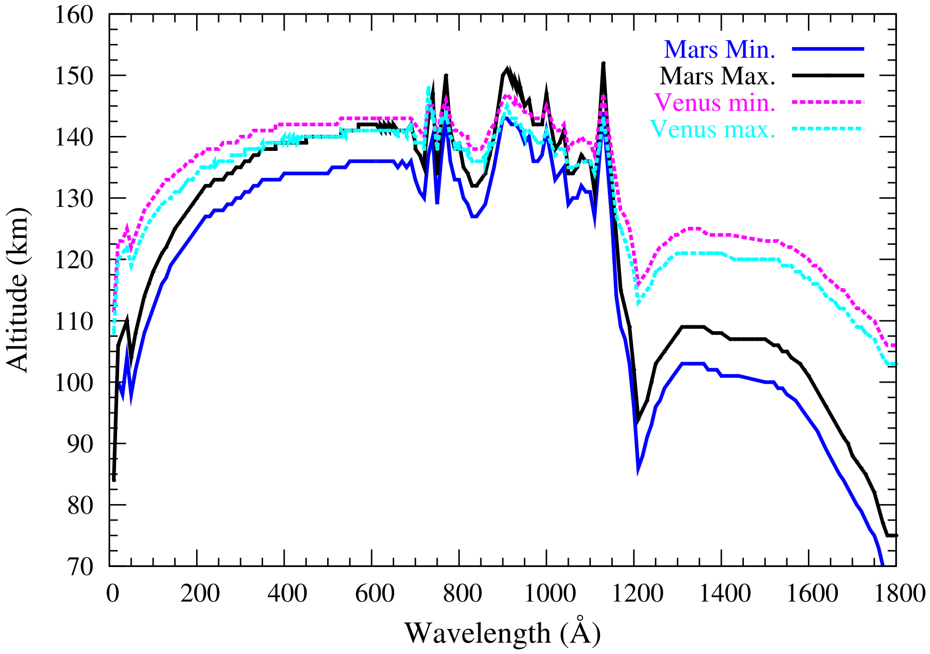

Figure 4.6: The altitude where optical depth τ becomes unity for SZA = 45°, at various wavelengths, on Mars and Venus for low and high solar activity conditions.

On Mars, maximum absorption of photons in wavelength range 200–1000 Å occurs at altitudes between 130 and 135 km in solar minimum condition. During solar maximum condition the altitude of maximum absorption of photons (between 200–1000 Å) is ∼140 km, an upward shift of 5 km compared to solar minimum condition. For few wavelengths altitude of unit optical depth is as high as 150 km. In general, on Mars maximum absorption of ionizing photons takes place at an altitude of around 135 km, which coincide with the altitude of maximum photoionization. For photons of wavelength >1200 Å, the maximum absorption occurs below 100 (110) km during solar minimum (maximum) condition. These photons do not have enough energy to ionize the gases but can dissociate atmospheric constituents, e.g., the production of O(^{1}S) and O(^{1}D) on Mars maximizes around 90 km, which is mainly because of solar photons at wavelengths higher than 1200 Å.

On Venus maximum deposition (for photons <100 Å) takes place below 130 km, while solar photons in wavelength range 200–1000 Å suffer maximum absorption at ∼140 km for both solar minimum and maximum conditions. On Venus, the difference in the altitude of unit optical depth for low and high solar activity conditions is small compared to that on Mars. Solar photons having wavelength between 1200 and 1600 Å deposit their maximum energy around 120 km.

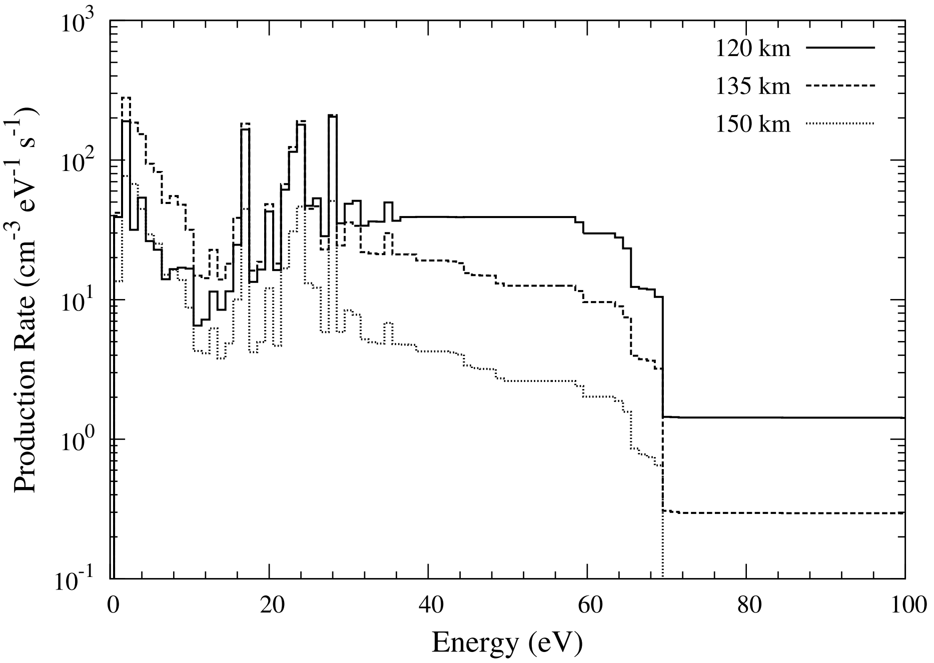

Figure 4.7: Primary photoelectron energy distribution on Mars at three different altitudes for solar minimum condition at SZA = 45°.

4.3 CO Cameron band and CO_2^+ doublet emissions on Mars

A model for CO Cameron band and CO_2^+ UV doublet emission in dayglow of Mars is developed using the input parameters described in the previous section. The results are presented in the following sections.

4.3.1 Photoelectron production rate and photoelectron flux

Figure 4.7 shows the primary photoelectron energy spectrum at three different altitudes calculated using Eq. 4.1. There is a sharp peak at 27 eV due to the ionization of CO_2 in the ground state by the solar He II Lyman α line at 303.78 Å. The peaks at 21 and 23 eV are due to ionization of CO_2 in the $A^2\Pi_u$ and $B^2\Sigma_u^+$ states of CO_2^+, respectively, by the 303.78 Å solar photons. To calculate the photoelectron flux the AYS technique is used, which has been described in Chapter 3. Using AYS the photoelectron flux has been calculated as [e.g. *Singhal and Haider*, 1984; *Bhardwaj and Michael*, 1999b; *Michael*, 2000]

$$\phi(Z,E) = \int_{W_{kl}}^{100} \frac{Q(Z,E)U(E,E_0)}{\sum_l n_l(Z)\sigma_{lT}(E)}\, dE_0 \tag{4.4}$$

where $\sigma_{lT}(E)$ is the total inelastic cross section for the lth gas, n_l is its density, $Q(Z,E)$ is the photoelectron production as described in Section 4.2, and $U(E,E_0)$ is the two-dimensional AYS, which embodies the non-spatial information of degradation process. It

Table 4.2: Amplitude parameters for the two-dimensional yield spectra (Eq. 4.5) for CO, N_2, O, and O_2 taken from *Singhal et al.* [1980].

Gas	C_0	C_1	C_2
CO	0.0204	5.29	176.9
N_2	0.0166	5.04	169.0
O	0.0140	5.02	246.9
O_2	0.0108	6.15	177.0

represents the equilibrium number of electrons per unit energy at an energy E resulting from the local energy degradation of an incident electron of energy E_0 (details are given Chapter 3).

For CO_2 the AYS is described in Chapter 3. For O_2, N_2, O, and CO, the AYS is taken from the work of *Singhal et al.* [1980] as

$$U(E, E_0) = C_0 + C_1\chi + C_2\chi^2 \tag{4.5}$$

Here C_0, C_1, and C_2 are external parameters which are independent of the energy, whose values are presented in Table 4.2 [*Singhal et al.*, 1980] and

$$\chi = \frac{E_k^\Omega}{E + L} \tag{4.6}$$

where Ω and L are intrinsic parameter having a value of 0.585 and 1 eV, respectively. E_k is the incident electron energy (in keV) and E is the spectral variable (in eV). The values of Ω and L are 0.585 and 1 eV, respective, for all gases [*Singhal et al.*, 1980].

Figure 4.8 shows the photoelectron fluxes in the atmosphere of Mars calculated using EUVAC and S2K solar flux models. Below 70 eV, photoelectron flux calculated using S2K is higher compared to that calculated using EUVAC model for low solar activity condition (Figure 4.8). Above 70 eV, photoelectron flux calculated using EUVAC model is higher than that calculated using S2K model, which is due to the larger solar EUV flux at shorter wavelengths (<250 Å) in EUVAC model (cf. Figure 4.5). During solar maximum condition, due to higher solar EUV flux at wavelength below 250 Å in EUVAC model, the photoelectron flux calculated by using EUVAC model is higher than that calculated using S2K model. Photoelectron fluxes calculated using both solar EUV flux models are similar in shape but peaks around 20–30 eV are more prominent when EUVAC model is used, which is due to the higher solar EUV flux at lines (e.g., He II Lyman-α line at 303.78 Å) (Figure 4.5).

The calculated photoelectron flux are employed to compute the volume excitation rate of $CO(a^3\Pi)$ and $CO_2^+(B^2\Sigma_u^+)$ molecules in electron impact processes as,

$$V_i(Z) = n(Z) \int_{E_{th}}^{E} \phi(Z, E)\sigma_i(E)dE, \tag{4.7}$$

where $n(Z)$ is the density at altitude Z, $\sigma_i(E)$ is the electron impact cross section for i^{th} process, for which the threshold is E_{th}, and $\phi(Z, E)$ is the photoelectron flux. Following

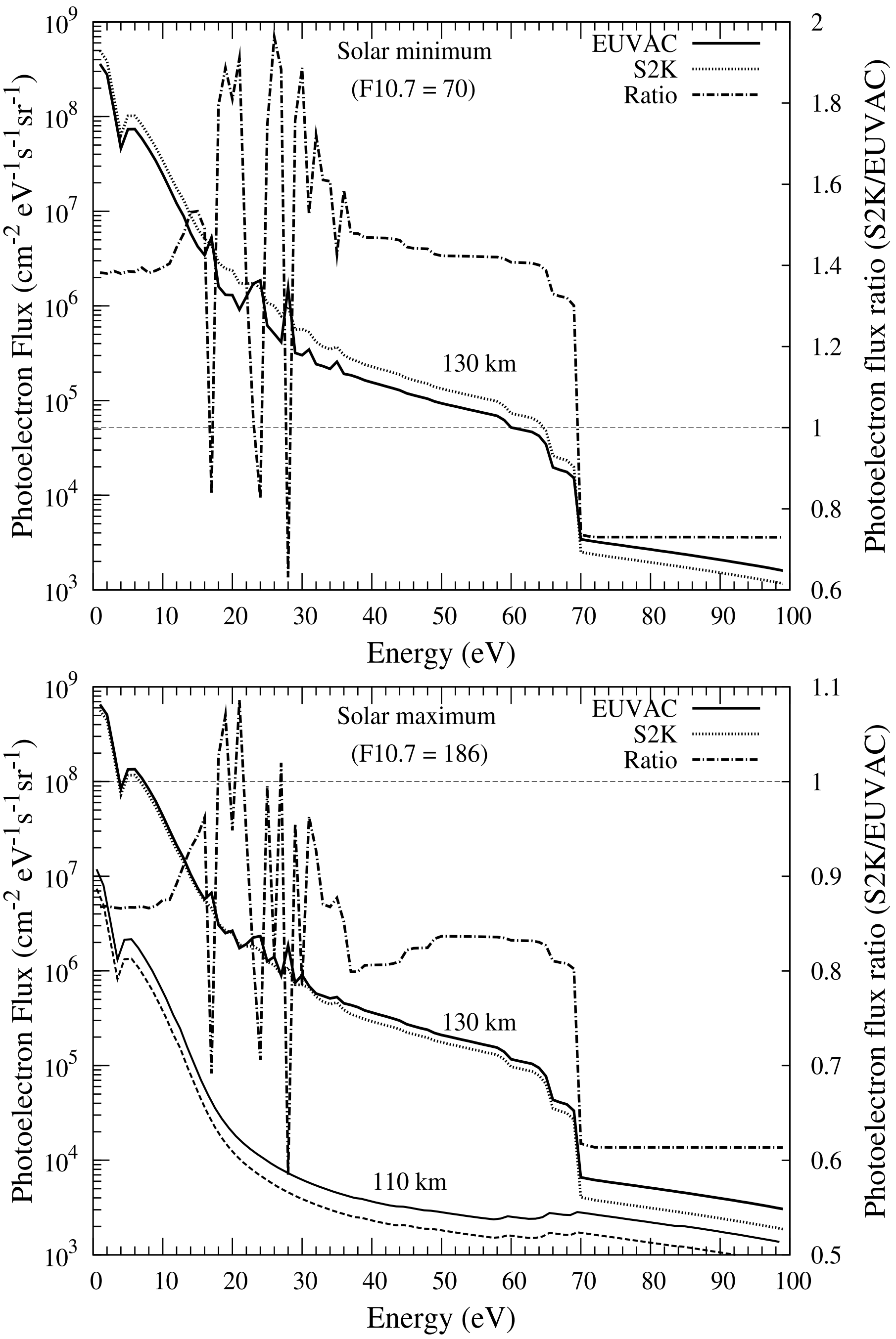

Figure 4.8: Calculated photoelectron fluxes on Mars for low (upper panel) and high (lower panel) solar activity conditions at SZA = 45°. The ratio of the photoelectron flux at 130 km calculated using the two solar flux models is also shown with magnitude on right side Y-axis. Thin dotted horizontal line is drawn for the ratio = 1.

sections describe the production of CO($a^3\Pi$) and $CO_2^+(B^2\Sigma_u^+)$ molecules and subsequent Cameron band and UV doublet emissions, respectively, in the atmosphere of Mars for different solar activity conditions.

4.3.2 Low solar activity condition

The model calculation is carried out for low solar activity condition (similar to Viking landing). The Sun-Mars distance D_{S-M} = 1.64 AU and solar zenith angle is taken as 45°.

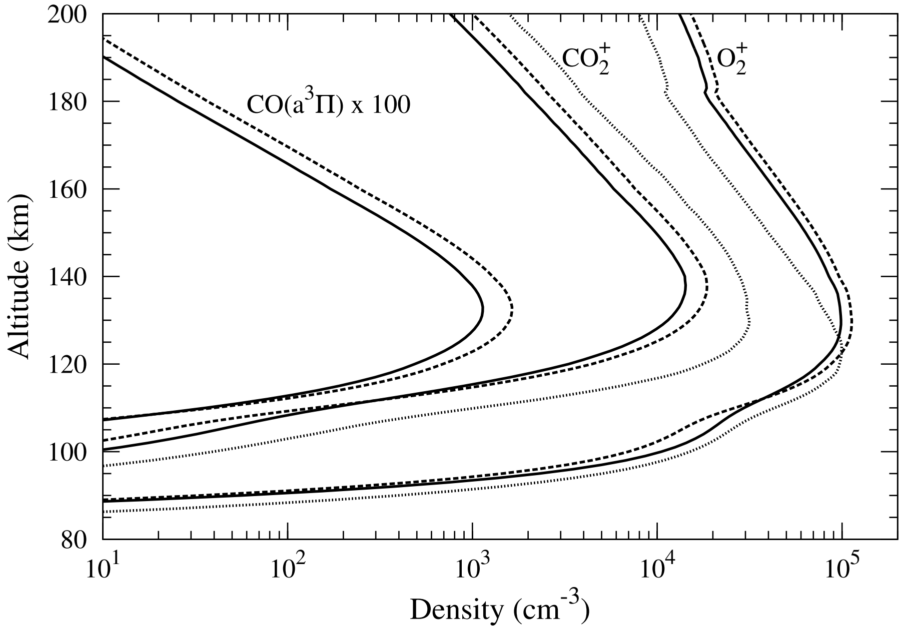

Figure 4.9: Densities of CO_2^+ and O_2^+ ions and $CO(a^3\Pi)$ molecule on Mars for solar minimum condition calculated using EUVAC (solid curve) and S2K (dashed curve) solar EUV flux models. Density of $CO(a^3\Pi)$ molecule is plotted after multiplying by a factor of 100. Dotted curves show the densities of CO_2^+ and O_2^+ ions for first case (Ls < 130°) using EUVAC solar flux.

Figure 4.9 shows the calculated densities of CO_2^+ and O_2^+ ions in the Martian upper atmosphere. The peak density of CO_2^+ calculated using S2K model is ~20% higher than that calculated using EUVAC, which is due to higher production rate of CO_2^+ when S2K model is used. Below 120 km, ion densities calculated by using EUVAC model are higher than that calculated using S2K model due to higher photon fluxes below 250 Å in EUVAC model (cf. Figure 4.5). There is a small discontinuity in the O_2^+ ion density around 180 km, which is due to the sudden change in the electron temperature at 180 km [see Figure 2 of *Fox*, 2009]. The calculated ion densities are consistent with calculations of *Fox* [2004].

Figure 4.10 (upper panel) shows the excitation rate profiles $CO(a^3\Pi)$ molecule calculated using EUVAC and S2K solar EUV flux models. Around the peak of $CO(a^3\Pi)$ production, the major source is photoelectron impact dissociation of CO_2, while at higher altitudes photodissociation excitation of CO_2 takes over. Contribution of dissociative recombination is about 20%, while photoelectron impact excitation of CO contributes ~13% to the $CO(a^3\Pi)$ production at the peak [when cross section measured by *Furlong*

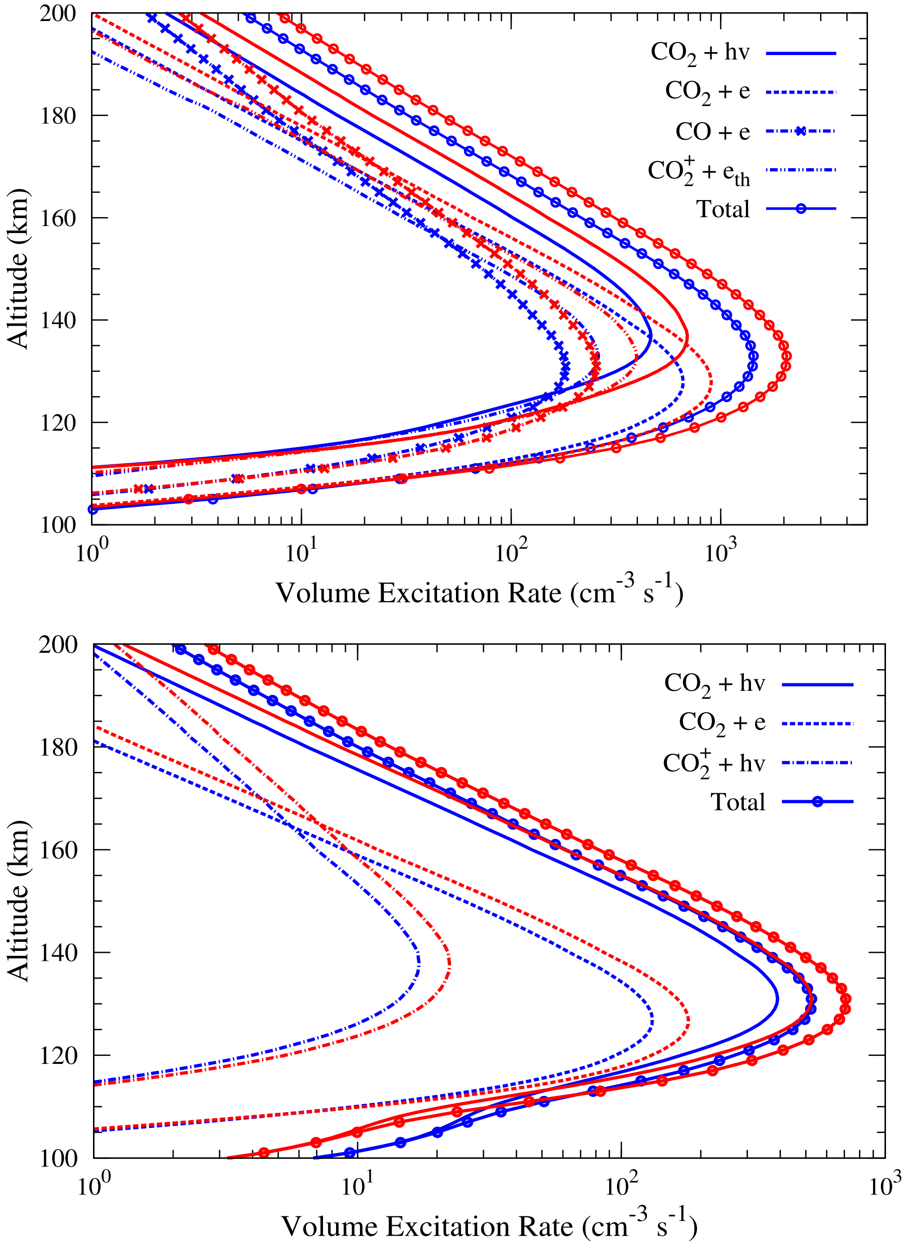

Figure 4.10: Calculated production rates of the CO(a$^3\Pi$) (upper panel) and CO$_2^+$(B$^2\Sigma_u^+$) (bottom panel) on Mars for low solar activity condition (Ls∼100–140°). DR stands for dissociative recombination. Blue curves show the production rates calculated using EUVAC model while red curves show them for S2K solar flux model.

and Newell, 1996, are used]. The altitude of peak CO(a$^3\Pi$) production remains the same for the two solar flux models. However, the magnitude of VERs calculated using S2K model are about 40% higher than those calculated using EUVAC model. Due to larger photon flux at longer (700–1050 Å) wavelengths (region where photodissociation of CO$_2$ becomes important) in S2K model compared to EUVAC model (cf. Figure 4.5), the CO(a$^3\Pi$) production in photodissociative excitation of CO$_2$ is ∼50% higher when S2K model is used. It is also clear from the upper panel of Figure 4.10 that the altitude where the photodissociation of CO_2 takes over electron impact dissociation of CO_2 in $CO(a^3\Pi)$ formation is slightly higher when EUVAC model is used. In the present model calculations, CO_2 photodissociation is the major source of $CO(a^3\Pi)$ at higher altitudes ($>$ 160 km) and is a factor of 2 higher than the electron impact dissociation of CO_2.

Figure 4.10 (bottom panel) shows the calculated production rates of CO_2^+ in $B^2\Sigma_u^+$ state. Production of $CO_2^+(B^2\Sigma_u^+)$ due to photoionization of CO_2 is about a factor of ∼3 higher than due to photoelectron impact ionization. The $CO_2^+(B^2\Sigma_u^+)$ production rate calculated using S2K is higher than that calculated using EUVAC flux by about 33%, but peak altitude remains the same in both cases.

Volume emission rates are height-integrated to calculate overhead intensities, which are presented in Table 4.3 for CO Cameron band and CO_2^+ UV doublet emissions. For CO Cameron band, the contribution of e-CO_2 process is maximum (38%) followed by photodissociation of CO_2 (28%). Contribution of both dissociative recombination and e-CO processes is ∼15%. For CO_2^+ doublet, the major (73%) contribution is from photoionization of CO_2, the rest is due to electron impact ionization of CO_2. Contribution of fluorescence scattering by CO_2^+ is very small (∼4%).

For comparing the model output with observed emission the volume emission rates are integrated along the line of sight. The abscissa r along the horizontal line of sight is calculated as

$$r = \sqrt{(R+z)^2 - (R+h)^2} \tag{4.8}$$

Where R is the radius of planet, z the local altitude of the emission, and h is the altitude of nearest tangent point (see Figure 4.11). Limb intensity at each tangent point is calculated as

$$I = 2\int_0^\infty \mathrm{V}(r)dr, \tag{4.9}$$

where V(r) is the volume emission rate (in $cm^{-3}\ s^{-1}$) at a particular emission point r. Multiplication by a factor of 2 is due to symmetry along the line of sight with respect to the tangent point. While calculating limb intensity it is assumed that the emission rate is constant along local longitude/latitude. For emissions considered in the present study the effect of absorption in the atmosphere is found to be negligible.

Figure 4.12 shows the calculated brightness profiles of the CO Cameron band and CO_2^+ UV doublet emissions along with the SPICAM-observed limb intensity taken from *Simon et al.* [2009]. Observed values are averaged over the orbits close to Viking 1 condition (Ls∼100–140°), low solar activity, and for SZA=45°. Below 100 km there is a sudden increase in the observed CO_2^+ doublet intensity, which is due to the significant solar contamination below 100 km [*Simon et al.*, 2009]. The limb intensities calculated using S2K flux are ∼40–50% higher than those calculated using EUVAC: depicting the effect of input solar EUV flux on the calculated intensities. The limb intensities of CO Cameron band and CO_2^+ doublet emissions calculated using EUVAC model are in

Table 4.3: Overhead intensities (in kR) of CO Cameron band and CO_2^+ UV doublet emissions on Mars.

Emissions	EUVAC						SOLAR2000					
	hν+CO_2	e+CO_2	e+CO	DR[§]	FS[¶]	Total	hν+CO_2	e+CO_2	e+CO	DR	FS	Total
Low solar activity (Viking condition)												
CO Cameron band	1.2	1.6	0.6 (0.4)[‡]	0.6	-	4.1 (3.9)[‡]	1.8	2.3	0.8 (0.5)	1	-	5.8 (5.6)
CO_2^+ UV doublet	1.1	0.3	-	-	6.4E-2	1.4 {0.7}[§]	1.4	0.4	-	-	9E-2	1.8 {0.9}[§]
SPICAM/Mars-Express, First Case (Ls <130°)												
CO Cameron band	1.4	2.4	0.8 (0.5)	1.7	-	6.4 (6.1)	2.2	2.6	0.9 (0.6)	2	-	7.6 (7.3)
CO_2^+ UV doublet	1.5	0.5	-	-	0.1	2.1 {1.1}	1.6	0.5	-	-	0.2	2.3 {1.2}
SPICAM/Mars-Express, Second Case (Ls >130°)												
CO Cameron band	1.6	2.7	2.1 (1.4)	1.1	-	7.5 (6.8)	2.6	2.9	2.4 (1.6)	1.3	-	9.3 (8.5)
CO_2^+ UV doublet	1.7	0.5	-	-	0.1	2.3 {1.2}	1.9	0.6	-	-	0.1	2.6 {1.3}
Higher solar activity (Mariner observations)												
CO Cameron band	2.3	5.2	4 (2.7)	2.5	-	14 (12.7)	3.6	4.5	3.7 (2.5)	2.3	-	14.1 (13)
CO_2^+ UV doublet	3.1	1.1	-	-	0.2	4.4 {2.2}	2.8	0.9	-	-	0.2	3.9 {2}

[§] Dissociative recombination (e + CO_2^+).

[¶] Fluorescent Scattering (hν + CO_2^+).

[‡] Calculate values in parenthesis are for CO($a^3\Pi$) cross section obtained by *LeClair et al.* [1994].

[§] Values in braces are calculated by taking the 50% cross over from B to A before radiating.

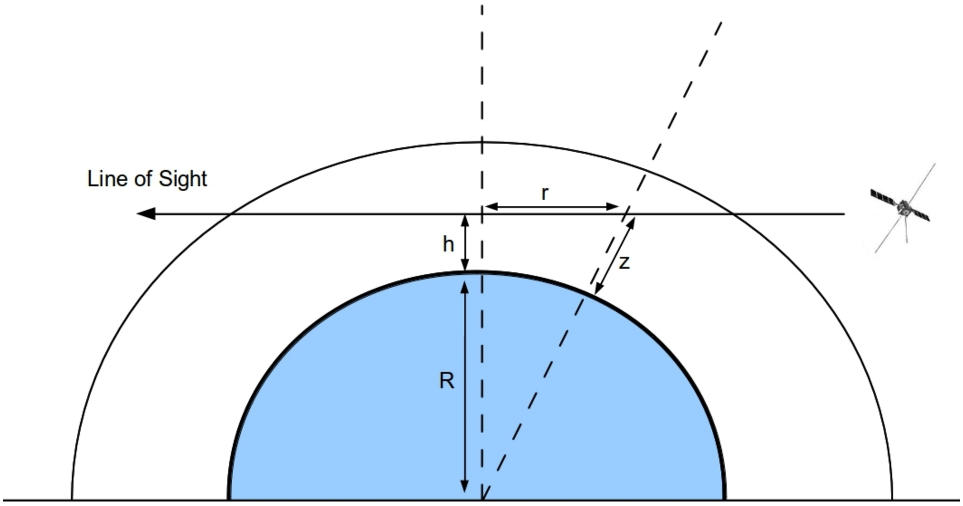

Figure 4.11: Schematic diagram of line of sight configuration for a typical limb measurement. The altitude of nearest point is h. R is the radius of the planet and r is the abscissa along the line of sight along which the intensities must be integrated.

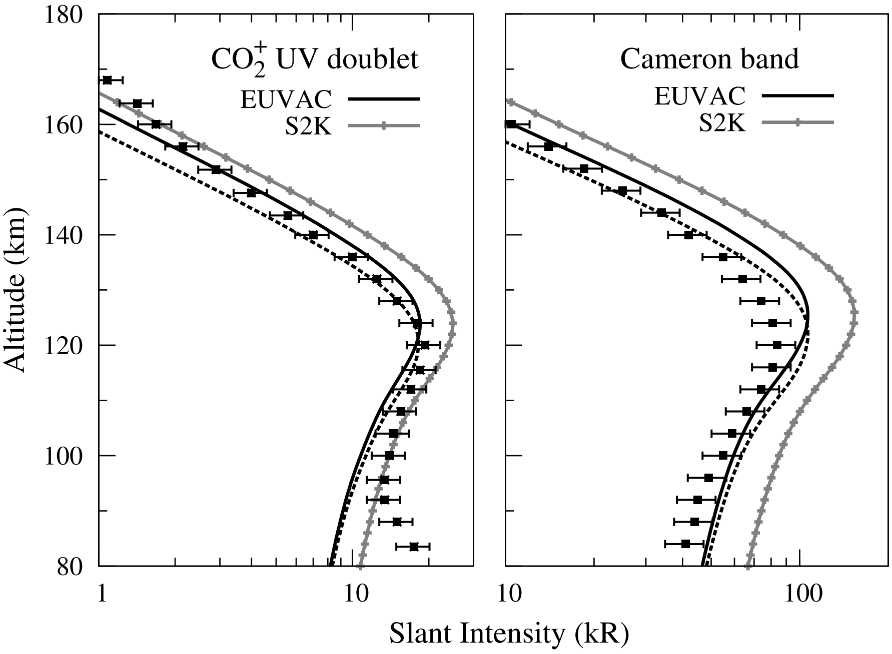

Figure 4.12: Calculated limb profiles of CO_2^+ UV doublet bands (left panel) and CO Cameron (right panel) on Mars for low solar activity condition. Solid squares with error bars represents the SPICAM-observed values taken from *Simon et al.* [2009]. Dashed curves show the calculated intensity (using EUVAC model) after reducing the density of CO_2 by a factor of 1.5.

agreement with the observation within the uncertainty of observation and model. For both emissions, the calculated intensity profile peaks at higher (∼5 km) altitude in comparison with the observation—indicating a denser neutral atmosphere in the model. The dashed curves in Figure 4.12 show the calculated intensities after reducing the CO_2

density by a factor of 1.5; a good agreement in the altitude of peak emission is seen between calculated and observed limb profiles.

4.3.3 SPICAM observations

Leblanc et al. [2006] have presented detailed analysis of SPICAM data during the period October 2004 to March 2005, spanning the solar longitude (Ls) from 101° to 171°. They divided the total data set into two periods of solar longitude: first, Ls = 101° to 130°, and second, Ls = 139° to 171° [cf. Table 2 of *Leblanc et al.*, 2006]. *Leblanc et al.* [2006] found that the altitude of peak emission for CO_2^+ UV doublet and CO Cameron band is around 10 km higher for Ls >138° (122.5 km and 132.5 km for UV doublet and Cameron bands, respectively) compared to Ls <130° (112.5 km and 117.5 km, for the same emissions). *Leblanc et al.* [2006] could not provide the reason for the higher altitude of peak emission for Ls >130° observations. Later, *Forget et al.* [2009] derived neutral densities in Martian upper atmosphere using the SPICAM instrument in stellar occultation mode for the same observation period. *Forget et al.* [2009] found that there is a sudden increase in the CO_2 density in the Martian upper atmosphere for Ls ∼ 130°–140°, which they attributed to a dust storm. Dust storm can heat the lower atmosphere and thus increase the densities at higher altitudes, which could explain the higher altitude for peak emission observed by the SPICAM for Ls >130° observations. Thus, the increase in the altitude of peak intensity of dayglow emissions clearly shows the effect of dust storms on Martian dayglow emissions.

First case (Ls <130°)

To model the SPICAM observations for Ls <130° the model atmosphere is based on MTGCM of *Bougher et al.* [1999] [taken from *Shematovich et al.*, 2008]. Calculations are made for MEx orbit 983 (24 Oct. 2004) when Mars is at heliocentric distance of 1.64 AU and F10.7 = 87.7 (F10.7A = 107.3).

Figure 4.13 (upper panel) shows the volume excitation rate of $CO(a^3\Pi)$. The total VER calculated using S2K flux is slightly higher (∼15%) than that obtained using EUVAC flux. However, the $CO(a^3\Pi)$ production rate due to photodissociative excitation of CO_2 is around 50% higher when S2K model is used. The CO_2^+ dissociative recombination (DR) contributes ∼26% to the production of $CO(a^3\Pi)$. This value is higher than the CO_2 photodissociative excitation (∼22%) and it is higher than that compared to the contribution of CO_2^+ DR in low solar activity (Viking condition) (see Table 4.3). *Leblanc et al.* [2006] mentioned that higher values of CO_2^+ can contribute up to 30% to the CO Cameron band production depending on the solar zenith angle. To account for DR in $CO(a^3\Pi)$ production, *Shematovich et al.* [2008] and *Cox et al.* [2010] have taken CO_2^+ and electron densities from *Fox* [2004] for low solar activity condition. Since SPICAM observations are made during moderate solar activity condition, the contribution of

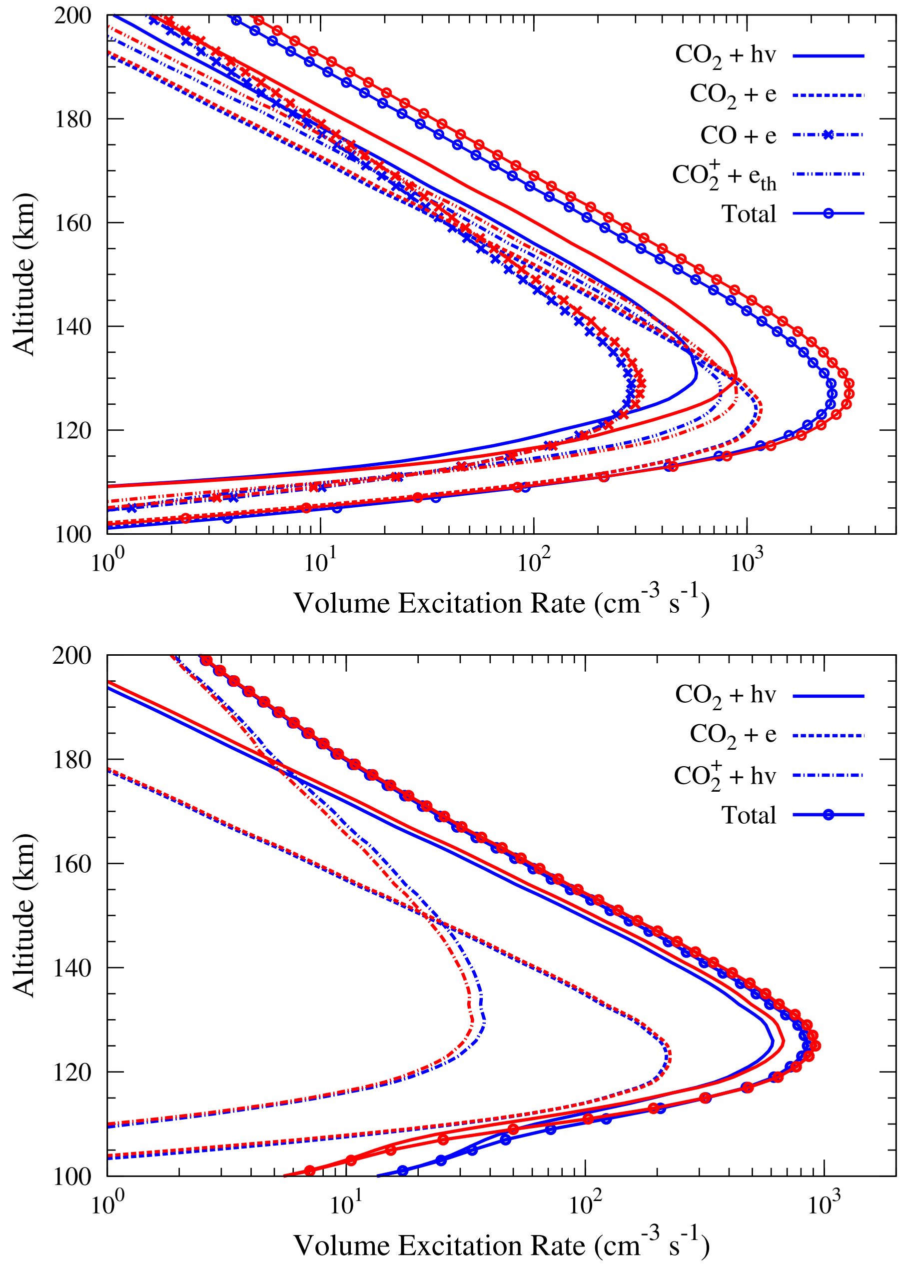

Figure 4.13: Calculated production rates of the $CO(a^3\Pi)$ (upper panel) and $CO_2^+(B^2\Sigma_u^+)$ (bottom panel) on Mars for solar longitude Ls <130°. DR stands for dissociative recombination. Blue curves show the calculated production rates using EUVAC model, while red curves show them for S2K solar flux model.

DR in $CO(a^3\Pi)$ production would be lower in their calculations. Figure 4.13 (bottom panel) shows the calculated production rate of $CO_2^+(B^2\Sigma_u^+)$ molecule. Total excitation rate calculated using both solar flux models peaks at same altitude (∼125 km), but total rate calculated using S2K model is higher (around 10%) than that calculated using EUVAC model. Table 4.3 shows the overhead intensities of CO Cameron band and CO_2^+ doublet emissions calculated using EUVAC and S2K models. For CO_2^+ UV doublet, photoionization of CO_2 is the dominant process contributing around 70% to the total overhead intensity.

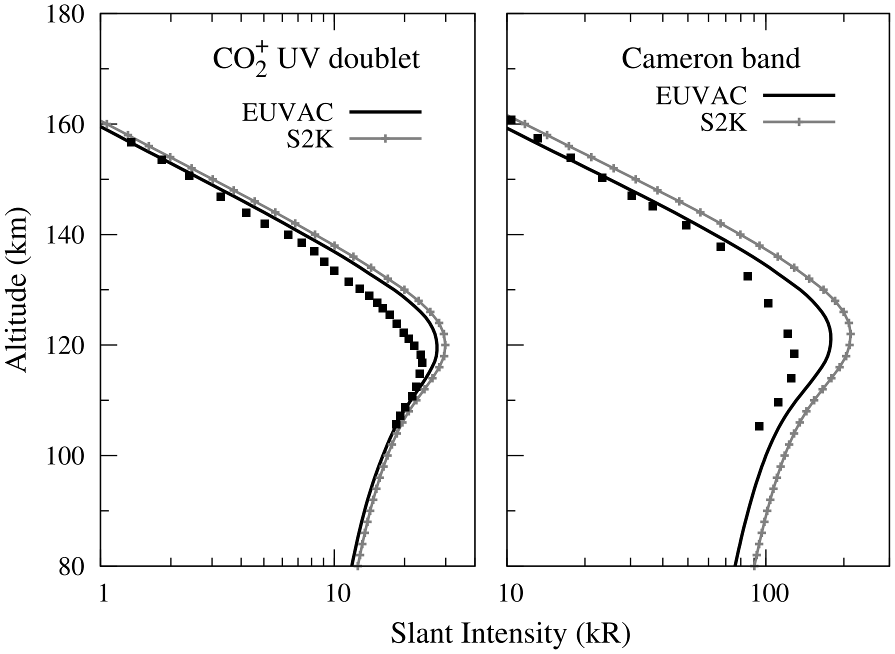

Figure 4.14: Calculated limb profiles of CO_2^+ UV doublet (left panel) and CO Cameron band emissions (right panel) on Mars for Ls <130°. Symbols represent the SPICAM-observed intensities taken from *Leblanc et al.* [2006].

Figure 4.14 shows the calculated limb intensities of CO Cameron and CO_2^+ doublet emissions. SPICAM-observed intensities of CO Cameron and CO_2^+ UV doublet emissions (for Ls = 100–130° with 10 orbit) taken from *Leblanc et al.* [2006] are also shown in Figure 4.14. Limb intensities of CO_2^+ UV doublet and Cameron bands calculated using the S2K model are ~6% and ~19%, respectively, higher compared to those obtained using EUVAC model. Calculated intensities of CO Cameron band and CO_2^+ UV doublet emissions for both solar flux models are higher than the SPICAM-observed values. The reason for the discrepancy between observed and calculated intensities might be that observations are averaged over several solar longitudes and solar zenith angles while model calculation is made for a single day and for a SZA. Altitude of the calculated intensity for both CO Cameron band and CO_2^+ UV doublet peaks ~2 to 3 km higher than the observation, which is well within the observational uncertainties.

Figure 4.15 shows the calculated intensity ratio of CO_2^+ UV doublet to CO Cameron band along with the observed ratio derived from SPICAM observations [*Leblanc et al.*, 2006]. At lower altitudes the calculated ratio is in agreement with the observation. The calculated ratio remains almost constant up to ~120 km (where Cameron band and UV doublet emission peaks), then starts to decrease with altitude and becomes gradually flat at higher altitudes. The observed ratio decreases almost monotonically from 100 km to 160 km. *Leblanc et al.* [2006] have not found any dependence of SZA on the UV doublet to Cameron band intensity ratio, though they have observed a weak dependence

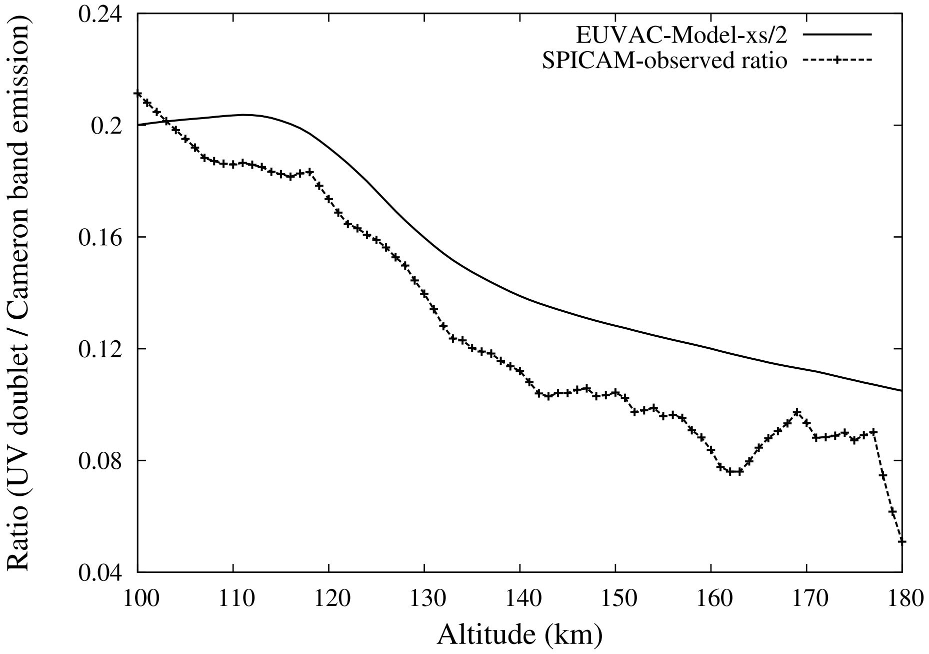

Figure 4.15: Altitude variation of intensity ratio of CO_2^+ UV doublet and CO Cameron band emissions on Mars. Model calculated ratio is shown for EUVAC solar flux model. SPICAM-observed ratio is from Figure 9(a) of *Leblanc et al.* [2006].

of this intensity ratio on the solar activity. From the observed intensity ratio profile it is clear that in upper atmosphere CO Cameron band intensity is increasing steadily compare to CO_2^+ UV doublet, which indicates source other than photon and electron impact on CO_2 is involved in the production of $CO(a^3\Pi)$ and $CO_2^+(B^2\Sigma_u^+)$. That source could be the dissociative recombination process which is sensitive to the density of CO_2^+ ion (as shown in the Figure 4.9).

Second case (Ls >130°)

As discussed earlier, due to dust storm during SPICAM observations for Ls greater than 130°, atmospheric densities were higher resulting in upward shift in the altitude of peak emission (~132.5 km for CO Cameron band emission). For Mariner 6 and 7 observations the intensity of CO Cameron band peaked at altitude of ~133 km. Mariner observations were carried out during solar maximum condition ($F10.7 \simeq 180$), whereas SPICAM observations are made during moderate solar activity condition. To model dayglow emissions for Ls >130°, the calculation is carried out for MEx orbit 1426 (26 Feb. 2005), taking model atmosphere from *Fox* [2004] for high solar activity condition. Sun-Mars distance is 1.5 AU, $F10.7 = 98$ ($F10.7A = 97$). The EUV flux at 1 AU calculated using EUVAC model remains same for first (Ls <130°) and second (Ls >130°) cases. This is because in EUVAC model the average of F10.7 and F10.7A (81-day average) is used to scale the solar flux, and in both cases average of F10.7 and F10.7A does not change (it is 97.5 in both cases), although the F10.7 flux increased by 10 unit (see Eq. 2.1

for detail). The solar EUV flux in S2K model depends not only on the F10.7, but also on other proxies (see Section 2.2) [*Tobiska*, 2004], hence flux calculated using S2K model is different on the two days.

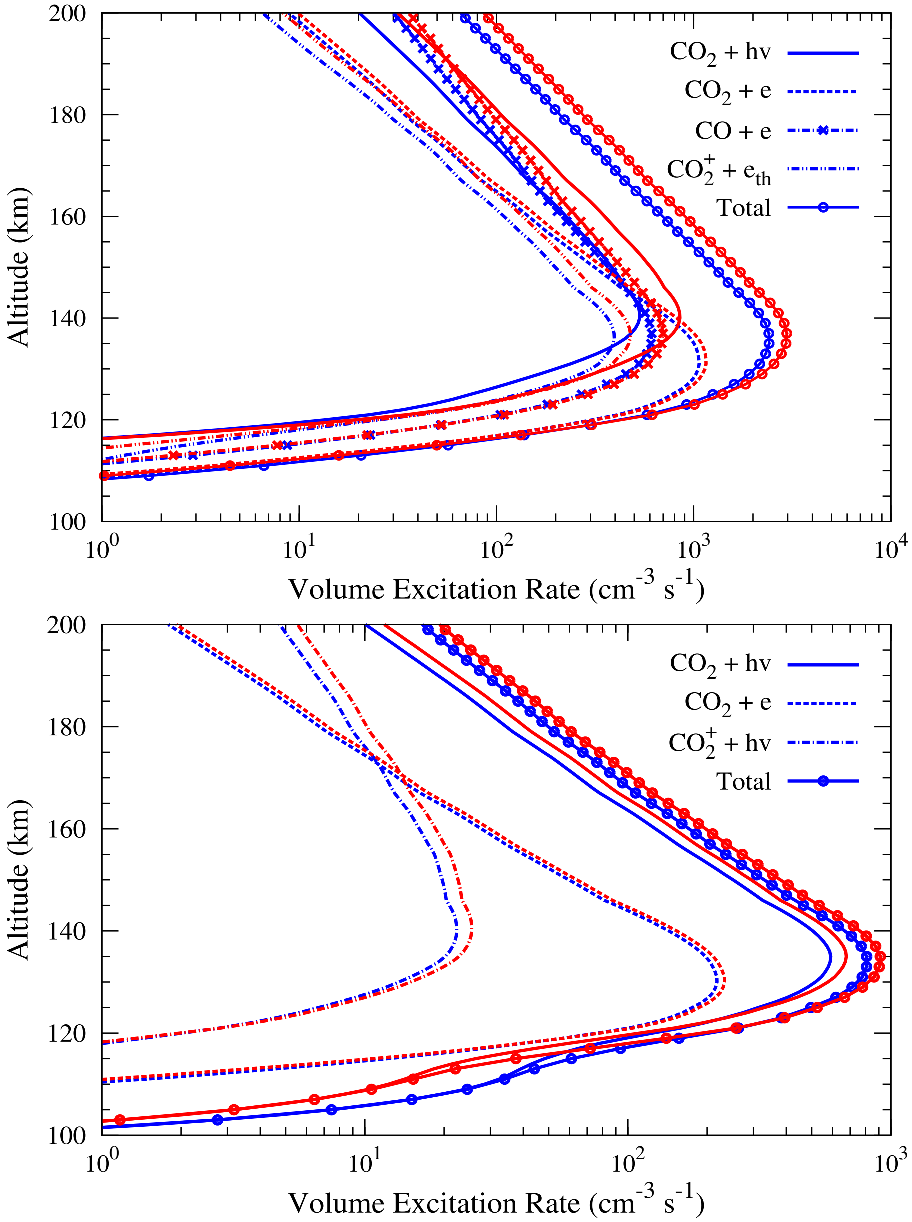

Figure 4.16: The calculated production rates of the $CO(a^3\Pi)$ (upper panel) and $CO_2^+(B^2\Sigma_u^+)$ (bottom panel) on Mars for solar longitude Ls >130°. DR stands for dissociative recombination. Blue curves show calculated production rates using EUVAC model, while red curves show them for S2K solar flux model.

Figure 4.16 (upper panel) shows the VER of $CO(a^3\Pi)$ calculated using S2K and EUVAC models. Total VER calculated using S2K is about 22% higher than that calculated using EUVAC model. Total $CO(a^3\Pi)$ production rate (calculated using EUVAC model) maximises at an altitude of 134 km with a value of about 2483 cm^{-3} s^{-1}, which is around 10 km higher than that in the first case (Ls <130°). Although

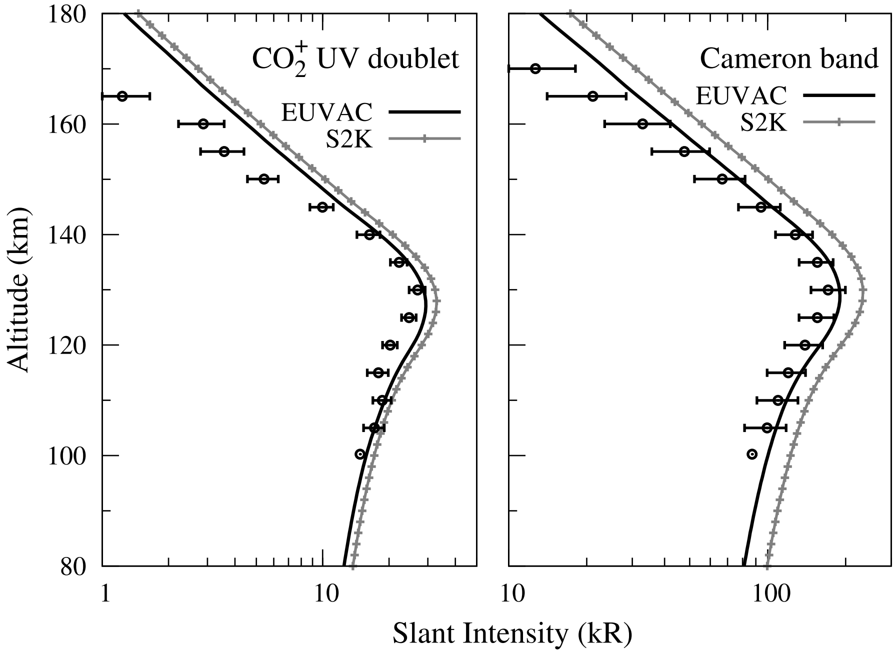

Figure 4.17: Calculated limb profiles of CO_2^+ UV doublet (left panel) and CO Cameron band emissions (right panel) on Mars for Ls >130°. Open circles with error bars represent the SPICAM-observed intensity taken from *Shematovich et al.* [2008].

production rate (2545 cm^{-3} s^{-1}) at peak altitude is higher in the first case, but at higher altitudes the rate increases faster in the second (Ls >130°) case, e.g., at 200 km, Cameron band production rate is 66 cm^{-3} s^{-1} in second case, whereas in first case it is only 3 cm^{-3} s^{-1}.

The contribution of electron impact on CO at the peak $CO(a^3\Pi)$ production is about 28% higher than that due to PD of CO_2 when the EUVAC model is used. The contribution of e-CO process in Cameron band production depends on the cross section for this process used in the model calculation. The effect of different e-CO cross sections on $CO(a^3\Pi)$ production will be discussed later. In both, first and second cases, for EUVAC model, the altitude where photodissociation of CO_2 takes over electron impact dissociation of CO_2 is slightly higher than that for S2K model.

Bottom panel of Figure 4.16 shows production rates of $CO_2^+(B^2\Sigma_u^+)$. Total excitation rate calculated using the S2K model is 12% higher than that calculated using EUVAC model. Similar to the $CO(a^3\Pi)$ production rate, $CO_2^+(B^2\Sigma_u^+)$ production rate at peak is lower than that in the first case, but at higher altitudes $CO_2^+(B^2\Sigma_u^+)$ production rate becomes higher in the second case. Table 4.3 shows the overhead intensities of CO Cameron and CO_2^+ UV doublet emissions. Contributions of photodissociation of CO_2, e-CO_2, e-CO, and CO_2^+ DR to the CO Cameron band emission are 21 (28%), 36 (31%), 28 (26%), and 14 (14%), respectively, when EUVAC (S2K) model is used.

Figure 4.17 shows the calculated limb intensity of CO_2^+ doublet and CO Cameron band emissions along with SPICAM-observed intensity (MEx orbit 1426 on 26 Feb.

2005) taken from the study of *Shematovich et al.* [2008]. Intensities calculated using S2K model are higher by ∼10–20% than those calculated using EUVAC model. The altitude of peak emission of calculated and observed intensity profiles is in good agreement (e.g., ∼128 km for Cameron band) within the uncertainties of observations and model calculations. Calculated intensities of CO Cameron band and CO_2^+ doublet emissions are in agreement with the observations.

4.3.4 Solar maximum (Mariner observations)

The observations by Mariner 6 and 7 were carried during the solar maximum conditions (July-August 1969; F10.7 = 186 at 1 AU). Mars was also at perihelion (distance between Sun and Mars was around 1.42 AU) during Mariner observations. The model calculations are carried out for the condition similar to the Mariner observation. Model atmosphere for solar maximum condition is taken from *Fox* [2004] which is shown in Figure 4.2.

Figure 4.18 (upper panel) shows the production rate of $CO(a^3\Pi)$ for higher solar activity condition, calculated using EUVAC and S2K solar flux models. Due to the higher photoelectron flux, $CO(a^3\Pi)$ production due to e-CO_2 and e-CO processes are higher when EUVAC model is used. $CO(a^3\Pi)$ production in PD of CO_2 is still 50% higher when S2K model is used, which is due to the higher EUV fluxes at longer wavelengths in the S2K model. Similar to that in the previous cases, the cross over point between photodissociation and electron impact dissociation of CO_2 forming $CO(a^3\Pi)$ occurs at higher altitude when EUVAC model is used. Bottom panel of Figure 4.18 shows the production rates of $CO_2^+(B^2\Sigma_u^+)$ molecule. The excitation rate calculated using EUVAC model is slightly higher than that calculated using S2K model. During solar minimum condition, volume production rate of $CO(a^3\Pi)$ and $CO_2^+(B^2\Sigma_u^+)$ calculated using S2K model is higher than that calculated using EUVAC model, whereas in solar maximum it is vice-versa. Except photodissociation excitation process, production rates of $CO(a^3\Pi)$ due to other mechanisms calculated using EUVAC model are higher than that calculated by using S2K model. In both, solar minimum and maximum conditions, $CO(a^3\Pi)$ production rate due to PD of CO_2 is about 50% higher, when S2K model is used.

Table 4.3 shows the overhead intensities of CO Cameron band and CO_2^+ doublet emissions. The PD of CO_2, electron impact on CO_2 and CO, and DR of CO_2^+ contribute 16 (25), 37 (32), 28 (26), and 18 (16)% to the Cameron band production when EUVAC (S2K) model is used. For solar maximum condition as well as for the second case (see Section 4.3.3), the present calculation shows that the e-CO and CO_2^+ dissociative recombination processes contribute significantly to the CO Cameron band emission. For CO_2^+ doublet emission, photoionization of CO_2 is the major contributor (70%) followed by electron impact ionization of CO_2 (25%). Contribution of fluorescence scattering by CO_2^+ is ∼5% only.

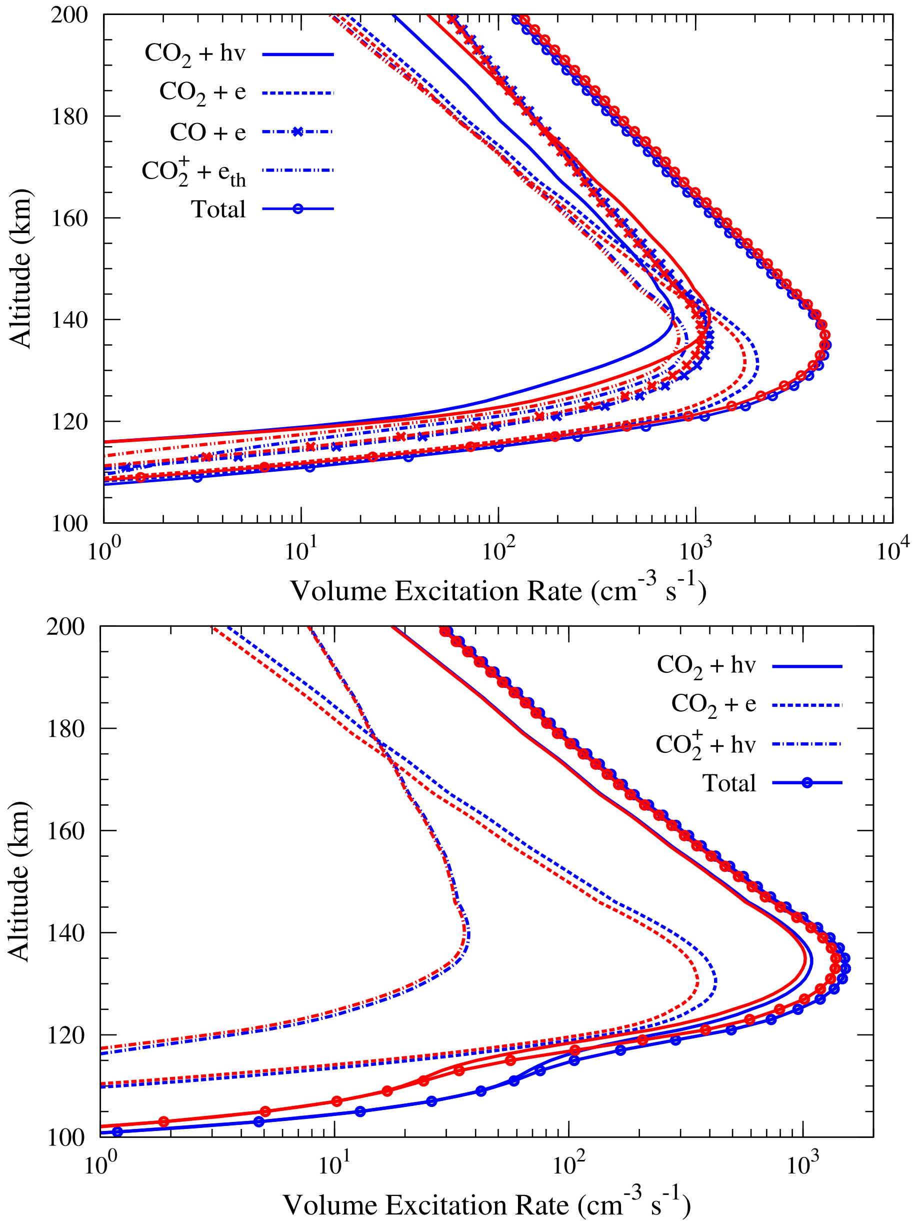

Figure 4.18: The calculated production rates of the CO($a^3\Pi$) (upper panel) and $CO_2^+(B^2\Sigma_u^+)$ (bottom panel) on Mars for solar maximum condition. DR stands for dissociative recombination. Blue curves show calculated production rates using EUVAC model, while red curves show them for S2K solar flux model.

Figure 4.19 shows model intensities of CO Cameron band and CO_2^+(B – X) UV doublet emissions calculated using both EUVAC and S2K models at SZA = 45° along with intensities observed by Mariner 6 and 7. Limb intensities measured by Mariner 6 and 7 on Mars are at SZA = 27° and 0°, and at SZA = 44° and 0°, respectively. Calculated limb intensities using EUVAC model at SZA = 0° are also shown in the Figure 4.19. Limb intensities calculated using EUVAC model are only slightly higher than those calculated using S2K model. Solar zenith angle effect is clearly visible at altitudes below 150 km, where intensity is larger and emission peak shift deeper in the

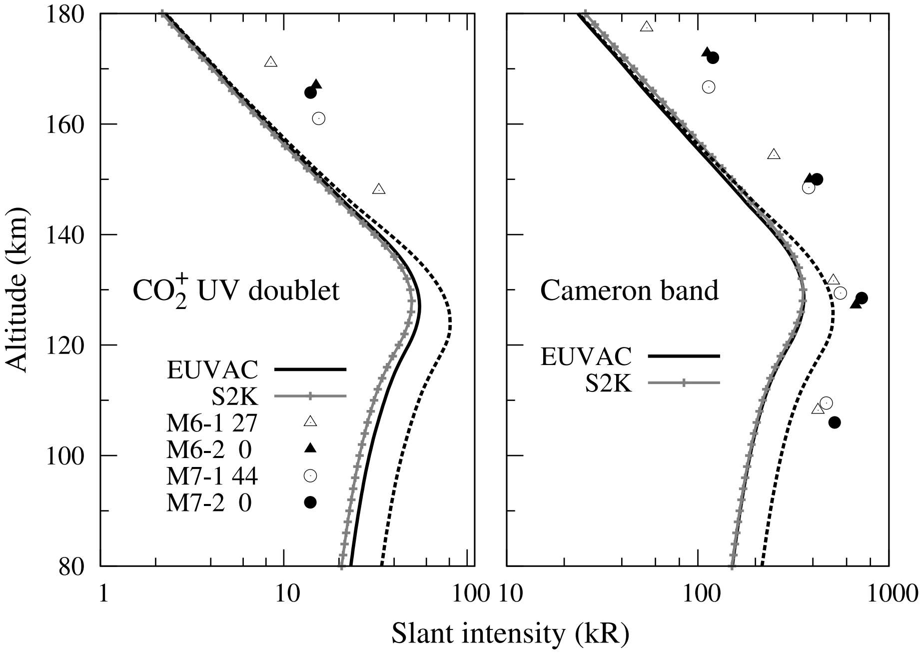

Figure 4.19: The calculated limb intensities of CO Cameron band (right panel) and CO_2^+ UV doublet (left panel) emissions on Mars for the higher solar activity condition similar to Mariner 6 and 7 flybys. Solid curves show the intensity calculated using EUVAC model at SZA = 45°. Solid curves with symbols show the limb intensity calculated using S2K model at SZA = 45°. Dashed curves show the calculated intensity (using EUVAC model) at SZA = 0°. Symbols represent the observed intensity of CO Cameron band and CO_2^+ UV doublet emissions measured by Mariner 6 and 7 [*Stewart*, 1972]. Observed values are shown for 2 orbits each of Mariner 6 (for SZA = 27 and 0°; open and solid triangle, respectively) and Mariner 7 (for SZA = 44 and 0°; open and solid circle, respectively).

atmosphere for lower SZA. Calculated intensities of CO Cameron and CO_2^+ doublet emissions are lower than the observed values. *Stewart et al.* [1972] have pointed out that due to calibration problem in Mariner 6 and 7 instrument the observed values might be higher. This may be the reason for the discrepancy between the calculated and observed brightness profiles of CO Cameron band and CO_2^+ doublet emissions.

4.3.5 CO($a^3\Pi$) density

The density of CO($a^3\Pi$) is calculated under photochemical equilibrium condition. Radiative decay is the dominant loss process of CO($a^3\Pi$), the loss from other processes is negligible [cf. *Bhardwaj and Raghuram*, 2011]. Figure 4.9 shows the calculated CO($a^3\Pi$) density using EUVAC and S2K EUV flux models for low solar activity condition. The calculated column density of CO($a^3\Pi$) molecule is 3.3×10^7 (1.3×10^8) cm^{-2} for the solar minimum condition using EUVAC (S2K) model. Except in the solar maximum condition, density of CO($a^3\Pi$) molecule calculated using S2K model is higher than that calculated using EUVAC model. During solar maximum condition, CO($a^3\Pi$) density calculated using EUVAC model is slightly higher at peak (around 5%), but at altitudes above 140 km, density calculated using S2K model becomes higher (~10% at 200 km).

The shape of the density of CO($a^3\Pi$) is similar to that of its production rate (cf. Figure 4.10) since the main loss mechanism of CO($a^3\Pi$) is radiative decay whose value is independent of altitude. Hence, the density of CO($a^3\Pi$) in the Martian atmosphere can be represented by

$$[\mathrm{CO(a^3\Pi)}] = \frac{[\mathrm{CO_2}]\,(\mathrm{K_1}+\mathrm{K_2}) + [\mathrm{CO}]\,\mathrm{K_3} + [\mathrm{CO_2^+}]\,[\mathrm{n_e}]\,\mathrm{K_4}}{\mathrm{K_5}} \tag{4.10}$$

K_1 and K_2 are photodissociation rate and electron impact dissociation rate of CO_2, respectively, K_3 is electron impact excitation rate of CO, K_4 is CO_2^+ dissociative recombination rate, K_5 is radiative decay loss frequency, and n_e is the electron density. The values of K_1 (photodissociation rate) in units of s^{-1} at the top of atmosphere in case of EUVAC (S2K) model are 7.5×10^{-8} (1.1×10^{-7}), 8.7×10^{-8} (1.3×10^{-7}), 1.03×10^{-7} (1.6×10^{-7}), and 1.5×10^{-7} (2.25×10^{-7}) in the solar minimum, first case, second case, and solar maximum, respectively.

4.3.6 Effect of e-CO cross section on CO Cameron band

The cross section of CO($a^3\Pi$) in electron impact excitation of CO plays an important role in determining the role of CO in the CO Cameron band production. To asses the effect of e-CO cross section on CO Cameron band emission, CO($a^3\Pi$) excitation rate calculations are made using the e-CO cross section (for CO($a^3\Pi$) production) measured by *LeClair et al.* [1994] (see Table 4.3).

In all cases, the contribution of electron impact excitation of CO in Cameron band emission reduces by ~50% when e-CO cross section measured by *LeClair et al.* [1994] is used in the model calculations instead of cross sections obtained by *Furlong and Newell* [1996]. In first two cases (low solar activity and 'First case') the e-CO process contributes ~10% to the CO Cameron band emission. While in later two cases (solar maximum and 'Second case') its contribution is about 20%, (roughly equal to the contribution of PD of CO_2, when EUVAC model is used).

The present calculation shows that contribution of e-CO process in CO Cameron band emission is significant for moderate and high solar activity conditions, and it is important to constrain the cross section for CO($a^3\Pi$) production in e-CO process for better understanding the role of CO in Cameron band emission.

4.4 CO Cameron band and CO_2^+ doublet emissions on Venus

Having calculated the Cameron and UV doublet dayglow emissions on Mars, the model is applied on Venus to calculate various production sources of CO Cameron and CO_2^+ UV doublet band emissions in the dayglow of Venus for low and high solar activity conditions. Results and discussion are presented in the following sections. The various input parameters in the model have been discussed in Section 4.2. The heliocentric distance of Venus is taken as 0.72 AU and solar zenith angle 45°. As mentioned in Section 4.1, the observation of CO Cameron band and CO_2^+ doublet emissions have very recently been reported for the first time in the dayglow of Venus [*Chaufray et al.*, 2012]. The model calculation is carried out for the condition similar to recent SPICAV observation and the calculated brightness profiles are compared with the observed profiles.

4.4.1 Results

4.4.1.1 Solar minimum condition

Figure 4.20 shows the calculated photoelectron flux on Venus at 150 km altitude for low (top panel) and high (bottom panel) solar activity conditions. On Venus, calculated photoelectron fluxes for low and high solar activity conditions show similar behaviour as in the case of Mars. In solar minimum condition, photoelectron flux calculated using S2K model is higher (below 70 eV) than that calculated using EUVAC model. While during solar maximum condition photoelectron flux calculated using S2K model is slightly lower than that calculated using EUVAC model. The cause for these differences in photoelectron fluxes has been discussed in Section 4.3.1.

Figure 4.21 shows the calculated volume excitation rates of $CO(a^3\Pi)$ and $CO_2^+(B^2\Sigma_u^+)$ on Venus for low solar activity condition. The altitude of peak production is at $\sim$140 km, which is $\sim$10 km higher than that on Mars (see Section 4.3). Major production of Cameron band at the peak is due to the e-CO process, whose contribution is about 44%; unlike on Mars, where electron impact on CO_2 is the major Cameron band production mechanism. Table 4.4 shows the height-integrated overhead intensity of CO Cameron band with contributions of different sources. The e-CO is the major source of Cameron band production with contribution of around 45%, followed by e-CO_2, photodissociation of CO_2, and dissociative recombination (DR) of CO_2^+, whose contributions are around 25, 23, and 7%, respectively.

Bottom panel of Figure 4.21 shows the volume production rate of $CO_2^+(B^2\Sigma_u^+)$ in the atmosphere of Venus. Photoionization of CO_2 is the dominant source (75%) of production of $CO_2^+(B^2\Sigma_u^+)$, followed by the electron impact ionization of CO_2 (21%). Con-

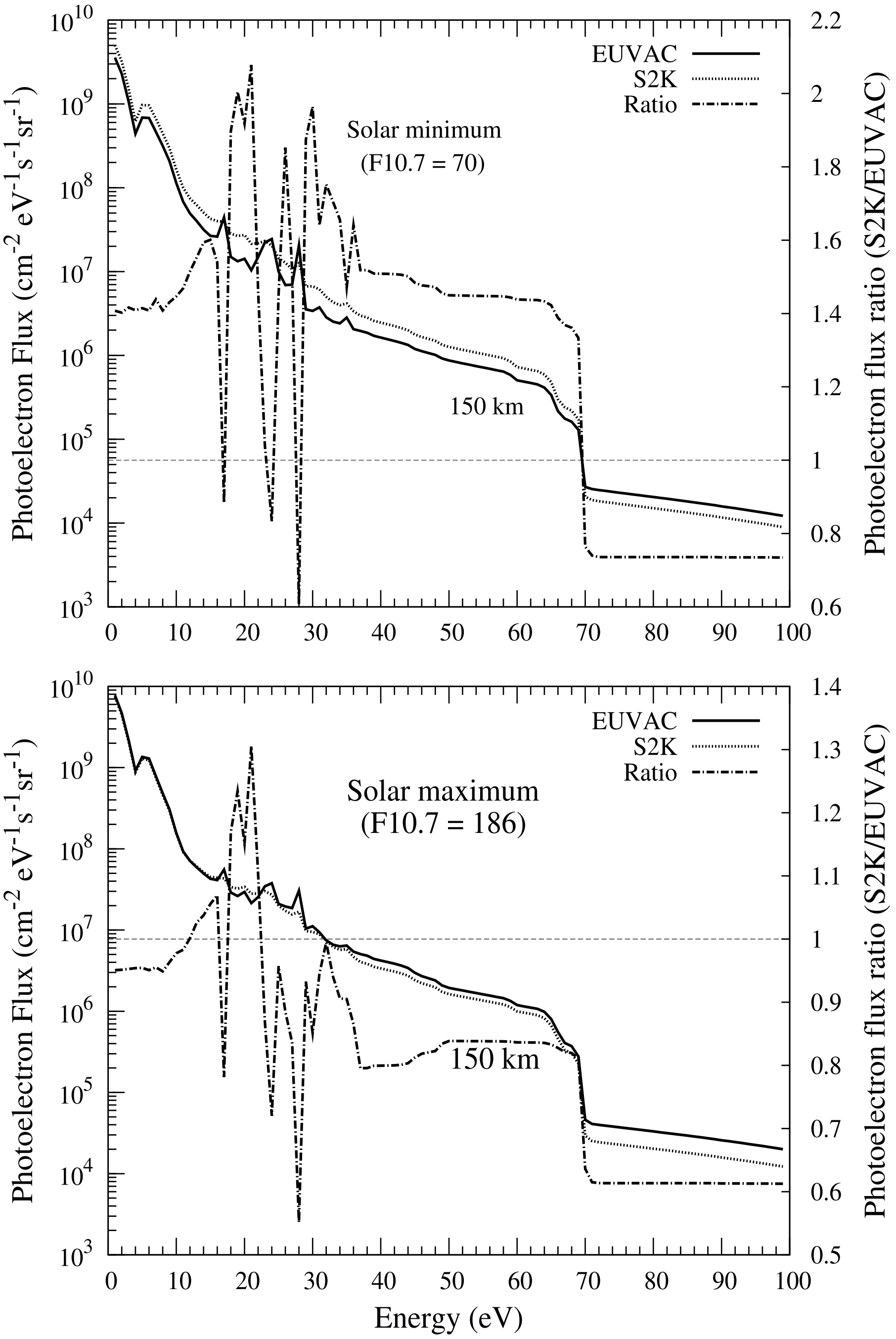

Figure 4.20: Calculated photoelectron fluxes on Venus for low (upper panel) and high (lower panel) solar activity conditions at SZA = 45°. The calculated ratio of the photoelectron flux at 150 km using the two solar flux models is also shown with magnitude on right side Y-axis. Thin dotted horizontal line depicts the S2K/EUVAC ratio = 1.

tribution of fluorescent scattering of CO_2^+ is negligible (∼4%) to the total $CO_2^+(B^2\Sigma_u^+)$ production. The height-integrated overhead intensity of CO_2^+ UV doublet band emission is given in Table 4.4. The overhead intensity of CO_2^+ UV doublet band is about a factor of 4.6 higher on Venus than that on Mars, while the intensity of Cameron band on Venus is about a factor of 6 larger compared to that on Mars (see Section 4.3).

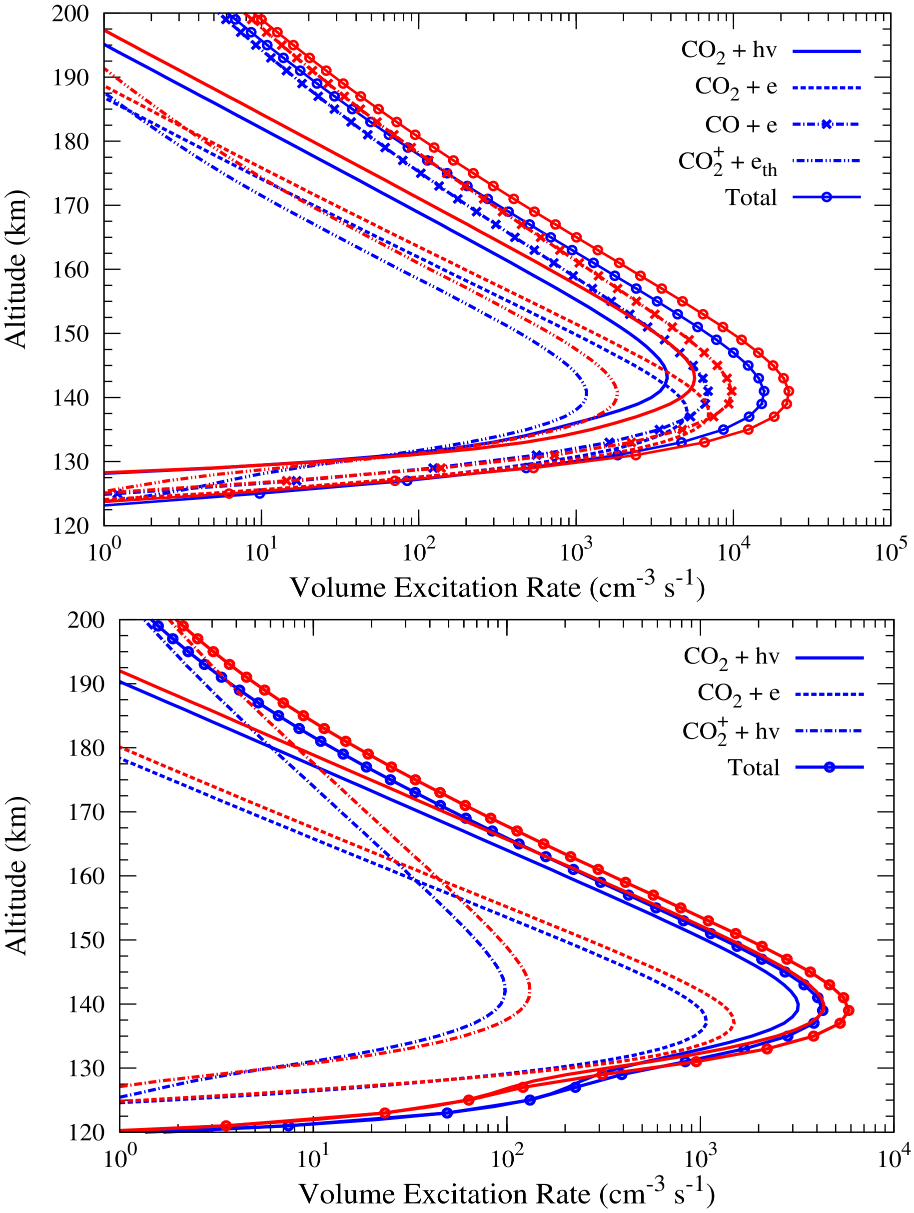

Figure 4.21: Calculated production rates of the CO($a^3\Pi$) (upper panel) and $CO_2^+(B^2\Sigma_u^+)$ (bottom panel) on Venus for low solar activity condition. Blue curves show calculated production rates using EUVAC model while red curves show them for S2K solar flux model.

Figure 4.22 shows the volume production rate of CO($a^3\Pi$) for low and high solar activity conditions calculated by using the e + CO → CO($a^3\Pi$) cross section measured by *LeClair et al.* [1994]. The height-integrated intensity of Cameron band is given in Table 4.4. The e-CO process is still the dominant source of Cameron band production, though its contribution in Cameron band production is reduced compared to the case when CO($a^3\Pi$) production cross section is taken from *Furlong and Newell* [1996].

The volume excitation rates are integrated along the line of sight to calculate the limb intensities of CO_2^+ UV doublet and CO Cameron band emissions in the dayglow

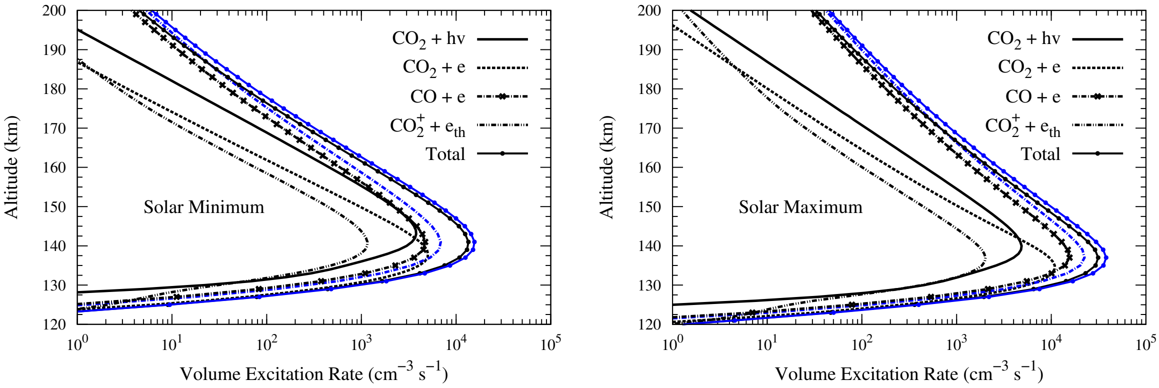

Figure 4.22: Calculated production rates of the CO($a^3\Pi$) on Venus for low (left panel) and high (right panel) solar activity conditions. Black curves show calculated production rates using EUVAC model and the CO($a^3\Pi$) cross section in e-CO process from *LeClair et al.* [1994], while blue curves show the production rate of CO($a^3\Pi$) in e-CO process and total production rate when CO($a^3\Pi$) cross section are taken from *Furlong and Newell* [1996].

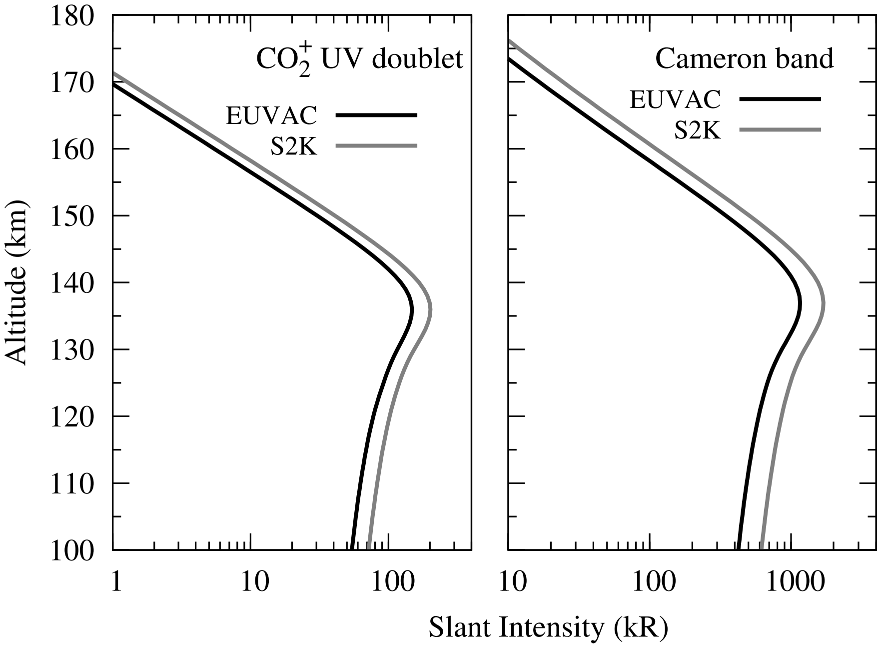

Figure 4.23: Calculated limb profiles of CO_2^+ UV doublet (left panel) and CO Cameron band (right panel) emissions on Venus for low solar activity condition.

of Venus. Figure 4.23 shows the limb intensities of CO_2^+ UV doublet and CO Cameron band emissions on Venus. The calculated limb intensity of Cameron band peaks at 137 km with a value of ∼1200 kR, while maximum limb intensity of CO_2^+ UV doublet is 183 kR at an altitude of 136 km.

Table 4.4: Overhead intensities (in kR) of CO Cameron band and CO_2^+ UV doublet emissions on Venus for low and high solar activity conditions.

Source	Intensity (kR)			
	CO Cameron Band		CO_2^+ UV doublet	
	Low SA*	High SA†	Low SA	High SA
		EUVAC		
CO_2 + hν	5.7 (6.2)§	7.5	4.8	9.5
e + CO_2	6.6 (7.8)	13.7	1.4	3
e + CO	11.4 [7.8]¶ (2.9)	36.3 [25.6]	-	-
e + CO_2^+	1.7 (2)	2.9	-	-
FS‡		-	0.2	0.3
Total	25.3 [22] (18)	60.4 [50]	6.4 {3.2}‖	12.8 {6.4}‖
		S2K		
CO_2 + hν	8.6	11.6	6.3	8.7
e + CO_2	9.2	11.7	1.9	2.5
e + CO	16.2	33.5	-	-
e + CO_2^+	2.6	2.6	-	-
FS	-	-	0.4	0.3
Total	36.3	59.4	8.6 {4.3}	11.4 {5.7}

*Low solar activity. †High solar activity. ‡Fluorensce scattering CO_2^+ + hν.

§Values in parenthesis are calculated by using the model atmosphere of *Fox and Dalgarno* [1981] and e-CO cross section from *Ajello* [1971b]. ¶Calculated values in square brackets are for the CO($a^3\Pi$) cross section of *LeClair et al.* [1994]. ‖Values in braces are calculated by taking the 50% cross over from *B* to *A* before radiating.

4.4.1.2 Solar maximum condition

Figure 4.20 (bottom panel) shows the calculated photoelectron flux on Venus at 150 km for solar maximum condition. As in the case of Mars, the photoelectron flux calculated using EUVAC model is higher than that calculated using S2K model. The solar EUV flux below 250 Å is higher in the EUVAC model which produces high energy photoelectrons. These high energy electron causes further ionization and compensate for higher EUV flux in S2K model at wavelengths >250 Å (cf. Figure 4.5).

Figure 4.24 shows the calculated volume excitation rates of CO($a^3\Pi$) (upper panel) and $CO_2^+(B^2\Sigma_u^+)$ (lower panel) for solar maximum condition. The production rate of Cameron band attains a maximum value of 3.8×10^4 cm^{-3} s^{-1} at an altitude of 137 km. The height-integrated overhead intensity is presented in Table 4.4. Electron impact on CO is by far the dominant mechanism of Cameron band production contributing about 60%, followed by electron impact on CO_2 (23%), photodissociation of CO_2 (12%), and dissociative recombination of CO_2^+ (4%). The CO($a^3\Pi$) production rate calculated using e-CO cross section from *LeClair et al.* [1994] is shown in Figure 4.22 and corresponding

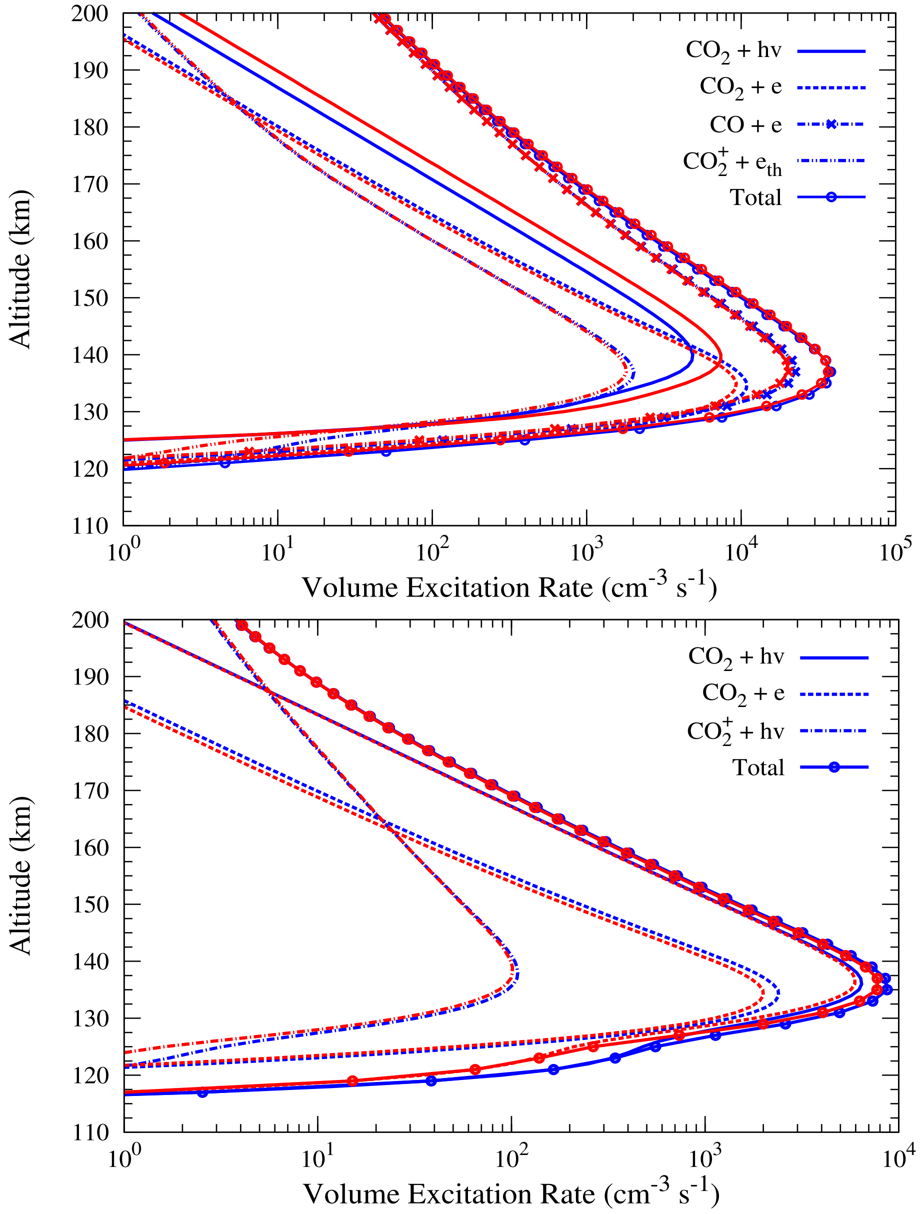

Figure 4.24: Calculated production rates of the CO($a^3\Pi$) (upper panel) and $CO_2^+(B^2\Sigma_u^+)$ (bottom panel) for high solar activity condition. Blue curves show calculated production rates using EUVAC model while red curves show them for S2K solar flux model.

height-integrating intensities in Table 4.4.

For the $CO_2^+(B^2\Sigma_u^+)$, maximum production rate occurs at an altitude of 135 km with a value of $\sim 8.7 \times 10^3$ cm^{-3} s^{-1}. The overhead intensity of CO_2^+ UV doublet band is presented in Table 4.4. The photodissociation of CO_2 is the dominant (74%) production source of UV doublet band emission followed by electron impact on CO_2 (23%) and fluorescent scattering by CO_2^+ (3%). Figure 4.25 shows the calculated line of sight intensities of CO Cameron band and CO_2^+ UV doublet emissions. The intensity of Cameron band peaks near 135 km with a value of 2700 kR, while the intensity of UV doublet band attains a maximum value of around 350 kR at an altitude of 132 km.

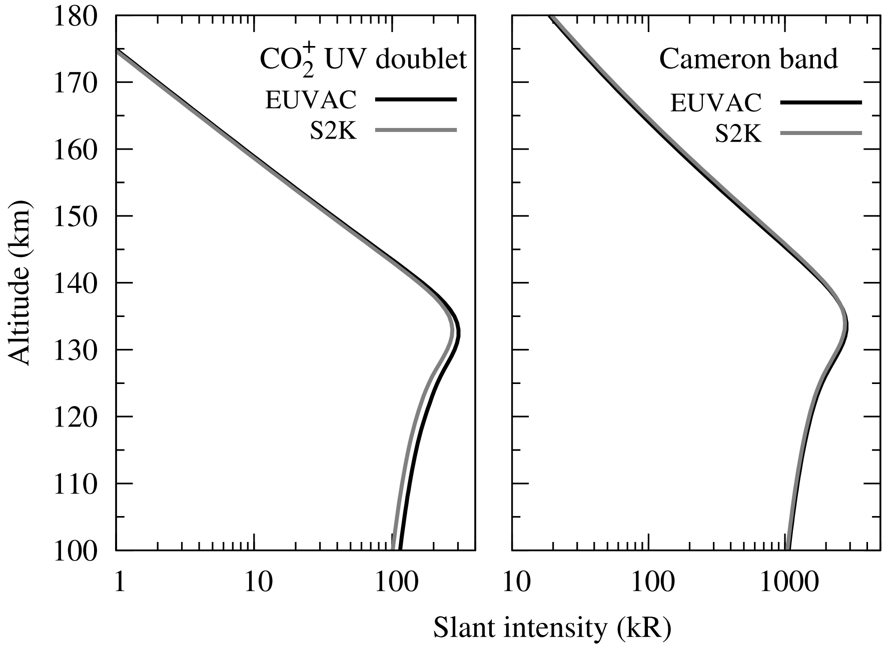

Figure 4.25: Calculated limb profiles of CO_2^+ UV doublet (left panel) and CO Cameron band (right panel) emissions on Venus for high solar activity condition.

Compared to Mars, the peak intensity of Cameron band and UV doublet emission on Venus is 8 and 5 times, respectively, larger.

4.4.2 Discussion

The present model calculation shows that the electron impact on CO is the dominant source of CO Cameron band production in the atmosphere of Venus for low, moderate, and high solar activity conditions using the CO($a^3\Pi$) cross sections of *Bhardwaj and Jain* [2009] and *Furlong and Newell* [1996] in electron impact on CO_2 and CO, respectively. For solar minimum condition *Fox and Dalgarno* [1981] and *Gronoff et al.* [2008] reported e-CO_2 process to be the major production source of Cameron band. *Gronoff et al.* [2008] have calculated CO Cameron band intensity of 17.3 kR; with 7 kR from electron impact on CO_2, 5.3 kR from PD of CO_2, 4 kR from electron impact on CO, and 1 kR from DR of CO_2^+. *Gronoff et al.* [2008] have used the cross section of *Ajello* [1971a] for electron impact on CO, while in the present study the cross section of *Furlong and Newell* [1996] has been used. Using the cross section of *Ajello* [1971a], our model calculated overhead Cameron band intensity is 18.6 kR, with contributions from PD of CO_2, e-CO_2, e-CO, and DR of CO_2^+ processes being 5.6, 6.7, 4.6, and 1.7 kR, respectively. The model calculated total CO Cameron band intensity is in good agreement with that of *Gronoff et al.* [2008]. *Fox and Dalgarno* [1981] reported the Cameron band intensity of about 20 kR, with contribution of ~25% from DR of CO_2^+ and 6% from e-CO process. The present calculation, as well as that of *Gronoff et al.* [2008], show that the contribution of DR of CO_2^+ (which depends on electron density and temperature) is smallest among the processes considered in the model (see Table 4.4). *Fox and Bougher* [1991] suggested that the source of DR was overestimated in the pre-Pioneer Venus model of *Fox and Dalgarno* [1981] because of low density of atomic oxygen, which led to larger densities of CO_2^+ ion. The mixing ratio of CO was lower in the model atmosphere used by *Fox and Dalgarno* [1981], whereas in the present calculation, as well as in the model of *Gronoff et al.* [2008], the VTS3 model atmosphere is used, which has larger CO mixing ratio. To evaluate the effect of low CO mixing ratio, the model calculation is also carried out by taking model atmosphere of *Fox and Dalgarno* [1981]; the results are shown in Table 4.4. The Cameron band intensity is 18 kR when the model atmosphere of *Fox and Dalgarno* [1981] and e-CO cross section of *Ajello* [1971a] are used, which is in agreement with the model result of *Fox and Dalgarno* [1981]. However, in the present calculation the contribution of DR is about 11%, which is lower than that reported by *Fox and Dalgarno* [1981]; this might be due to the difference in DR rate coefficient for $CO(a^3\Pi)$ production in the two calculations.

For solar maximum condition, *Fox and Bougher* [1991] have reported total Cameron band intensity of 57 kR, which is in agreement with the calculated value of 60 kR in the present study. However, the contribution of individual processes is different in the two studies. In the present study the e-CO is the dominant process; whereas in the model calculation of *Fox and Bougher* [1991] the photon and electron impact on CO_2 played the dominant role with contribution of about 36% from each, while the contributions of electron impact on CO and DR of CO_2^+ were 20 and 8%, respectively.

The present study shows that the contribution of e-CO process in $CO(a^3\Pi)$ production is directly related to the cross section used in the calculation. For $CO(a^3\Pi)$ cross section of *LeClair et al.* [1994], the model calculations demonstrate that the e-CO process is the dominant source of CO Cameron band (see Figure 4.22 and Table 4.4). Thus, the role of electron impact on CO in the Cameron band production might have been underestimated in the earlier calculations [*Fox and Dalgarno*, 1981; *Gronoff et al.*, 2008] due to the choice of e-CO cross section for $CO(a^3\Pi)$ production.

4.4.2.1 Effect of solar EUV flux models

During the solar minimum condition, the CO Cameron band excitation rate calculated using the S2K model is about 45% larger than that calculated using the EUVAC model, while the production in the photodissociation of CO_2 is about 50% higher when S2K model is used. However, the altitude of peak production is same for both solar EUV flux models (see Figure 4.21). The limb intensities calculated using the S2K model are about 40% larger than those calculated using the EUVAC model (see Figure 4.23).

For solar maximum condition, the calculated intensity of CO Cameron and CO_2^+ UV doublet band emissions using the EUVAC model is about 2% and 10%, respectively, higher than those calculated using the S2K model. This is due to the higher solar EUV flux in EUVAC model at wavelengths $\leq$ 250 Å that produces energetic photoelectrons which further ionize the medium and compensate for the higher photoionization by solar EUV flux at wavelengths > 250 Å in the S2K model. Similar variation in the emission intensities due to the change in EUV flux models for solar minimum and maximum conditions have been found on Mars (see Section 4.3).

For both, low and high solar activity conditions, the contribution of photodissociation of CO_2 to the Cameron band production is 50% higher when the S2K solar flux model is used. This is because of an order of magnitude higher solar EUV flux in the 1000–1050 Å bin in the S2K model compared to that in the EUVAC model. Solar EUV flux in the 1000-1050 Å bin does not significantly contribute to the photoionization, but significantly affects the photodissociation of CO_2: thus affecting the Cameron band production in the photodissociation of CO_2.

For solar maximum condition, the calculated intensities using the EUVAC model are about two times higher than those calculated for solar minimum. When S2K model is used, the calculated intensities of UV doublet and Cameron band emissions are 1.3 and 1.6, respectively, times larger in high solar activity that those in low solar activity condition. For the EUVAC solar flux model, the variation in contribution of electron impact processes are more prominent for change in solar activity from low to high due to a change of more than a factor of 2 in the solar EUV flux below 250 Å, whereas solar EUV flux in the S2K model varies by less than a factor of 2 from solar minimum to maximum condition (see Figure 4.5).

4.4.3 Comparison of model calculations with SPICAV observation

Very recently *Chaufray et al.* [2012] have reported the first Venusian dayglow observation of CO Cameron band and CO_2^+ UV doublet emissions using the SPICAV aboard Venus Express. The SPICAV observations were made between October and December 2011, with solar zenith angles vary between 20° and 30°. We have carried out calculation for the similar condition as reported by *Chaufray et al.* [2012] by taking SZA of 25° and VTS3 model atmosphere for 15 November 2011 (F10.7 = 148 and F10.7-81 day average = 144). Figure 4.26 shows the calculated CO Cameron band and CO_2^+ UV doublet brightness profiles along with the SPICAV-observed profiles taken from *Chaufray et al.* [2012].

The model calculated brightness of CO Cameron band peaks at 134 km with a value of 3200 kR. The SPICAV-observed peak of Cameron band brightness is situated at 137±1.5 km and the magnitude of limb intensity at this altitude is ~2000 kR [*Chaufray et al.*, 2012]. The calculated intensity at the peak is about 50% higher than the observed value. When the CO($a^3\Pi$) production cross section in e-CO collision of *LeClair et al.* [1994] is used, the limb intensity of Cameron band at the peak altitude is 2700 kR. As mentioned

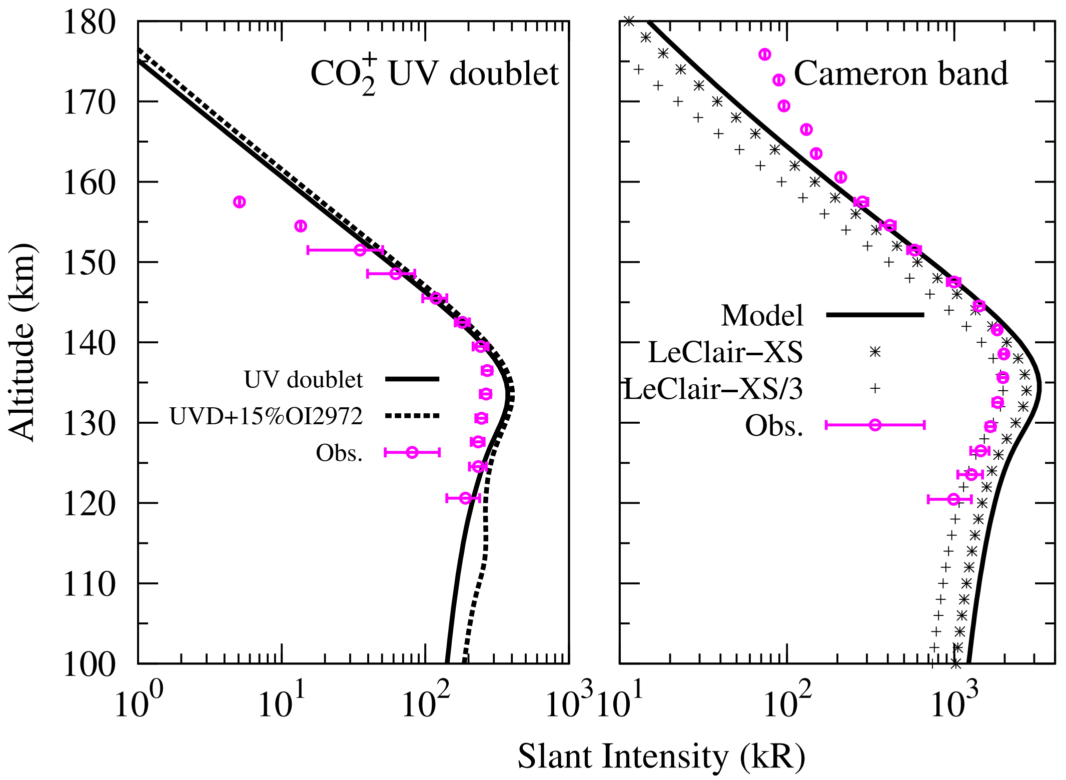

Figure 4.26: The calculated (using EUVAC solar flux model) limb profiles of CO_2^+ UV doublet and CO Cameron band emissions on Venus for conditions similar to SPICAV observations (F10.7 = 144 and SZA = 25°) along with observed profiles taken from *Chaufray et al.* [2012]. Limb intensities of CO Cameron band, calculated by using the actual and corrected cross sections of $a^3\Pi$ state in e-CO process measured by *LeClair et al.* [1994] are also shown. CO_2^+ doublet emission intensity with 15% contribution from OI 2972 Å emission is also shown (UVD+15%OI294).

earlier, the cross section obtained by *LeClair et al.* [1994] might be overestimated by a factor of 3 (see Section 4.2). On deceasing the *LeClair et al.*'s measured cross section by a factor of 3, the calculated CO Cameron band brightness at the peak is ∼2000 kR. For CO_2^+ ultraviolet doublet emission, maximum limb intensity of ∼370 kR is obtained at an altitude of 133 km, which is about 30% higher than the SPICAV-observed value of 270 kR (at 135.5 ± 2.5 km) [*Chaufray et al.*, 2012].

Chaufray et al. [2012] have derived the overhead intensity of 25.3 kR and 3.2 kR for Cameron band and CO_2^+ UV doublet emissions, respectively, by converting the limb intensity to zenith brightness above sub-solar point. These values are significantly lower than our model calculated hight-integrated overhead intensities of of 70 and 8 kR (at SZA = 25°) for Cameron band and CO_2^+ UV doublet emissions, respectively. This discrepancy in the calculated and observation-derived overhead intensity is significant and it is difficult to comment on the cause for this difference at present, since it is not clear to us the methodology used by *Chaufray et al.* [2012] for calculating zenith intensity.

The calculated altitude of peak brightness of both CO Cameron band and CO_2^+ UV doublet emissions is lower by ∼5 km than the observation. The difference in peak altitude of observed and calculated emissions shows that the neutral density in Venus model atmosphere is lower in the present calculation. Recent, Venus Thermospheric General Circulation Model (VTGCM) also suggests that VTS3 empirical model is inadequate to properly represent lower thermosphere thermal structure [*Brecht and Bougher*, 2012]. Density profile of CO_2 calculated by VTGCM differs from that calculated by VTS3 model above 100 km.

The profile of observed CO_2^+ UV doublet emission may contain small portion of OI 2972 Å emission [*Chaufray et al.*, 2012], which makes the shape of observed profile different than the calculated emission profile at lower altitudes. The calculated CO_2^+ UV doublet emission profile with 15% OI 2972 Å emission is also shown in Figure 4.26.

A more detailed study of these emissions with VTGCM needs to be carried out to understand the recent SPICAV observations.

4.5 CO(a', d, e) triplet emissions on Mars and Venus

The photodissociation of CO_2 below 1080 Å leads to the formation of CO($a^3\Pi$), but at photon energies greater than 12.4 eV (wavelength $<$ 1000 Å) other channels open up. The photodissociation of CO_2 in the 10.3-13.8 eV (1200–900 Å) region leads to the channel CO* + O(^{3}P), where CO* corresponds to four triplet levels $a^3\Pi$, $a'^3\Sigma^+$, $d^3\Delta$, and $e^3\Sigma^-$ (see Figure 4.1). Emissions arising due to the transition from the a', d, and e states down to $a^3\Pi$ state are called Asundi, Triplet, and Herman bands, respectively. *Conway* [1981] has reported that the CO Cameron band spectra observed by Mariner showed a very hot rotational distribution. His analysis showed a bimodal fit with temperatures 1600 K and 10,000 K. Analysis of SPICAM/MEx data also showed similar hot distribution [*Kalogerakis et al.*, 2012]. Recently, *Kalogerakis et al.* [2012] studied the EUV photodissociation of CO_2 in laboratory and found strong emissions in the visible and near-IR region arising from the CO(a', d, e) triplet states. They attributed these triplet band emissions to be the primary source for the CO(a–X) Cameron bands. *Kalogerakis et al.* concluded that most of the observed Cameron band arising from photodissociation of CO_2 is preceded by the cascading from the CO(a', d, e) triplet states, and predicted that the visible and near-IR (6000 to >14000 Å) emissions from these triplet states is of the same magnitude as the CO Cameron band.

Based on the study of *Kalogerakis et al.* [2012], one can predict the lower limit of Asundi, triplet, and Herman bands in the atmospheres of Mars and Venus, if only photodissociation of CO_2 is considered as the primary source of these CO(a', d, e) triplet states. Results from the present study show that for solar minimum condition the contribution of photodissociation of CO_2 to the CO Cameron band production on Mars and Venus is 1.2 and 5.7 kR, respectively (see Tables 4.3 and 4.4). Thus, the CO(a', d, e)

triplet band emissions would be about 1.2 and 5.7 kR on Mars and Venus, respectively, spread over the 6000 to >14000 Å range. The Asundi $a' - a$ (5-0) band at 7830 Å is about 10% of the total triplet band emissions [*Kalogerakis et al.*, 2012], thus its overhead intensity on Mars and Venus would be ∼120 and 570 R, respectively. Similarly, during solar maximum condition the intensity of CO(a', d, e) triplet and Asundi $a' - a$ (5-0) bands on Mars (Venus) would be 3.1 (7.5) kR and 310 (750) R, respectively. The maximum fraction of Cameron band originate from electron impact on CO_2 and CO on Mars and Venus and these processes do not exclude similar CO product [*Kalogerakis et al.*, 2012]. The magnitude of CO(a', d, e) triplet bands on Venus reported above would be a lower limit: an upper limit could be larger by a factor of 2 to 4.

4.6 Summary and conclusion

The present study deals with the calculations of CO Cameron band and CO_2^+ doublet ultraviolet emissions in the dayglow of Mars and Venus and the impact of solar EUV flux on the calculated intensities. Emission rates of CO Cameron band and CO_2^+ UV doublet emissions due to photon and electron impact on CO_2 have been calculated using EUVAC and S2K solar EUV flux models. The excitation rates of CO($a^3\Pi$) and $CO_2^+(B^2\Sigma_u^+)$ are height-integrated to calculate the overhead intensity and along the line of sight to obtain the limb intensities. The intensities of CO(a', d, e) triplet band emissions on Mars and Venus are predicted. Calculated limb intensities on Mars are compared with the SPICAM and UV spectrometer/Mariner observed intensities. The calculated brightness profiles of CO Cameron band and CO_2^+ doublet emissions are in agreement with the SPICAM-observations, however, in solar maximum condition the calculated intensities are lower than that observed by Mariner 6 and 7 ultraviolet spectrometers.

On Venus, the calculated brightness of CO Cameron band and CO_2^+ doublet emissions is compared with the recent SPICAV-observation. The calculated intensity of CO Cameron band at the peak altitude is about 50% higher than the observation. However, when the CO($a^3\Pi$) production cross section in e-CO collision measured by *LeClair et al.* [1994] is used in the model calculation this difference reduces to 30%, and with a correction by a factor of 3 in cross section, the magnitude of calculated brightness at peak is in good agreement with the observation. The calculated limb intensity of CO_2^+ doublet emission is 30% higher than the SPICAV-observation. The calculated overhead intensities of the two emissions is significantly higher than those derived from the observations. Presently, it is difficult to comment on this discrepancy and further investigation is needed. The model calculated peak altitude of CO Cameron band and CO_2^+ UV doublet emission profiles is lower than that observed by SPICAV, indicating lower neutral density in the VTS3 model atmosphere for Venus.

Following conclusion can be drawn from the present study:

1. On Mars, photoelectron impact on CO_2 is the dominant process for the production of Cameron band. The PD of CO_2 is the second most important source of Cameron band in low solar activity condition, while photoelectron impact on CO becomes an important processes in moderate and high solar activity.

2. On Venus, electron impact on CO is the major process of Cameron band production, followed by photoelectron impact on CO_2 and PD of CO_2. Thus, the situation on Venus is quite different than that on Mars.

3. For CO_2^+ UV doublet emissions on Mars and Venus, photoionization of CO_2 is the dominant processm followed by electron impact on CO_2.

4. Generally, solar EUV fluxes in bands are higher in S2K model compared to EUVAC model except at few bands at shorter wavelength range (< 250 Å). Solar EUV fluxes at longer wavelengths are higher in the S2K model, specially in the 1000-1050 Å bin, where the flux is around an order of magnitude higher than the corresponding flux in the EUVAC model. Solar EUV flux at lines is smaller in the S2K model compared to that in the EUVAC model.

5. Due to higher EUV flux at lines in the EUVAC model, the peaks in the 20–30 eV range in the photoelectron flux are more prominent when EUVAC model is used.

6. During the high solar activity condition, calculated photoelectron fluxes are higher for EUVAC model due to higher EUV fluxes below 250 Å in the EUVAC model. Hence, intensities calculated using the EUVAC model are higher by 5–10% than those calculated using the S2K model.

7. During both solar conditions, the Cameron band production due to photodissociative excitation of CO_2 is about 50% higher when the S2K solar EUV flux model is used.

8. The altitude of peak production rate of Cameron and CO_2^+ UV doublet bands is independent of the solar EUV flux model used in the calculations.

The present study clearly demonstrates that the cross section of $a^3\Pi$ state in e-CO process is important in modelling CO Cameron band emission on Mars and Venus. The contribution of e-CO process in CO Cameron band production also depends on the density of CO in the atmosphere. Hence, it is difficult to constrain the former without fixing the later. However, the calculations carried out in this chapter suggest that the role of electron impact on CO in Cameron band production on Mars and Venus needs to be reconsidered.

Recently, SPICAM/Mars Express observed N_2 VK band emission on Mars. Since, N_2 is second most abundant gas on Venus, the N_2 triplet band features are expected on Venus also. The application of AYS to the calculation of N_2 triplet dayglow band emissions on Mars and Venus is presented in the next Chapter.

Chapter 5

N_2 triplet band emissions on Mars and Venus

5.1 Introduction

Emissions from excited states of N_2 have been studied extensively in the terrestrial airglow and aurora [e.g., *Sharp*, 1971; *Conway and Christensen*, 1985; *Meier*, 1991; *Morrill and Benesch*, 1996; *Broadfoot et al.*, 1997; *Campbell et al.*, 2006; *Slanger et al.*, 2008]. But the absence of any emission feature of N_2 during Mariner observations of Mars [*Barth et al.*, 1971] surprised the planetary scientists who attributed it to the low fractional abundance by volume of molecular nitrogen on Mars [*Dalgarno and McElroy*, 1970]. On Venus, solar scattering from haze and cloud makes it very difficult to observe these emissions by Pioneer Venus Orbiter Ultraviolet Spectrometer (PVOUVS). Earlier, N_2 emissions on Mars and Venus were predicted by Fox and co-workers [*Fox et al.*, 1977; *Fox and Dalgarno*, 1979a, 1981], who suggested that a high resolution UV spectrometer could detect the N_2 UV emissions on Mars. *Fox and Dalgarno* [1979a] and *Fox and Dalgarno* [1981] have predicted the intensity of various N_2 triplet state emissions (Vegard-Kaplan, First positive, Second Positive, $W-B$), along with LBH band of N_2 and First Negative band of N_2^+ on Mars and Venus. In the terrestrial atmosphere emissions from Vegard-Kaplan (VK) bands are weak due to efficient quenching by atomic oxygen, but CO_2 is not that good at quenching VK bands [*Fox and Dalgarno*, 1979a; *Dreyer et al.*, 1974], so the intensity of these band should be appreciable in the dayglow of Mars and Venus.

All transitions between the triplet states of N_2 and the ground state are spin forbidden; therefore, the excitation of these states is primarily due to the electron impact on N_2. Thus, these emissions provide vital information about the N_2 density on planet. Since N_2 constitutes a small fraction ($\sim$3%) of the atmospheres of Mars and Venus, a large uncertainty persist in determining the N_2 concentration in these planets. Emissions from N_2 triplet states, thus, can be a useful tool to infer the N_2 density in the atmospheres of Mars and Venus. Apart from that, the width and shape of VK bands are quite sensitive to the rotational temperature, making them a useful monitor of the neutral temperature of the upper atmosphere [*Broadfoot et al.*, 1997].

In this Chapter a detailed model for the production of the N_2 triplet states in the atmospheres of Mars and Venus is presented. A brief introduction of N_2 triplet states is given in Section 5.2. The degradation of photoelectrons produced due to the photon impact in the atmosphere of Mars and Venus is based on Monte Carlo model which is described in Chapter 3. The calculated photoelectron flux is employed to calculate the volume excitation rates of N_2 triplet states, which is given in Section 5.3.3. The calculated line of sight intensity of N_2 VK band is presented in Section 5.3.4. The calculated intensity in the model depend on various input parameters. The effect of various input parameters on the N_2 triplet band emission on Mars is discussed in Section 5.3.6. Having calculated the production of N_2 triplet state in the upper atmosphere of Mars, the density of N_2 triplet state and their subsequent emissions in the dayglow of Venus is calculated for both solar minimum and maximum conditions in Section 5.4. The similar model is applied to the atmosphere of Titan to explain the first observations of N_2 VK bands by Ultraviolet Imaging Spectrograph (UVIS) instrument on-board Cassini in Section 5.5.

5.2 N_2 triplet states

The N_2 triplet band emissions span a wide spectrum of electromagnetic radiation covering EUV-FUV-MUV, visible, and infrared [*Jain and Bhardwaj*, 2011; *Bhardwaj and Jain*, 2012a]. Major emissions in N_2 VK band lie in the wavelength range 200–400 nm, and a few significant emissions in the visible. N_2 triplet First Positive ($B \rightarrow A$), Wu-Benesch ($W \rightarrow B$), and $B' \rightarrow B$ bands have prominent emissions in the infrared region. Thus, beside observations of Titan's dayglow by the Cassini UVIS in EUV and FUV region, the Cassini Visual and Infrared Mapping Spectrometer (VIMS), which has a wide spectral range 300–5100 nm [*Brown et al.*, 2004] and Imagining Science Subsystem (ISS, 250–1100 nm) [*Porco et al.*, 2004], might be able to detect some of the bright emissions of N_2 triplet bands in the MUV, visible, and infrared wavelengths that are predicted by present calculation.

Figure 5.1 shows schematic diagram of N_2 triplet states energy level with excitation and subsequent cascading processes. The transition from the ground state ($X^1\Sigma_g^+$) to the $A^3\Sigma_u^+$ state is dipole forbidden, so photoelectron impact is the primary excitation source for this state. In addition to the direct excitation from the ground state, cascade from higher triplet states C, B, W, and B' are also important. All excitations of higher triplet states will eventually cascade into the $A^3\Sigma_u^+$ state [*Cartwright et al.*, 1971; *Cartwright*, 1978]. The higher lying states C, W, and B' populate the B state, which in turn radiates to the A state. Inter-state cascading $B^3\Pi_g \rightleftharpoons A^3\Sigma_u^+$ and $B^3\Pi_g \rightleftharpoons W^3\Delta_u$ is important in populating the B state [*Cartwright et al.*, 1971; *Cartwright*, 1978].

Direct excitation of the $\nu' = 0$ vibrational level of the $A^3\Sigma_u^+$ state by electron impact is extremely small, because Frank-Condon factor to the $\nu'' = 0$ level of the ground

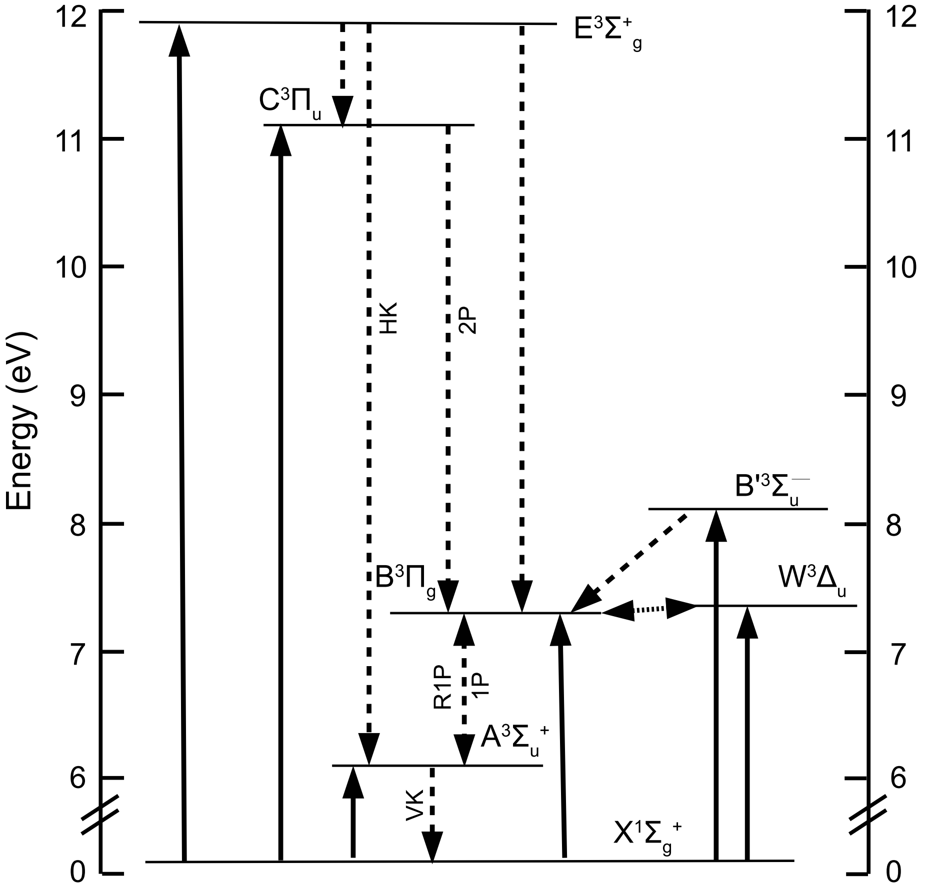

Figure 5.1: Energy level diagram for the excitation of N_2 triplet states and subsequent inter-state cascading processes. Solid arrows show the excitation from ground state to higher states, and dashed arrows represent the transitions between different states (HK: Herman-Kaplan; 1P: First Positive; R1P: Reverse First Positive; 2P: Second Positive; VK: Vegard-Kaplan band system). Excitation thresholds for all the triplet states are given in Table 5.1.

electronic state, q_{00}, is only 9.77×10^{-4} [*Gilmore et al.*, 1992; *Piper*, 1993]. Contributions to $\nu' = 0$ level of A state come from the higher states cascading. The various triplet state transitions, viz., $E \rightarrow B$, $E \rightarrow C$, $E \rightarrow A$, $B \rightarrow W$, and reverse first positive $A \rightarrow B$ are included in the present calculation. The effect of reverse first positive transition is important in populating the lower vibrational levels of B state, which in turn populate the lower vibrational levels of the A state [*Sharp*, 1971; *Cartwright et al.*, 1971; *Cartwright*, 1978]. Thus, to calculate the production rate of any vibrational level of triplet state of N_2, one must take into account direct excitation as well as inter-state cascading effects.

5.3 N_2 triplet band emissions on Mars

Recent observations by SPICAM on-board MEx have, for the first time, observed N_2 emissions in the dayglow of Mars [*Leblanc et al.*, 2006, 2007]. Figure 5.2 shows a typical spectra of Martian dayglow observed by SPICAM. The signatures of N_2 VK band are present above 2400 Å. The main emissions observed are N_2 VK (0, 5) at 2605 Å, (0, 6) at 2762 Å, and (0, 7) at 2937 Å, emissions, which originate from triplet $A^3\Sigma_u^+$ state of excited N_2 molecule. The overhead intensity of the N_2 VK (0, 6) band derived from the SPICAM observation is found to be ~3 times smaller than the intensity calculated by *Fox and Dalgarno* [1979a].

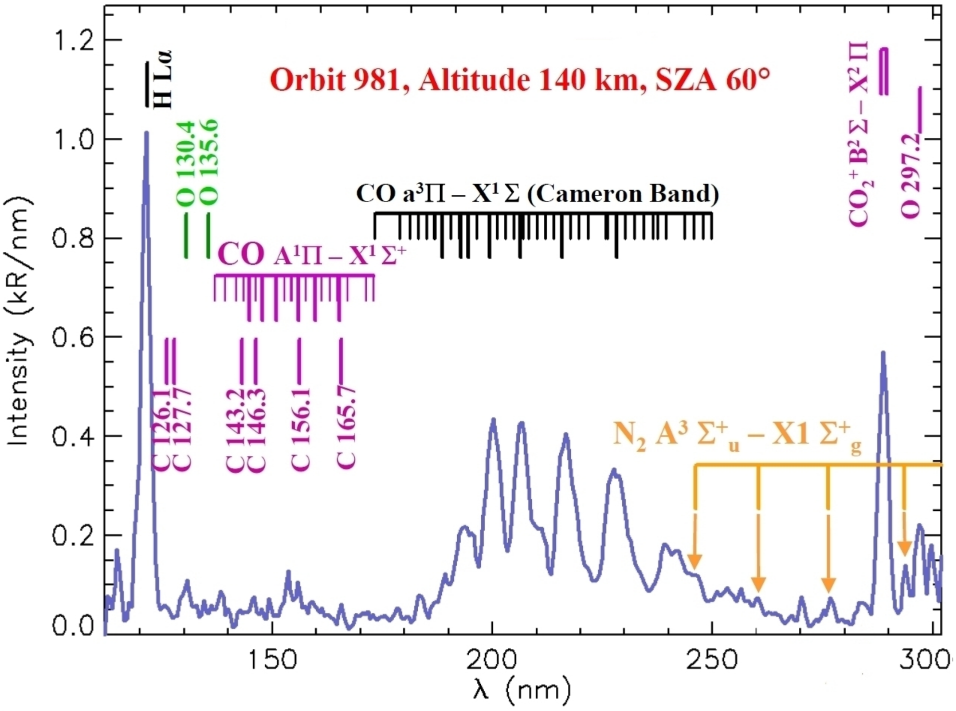

Figure 5.2: A typical spectra of dayglow emission on Mars observed by SPICAM. Image credit *Leblanc et al.* [2006].

There have been several measurements of electron impact cross sections of triplet states of N_2 since *Fox and Dalgarno* [1979a] carried out their calculations. With new cross sections and updated molecular parameters (transition probability and Franck-Condon factor) a model of N_2 dayglow emission on Mars is necessary for a better understanding of the recent SPICAM observations. In the present work, a model has been developed to calculate the N_2 triplet band dayglow emissions on Mars using the AYS approach described in Chapter 3. While calculating the emission of VK bands of N_2, cascading from the higher lying states and quenching by atmospheric constituents are considered and the population of any given vibrational level of a state is calculated under statistical equilibrium. Height-integrated overhead intensities are calculated for major vibrational bands of N_2 VK, First Positive ($B^3\Pi_g$ – $A^3\Sigma_u^+$), Second Positive ($C^3\Pi_u$ – $B^3\Pi_g$), and Wu-Benesch ($W^3\Delta_u$ – $B^3\Pi_g$) bands. Limb profiles of VK (0, 5), (0, 6), and (0, 7) bands are calculated. The limb profile of VK (0, 6) band is compared with that reported by the SPICAM observations. The present model has been used to predict the N_2 triplet band intensities on the Venus (Section 5.4) [*Bhardwaj and Jain*, 2012a].

5.3.1 Development of model

The model atmosphere considering five gases (CO_2, CO, N_2, O, and O_2) is taken from the MTGCM of *Bougher et al.* [1990, 1999, 2000] for a solar longitude of 180°, latitude of 47.5°N, and at 1200 LT; and is same as used in the study of *Shematovich et al.* [2008]. The EUVAC model of *Richards et al.* [1994] has been used to calculate the 37-bin solar EUV flux for the day of observation, which is based on the F10.7 and F10.7A (81-day average) solar index. The F10.7 flux as seen by Mars (by accounting for the Mars-Sun-Earth angle) is used to derive the 37-bin solar EUV flux. The EUVAC solar spectrum thus obtained is then scaled for the heliocentric distance of Mars for the day, considered in the present study. To assess the impact of solar EUV flux on model calculations, solar flux from S2K v.2.36 model of *Tobiska* [2004] is also considered in the model (cf. Chapter 2 for details on S2K solar flux model).

Table 5.1: Fitting parameters (Eq. 2.5) for N_2 triplet state cross sections.

Parameter	N_2 states					
	$A^3\Sigma_u^+$	$B^3\Pi_g$	$C^3\Pi_u$	$W^3\Delta_u$	$B'^3\Sigma_u^-$	$E^3\Sigma_g^+$
Th*	6.17	7.35	11.03	7.36	8.16	11.9
α	1.00	3.00	3.20	1.50	1.70	1.70
β	1.55	2.33	1.00	2.30	1.50	3.00
Ω	2.13	2.50	2.70	2.60	2.12	3.00
F	0.20	0.178	0.248	0.378	0.08	0.03
W	6.99	7.50	11.05	8.50	8.99	12.0

*Threshold in eV.

Details of photoabsorption and photoionization cross sections, and electron impact cross sections of various inelastic processes for the species considered in the model are given in Chapter 2. For calculating the intensity of a specific band $\nu'-\nu''$, Franck-Condon factors and transition probabilities are required. For N_2 these are taken from *Gilmore et al.* [1992]. Electron impact cross sections for N_2 triplet excited states (A, B, C, W, B', and E) were measured by *Cartwright et al.* [1977] up to 50 eV. These cross sections were renormalized later by *Trajmar et al.* [1983] with the use of improved data on elastic cross sections. More recently, N_2 triplet state cross sections have been measured by *Campbell et al.* [2001] and *Johnson et al.* [2005]. *Itikawa* [2006] reviewed the cross sections of the N_2 triplet excited states and recommended the best values determined by *Brunger et al.* [2003]. The N_2 triplet states cross sections are taken from from *Itikawa* [2006], which are fitted analytically using Eq. 2.5. Table 5.1 shows the corresponding parameters. Figure 5.3 shows the fitted cross sections of the N_2 triplet A, B, C, and W states along with the recommended cross sections of *Itikawa* [2006].

The model is run for the similar lighting conditions as for the MEx observation on 16 Dec. 2004 (Sun-Mars distance = 1.59 AU, and F10.7 at Mars = 35.6), taking SZA as 45°,

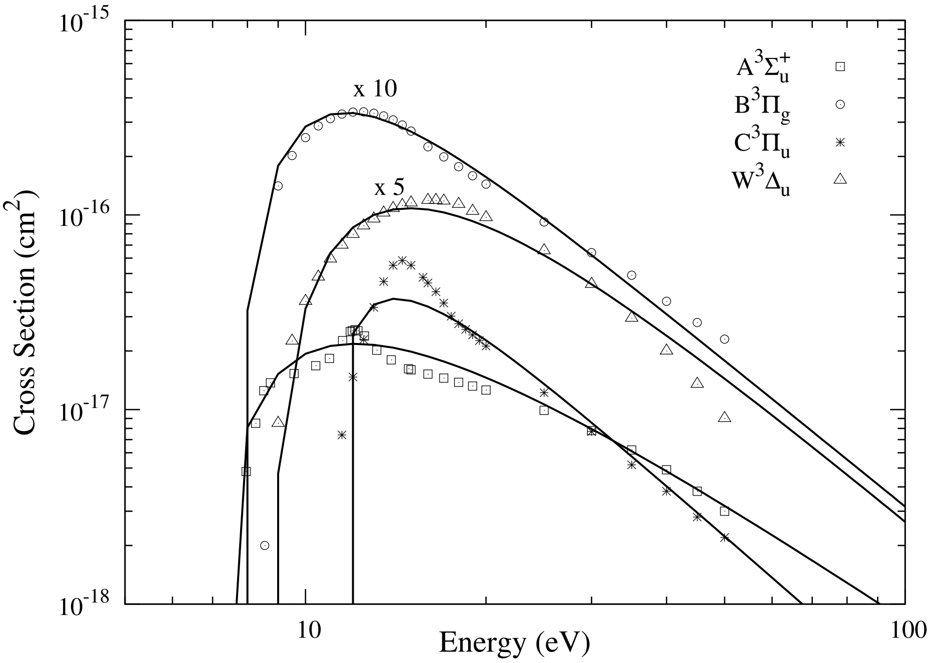

Figure 5.3: The triple states cross sections due to electron impact on N_2. Symbols represent the values of *Itikawa* [2006] and the solid curve represents the analytical fits using Eq. 2.5. Cross sections of B and W have been plotted after multiplying by a factor of 10 and 5, respectively.

solar EUV flux from the EUVAC model, and MTGCM model atmosphere. Hereafter, it is referred as the "standard case".

5.3.2 Photoelectron flux

The AYS technique is used to calculate the photoelectron flux on Mars, which has been already presented in Chapter 4. The calculated photoelectron flux at 130 km altitude is shown in Figure 5.4 for the standard case as well as for conditions similar to those of Viking 1 (see Section 5.3.4). The photoelectron flux calculated by *Simon et al.* [2009] and *Fox and Dalgarno* [1979a] are also shown in Figure 5.4 at same altitude. Overall important peak structures are similar in all the three calculated fluxes, *e.g.*, the peak at 27 eV and broad peak at 21-23 eV. A sharp dip at around 3 eV is prominent in all three photoelectron fluxes, which is due to large vibrational cross sections at 3.8 eV for electron impact on CO_2. The calculated fluxes decrease exponentially with increasing energy. The sudden decrease in the photoelectron flux at higher energies is due to the presence of these features in the primary photoelectron energy spectrum (cf. Figure 4.7 of Chapter 4).

5.3.3 Volume excitation rates

The volume excitation rates of N_2 triplet states are calculated using Eq. 4.7. Figure 5.5 (upper panel) shows the volume excitation rates of the N_2 triplet states (A, B,

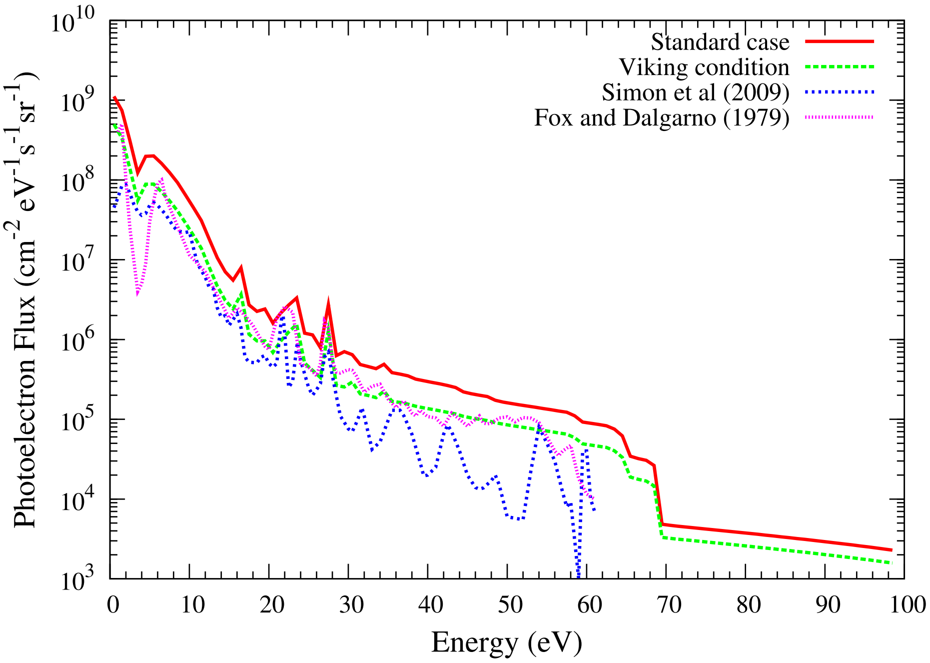

Figure 5.4: Model steady-state photoelectron flux on Mars calculated at 130 km for standard case and for Viking condition. Flux calculated by *Simon et al.* [2009] and *Fox and Dalgarno* [1979a] at 130 km are also shown for comparison.

C, W, B', and E) excited by photoelectron impact. The altitude of peak production for all states is ∼126 km for the standard case. The volume excitation rate of N_2(A) state calculated using the S2K solar flux model is also shown in the upper panel of Figure 5.5. The peak of excitation rate occurs at the same altitude for both solar EUV flux models but the magnitude of excitation rate is slightly higher when the S2K model is used. More discussion about the effect of solar EUV flux model on emission intensities is given in Section 5.3.6.2.

To calculate the contribution of cascading from higher triplet states and interstate cascading between different states, the equation for statistical equilibrium is solved, based on the formulation of *Cartwright* [1978] assuming that only excitation from the lowest vibrational level of the electronic ground state is important. At a specified altitude, for a vibrational level ν of a state α, the population is determined using statistical equilibrium as

$$V^{\alpha} q_{0\nu} + \sum_{\beta} \sum_{s} A^{\beta\alpha}_{s\nu} n^{\beta}_{s} = \{K^{\alpha}_{q\nu} + \sum_{\gamma} \sum_{r} A^{\alpha\gamma}_{\nu r}\} n^{\alpha}_{\nu} \tag{5.1}$$

where

V^{α}	electron impact volume excitation rate (cm^{-3} s^{-1}) of state α;
$q_{0\nu}$	Franck-Condon factor for the excitation from ground level to ν level of state α;
$A^{\beta\alpha}_{i\nu}$	transition probability (s^{-1}) from state $\beta(i)$ to $\alpha(\nu)$;
$K^{\alpha}_{q\nu}$	total electronic quenching frequency (s^{-1}) of level ν of state α by the all

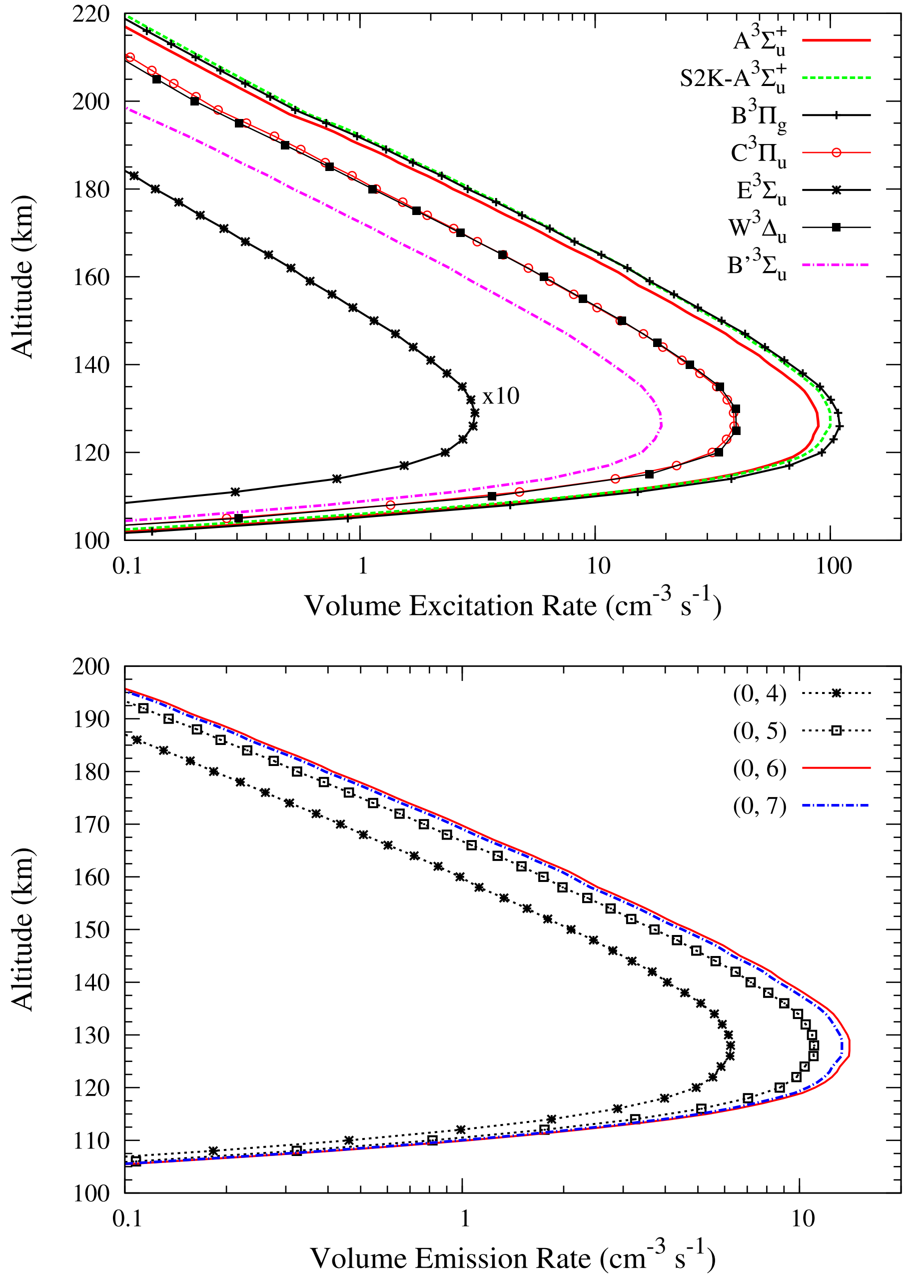

Figure 5.5: (Upper panel) The volume excitation rates of various triplet states of N_2 by direct electron impact excitation for the standard case. Dashed curve shows the excitation rate of A state calculated using S2K model. The excitation rate of the E state has been multiplied by a factor of 10. (Bottom panel) The volume emission rates of the VK (0, 4), (0, 5), (0, 6), and (0, 7) bands.

gases defined as: $\sum_l K^{\alpha}_{q(l)\nu} \times n_l$; where, $K^{\alpha}_{q(l)\nu}$ is the quenching rate coefficient of level ν of α by gas l of density n_l;

$A^{\alpha\gamma}_{\nu r}$ transition from level ν of state α to vibrational level r of state γ;

n density (cm^{-3});

α, β, γ electronic states;

s, r source and sink vibrational levels, respectively.

While calculating the cascading from C state, the predissociation is also taken into account. The C state predissociates approximately half the time (this is an average value for all vibrational levels of the C state; 0 and 1 levels do not predissociate at all) [cf. *Daniell and Strickland*, 1986]. In the terrestrial thermosphere, the N_2(A) state is effectively quenched by atomic oxygen. In the case of Mars the main constituent CO_2 does not quench N_2(A) level that efficiently, but still there will be some collisional deactivation by other atmospheric constituents of Mars. The electronic quenching rates for vibrational levels of N_2 triplet states by O, O_2, and N_2 are adopted from *Morrill and Benesch* [1996] and *Cartwright* [1978] and by CO_2 and CO are taken from *Dreyer et al.* [1974].

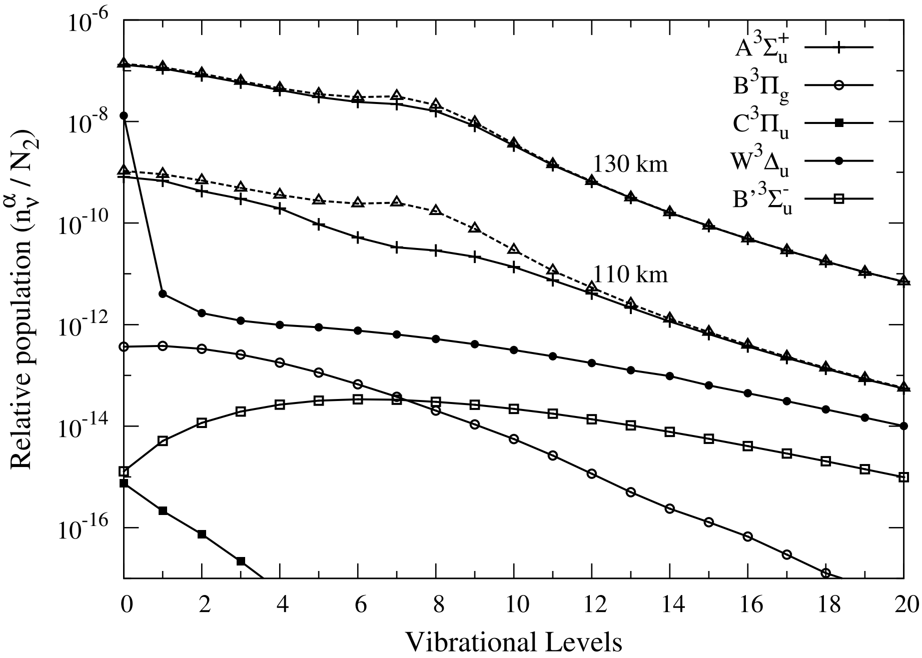

Figure 5.6: The relative populations of vibrational levels of different triplet states of N_2 on Mars with respect to the N_2 density at 130 km. Dashed line with triangle shows the relative vibrational populations of A at 110 and 130 km, respectively, without considering the quenching.

Figure 5.6 shows the population of different vibrational levels of triplet states of N_2 relative to the ground state at 130 km. The relative population of N_2(A) at 110 km is also shown in the figure. The model calculated relative vibrational populations agree well with the earlier calculations [*Morrill and Benesch*, 1996; *Cartwright*, 1978]. To show the effect of quenching the relative vibrational populations of N_2(A) state calculated without quenching at 110 and 130 km are also shown in Figure 5.6. The quenching does affect the vibrational population of N_2(A) state mainly for vibrational levels between 5 and 10 at lower altitudes (<130 km), as the altitude increases the effect of quenching

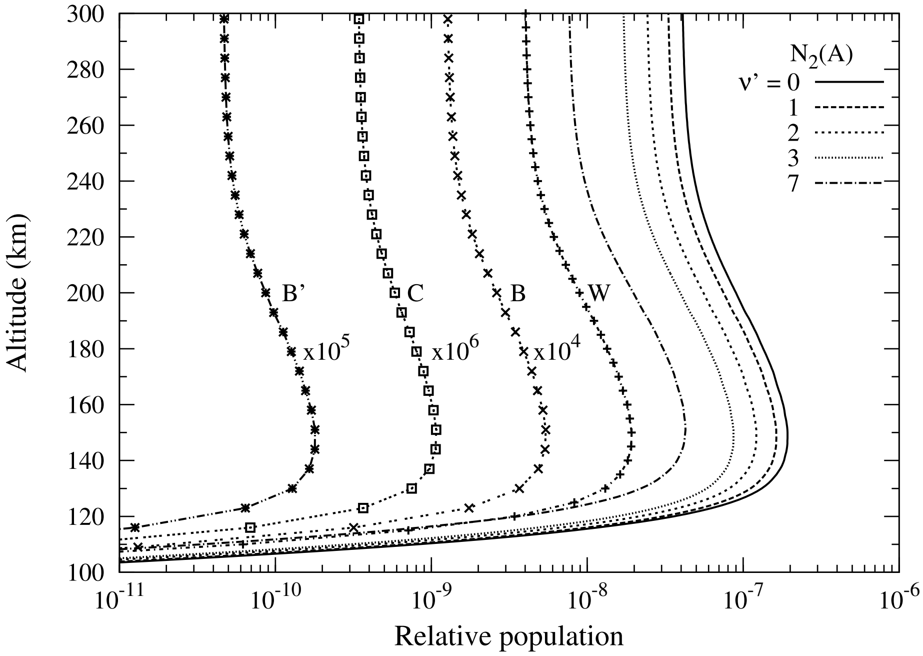

Figure 5.7: Altitude profiles of the relative populations of selected vibrational levels of the N_2(A) state, and 0 level of the B, B', C, and W states on Mars with respect to those of N_2(X). Population of B, B', and C have been plotted after multiplying by a factor of $10^4, 10^5$, and 10^6, respectively.

decreases. Figure 5.7 shows the steady state fractional population altitude profiles of a few vibrational levels of A state and $\nu' = 0$ level of B, C, W, and B' excited states of N_2.

After calculating the steady state density of different vibrational levels of excited states of N_2, the volume emission rate $V^{\alpha\beta}_{\nu'\nu''}$ of a vibration band $\nu' \rightarrow \nu''$ can be obtained using

$$V^{\alpha\beta}_{\nu'\nu''} = n^{\alpha}_{\nu'} \times A^{\alpha\beta}_{\nu'\nu''} \quad (cm^{-3}\ s^{-1}) \tag{5.2}$$

where $n^{\alpha}_{\nu'}$ is the density of vibrational level ν' of state α, and $A^{\alpha\beta}_{\nu'\nu''}$ is the transition probability (s^{-1}) for the transition from the ν' level of the α state to the ν'' level of the β state. Figure 5.5 (bottom panel) shows the volume emission rates for the VK (0, 4), (0, 5), (0, 6), and (0, 7) bands. The volume emission rates are vertically-integrated to calculate the overhead intensities. Table 5.2 shows the total overhead intensity for VK ($A \rightarrow X$), First positive ($B \rightarrow A$), Second Positive ($C \rightarrow B$), Herman–Kaplan ($E \rightarrow A$), $E \rightarrow B$, Reverse First Positive ($A \rightarrow B$), and $E \rightarrow C$ triplet bands of N_2 for standard case. The VK band spans a wide range of electromagnetic spectrum, from FUV to visible wavelengths. The overhead intensities in different wavelength regions of N_2 VK bands are also presented in Table 5.2. Emissions in the 300–400 nm constitute a major fraction of the total VK band emission followed closely by emissions in the 200–300 nm band, with contributions of around 39% and 35%, respectively. The 150–200 nm emission band contributes ∼4% to the total VK band intensity. Contribution of

Table 5.2: Height-integrated overhead intensities of triplet transitions of N_2 on Mars.

Band	Intensity (R)			
	Std.* case	Viking cond.	S2K† flux	Max.‡
Vegard-Kaplan ($A \rightarrow X$) (137–1155 nm)	795	475	911	1187
130–150 nm	2.4E-1§	1.5E-1	2.8E-1	3.8E-1
150–200 nm	33	20	38	51
200–300 nm	279	167	320	418
300–400 nm	313	187	359	466
400–800 nm	169	101	194	252
400–500 nm	123	73.5	141	183
500–800 nm	46	27.5	53	69
First Positive ($B \rightarrow A$) (263–94129 nm)	753	470	861	1170
600–800 nm	383	239	437	594
Second Positive ($C \rightarrow B$) (268–1140 nm)	94	59	109	148
300–400 nm	86	54	101	137
Wu–Benesch ($W \rightarrow B$) (399–154631 nm)	133	84	153	207
$B' \rightarrow B$ (312–37699 nm)	58	36	67	90
$E \rightarrow A$ (207–303 nm)	0.25	0.36	0.63	0.97
$E \rightarrow B$ (259–483 nm)	4E-2	5.6E-2	0.1	0.15
$E \rightarrow C$ (1113–10127 nm)	0.33	0.21	0.37	0.57
R1P¶ ($A \rightarrow B$) (739–74175 nm)	138	85	157	215

*Standard case. See text for details.

†SOLAR2000 model of *Tobiska* [2004].

‡Solar maximum flux for condition similar to Mariner 6 flyby (F10.7 ≃ 190)

§2.4E-1 = 2.4×10^{-1}.

visible wavelength region (400–800 nm) is also significant (21%) in the total VK band intensity, in which wavelength region 400–500 nm contributes ∼15% of the total VK band intensity or 73% of total visible band emission.

The overhead intensities of various N_2 VK transitions are tabulated in Table 5.3 (standard case). The VK (0, 6) emission (at 276.2 nm) is the strongest emission in the VK band system having an overhead intensity of ∼44 R, which is around 5% of the total VK band intensity and comprises around 16% of VK band emissions in the 200–300 nm range. For the VK (0, 5) and (0, 7) bands the model calculated overhead intensity is 34 and 42 R, respectively. Apart from that, Table 5.4 shows the overhead intensity for all the vibrational levels of N_2 VK bands for the standard case.

The calculated overhead intensities of N_2 First Positive (1P) transitions are presented in Table 5.5 for the standard case. Prominent transitions in this band lies above 600 nm. The 1P (1, 0) emission at 888.3 nm is the brightest, followed by (0, 0) emission at 1046.9 nm, which contribute around 13% and 8%, respectively, to the total 1P emission. Emissions between 600 and 800 nm wavelength consist of about 50% of the total 1P band

Table 5.3: Height-integrated overhead intensities of prominent transitions of N_2 VK band on Mars.

Band $\nu' - \nu''$	Band Origin (Å)	Overhead Intensity (R)						
		Std.* case	$\rho[N_2]$ /3.0	Viking Cond.	Cross section CS-A†	Cross section CS-B‡	Flux S2K§	Max.¶
0-2	2216	1.5	0.5	0.9	1	1.4	1.7	2.3
0-3	2334	7.2	2.5	4.4	5	6.8	8.3	10.9
0-4	2463	19.4	6.8	11.7	13.3	18.3	22.2	29.3
0-5	2605	34.3	12.1	20.7	23.5	32.4	39.4	51.8
0-6	2762	43.7	15.4	26.3	30	41.3	50.1	66.0
0-7	2937	41.5	14.6	25.0	28.5	39.2	47.6	62.7
0-8	3133	30.7	10.8	18.5	21	29	35.2	46.4
0-9	3354	18	6.3	10.8	12.3	17	20.6	27.0
1-8	2998	25.9	9.1	15.5	18.8	25.3	29.6	38.4
1-9	3200	38	13.4	22.8	27.8	37.4	43.7	56.6
1-10	3427	35.9	12.7	21.5	26	35.1	41	53.2
1-11	3685	24	8.5	14.4	17.5	23.5	27.5	35.6
2-10	3270	12	4.2	7.1	8.8	11.9	13.6	17.3
2-11	3503	24.9	8.8	14.8	18.5	24.9	28.5	36.3
2-12	3769	26.9	9.5	16.0	20	26.9	30.8	39.3
2-13	4074	18.9	6.7	11.3	14	18.9	21.7	27.6
3-13	3857	16.3	5.7	9.7	12.3	16.5	18.7	24.0
3-14	4171	18.1	6.4	10.8	13.7	18.3	20.7	26.7

*Standard case. See text for details

†Cross sections taken from *Johnson et al.* [2005].

‡Cross sections taken from *Trajmar et al.* [1983].

§SOLAR2000 model of *Tobiska* [2004].

¶Solar maximum flux for condition similar to Mariner 6 flyby (F10.7 $\simeq$ 190).

system. The calculated overhead intensities of Second Positive (2P) band transitions for the standard case are presented in Table 5.6. Major portion of 2P band emission lies in wavelengths between 300 and 400 nm, which is more than 90% of the total 2P band overhead intensity. Prominent emissions in the 2P band system are (0, 0), (0, 1), (0, 2), and (1, 0) transitions, having overhead intensities of around 32, 22, 8.8, and 8.3 R, thus contributing around 34, 24, 9, and 9%, respectively, to the total 2P emission.

Table 5.7 shows the calculated overhead intensities of Herman–Kaplan ($E \rightarrow A$), $E \rightarrow B$, and $E \rightarrow C$ bands of N_2, and Table 5.8 shows the overhead intensities of Reverse First Positive (R1P) band emissions. Prominent emissions in the R1P band system are in infrared region, with (10, 1) emission being the strongest having the overhead intensity of 14 R, which is around 10% of the total R1P emission. Tables 5.9 and 5.10 show the calculated overhead intensities of $B' \rightarrow B$ and Wu-Benesch ($W \rightarrow B$) band emissions, respectively, for the standard case. Most of the emissions in $W \rightarrow B$

band are in infrared region with a little or negligible contribution from emissions below 800 nm. Similar is the case in $B' \to B$ band system.

5.3.4 Line of sight intensity

To compare the calculated brightness profiles with SPICAM observation, the calculated emission rate is integrated along the line of sight to compute the limb profile of N_2 VK bands (see Eq. 4.9). For the emissions considered in the present study, the effect of absorption in the atmosphere is found to be negligible. As mentioned earlier [cf. *Leblanc et al.*, 2007], the main N_2 emission features observed by SPICAM are (0, 5) and (0, 6) transitions of the Vegard-Kaplan ($A^3\Sigma_u^+ - X^1\Sigma_g^+$) band. *Leblanc et al.* [2006] also reported the detection of VK (0, 7) band, but it is characterized by a large uncertainty because it falls between two intense emissions at 289 nm and 297.2 nm of CO_2^+ UV doublet and oxygen line emission, respectively. Otherwise, as shown in Table 5.3, VK(0, 7) band would have been more intense than the (0, 5) band. The ratio between calculated intensity of the VK (0, 6) and (0, 5) bands is 1.3, which is in good agreement with the results of *Leblanc et al.* [2007] and *Fox and Dalgarno* [1979a].

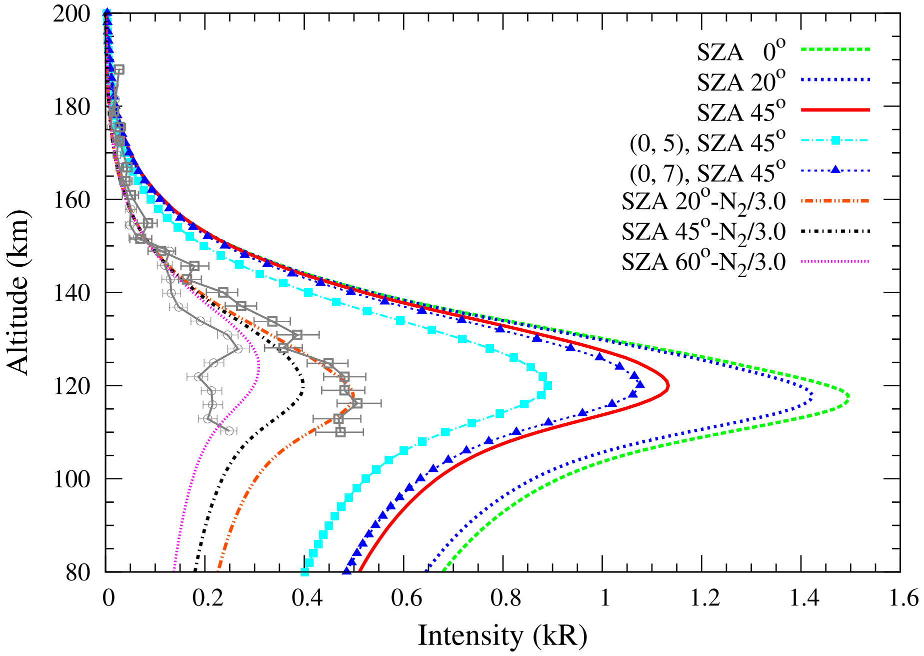

Figure 5.8: Calculated limb intensity of the N_2 VK (0, 6) band on Mars at different solar zenith angles and for the VK (0, 5) and (0, 7) at SZA = 45° for the standard case. Lines with symbols (open squares, SZA = 8°–36°; open circles, SZA = 36°– 64°) represent the averaged observed value of the VK (0, 6) band for solar longitude (Ls) between 100° and 171° taken from *Leblanc et al.* [2007]. The calculated intensities, when the N_2 density is reduced by a factor of 3, are also shown.

Figure 5.8 shows the limb profiles of the VK (0, 6) band at different solar zenith angles along with the SPICAM observed profiles averaged over the solar longitude (Ls) 100°–

171° and SZA 8°–36° and 36°–64°, taken from *Leblanc et al.* [2007]. The effect of SZA on the calculated profiles is clearly visible in Figure 5.8; the peak of the altitude profile rises while the intensity decreases with increasing SZA. The calculated limb profiles of the VK (0, 5) and (0, 6) bands at SZA=45° are also plotted in Figure 5.8. For the standard case (SZA=45°), the peak intensities of the VK (0, 5), (0, 6), and (0, 7) bands are ∼0.9, 1.1, and 1 kR, respectively, at 120 km. For SZA values of 20° and 60°, the N_2 VK (0, 6) band peaks at 118 and 124 km with a value of 1.4 and 0.9 kR, respectively.

The shapes of calculated and observed limb intensities are in agreement with each other but the magnitude of calculated intensities are larger by a factor of ∼3 at SZA = 20°. This difference could be due to the larger abundance of N_2 in the model atmosphere used in the present study. Other factors (viz., electron impact cross section of N_2triplet states, and solar EUV flux models) can also affect the calculated intensities, but their combined variabilities cannot account for the difference by a factor of 3 in the calculated and observed intensities. Figure 5.8 also shows the computed limb intensity of the VK (0, 6) emission at SZA 20°, 45°, and 60° obtained after reducing the density of N_2 by a factor of 3, which compares favourably in both shape and magnitude with the observed emission. The N_2/CO_2 ratio, after reducing the N_2 density by a factor of 3, is 0.9, 2.1, and 7.1% at altitudes of 120, 140, and 170 km, respectively. The calculated overhead intensities of VK bands after reducing N_2 density by a factor of 3 (for the standard case) are depicted in column 3 of Table 5.3. It may however be noted that the observed limb profiles [*Leblanc et al.*, 2007] are averaged over several days of observation (L_s=101°-171°) and range of SZA values (8–36°), while the model profile is for a single day (16 Dec. 2004) at L_s = 130° and SZA = 20°.

The overhead intensity for the condition similar to that of Viking landing (Sun-Mars distance = 1.65 AU, and F10.7 = 68) is also calculated. The model atmosphere was taken from *Fox* [2004] for the low solar activity condition and SZA of 45°. For the VK (0, 6) band model calculated intensity is 26 R, which is consistent with results (20 R) of *Fox and Dalgarno* [1979a] for the similar condition. The minor difference may be due to the updated cross sections and transition probabilities. For the condition similar to that of Viking, *Leblanc et al.* [2007] have measured an intensity of ∼180 R for the VK (0, 6) band, which corresponds to a nadir intensity of ∼6 R. The measured value is about 4 times smaller than the calculated intensity. Such a difference by a factor of 4 between observed and calculated intensities might be due to the higher density of N_2 taken in the model atmosphere. *Leblanc et al.* [2007] mentioned that difference by factor of 3 between the estimated and nadir intensity calculated by *Fox and Dalgarno* [1979a] could have been due to the larger N_2/CO_2 ratio in the model atmosphere of *Fox and Dalgarno* [1979a]. *Leblanc et al.* [2007] have suggested that ratio of the integrated column densities of N_2 and CO_2 between 120 and 170 km, which is the mixing ratio between N_2 and CO_2 for a uniformly mixed atmosphere, would be 0.9% for an overhead intensity of 6 R. For the same altitude range, the ratio of N_2/CO_2 density is 3.5% and 3.7% in model atmosphere used in the work of *Fox* [2004] and MTGCM, respectively, which is a factor of 4 higher than that suggested by *Leblanc et al.* [2007].

To summarize, the above results indicate that the N_2 density in the MTGCM atmosphere, as well as in the model atmosphere of *Fox* [2004], has to be reduced by a factor of ~3 to obtain agreement between the SPICAM observation of N_2 VK band emission and the calculated intensity.

5.3.5 Variation with solar zenith angle and solar 10.7 flux

Figure 5.9 shows the variation of the VK (0, 6) band intensity, averaged between 120 and 170 km, with SZA and its comparison with SPICAM observations. Calculated intensities are for standard case obtained after reducing the N_2 density profile in the MTGCM atmosphere by a factor of 3 (see discussion in the previous section). Model intensity shows a cosine SZA dependence, with larger attenuation of solar EUV flux at higher SZA, resulting in a decrease in the intensity at higher SZA. The calculated intensities are in agreement with the observed values, within observational and model uncertainties.

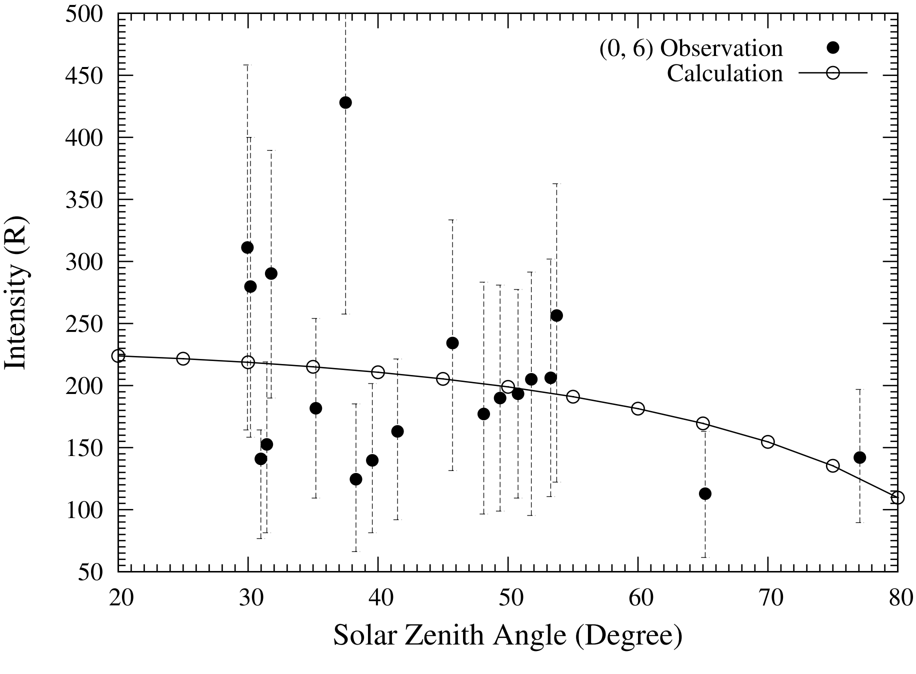

Figure 5.9: The variation of the intensity of the N_2 VK (0, 6) emission with respect to solar zenith angle on Mars. The observed intensity of the VK (0, 6) band is taken from Figure 2 of *Leblanc et al.* [2007]. The calculated intensity is averaged-value between 120 and 170 km for the standard case with N_2 density in the atmosphere reduced by a factor of 3.

Another important model parameter, which affects the emission intensities is the solar EUV flux, whose variation is assumed to be given by the F10.7 index. Solar EUV

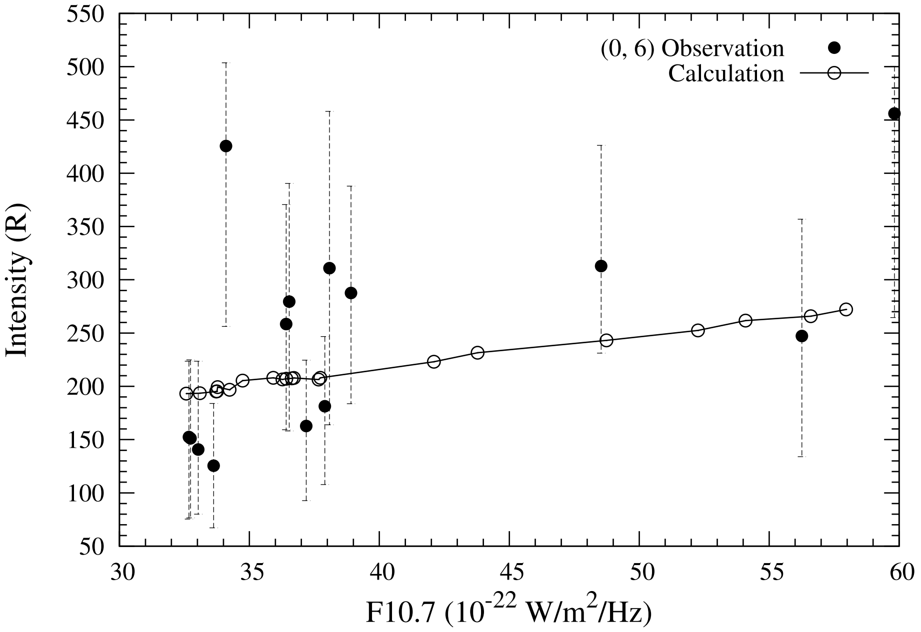

Figure 5.10: Intensity variation of the N_2 VK (0, 6) band with respect to solar index F10.7 ($W/m^2/Hz$) at Mars (scaled from the measured value at Earth). The observed intensity of the VK (0, 6) band is taken from Figure 3 of *Leblanc et al.* [2007]. The calculated intensity is averaged-value between 120 and 170 km for the standard case with N_2 density in the atmosphere reduced by a factor of 3.

flux has been calculated using the F10.7 flux for the day of observation and scaled to the Mars according to its heliocentric distance. For the observations reported by *Leblanc et al.* [2007] the solar longitude of Mars varied between 101° and 171°, which correspond to change in the heliocentric distance of Mars from 1.64 to 1.49 AU. Figure 5.10 shows the variation of VK (0, 6) band intensity with respect to the F10.7 solar index at Mars (for the standard case with the N_2 density in the MTGCM model reduced by a factor 3). Model calculated intensities are consistent with the observed values within the uncertainties of observation and model.

5.3.6 Effect of various model parameters on N_2 triplet emissions

To evaluate the effect of various model input parameters, such as solar flux, cross sections, and model atmosphere on the triplet band emissions, the model calculations are carried out by changing one parameter at a time and compare the results with those of the standard case. The results are presented in Table 5.3 and discussed below.

5.3.6.1 Electron impact cross sections for the triplet states

Since electron impact on N_2 is the source of excitation of forbidden triplet states of N_2, any change in electron impact cross sections will directly affect the VK band emission intensities. Various measurements of the N_2 triplet state cross sections were discussed in Section 5.3.1. In the standard case the recommended cross sections of *Itikawa* [2006] are taken, which are fitted using the semiempirical relation as given in Eq. (2.5) (cf. Table 5.1 and Figure 5.3). Instead of analytically fitted cross sections, if the triplet state cross sections of *Itikawa* [2006] are used in the model, the calculated triplet band intensities differ from the standard case by less than 10%.

Itikawa's recommended cross sections are based on the best values determined by the *Brunger et al.* [2003]. For the triplet states cross section, *Brunger et al.* [2003] have estimated the uncertainty of the recommended cross sections as ±35% (±40% at energies below 15 eV) for $A^3\Sigma_u^+$, ±35% for $B^3\Pi_g$ and $W^3\Delta_u$, ±40% for $B'^3\Sigma_u^-$, ±30% for $C^3\Pi_u$, and ±40% for $E^3\Sigma_g^+$ state. The integral cross sections (ICS) of *Johnson et al.* [2005] are derived from the differential cross sections (DCS) of *Khakoo et al.* [2005]. *Johnson et al.* [2005] have given the ICS at 8 energies between 10 and 100 eV, with uncertainty for all states cross sections varying between ±20% to ±22%; at a few energy points it is as high as ±35%.

To evaluate the effect of electron impact cross sections on the VK band emissions two sets of cross sections are considered; one from *Cartwright et al.* [1977], which were renormalized by *Trajmar et al.* [1983], and second from the recent cross sections given by *Johnson et al.* [2005]. The resulting VK band intensities are shown in Table 5.3. The intensities calculated with the cross sections of *Trajmar et al.* [1983] are almost the same as in the standard case. However, when the cross sections of *Johnson et al.* [2005] are used, the VK band intensities are reduces by 45%, compared to the intensities computed for the standard case, which is due to smaller cross sections of *Johnson et al.* [2005]. The effect of the smaller triplet state cross sections of *Johnson et al.* [2005] is also seen on the limb intensities shown in the Figure 5.11 where a reduction in N_2 density by a factor 2 is sufficient to fit the SPICAM observed profile. Thus, the electron impact triplet state excitation cross sections of N_2 also help in constraining the N_2 density in the model atmosphere.

5.3.6.2 Input solar EUV flux model

SOLAR2000 model of *Tobiska* [2004] and EUVAC model of *Richards et al.* [1994] are the two widely used solar flux models in the aeronomical calculations. In the standard case EUVAC model is used. To see the effect of input solar flux on the VK emission intensities, model calculations are carried out by taking the solar EUV flux from S2K model of *Tobiska* [2004] at 37 wavelength bins (see Chapter 2); the other input parameters remain the same as in the standard case. The calculated integrated overhead intensities are shown in the Table 5.3. The calculated intensities of VK bands using S2K model are ∼15% larger than those calculated by using the EUVAC model. This results in the requirement of a larger reduction in the N_2 density, i.e., a factor of

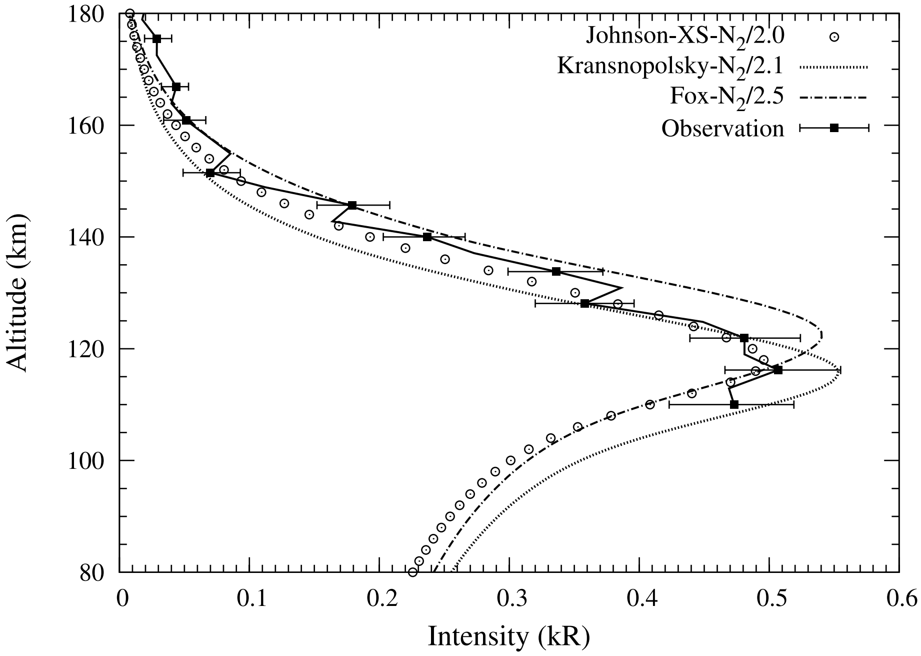

Figure 5.11: The calculated limb intensity of the N_2 VK (0, 6) band on Mars at SZA = 20°. The observed values are taken from *Leblanc et al.* [2007]. The calculated intensities are shown for the model atmospheres of *Fox* [2004] (when the density of N_2 is reduced by a factor of 2.5) and *Krasnopolsky* [2002] (the N_2 density reduced by a factor of 2.1). The intensity calculated by using the electron impact cross sections of *Johnson et al.* [2005] is shown when the N_2 density is reduced by a factor of 2.

3.4 compared to 3 for the standard case to fit the observed limb profile of the VK (0, 6) band.

5.3.6.3 Model atmosphere

The importance of model atmosphere on the calculated intensities has been demonstrated in Section 5.3.4. The N_2/CO_2 ratio, which describes the abundance of molecular nitrogen in the atmosphere of Mars, is different in different model atmospheres. For the present study the atmosphere from Bougher's MTGCM [*Bougher et al.*, 1990, 1999, 2000] is taken in the model [*Shematovich et al.*, 2008] where the N_2/CO_2 ratio is 2.8, 6.4 and 21% at 120, 140 and 170 km, respectively. *Leblanc et al.* [2007] suggested that N_2/CO_2 ratio is higher in the model atmosphere used by *Fox and Dalgarno* [1979a]. The recent models of *Krasnopolsky* [2002] are characterized by smaller abundances of N_2 than that of *Fox and Dalgarno* [1979a]. The N_2/CO_2 ratios are 2.6, 3.8, and 8.6% at 120, 140 and 170 km, respectively in model atmosphere of *Krasnopolsky* [2002].

The model atmospheres of *Krasnopolsky* [2002] and *Fox* [2004] are also used to study the effect of model atmosphere on the N_2 VK emission intensities. Figure 5.11 shows the calculated limb intensity of the VK (0, 6) band for both model atmospheres at SZA 20° (all other conditions are similar to the standard case). The emission peaks at ~116 km in the case of *Krasnopolsky* [2002] model atmosphere, which is almost similar to standard case (∼118 km). But the emission peaks at higher altitude (∼123 km) when the model atmosphere of *Fox* [2004] is used, which is due to higher CO_2 abundance in her model. The intensities calculated using both models are found to be larger than the observed values. To fit the observed limb profile, the N_2 density in the *Krasnopolsky* [2002] model has to be reduced by a factor of 2.1, the N_2/CO_2 ratios thus become 1.3, 1.8, and 4.4% at 120, 140, and 170 km, respectively. In the case of *Fox* [2004] model atmosphere, the required decrease in N_2 density is a factor of 2.5, which corresponds to the N_2/CO_2 ratios of 1.1, 1.9, and 5.3% at 120, 140, and 170 km, respectively.

5.3.6.4 Solar cycle

The solar cycle is approaching high solar activity, and the MEx is currently orbiting Mars. To observe the effect of high solar activity condition on the Martian dayglow emissions the calculations are carried out for high solar activity condition. Solar EUV flux is taken for the similar lighting condition as on Mariner 6 and 7 flybys observations (F10.7$\simeq$ 190 at 1 AU). The model atmosphere for solar maximum condition was taken from *Fox* [2004]; other model parameters are same as in the standard case. The calculated height-integrated overhead intensities for the VK bands are presented in the Table 5.3. The calculated solar maximum intensities are larger by a factor of ∼1.5 than those of the standard case, and ∼2.5 times larger than those for Viking conditions. As mentioned in section 5.3.4, the calculated and observed limb profiles are consistent with each other when the N_2 density in the atmosphere is reduced by a factor of 3. If a similar situation prevails during high solar activity conditions, then the calculated intensity of N_2 VK band system would be smaller by a factor of 2 to 3.

Table 5.4: Overhead intensities (in R) of N_2 Vegard-Kaplan ($A^3\Sigma_u^+ \rightarrow X^1\Sigma_g^+$) band on Mars standard case.

$\nu' \setminus \nu''$	0	1	2	3	4	5	6	7	8	9
0	8.4E-5	1.2E-1	1.5E+0	7.2E+0	1.9E+1	3.4E+1	4.4E+1	4.2E+1	3.1E+1	1.8E+1
	(2010)	(2109)	(2216)	(2334)	(2463)	(2605)	(2762)	(2937)	(3133)	(3354)
1	2.0E-2	7.2E-2	1.8E+0	6.7E+0	9.8E+0	5.0E+0	1.1E-6	7.8E+0	2.6E+1	3.8E+1
	(1954)	(2047)	(2148)	(2258)	(2379)	(2511)	(2657)	(2819)	(2998)	(3200)
2	2.0E-1	1.8E-2	5.6E-1	1.8E+0	4.6E-1	1.2E+0	8.3E+0	1.1E+1	3.3E+0	7.2E-1
	(1901)	(1990)	(2085)	(2189)	(2302)	(2425)	(2561)	(2711)	(2877)	(3062)
3	7.0E-1	3.9E-1	1.5E-2	8.3E-2	4.0E-1	3.0E+0	2.7E+0	5.4E-7	4.5E+0	9.5E+0
	(1853)	(1936)	(2027)	(2125)	(2231)	(2347)	(2474)	(2614)	(2768)	(2938)
4	1.5E+0	9.8E-1	4.1E-2	1.2E-2	5.5E-1	8.1E-1	2.5E-2	2.5E+0	3.3E+0	1.5E-1
	(1808)	(1887)	(1973)	(2065)	(2166)	(2275)	(2394)	(2524)	(2668)	(2826)
5	2.4E+0	1.3E+0	3.3E-2	1.0E-3	1.4E-1	3.0E-3	7.5E-1	1.3E+0	7.7E-4	2.1E+0
	(1765)	(1841)	(1923)	(2011)	(2106)	(2209)	(2321)	(2443)	(2577)	(2724)
6	3.6E+0	1.2E+0	4.9E-3	4.0E-2	2.9E-3	8.7E-2	4.9E-1	2.2E-2	9.2E-1	1.4E+0
	(1726)	(1798)	(1876)	(1960)	(2050)	(2147)	(2253)	(2368)	(2494)	(2632)
7	5.2E+0	9.4E-1	2.0E-1	1.6E-1	1.2E-3	7.0E-2	7.1E-2	2.3E-1	8.3E-1	5.3E-3
	(1689)	(1758)	(1833)	(1912)	(1998)	(2090)	(2191)	(2299)	(2418)	(2547)
8	5.2E+0	3.2E-1	5.4E-1	1.4E-1	6.1E-3	4.1E-3	4.3E-3	2.6E-1	7.0E-2	4.0E-1
	(1655)	(1721)	(1792)	(1868)	(1950)	(2038)	(2133)	(2236)	(2347)	(2469)
9	3.3E+0	1.5E-2	5.4E-1	2.7E-2	4.1E-2	1.8E-3	1.1E-2	4.7E-2	2.4E-2	2.6E-1
	(1622)	(1686)	(1754)	(1827)	(1905)	(1989)	(2079)	(2177)	(2283)	(2398)
10	1.6E+0	1.9E-2	3.1E-1	8.6E-4	4.7E-2	3.9E-4	6.9E-4	6.5E-4	3.5E-2	2.8E-2
	(1592)	(1653)	(1718)	(1788)	(1863)	(1943)	(2030)	(2122)	(2223)	(2332)
11	7.3E-1	5.9E-2	1.3E-1	1.7E-2	2.6E-2	1.1E-3	5.0E-4	4.7E-4	9.3E-3	2.4E-4
	(1563)	(1622)	(1685)	(1752)	(1824)	(1901)	(1983)	(2072)	(2168)	(2271)
12	3.6E-1	7.4E-2	4.7E-2	2.8E-2	8.9E-3	4.6E-3	7.7E-4	9.9E-5	7.6E-4	3.5E-3
	(1536)	(1593)	(1654)	(1719)	(1788)	(1861)	(1940)	(2025)	(2116)	(2215)
13	1.7E-1	6.6E-2	1.2E-2	2.6E-2	1.1E-3	5.8E-3	1.2E-4	8.1E-5	2.0E-6	1.9E-3
	(1511)	(1566)	(1625)	(1687)	(1754)	(1824)	(1900)	(1981)	(2069)	(2163)
14	8.6E-2	5.1E-2	1.4E-3	1.8E-2	1.1E-4	4.3E-3	9.0E-5	3.0E-4	1.8E-5	3.5E-4
	(1487)	(1541)	(1597)	(1658)	(1722)	(1790)	(1863)	(1941)	(2024)	(2114)
15	4.4E-2	3.7E-2	5.5E-5	1.1E-2	1.3E-3	2.2E-3	5.6E-4	2.3E-4	4.6E-6	1.2E-5
	(1465)	(1517)	(1572)	(1630)	(1692)	(1758)	(1828)	(1903)	(1983)	(2070)
16	2.2E-2	2.5E-2	1.1E-3	5.4E-3	2.2E-3	7.4E-4	8.8E-4	5.3E-5	6.2E-5	2.5E-6
	(1444)	(1494)	(1548)	(1604)	(1664)	(1728)	(1796)	(1868)	(1945)	(2028)
17	1.2E-2	1.7E-2	2.1E-3	2.2E-3	2.4E-3	9.8E-5	8.3E-4	1.4E-6	9.8E-5	3.1E-7
	(1425)	(1473)	(1525)	(1580)	(1638)	(1700)	(1765)	(1835)	(1910)	(1990)
18	6.2E-3	1.1E-2	2.6E-3	7.1E-4	2.0E-3	8.2E-6	5.8E-4	6.1E-5	7.3E-5	5.2E-6
	(1406)	(1454)	(1504)	(1557)	(1614)	(1674)	(1737)	(1805)	(1877)	(1954)
19	3.3E-3	7.0E-3	2.6E-3	1.3E-4	1.4E-3	1.2E-4	3.0E-4	1.3E-4	2.8E-5	2.0E-5
	(1389)	(1435)	(1484)	(1536)	(1591)	(1649)	(1711)	(1777)	(1846)	(1921)
20	1.8E-3	4.5E-3	2.3E-3	3.2E-7	8.8E-4	2.4E-4	1.2E-4	1.6E-4	2.7E-6	2.9E-5
	(1373)	(1418)	(1466)	(1517)	(1570)	(1627)	(1687)	(1750)	(1818)	(1890)

Values in brackets show the band origin in Å.

Table 5.4: contd.

$\nu' \setminus \nu''$	10	11	12	13	14	15	16	17	18	19	20
0	8.5E+0 (3604)	3.2E+0 (3890)	1.0E+0 (4221)	2.5E-1 (4606)	5.2E-2 (5062)	8.6E-3 (5608)	1.1E-3 (6274)	1.2E-4 (7106)	1.0E-5 (8171)	6.3E-7 (9584)	2.9E-8 (11548)
1	3.6E+1 (3427)	2.4E+1 (3685)	1.2E+1 (3980)	4.7E+0 (4321)	1.5E+0 (4719)	3.5E-1 (5191)	6.9E-2 (5757)	1.0E-2 (6449)	1.2E-3 (7315)	1.1E-4 (8427)	7.9E-6 (9908)
2	1.2E+1 (3270)	2.5E+1 (3503)	2.7E+1 (3769)	1.9E+1 (4074)	9.6E+0 (4426)	3.7E+0 (4838)	1.1E+0 (5326)	2.4E-1 (5913)	4.2E-2 (6633)	5.7E-3 (7535)	5.8E-4 (8697)
3	4.6E+0 (3129)	2.5E-2 (3342)	6.6E+0 (3583)	1.6E+1 (3857)	1.8E+1 (4171)	1.3E+1 (4536)	6.1E+0 (4962)	2.2E+0 (5468)	5.7E-1 (6078)	1.1E-1 (6826)	1.7E-2 (7767)
4	2.7E+0 (3002)	7.2E+0 (3198)	3.6E+0 (3418)	1.2E-2 (3666)	4.7E+0 (3949)	1.1E+1 (4274)	1.2E+1 (4650)	7.4E+0 (5092)	3.2E+0 (5617)	1.0E+0 (6250)	2.4E-1 (7030)
5	2.9E+0 (2887)	1.1E-1 (3068)	2.2E+0 (3270)	5.2E+0 (3497)	2.1E+0 (3753)	1.1E-1 (4065)	3.9E+0 (4381)	7.7E+0 (4771)	6.9E+0 (5229)	3.9E+0 (5773)	1.5E+0 (6432)
6	2.0E-3 (2783)	2.1E+0 (2951)	2.3E+0 (3137)	5.4E-3 (3346)	2.4E+0 (3579)	3.9E+0 (3844)	9.5E-1 (4146)	4.5E-1 (4494)	3.8E+0 (4897)	5.6E+0 (5372)	4.2E+0 (5938)
7	1.3E+0 (2689)	1.3E+0 (2845)	9.5E-2 (3018)	2.5E+0 (3210)	1.6E+0 (3424)	1.1E-1 (3666)	2.9E+0 (3940)	2.9E+0 (4252)	2.2E-1 (4612)	1.1E+0 (5030)	4.0E+0 (5523)
8	7.2E-1 (2602)	2.6E-2 (2748)	1.3E+0 (2909)	6.1E-1 (3087)	3.7E-1 (3285)	2.0E+0 (3507)	5.7E-1 (3757)	4.8E-1 (4040)	2.4E+0 (4363)	1.3E+0 (4736)	6.0E-3 (5170)
9	7.6E-3 (2523)	4.0E-1 (2660)	2.9E-1 (2810)	1.3E-1 (2976)	7.9E-1 (3160)	9.2E-2 (3364)	4.9E-1 (3594)	9.1E-1 (3852)	3.8E-2 (4144)	5.9E-1 (4480)	1.1E+0 (4866)
10	5.0E-2 (2450)	1.3E-1 (2579)	8.1E-3 (2720)	2.4E-1 (2875)	4.3E-2 (3046)	1.7E-1 (3236)	2.8E-1 (3448)	1.4E-3 (3684)	3.4E-1 (3952)	2.3E-1 (4255)	1.8E-2 (4602)
11	3.7E-2 (2383)	3.5E-3 (2505)	5.5E-2 (2638)	3.6E-2 (2783)	3.3E-2 (2743)	1.0E-1 (3120)	1.0E-4 (3316)	1.2E-1 (3535)	5.6E-2 (3780)	3.5E-2 (4057)	1.6E-1 (4371)
12	7.8E-3 (2321)	5.0E-3 (2437)	2.3E-2 (2562)	1.2E-3 (2699)	4.1E-2 (2850)	2.7E-3 (3015)	4.1E-2 (3198)	2.8E-2 (3400)	1.5E-2 (3627)	6.3E-2 (3881)	2.4E-3 (4168)
13	1.7E-4 (2264)	6.5E-3 (2374)	1.7E-3 (2493)	9.7E-3 (2622)	7.0E-3 (2764)	7.9E-3 (2919)	1.7E-2 (3090)	1.8E-3 (3279)	2.7E-2 (3489)	1.7E-3 (3724)	2.2E-2 (3987)
14	2.7E-4 (2211)	2.3E-3 (2316)	3.9E-4 (2429)	5.3E-3 (2552)	8.8E-5 (2686)	8.6E-3 (2832)	2.8E-4 (2993)	1.0E-2 (3169)	3.2E-3 (3365)	7.0E-3 (3583)	9.7E-3 (3826)
15	3.6E-4 (2162)	2.6E-4 (2262)	1.2E-3 (2370)	8.4E-4 (2487)	1.9E-3 (2614)	2.0E-3 (2752)	1.9E-3 (2904)	3.9E-3 (3070)	9.3E-4 (3253)	6.1E-3 (3456)	1.4E-5 (3682)
16	1.3E-4 (2117)	2.6E-6 (2213)	7.1E-4 (2316)	3.5E-6 (2427)	1.5E-3 (2548)	1.4E-6 (2679)	2.3E-3 (2823)	8.7E-5 (2980)	2.7E-3 (3152)	5.2E-4 (3342)	2.5E-3 (3553)
17	1.6E-5 (2075)	5.2E-5 (2167)	1.8E-4 (2266)	2.0E-4 (2372)	4.2E-4 (2488)	3.7E-4 (2613)	7.3E-4 (2749)	4.2E-4 (2897)	1.1E-3 (3060)	3.1E-4 (3239)	1.6E-3 (3436)
18	1.4E-9 (2036)	4.0E-5 (2125)	1.3E-5 (2220)	2.1E-4 (2322)	2.1E-5 (2432)	4.4E-4 (2551)	3.1E-5 (2681)	6.6E-4 (2822)	6.1E-5 (2976)	8.2E-4 (3145)	1.4E-4 (3331)
19	8.4E-7 (2000)	1.2E-5 (2086)	2.3E-6 (2177)	9.6E-5 (2275)	1.8E-5 (2381)	2.1E-4 (2495)	5.0E-5 (2619)	3.1E-4 (2754)	7.8E-5 (2900)	6.1E-4 (3060)	7.9E-5 (3236)
20	2.6E-8 (1967)	9.7E-7 (2050)	8.5E-6 (2138)	2.3E-5 (2232)	5.1E-5 (2334)	4.2E-5 (2444)	1.2E-4 (2563)	4.9E-5 (2691)	2.0E-4 (2831)	5.6E-5 (2984)	2.6E-4 (3150)

Values in brackets show the band origin in Å.

Table 5.5: Overhead intensities (in R) of N_2 First Positive ($B^3\Pi_g \rightarrow A^3\Sigma_u^+$) band on Mars standard case.

$\nu' \setminus \nu''$	0	1	2	3	4	5	6	7	8	9
0	6.1E+1 (10469)	3.3E+1 (12317)	9.8E+0 (14895)	2.1E+0 (18739)	3.2E-1 (25084)	3.3E-2 (37523)	1.5E-3 (72916)	2.3E-7 (941292)	– –	– –
1	9.6E+1 (8883)	4.3E-1 (10179)	1.8E+1 (11878)	1.4E+1 (14201)	5.0E+0 (17569)	1.2E+0 (22882)	1.8E-1 (32502)	1.5E-2 (55202)	1.9E-4 (173933)	– –
2	4.7E+1 (7732)	6.1E+1 (8695)	1.1E+1 (9905)	2.3E+0 (11471)	8.5E+0 (13572)	5.7E+0 (16538)	2.0E+0 (21039)	4.6E-1 (28671)	6.2E-2 (44420)	2.8E-3 (95828)
3	9.8E+0 (6858)	6.4E+1 (7606)	1.7E+1 (8516)	2.0E+1 (9648)	5.3E-1 (11092)	2.5E+0 (12997)	3.9E+0 (15624)	2.1E+0 (19474)	7.0E-1 (25651)	1.4E-1 (37163)
4	9.6E-1 (6173)	2.0E+1 (6772)	4.9E+1 (7484)	8.8E-1 (8345)	1.5E+1 (9404)	3.7E+0 (10739)	8.8E-2 (12471)	1.6E+0 (14807)	1.5E+0 (18126)	7.2E-1 (23207)
5	4.5E-2 (5622)	2.5E+0 (6114)	2.2E+1 (6689)	2.6E+1 (7368)	1.0E+0 (8181)	6.2E+0 (9173)	4.6E+0 (10408)	3.1E-1 (11987)	2.8E-1 (14072)	7.4E-1 (16954)
6	9.3E-4 (5168)	1.4E-1 (5582)	3.5E+0 (6057)	1.8E+1 (6608)	1.0E+1 (7255)	3.2E+0 (8025)	1.4E+0 (8954)	3.2E+0 (10098)	8.8E-1 (11539)	1.5E-4 (13407)
7	6.9E-6 (4789)	3.3E-3 (5142)	2.3E-1 (5543)	3.6E+0 (6001)	1.2E+1 (6530)	2.7E+0 (7147)	3.4E+0 (7875)	6.2E-2 (8746)	1.5E+0 (9806)	9.2E-1 (11124)
8	7.0E-9 (4448)	2.7E-5 (4774)	6.3E-3 (5117)	2.8E-1 (5505)	3.1E+0 (5947)	6.6E+0 (6454)	3.8E-1 (7042)	2.3E+0 (7730)	7.7E-2 (8548)	4.6E-1 (9532)
9	2.0E-11 (4192)	2.7E-8 (4460)	5.8E-5 (4758)	9.0E-3 (5092)	2.9E-1 (5468)	2.3E+0 (5894)	3.3E+0 (6380)	3.6E-4 (6940)	1.2E+0 (7592)	2.4E-1 (8358)
10	8.9E-13 (3953)	2.4E-10 (4190)	5.4E-8 (4453)	8.8E-5 (4744)	1.0E-2 (5068)	2.5E-1 (5432)	1.5E+0 (5842)	1.4E+0 (6309)	7.3E-2 (6843)	4.5E-1 (7459)
11	5.0E-14 (3744)	3.8E-13 (3956)	5.2E-10 (4189)	7.3E-8 (4446)	1.0E-4 (4729)	9.5E-3 (5045)	1.8E-1 (5397)	8.3E-1 (5792)	4.8E-1 (6239)	1.2E-1 (6748)
12	5.8E-13 (3560)	5.3E-14 (3751)	5.5E-12 (3960)	9.3E-10 (4188)	7.4E-8 (4439)	9.4E-5 (4716)	7.3E-3 (5022)	1.1E-1 (5363)	4.0E-1 (5744)	1.3E-1 (6172)
13	1.5E-13 (3396)	2.1E-13 (3570)	7.1E-13 (3758)	2.3E-11 (3963)	1.4E-9 (4187)	6.4E-8 (4433)	7.7E-5 (4702)	5.1E-3 (5000)	6.7E-2 (5329)	1.8E-1 (5696)
14	3.0E-15 (3250)	2.9E-13 (3409)	6.4E-13 (3580)	5.0E-12 (3766)	5.9E-11 (3968)	1.9E-9 (4187)	5.3E-8 (4427)	6.4E-5 (4690)	3.7E-3 (4978)	4.1E-2 (5297)
15	3.8E-14 (3119)	4.2E-14 (3265)	4.8E-13 (3422)	2.6E-12 (3591)	1.2E-11 (3774)	1.1E-10 (3972)	2.5E-9 (4188)	4.6E-8 (4422)	5.7E-5 (4678)	2.9E-3 (4958)
16	8.2E-15 (3001)	9.2E-16 (3136)	2.0E-13 (3280)	9.3E-13 (3436)	4.4E-12 (3603)	2.0E-11 (3783)	1.9E-10 (3978)	2.8E-9 (4188)	3.6E-8 (4417)	4.6E-5 (4666)
17	1.6E-15 (2894)	4.2E-16 (3020)	3.5E-14 (3153)	2.0E-13 (3296)	1.2E-12 (3450)	6.7E-12 (3615)	2.7E-11 (3792)	2.3E-10 (3983)	2.3E-9 (4190)	2.3E-8 (4413)
18	5.7E-15 (2797)	2.2E-15 (2914)	1.5E-15 (3039)	2.9E-14 (3171)	2.8E-13 (3313)	1.7E-12 (3465)	6.9E-12 (3627)	2.8E-11 (3802)	2.2E-10 (3989)	1.7E-9 (4191)
19	2.6E-15 (3709)	3.8E-15 (2818)	1.7E-16 (2935)	3.2E-15 (3058)	6.4E-14 (3190)	3.7E-13 (3330)	2.0E-12 (3480)	7.9E-12 (3641)	3.3E-11 (3812)	2.6E-10 (3996)
20	3.9E-17 (2628)	5.1E-16 (2731)	3.1E-16 (2840)	8.8E-17 (2956)	7.0E-15 (3079)	5.2E-14 (3209)	3.6E-13 (3348)	1.7E-12 (3496)	6.7E-12 (3654)	3.0E-11 (3823)

Values in brackets show the band origin in Å.

Table 5.5: contd.

$\nu' \setminus \nu''$	10	11	12	13	14	15	16	17	18	19	20
3	1.3E-2	9.3E-5	–	–	–	–	–	–	–	–	–
	(66117)	(274786)	–	–	–	–	–	–	–	–	–
4	2.1E-1	3.3E-2	1.6E-3	–	–	–	–	–	–	–	–
	(31941)	(50449)	(115737)	–	–	–	–	–	–	–	–
5	5.4E-1	2.2E-1	5.3E-2	6.1E-3	4.3E-5	–	–	–	–	–	–
	(21186)	(27999)	(40761)	(73199)	(311787)	–	–	–	–	–	–
6	2.1E-1	2.9E-1	1.7E-1	6.0E-2	1.2E-2	7.6E-4	–	–	–	–	–
	(15923)	(19487)	(24916)	(34172)	(53448)	(117886)	–	–	–	–	–
7	1.1E-1	2.0E-2	1.1E-1	1.0E-1	5.1E-2	1.6E-2	2.4E-3	5.3E-5	–	–	–
	(12802)	(15009)	(18036)	(22434)	(29394)	(42028)	(71926)	(229296)	–	–	–
8	6.1E-1	1.9E-1	5.1E-3	2.1E-2	4.3E-2	3.3E-2	1.5E-2	4.0E-3	4.6E-4	8.6E-7	–
	(10737)	(12248)	(14192)	(16781)	(20392)	(25765)	(34576)	(51601)	(98056)	(718231)	–
9	7.7E-2	3.0E-1	1.8E-1	3.3E-2	1.6E-4	1.2E-2	1.6E-2	1.1E-2	4.4E-3	1.1E-3	9.7E-5
	(9272)	(10377)	(11739)	(13456)	(15683)	(18679)	(22912)	(29322)	(40124)	(62048)	(129839)
10	2.6E-1	3.1E-4	1.0E-1	1.1E-1	4.4E-2	4.3E-3	9.5E-4	5.3E-3	5.7E-3	3.5E-3	1.4E-3
	(8178)	(9025)	(10038)	(11268)	(12789)	(14713)	(17219)	(20605)	(25412)	(32758)	(45186)
11	1.3E-1	1.7E-1	1.2E-2	2.1E-2	5.1E-2	3.3E-2	9.0E-3	3.6E-4	7.2E-4	2.0E-3	1.9E-3
	(7330)	(8004)	(8791)	(9720)	(10831)	(12181)	(13849)	(15958)	(18697)	(22383)	(27577)
12	1.0E-1	1.3E-2	8.0E-2	2.1E-2	1.0E-3	1.6E-2	1.7E-2	8.2E-3	1.7E-3	9.8E-6	3.5E-4
	(6656)	(7207)	(7838)	(8568)	(9420)	(10424)	(11623)	(13072)	(14855)	(17091)	(19962)
13	2.9E-2	6.0E-2	7.6E-4	3.0E-2	1.7E-2	5.8E-4	3.0E-3	6.6E-3	5.0E-3	2.0E-3	3.2E-4
	(6106)	(6566)	(7087)	(7678)	(8355)	(9136)	(10043)	(11108)	(12369)	(13881)	(15717)
14	8.6E-2	4.4E-3	3.3E-2	6.9E-4	9.7E-3	1.1E-2	2.1E-3	1.7E-4	2.0E-3	2.5E-3	1.5E-3
	(5650)	(6042)	(6479)	(6970)	(7524)	(8151)	(8866)	(9685)	(10630)	(11728)	(13012)
15	2.7E-2	4.3E-2	1.3E-4	1.7E-2	2.5E-3	2.5E-3	6.2E-3	2.7E-3	1.1E-4	4.0E-4	1.1E-3
	(5265)	(5604)	(5979)	(6394)	(6857)	(7374)	(7955)	(8608)	(9347)	(10185)	(11140)
16	2.1E-3	1.6E-2	2.0E-2	3.3E-4	7.6E-3	2.9E-3	2.9E-4	2.7E-3	2.1E-3	4.6E-4	6.1E-6
	(4938)	(5234)	(5560)	(5917)	(6312)	(6747)	(7230)	(7765)	(8312)	(9026)	(9768)
17	3.0E-5	1.2E-3	8.2E-3	7.3E-3	7.7E-4	2.4E-3	2.0E-3	5.1E-6	7.7E-4	1.1E-3	4.9E-4
	(4655)	(4918)	(5204)	(5516)	(5857)	(6230)	(6639)	(7089)	(7582)	(8124)	(8721)
18	1.3E-8	1.9E-5	7.0E-4	3.9E-3	2.4E-3	7.5E-4	6.1E-4	1.0E-3	1.0E-4	1.4E-4	4.3E-4
	(4409)	(4644)	(4899)	(5174)	(5473)	(5798)	(6150)	(6534)	(6951)	(7404)	(7896)
19	1.4E-9	1.0E-8	1.5E-5	5.0E-4	2.4E-3	9.8E-4	6.8E-4	1.4E-4	6.0E-4	1.8E-4	1.0E-5
	(4194)	(4406)	(4634)	(4880)	(5145)	(5431)	(5739)	(6072)	(6430)	(6816)	(7231)
20	2.3E-10	9.4E-10	6.7E-9	9.9E-6	3.0E-4	1.2E-3	2.9E-4	4.4E-4	8.9E-6	2.5E-4	1.5E-4
	(4003)	(4196)	(4403)	(4624)	(4862)	(5116)	(5389)	(5681)	(5993)	(6327)	(6683)

Values in brackets show the band origin in Å.

Table 5.6: Overhead intensities (in R) of N_2 Second Positive ($C^3\Pi_u \rightarrow B^3\Pi_g$) band on Mars standard case.

$\nu' \setminus \nu''$	0	1	2	3	4	5	6	7	8	9
0	3.2E+1	2.2E+1	8.8E+0	2.7E+0	7.2E-1	1.7E-1	3.8E-2	8.1E-3	1.7E-3	3.3E-4
	(3370)	(3576)	(3804)	(4058)	(4343)	(4665)	(5032)	(5452)	(5938)	(6507)
1	8.3E+0	4.1E-1	3.9E+0	3.5E+0	1.7E+0	6.3E-1	1.9E-1	5.4E-2	1.4E-2	3.3E-3
	(3158)	(3338)	(3536)	(3754)	(3997)	(4268)	(4573)	(4317)	(5309)	(5759)
2	9.7E-1	2.5E+0	2.0E-1	4.2E-1	9.9E-1	7.7E-1	3.8E-1	1.5E-1	5.0E-2	1.5E-2
	(2976)	(3135)	(3309)	(3499)	(3709)	(3942)	(4200)	(4489)	(4813)	(5180)
3	3.7E-2	5.2E-1	4.2E-1	2.0E-1	8.1E-3	1.7E-1	2.1E-1	1.4E-1	6.9E-2	2.8E-2
	(2818)	(2961)	(3115)	(3284)	(3468)	(3671)	(3894)	(4140)	(4415)	(4722)
4	2.6E-4	2.5E-2	1.7E-1	5.7E-2	7.0E-2	2.3E-3	1.9E-2	4.4E-2	4.0E-2	2.3E-2
	(2684)	(2812)	(2952)	(3102)	(3266)	(3445)	(3641)	(3856)	(4093)	(4355)

$\nu' \setminus \nu''$	10	11	12	13	14	15	16	17	18	19	20
0	6.4E-5	1.2E-5	2.1E-6	3.4E-7	5.1E-8	6.6E-9	6.7E-10	3.7E-11	2.8E-15	1.3E-12	3.8E-13
	(7181)	(7992)	(8985)	(10228)	(11828)	(13962)	(16944)	(21403)	(28779)	(43302)	(84991)
1	7.5E-4	1.7E-4	3.5E-5	7.1E-6	1.3E-6	2.3E-13	3.4E-8	3.8E-9	2.2E-10	1.1E-13	1.1E-11
	(6281)	(6893)	(7619)	(8495)	(9571)	(10921)	(12665)	(15000)	(18285)	(23236)	(31536)
2	4.2E-3	1.1E-3	2.7E-4	6.6E-5	1.5E-5	3.2E-6	6.2E-7	1.1E-7	1.4E-8	1.2E-9	8.8E-12
	(5599)	(6080)	(6638)	(7293)	(8071)	(9011)	(10166)	(11618)	(13495)	(16014)	(19563)
3	9.7E-3	3.1E-3	9.1E-4	2.5E-4	6.8E-5	1.7E-5	4.1E-6	8.9E-7	1.7E-7	2.8E-8	3.5E-9
	(5067)	(5458)	(5904)	(6416)	(7011)	(7709)	(8539)	(9541)	(10771)	(12317)	(14315)
4	1.1E-2	4.4E-3	1.6E-3	5.2E-4	1.6E-4	4.7E-5	1.3E-5	3.5E-6	8.5E-7	1.9E-7	3.6E-8
	(4648)	(4974)	(5342)	(5758)	(6233)	(6778)	(7412)	(8155)	(9037)	(10101)	(11406)

Values in brackets show the band origin in Å.

Table 5.7: Overhead intensities (in R) of N_2 $E^3\Sigma_g^+ \to A^3\Sigma_u^+$, $E^3\Sigma_g^+ \to B^3\Pi_g$, and $E^3\Sigma_g^+ \to C^3\Pi_u$ bands on Mars standard case.

$\nu' \setminus \nu''$	0	1	2	3	4	5	6	7	8	9	10	
					$E^3\Sigma_g^+ \to A^3\Sigma_u^+$							
0	2.0E-2	6.2E-2	1.0E-1	1.1E-1	9.1E-2	6.2E-2	3.5E-2	1.7E-2	7.3E-3	2.7E-3	8.6E-4	
	(2173)	(2243)	(2316)	(2392)	(2472)	(2555)	(2643)	(2734)	(2830)	(2930)	(3035)	
1	6.0E-3	1.4E-2	1.5E-2	1.1E-2	4.8E-3	1.2E-3	8.7E-5	4.4E-5	1.9E-4	2.3E-4	1.7E-4	
	(2074)	(2138)	(2204)	(2273)	(2345)	(2420)	(2498)	(2580)	(2665)	(2754)	(2846)	
					$E^3\Sigma_g^+ \to B^3\Pi_g$							
0	1.7E-2	2.5E-2	2.0E-2	1.3E-2	6.5E-3	3.0E-3	1.3E-3	4.9E-4	1.8E-4	6.6E-5	2.3E-5	
	(2742)	(2877)	(3022)	(3181)	(3353)	(3542)	(3749)	(3978)	(4230)	(4511)	(4826)	
1	1.3E-3	4.4E-4	2.2E-6	1.3E-4	2.6E-4	2.6E-4	1.8E-4	1.0E-4	5.1E-5	2.4E-5	1.0E-5	
	(2587)	(2707)	(2835)	(2974)	(3124)	(3288)	(3465)	(3660)	(3872)	(4107)	(4365)	
					$E^3\Sigma_g^+ \to C^3\Pi_u$							
0	2.9E-1	2.5E-2	9.0E-4	5.8E-6	–	–	–	–	–	–	–	–
	(14713)	(20824)	(34947)	(101275)	–	–	–	–	–	–	–	
1	5.2E-3	5.0E-3	1.2E-3	8.6E-5	1.6E-6	–	–	–	–	–	–	
	(11134)	(14312)	(19816)	(31522)	(71884)	–	–	–	–	–	–	

Values in brackets show the band origin in Å.

Table 5.8: Overhead intensities (in R) of N_2 Reverse First Positive ($A^3\Sigma_u^+ \rightarrow B^3\Pi_g$) band on Mars for standard case.

$\nu' \setminus \nu''$	0	1	2	3	4	5	6	7	8
8	7.5E+0	–	–	–	–	–	–	–	–
	(88467)	–	–	–	–	–	–	–	–
9	1.1E+1	4.0E+0	–	–	–	–	–	–	–
	(42771)	(158042)	–	–	–	–	–	–	–
10	5.0E+0	1.4E+1	5.2E-2	–	–	–	–	–	–
	(28438)	(55215)	(741757)	–	–	–	–	–	–
11	1.6E+0	9.6E+0	7.8E+0	–	–	–	–	–	–
	(21436)	(33788)	(77920)	–	–	–	–	–	–
12	5.0E-1	4.4E+0	1.0E+1	2.0E+0	–	–	–	–	–
	(17292)	(24523)	(41640)	(132578)	–	–	–	–	–
13	1.4E-1	1.6E+0	6.2E+0	6.4E+0	5.1E-2	–	–	–	–
	(14555)	(19361)	(28664)	(54305)	(448147)	–	–	–	–
14	4.1E-2	5.6E-1	2.9E+0	5.8E+0	2.5E+0	–	–	–	–
	(12617)	(16076)	(22007)	(34521)	(78216)	–	–	–	–
15	1.2E-2	1.9E-1	1.2E+0	3.6E+0	4.1E+0	4.6E-1	–	–	–
	(11175)	(13806)	(17964)	(25513)	(43455)	(140462)	–	–	–
16	3.7E-3	6.5E-2	4.8E-1	1.8E+0	3.3E+0	1.9E+0	3.3E-3	–	–
	(10063)	(12148)	(15254)	(20373)	(30393)	(58790)	(710500)	–	–
17	1.2E-3	2.2E-2	1.8E-1	8.3E-1	2.0E+0	2.3E+0	5.4E-1	–	–
	(9181)	(10886)	(13316)	(17057)	(23560)	(37662)	(91328)	–	–
18	3.8E-4	7.6E-3	7.0E-2	3.6E-1	1.1E+0	1.8E+0	1.2E+0	4.4E-2	–
	(8468)	(9897)	(11865)	(14747)	(19370)	(27985)	(49675)	(207470)	–
19	1.2E-4	2.7E-3	2.6E-2	1.5E-1	5.4E-1	1.2E+0	1.3E+0	4.0E-1	–
	(7880)	(9103)	(10763)	(13052)	(16548)	(22452)	(34558)	(73390)	–
20	4.2E-5	9.5E-4	1.0E-2	6.3E-2	2.6E-1	6.7E-1	1.0E+0	6.8E-1	5.4E-2
	(7390)	(8456)	(9852)	(11761)	(14525)	(18884)	(26773)	(45371)	(142399)

Values in brackets show the band origin in Å.

Table 5.9: Overhead intensities (in R) of N_2 $B'^3\Sigma_u^- \rightarrow B^3\Pi_g$ band on Mars standard case.

$\nu' \setminus \nu''$	0	1	2	3	4	5	6	7	8	9
0	7.1E-2	2.1E-2	1.5E-3	2.1E-5	–	–	–	–	–	–
	(15280)	(20664)	(31616)	(65977)	–	–	–	–	–	–
1	3.8E-1	1.8E-2	6.6E-2	1.0E-2	1.9E-4	–	–	–	–	–
	(12442)	(15793)	(21479)	(33241)	(71941)	–	–	–	–	–
2	6.3E-1	5.3E-1	2.0E-2	7.8E-2	2.5E-2	6.1E-4	–	–	–	–
	(10520)	(12820)	(16329)	(22337)	(34981)	(78778)	–	–	–	–
3	5.8E-1	1.4E+0	2.9E-1	1.6E-1	4.6E-2	3.7E-2	1.1E-3	–	–	–
	(9132)	(10816)	(13212)	(16887)	(23237)	(36843)	(86653)	–	–	–
4	3.6E-1	1.6E+0	1.5E+0	3.6E-2	2.9E-1	1.1E-2	3.9E-2	1.5E-3	–	–
	(8083)	(9375)	(11123)	(13618)	(17468)	(24181)	(38831)	(95765)	–	–
5	1.8E-1	1.2E+0	2.3E+0	9.8E-1	2.5E-2	3.2E-1	1.8E-4	3.2E-2	1.5E-3	–
	(7262)	(8289)	(9626)	(11440)	(14040)	(18072)	(25169)	(40949)	(106355)	–
6	7.3E-2	6.7E-1	2.0E+0	2.2E+0	3.9E-1	1.7E-1	2.4E-1	1.1E-2	2.2E-2	1.3E-3
	(6603)	(7441)	(8501)	(9886)	(11769)	(14476)	(18699)	(26201)	(43199)	(118707)
7	2.6E-2	3.1E-1	1.3E+0	2.4E+0	1.6E+0	6.3E-2	3.0E-1	1.3E-1	2.7E-2	1.2E-2
	(6062)	(6761)	(7625)	(8721)	(10154)	(12107)	(14927)	(19349)	(27275)	(45581)
8	8.4E-3	1.2E-1	6.7E-1	1.8E+0	2.2E+0	8.3E-1	3.3E-3	3.2E-1	5.4E-2	3.5E-2
	(5610)	(6204)	(6924)	(7815)	(8947)	(10430)	(12457)	(15392)	(20021)	(28389)
9	2.6E-3	4.3E-2	2.9E-1	1.0E+0	1.9E+0	1.6E+0	3.1E-1	7.0E-2	2.6E-1	1.3E-2
	(5227)	(5739)	(6350)	(7092)	(8011)	(9180)	(10714)	(12817)	(15872)	(20712)
10	7.4E-4	1.4E-2	1.1E-1	4.9E-1	1.2E+0	1.6E+0	9.5E-1	6.6E-2	1.4E-1	1.7E-1
	(4890)	(5345)	(5872)	(4500)	(7264)	(8213)	(9419)	(11007)	(13187)	(16364)
11	2.1E-4	4.4E-3	4.0E-2	2.1E-1	6.5E-1	1.2E+0	1.2E+0	4.6E-1	7.7E-4	1.6E-1
	(4614)	(5008)	(5467)	(6008)	(6655)	(7442)	(8420)	(9666)	(11308)	(13566)
12	5.6E-5	1.3E-3	1.3E-2	8.0E-2	3.0E-1	7.1E-1	1.0E+0	7.7E-1	1.8E-1	1.5E-2
	(4365)	(4716)	(5121)	(5592)	(6149)	(6815)	(7625)	(8633)	(9919)	(11616)
13	1.5E-5	3.8E-4	4.3E-3	2.9E-2	1.2E-1	3.6E-1	6.7E-1	7.6E-1	4.2E-1	4.4E-2
	(4145)	(4460)	(4821)	(5236)	(5721)	(6294)	(6979)	(7817)	(8853)	(10179)
14	4.0E-6	1.1E-4	1.3E-3	9.8E-3	4.8E-2	1.6E-1	3.7E-1	5.6E-1	5.0E-1	2.0E-1
	(3950)	(4235)	(4559)	(4929)	(5356)	(5854)	(6443)	(7148)	(8007)	(9078)
15	1.0E-6	3.0E-5	4.0E-4	3.2E-3	1.8E-2	6.7E-2	1.8E-1	3.4E-1	4.2E-1	2.9E-1
	(3775)	(4035)	(4328)	(4660)	(5040)	(5479)	(5991)	(6596)	(7322)	(8206)
16	2.7E-7	8.3E-6	1.2E-4	1.0E-3	6.1E-3	2.6E-2	8.0E-2	1.8E-1	2.8E-1	2.8E-1
	(3619)	(3857)	(4123)	(4424)	(4765)	(5155)	(5606)	(6132)	(6754)	(7500)
17	6.9E-8	2.3E-6	3.4E-5	3.2E-4	2.1E-3	9.6E-3	3.3E-2	8.5E-2	1.6E-1	2.1E-1
	(3477)	(3696)	(3940)	(4214)	(4522)	(4872)	(5273)	(5737)	(6277)	(6917)
18	1.7E-8	6.1E-7	9.8E-6	9.8E-5	6.8E-4	3.4E-3	1.3E-2	3.8E-2	8.2E-2	1.3E-1
	(3349)	(3552)	(3776)	(4027)	(4308)	(4624)	(4984)	(5395)	(5871)	(6427)
19	4.1E-9	1.6E-7	2.8E-6	2.9E-5	2.2E-4	1.2E-3	4.9E-3	1.6E-2	3.9E-2	7.2E-2
	(3232)	(3420)	(3629)	(3859)	(4116)	(4404)	(4729)	(5099)	(5521)	(6010)
20	8.8E-10	3.9E-8	7.5E-7	8.7E-6	6.9E-5	4.0E-4	1.8E-3	6.3E-3	1.7E-2	3.6E-2
	(3125)	(3301)	(3495)	(3708)	(3945)	(4209)	(4504)	(4838)	(5217)	(5651)

Values in brackets show the band origin in Å.

Table 5.9: contd.

$\nu' \setminus \nu''$	10	11	12	13	14	15	16	17	18	19	20
7	9.5E-4	–	–	–	–	–	–	–	–	–	–
	(133152)	–	–	–	–	–	–	–	–	–	–
8	5.9E-3	6.1E-4	–	–	–	–	–	–	–	–	–
	(48087)	(150065)	–	–	–	–	–	–	–	–	–
9	3.5E-2	2.3E-3	3.6E-4	–	–	–	–	–	–	–	–
	(29540)	(50709)	(169831)	–	–	–	–	–	–	–	–
10	6.7E-4	2.8E-2	7.3E-4	2.0E-4	–	–	–	–	–	–	–
	(21422)	(30723)	(53427)	(192800)	–	–	–	–	–	–	–
11	9.6E-2	1.1E-3	2.0E-2	1.5E-4	1.0E-4	–	–	–	–	–	–
	(16868)	(22148)	(31929)	(56215)	(219162)	–	–	–	–	–	–
12	1.4E-1	4.5E-2	4.6E-3	1.3E-2	8.8E-6	5.2E-5	–	–	–	–	–
	(13955)	(17383)	(22886)	(33152)	(59037)	(248754)	–	–	–	–	–
13	4.0E-2	1.0E-1	1.7E-2	6.8E-3	7.8E-3	6.1E-6	2.6E-5	–	–	–	–
	(11932)	(14352)	(17907)	(23633)	(34378)	(61844)	(280746)	–	–	–	–
14	3.7E-3	5.2E-2	6.4E-2	4.9E-3	7.0E-3	4.4E-3	2.7E-5	1.3E-5	–	–	–
	(10446)	(12255)	(14756)	(18437)	(24383)	(35595)	(64575)	(313255)	–	–	–
15	7.7E-2	1.3E-3	4.9E-2	3.6E-2	7.4E-4	6.0E-3	2.4E-3	3.8E-5	6.9E-6	–	–
	(9308)	(10718)	(12584)	(15166)	(18972)	(25131)	(36786)	(67157)	(343066)	–	–
16	1.5E-1	2.2E-2	8.2E-3	3.9E-2	1.8E-2	7.3E-10	4.6E-3	1.2E-3	3.8E-5	3.9E-6	–
	(8410)	(9545)	(10996)	(12918)	(15581)	(19507)	(25869)	(37932)	(69506)	(365813)	–
17	1.7E-1	7.2E-2	3.4E-3	1.3E-2	2.7E-2	8.2E-3	2.4E-4	3.2E-3	6.2E-4	3.1E-5	2.5E-6
	(7683)	(8619)	(9786)	(11280)	(13258)	(15997)	(20039)	(26589)	(39011)	(71531)	(376997)
18	1.4E-1	9.8E-2	2.9E-2	7.8E-9	1.4E-2	1.7E-2	3.3E-3	5.4E-4	2.1E-3	3.0E-4	2.3E-5
	(7084)	(7872)	(8834)	(10033)	(11568)	(13600)	(16414)	(20564)	(27283)	(40001)	(73141)
19	9.8E-2	9.2E-2	5.0E-2	9.1E-3	1.2E-3	1.2E-2	9.6E-3	1.1E-3	6.6E-4	1.3E-3	1.5E-4
	(6581)	(7255)	(8065)	(9052)	(10284)	(11859)	(13944)	(16829)	(21077)	(27939)	(40875)
20	5.9E-2	6.9E-2	5.5E-2	2.3E-2	2.0E-3	2.6E-3	8.6E-3	5.1E-3	2.9E-4	6.2E-4	8.2E-4
	(6153)	(6739)	(7432)	(8262)	(9276)	(10539)	(12154)	(14289)	(17238)	(21572)	(28548)

Values in brackets show the band origin in Å.

Table 5.10: Overhead intensities (in R) of N_2 Wu-Benesch ($W^3\Delta_u \rightarrow B^3\Pi_g$) band on Mars standard case.

$\nu' \setminus \nu''$	0	1	2	3	4	5	6	7	8	9
0	1.3E+0	–	–	–	–	–	–	–	–	–
	(1361044)	–	–	–	–	–	–	–	–	–
1	2.9E+0	–	–	–	–	–	–	–	–	–
	(64311)	–	–	–	–	–	–	–	–	–
2	4.1E+0	4.6E-1	–	–	–	–	–	–	–	–
	(33206)	(76556)	–	–	–	–	–	–	–	–
3	3.5E+0	3.0E+0	5.5E-2	–	–	–	–	–	–	–
	(22505)	(36522)	(94180)	–	–	–	–	–	–	–
4	2.1E+0	5.1E+0	1.5E+0	1.1E-3	–	–	–	–	–	–
	(17092)	(24124)	(40502)	(121693)	–	–	–	–	–	–
5	1.1E+0	4.7E+0	4.5E+0	5.3E-1	1.1E-3	–	–	–	–	–
	(13825)	(18090)	(25962)	(45362)	(170594)	–	–	–	–	–
6	4.8E-1	3.1E+0	5.8E+0	2.9E+0	1.1E-1	9.2E-4	–	–	–	–
	(11639)	(14521)	(19193)	(28067)	(51426)	(281484)	–	–	–	–
7	1.8E-1	1.6E+0	4.7E+0	5.1E+0	1.4E+0	5.2E-3	6.4E-5	–	–	–
	(10075)	(12165)	(15281)	(20421)	(30501)	(59196)	(774629)	–	–	–
8	6.1E-2	6.9E-1	2.9E+0	5.2E+0	3.5E+0	4.9E-1	3.2E-3	–	–	–
	(8900)	(10493)	(12732)	(16112)	(21794)	(33343)	(69497)	–	–	–
9	1.9E-2	2.7E-1	1.4E+0	3.7E+0	4.4E+0	2.0E+0	1.1E-1	9.1E-3	–	–
	(7986)	(9246)	(10941)	(13347)	(17024)	(23339)	(36704)	(83791)	–	–
10	5.8E-3	9.4E-2	6.2E-1	2.1E+0	3.7E+0	3.1E+0	8.7E-1	9.2E-3	7.2E-3	–
	(7255)	(8280)	(9614)	(11424)	(14014)	(18030)	(25088)	(40735)	(104922)	–
11	1.7E-3	3.1E-2	2.4E-1	1.0E+0	2.4E+0	3.1E+0	1.9E+0	3.0E-1	1.2E-3	3.2E-3
	(6658)	(7511)	(8592)	(10009)	(11943)	(14742)	(19145)	(27084)	(45654)	(139282)
12	4.7E-4	9.6E-3	8.6E-2	4.3E-1	1.3E+0	2.3E+0	2.2E+0	9.3E-1	7.4E-2	7.9E-3
	(6160)	(6883)	(7781)	(8925)	(10432)	(12505)	(15536)	(20386)	(29381)	(51783)
13	1.3E-4	2.9E-3	2.9E-2	1.7E-1	6.0E-1	1.4E+0	1.9E+0	1.4E+0	4.0E-1	8.5E-3
	(5740)	(6363)	(7122)	(8069)	(9281)	(10886)	(13114)	(16408)	(21774)	(32050)
14	3.7E-5	9.1E-4	1.0E-2	6.6E-2	2.8E-1	7.5E-1	1.3E+0	1.4E+0	8.1E-1	1.5E-1
	(5380)	(5924)	(6577)	(7376)	(8375)	(9661)	(11376)	(13776)	(17369)	(23337)
15	8.9E-6	2.4E-4	3.0E-3	2.2E-2	1.0E-1	3.2E-1	7.1E-1	1.0E+0	8.6E-1	3.6E-1
	(5069)	(5549)	(6118)	(6803)	(7645)	(8702)	(10070)	(11905)	(14497)	(18431)
16	2.2E-6	6.7E-5	9.0E-4	7.2E-3	3.8E-2	1.4E-1	3.6E-1	6.3E-1	7.3E-1	4.9E-1
	(4798)	(5225)	(5727)	(6323)	(7044)	(7932)	(9052)	(10509)	(12478)	(15286)
17	5.4E-7	1.8E-5	2.7E-4	2.3E-3	1.4E-2	5.6E-2	1.6E-1	3.5E-1	5.1E-1	4.8E-1
	(4559)	(4943)	(5390)	(5915)	(6541)	(7300)	(8238)	(9427)	(10982)	(13100)
18	1.2E-7	4.6E-6	7.6E-5	7.2E-4	4.7E-3	2.1E-2	7.1E-2	1.7E-1	3.0E-1	3.7E-1
	(4347)	(4695)	(5096)	(5564)	(6114)	(6772)	(7572)	(8565)	(9830)	(11493)
19	2.3E-8	1.1E-6	2.0E-5	2.2E-4	1.5E-3	7.7E-3	2.9E-2	7.9E-2	1.6E-1	2.4E-1
	(4159)	(4476)	(4839)	(5259)	(5748)	(6325)	(7018)	(7863)	(8916)	(10263)
20	3.2E-9	2.3E-7	5.1E-6	6.2E-5	4.9E-4	2.7E-3	1.1E-2	3.4E-2	8.0E-2	1.4E-1
	(3990)	(4281)	(4612)	(4991)	(5430)	(5943)	(6550)	(7280)	(8174)	(9292)

Values in brackets show the band origin in Å.

Table 5.10: contd.

$\nu' \setminus \nu''$	10	11	12	13	14	15	16	17
12	8.1E-4	–	–	–	–	–	–	–
	(204814)	–	–	–	–	–	–	–
13	9.0E-3	8.8E-5	–	–	–	–	–	–
	(59621)	(378656)	–	–	–	–	–	–
14	1.0E-4	6.6E-3	2.9E-7	–	–	–	–	–
	(35186)	(69984)	(2189094)	–	–	–	–	–
15	3.6E-2	3.2E-3	3.1E-3	–	–	–	–	–
	(25109)	(38919)	(84300)	–	–	–	–	–
16	1.5E-1	5.1E-3	4.7E-3	1.2E-3	–	–	–	–
	(19612)	(27132)	(43431)	(105325)	–	–	–	–
17	2.6E-1	5.2E-2	1.4E-5	3.9E-3	3.3E-4	–	–	–
	(16153)	(20931)	(29461)	(48989)	(139141)	–	–	–
18	2.9E-1	1.2E-1	1.4E-2	8.6E-4	2.4E-3	6.2E-5	–	–
	(13778)	(17109)	(22413)	(32169)	(55990)	(202357)	–	–
19	2.5E-1	1.6E-1	4.9E-2	2.4E-3	1.7E-3	1.2E-3	5.6E-6	–
	(12047)	(14519)	(18167)	(24089)	(35352)	(65067)	(362190)	–
20	1.8E-1	1.5E-1	7.9E-2	1.7E-2	5.9E-5	1.6E-3	5.1E-4	3.4E-8
	(10731)	(12649)	(15332)	(19345)	(25997)	(39142)	(77278)	(1546312)

Values in brackets show the band origin in Å.

5.4 N_2 triplet band emissions on Venus

The Ultraviolet emissions of Venus have been studied for decades by rocket-borne spectrometers, Mariner 10, Venera 11 and 12, and Galileo spacecraft flybys, Pioneer Venus Orbiter, and Hopkins Ultraviolet Telescope aboard Space Shuttle [e.g., *Fox and Bougher*, 1991; *Paxton and Anderson*, 1992; *Feldman et al.*, 2000; *Gérard et al.*, 2008a]. More recently, Venusian UV emissions observed during the Cassini flyby have been reported [*Gérard et al.*, 2011a; *Hubert et al.*, 2010]. The major UV emissions observed by several space missions are from H, He, C, N, O, CO, and CO_2^+. However, so far no N_2 emissions have been observed on Venus. As mentioned in Section 5.3, SPICAM on-board MEx has observed, for the first time, emissions from N_2 VK on Mars. The main emissions observed are the (0, 6) and (0, 5) bands of the VK transitions of N_2 [*Leblanc et al.*, 2006, 2007]. On Venus, the VK bands would be more intense compared to those on Mars because of its proximity to the Sun and higher N_2 abundances. SPICAV on VEx orbiter mission, which is similar to SPICAM, can observe these emissions in the Venusian dayglow.

The model developed for the calculation of N_2 triplet band emissions on Mars is employed to calculate the N_2 dayglow emission on Venus for solar maximum and minimum conditions. In the following sections the results of model calculation of N_2 triplet band emission on Venus are discussed. Calculation of photoelectron flux and its comparison with observation are presented in Sections 5.4.2, followed by volume emission rate and limb profiles of N_2 triplet band emission in Section 5.4.3.

5.4.1 Model input parameters

The model atmosphere considering five gases (CO_2, CO, N_2, O, and O_2) is taken from the VTS3 model of *Hedin et al.* [1983] for the low (F10.7 = 80) and high (F10.7 = 200) solar activity conditions. The EUVAC model of *Richards et al.* [1994] has been used to calculate the 37-bin solar EUV flux, which is based on the F10.7 solar index. The EUVAC solar spectrum is scaled for the heliocentric distance of Venus (0.72 AU). All calculations are made at SZA = 60° unless otherwise noted. Other input parameters remains same as discussed in Section 5.3.1.

5.4.2 Photoelectron flux on Venus

The photoelectron flux on Venus is calculated in the same manner as described in Section 5.3.2. Model calculated photoelectron fluxes at 130, 150, and 250 km altitudes for solar minimum condition at SZA=60°, are shown in the upper panel of Figure 5.12. The peak structures in the calculated photoelectron flux on Venus is similar to that on Mars since CO_2 is the dominant gas on both planets. Peak structures around 20-30 eV are clearly seen in the photoelectron flux at 150 km, whereas they are smoothed

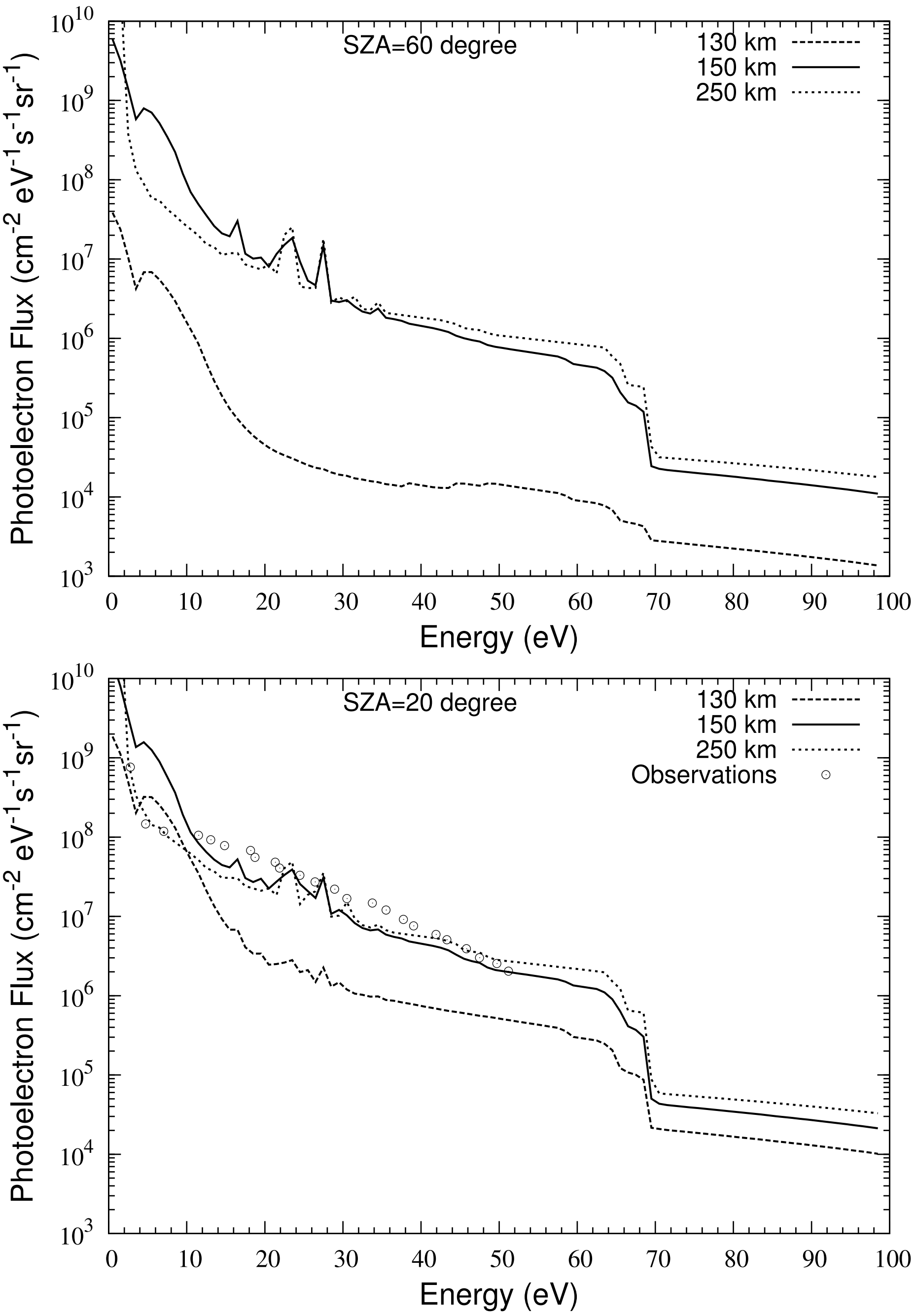

Figure 5.12: Model calculated photoelectron flux on Venus for low (upper panel) and high (bottom panel) solar activity conditions at 130, 150, and 230 km. Symbols in bottom panel represent the Pioneer Venus Orbiter-observed values averaged over 206-296 km and 8°-35° SZA, taken from *Spenner et al.* [1997].

out at 130 km, indicating that solar He II Lyman α photons are largely degraded at higher altitudes and do not reach altitudes of 130 km. The calculated flux decreases exponentially with increasing energy.

Figure 5.12 (bottom panel) shows the calculated photoelectron fluxes for solar maximum condition (F10.7=200) at SZA = 20°. The photoelectron flux features are similar to those in solar minimum conditions. This figure also shows the electron flux measured by the Pioneer Venus Orbiter Retarded Potential Analyser [*Spenner et al.*, 1997]. A good agreement both in shape and magnitude, is observed between the calculated and measured fluxes. *Spenner et al.* [1997] found that the average electron fluxes do not vary much for SZA between 0° and 70°.

5.4.3 Volume emission rate and limb intensity of N_2 triplet bands on Venus

Figure 5.13 shows the excitation rates of N_2 triplet states (A, B, C, W, B', and E) by photoelectron impact excitation. During both solar minimum and maximum conditions, excitation rate for all the states peaks at ∼135–140 km. However, at the peak, the excitation rates during solar maximum are higher by a factor of 2 than that during solar minimum.

After calculating the steady state density of different vibrational levels of excited triplet states of N_2 as described in Section 5.3.3, the volume emission rate $V^{\alpha\beta}_{\nu'\nu''}$ of a vibration band $\nu' \rightarrow \nu''$ is calculated using Eq. 5.1. Volume emission rates are height-integrated to calculate the overhead intensities. Table 5.11 shows the total overhead intensity for triplet transitions of N_2 during low and high solar activity at SZA=60° calculated by adding all the band emissions. Table 5.13 shows the nadir intensity (SZA=60°) during solar minimum and maximum conditions for the prominent VK bands of N_2; for other triplet emissions (viz., First Positive, Second Positive, and Wu-Benesch) overhead intensities are given in Table 5.12. The increase in the VK band intensity from solar minimum to maximum is ∼60–70%. The strongest VK band emissions (0, 5), (0, 6), (0, 7), (0, 8), (1, 9), and (1, 10) have intensities of 94 (160), 120 (204), 114 (194), 94 (155), and 88 (145) R, respectively, during solar minimum (maximum) condition.

On Venus, the overhead intensity of N_2 VK band is about 60% smaller than that of N_2 First Positive band (see Table 5.11), whereas on Mars, the intensity of N_2 VK band is about 5% higher than that of First Positive band. Since the N_2(A) state gets effectively quenched by atomic oxygen compared to other triplet states, the density of N_2(A) state on Mars does not get quenched as effectively as on Venus due to higher concentration of atomic oxygen on Venus compared to that on Mars. The large quenching of N_2(A) state on Venus is responsible for lower N_2 VK band intensity on Venus compared to 1P band emission.

The calculated band emission rate can be integrated along the line of sight at a projected distance from the centre of Venus to obtain limb profiles. Figure 5.14 shows the limb profiles of VK (0, 6) band at SZA of 0° and 60° for solar minimum and maximum conditions. In the case of solar minimum, the limb profile peaks at 133 (136) km for SZA=0° (60°), with a value of ∼10 (∼5) kR. During high solar activity, the peak value of ∼20 (∼10) kR in the profiles occurs at 131 (134 km) for SZA=0° (60°). Thus, the intensity increases by a factor of 2 at the peak for a low to high solar activity change.

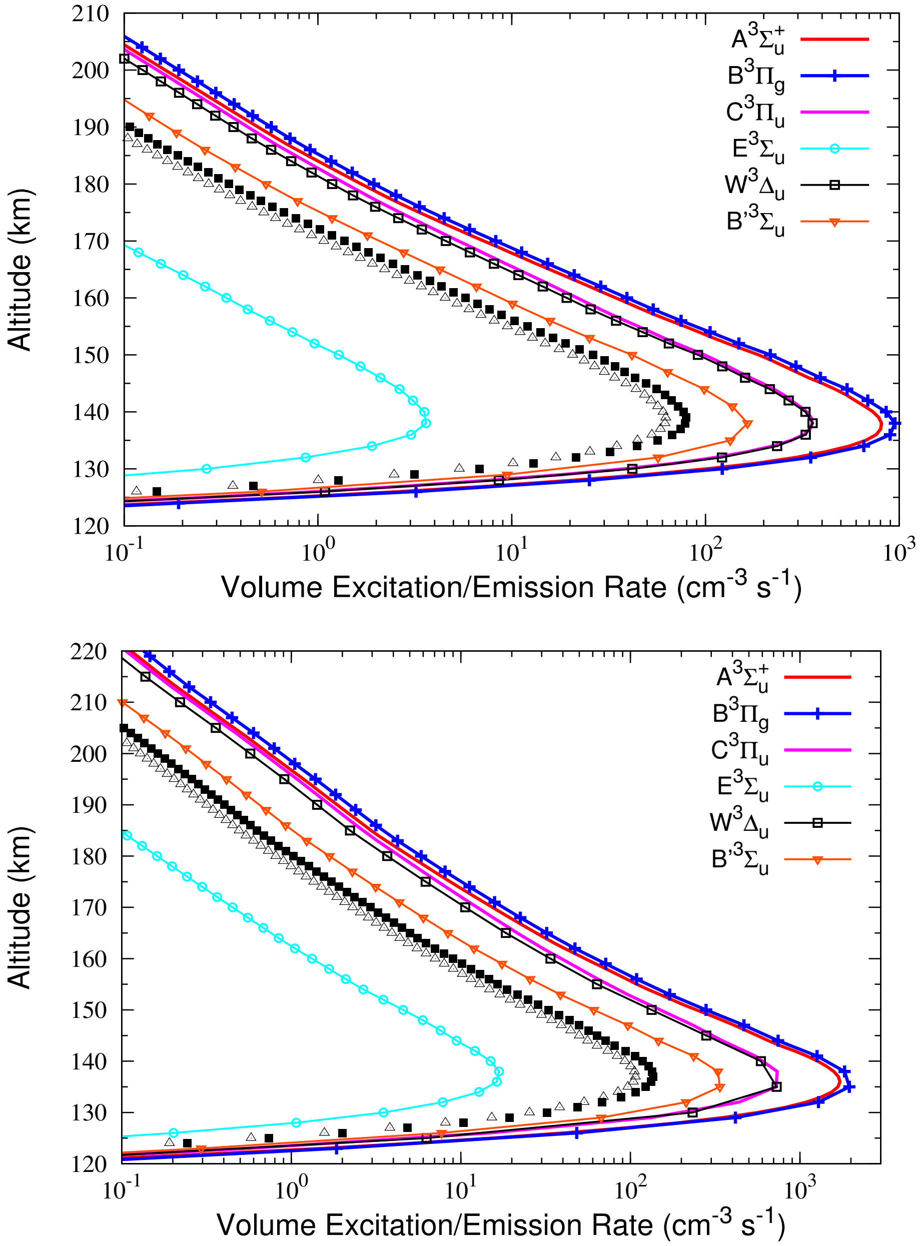

Figure 5.13: Volume excitation rates of various triplet states of N_2 on Venus by direct electron impact excitation in solar minimum (upper panel) and maximum (bottom panel) conditions at SZA = 60°. The rate of $E^3\Sigma_u$ state is plotted after multiplying by 2. Solid square and open triangle represent the volume emission rates of the VK (0, 6) and VK (0, 5) bands, respectively.

The effect of the SZA is observed at lower altitudes (<160 km) only. Above 150 km the shape of the limb profile in minimum and maximum condition are different, which is due to the difference in the Venus model atmosphere in the two solar conditions. The limb intensities of the VK (0, 4), (0, 5), and (0, 7) bands are also calculated in the model. The shape of the limb profiles of VK (0, 4), (0, 5), and (0, 7) bands are similar to that of the VK (0, 6) band, but their limb intensity at the peak is around 44, 78, and 95%,

Table 5.11: Height-integrated overhead intensities of triplet transitions of N_2 on Venus.

Band	Intensity (kR)	
	Min*	Max.†
Vegard-Kaplan ($A \rightarrow X$)	1.9 (1.5)	3.2
First Positive ($B \rightarrow A$)	3 (2.0)	6
Second Positive ($C \rightarrow B$)	0.4 (0.1)	0.8
Wu-Benesch ($W \rightarrow B$)	0.5 (0.4)	1.1
$B' \rightarrow B$	0.2 (0.08)	0.5
$E \rightarrow A$	3E-3 (3E-3)‡	7E-3
$E \rightarrow B$	5E-4 (5E-4)	1E-3
$E \rightarrow C$	2E-3 (2E-3)	4E-3
R1P§ ($A \rightarrow B$)	0.5 (0.4)	0.9

*Solar minimum (F10.7=80). Values in the bracket is for e-N_2 cross sections taken from *Johnson et al.* [2005].

†Solar maximum (F10.7=200).

‡3E-3 = 3×10^{-3}.

§Reverse First Positive.

respectively, of the limb intensity of the VK (0, 6) band at the peak.

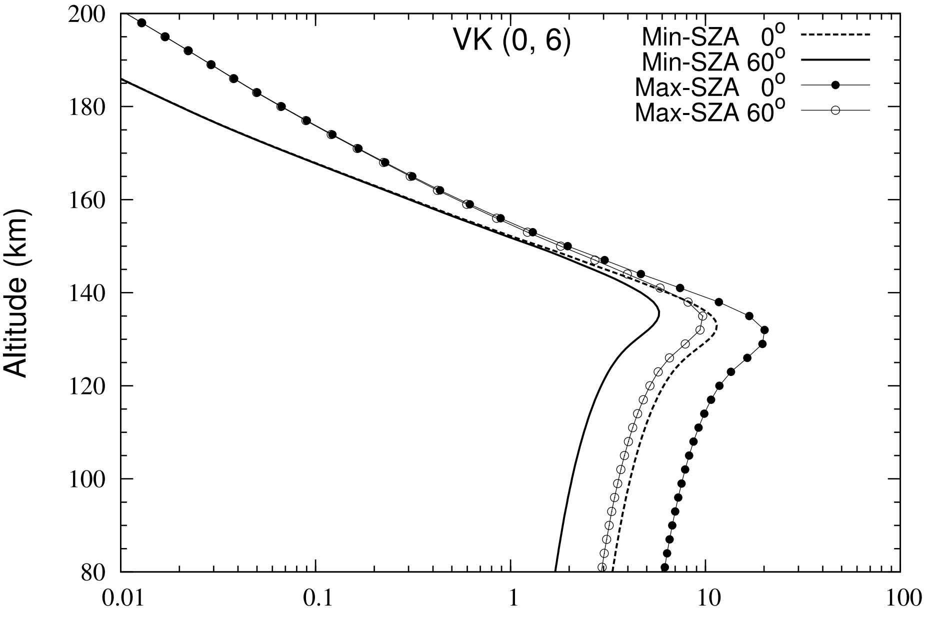

Figure 5.14: Calculated limb intensity of VK (0, 6) transition on Venus for low (min) and high (max) solar activity conditions, at SZA of 0° and 60°.

On Mars, the SPICAM has observed limb profiles of (0, 5) and (0, 6) bands of VK emissions, since they are the strong emissions below 3000 Å (see Table 5.13). The peak intensity of VK (0, 6) band on Mars is ~0.5 kR [*Leblanc et al.*, 2007]. This value is about a factor of 10 lower than that calculated on Venus during low solar activity. Only a factor

Table 5.12: Calculated height-integrated overhead intensity of N_2 triplet emissions on Venus.

Band	Band Origin	Intensity (R)		Band	Band Origin	Intensity (R)	
($\nu' - \nu''$)	Å	Min.*	Max.†	($\nu' - \nu''$)	Å	Min.*	Max.†
First Positive $B^3\Pi_g$– $A^3\Sigma_u^+$				Reverse first positive ($A^3\Sigma_u^+$– $B^3\Pi_g$)			
0-0	10469	229	465	9-0	42700	29	51
0-1	12317	123	250	10-1	55100	45	84
0-2	14895	37	75				
1-0	8883	367	744	Herman-Kaplan ($E^3\Sigma_g^+$– $A^3\Sigma_u^+$)			
1-2	11878	68	138	0-1	2243	0.35	0.8
1-3	14201	52	105	0-2	2316	0.57	1.3
2-0	7732	182	372	0-3	2392	0.63	1.4
2-1	8695	236	480	0-4	2472	0.52	1.2
2-2	9905	44	89				
2-4	13572	33	68	$E^3\Sigma_g^+$– $B^3\Pi_g$			
3-1	7606	252	515	0-1	2877	0.14	0.3
3-2	8516	66	135	0-2	3181	0.11	0.3
3-3	9648	79	162				
4-1	6772	77	158	$E^3\Sigma_g^+$– $C^3\Pi_u$			
4-2	7484	193	395	0-0	14713	1.7	3.8
4-4	9404	58	119	0-1	20824	0.14	0.3
5-2	6689	87	178				
5-3	7368	103	211	$B'^3\Sigma_u^-$– $B^3\Pi_g$			
6-3	6608	71	145	3-1	10816	5.4	11.2
7-4	6530	47	96	4-1	9375	6.3	13
Wu-Benesch ($W^3\Delta_u$– $B^3\Pi_g$)				4-2	8990	5.8	12.2
2-0	33206	16	34	5-2	9626	9.1	19
3-0	22505	14	29	6-2	8501	8	16.9
3-1	36522	12	25	6-3	9886	8.7	18.2
4-1	24124	21	43	8-4	8947	8.6	18
5-1	18090	19	40	9-4	8011	7.5	15.6
5-2	25962	18	38	9-5	9180	6.3	13
6-2	19193	23	49	10-4	7264	4.8	10.1
7-2	15281	19	39	10-5	8213	6.5	13.6
7-3	20421	21	43	Second Positive $C^3\Pi_u$– $B^3\Pi_g$			
8-3	16112	21	43	0-0	3370	137	291
9-3	13347	15	31	0-1	3576	92	196
9-4	17024	18	37	0-2	3804	37	79
10-4	14014	15	31	1-0	3158	35	75
10-5	18030	12.5	26	1-2	3536	16	35

*Solar minimum condition. †Solar maximum condition.

of 5 difference in intensity is expected due to the difference in heliocentric distances of Mars and Venus. A much larger difference is due to the higher N_2 density around the peak on Venus (138 km, 8×10^9 cm^{-3}) compared to that on Mars (126 km, 1.5×10^9 cm^{-3}); the N_2/CO_2 ratio being 0.12 on Venus and 0.03 on Mars at the intensity peak. However, at higher altitudes the density of N_2 on Mars is larger compared to that on

Table 5.13: N_2 Vegard-Kaplan Band ($A^3\Sigma_u^+ \rightarrow X^1\Sigma_g^+$) height-integrated overhead intensity on Venus.

Band $\nu' - \nu''$	Band Origin	Overhead Intensity (R) Min.*	 Max.†
0-2	2216	4	7
0-3	2334	20	34
0-4	2463	53	91
0-5	2605	94	160
0-6	2762	120	204
0-7	2937	114	194
0-8	3133	84	143
0-9	3354	49	84
1-3	2258	16	27
1-4	2379	24	40
1-8	2998	63	105
1-9	3200	94	155
1-10	3427	88	145
1-11	3685	59	97
1-12	3980	30	49
1-13	4321	12	19
2-10	3270	26	41
2-11	3503	54	86
2-12	3769	58	93
2-13	4074	41	66
3-12	3583	15	24
3-13	3857	37	60
3-14	4171	41	67
4-11	3198	16	26
4-15	4274	25	41
4-16	4650	26	42
5-17	4771	18	29
5-18	5229	16	26
6-19	5372	13	21
7-0	1689	11	18
8-0	1655	12	20
9-0	1622	9	16

*Solar minimum condition. †Solar maximum condition.

Venus; *e.g.*, at 200 km, the N_2 density at Mars and Venus is 7.5×10^6 and 2.4×10^6 cm^{-3}, respectively.

A detailed calculation on the effect of electron impact cross sections of N_2 on the calculated VK band intensities on Mars have been carried out in Section 5.3.6, which shows that the use of different electron impact cross sections can change the calculated VK band intensities up to 50%. The effect of using e-N_2 cross sections of *Johnson et al.* [2005] on the calculated overhead intensities of total VK, First Positive, Second Positive, and Wu-Benesch bands on Venus is shown in Table 5.11; intensities are smaller due to the lower cross sections of *Johnson et al.* [2005]. The effect of solar EUV flux models on N_2 triplet band emission intensity on Mars is discussed in Section 5.3.6.2 and shown in Table 5.3. A similar effect is found on Venus when S2K model of *Tobiska et al.* [2000] is used.

The intensities for triplet transitions are also calculated by taking the model atmosphere as used in *Fox and Dalgarno* [1981] for low solar activity at SZA = 45°. The calculated intensities for the VK bands are about 30% higher (similar results have been seen in the case of Mars also; cf. Section 5.3) than those of *Fox and Dalgarno* [1981], except for the VK (0, 2) band, which is a factor of ∼8 lower than the value of *Fox and Dalgarno* [1981]. Similar difference has been observed in the overhead intensity of VK (0, 2) band on Mars [see Secton 5.3 and also *Jain and Bhardwaj*, 2011]. The factor which controls the intensity of VK (0, 2) band is the transition probability for that band whose value is 3.54×10^{-3} in the model, taken from *Gilmore et al.* [1992]. *Piper* [1993] has also reported similar value for the VK (0, 2) band transition probability ($\sim 4.0 \times 10^{-3}$).

Differences between the present calculation and *Fox and Dalgarno* [1981] calculated overhead intensities of First Positive bands ($B \rightarrow A$) are between 10 and 50%; but for a few bands, *e.g.,* (2, 0), (2, 1), (3, 1), (4, 2), and (5, 3), the calculated intensities are a factor of 2 to 4 higher. For Second Positive bands ($C \rightarrow B$) the values for transitions from 0 level of C state, are ∼50% higher than the values of *Fox and Dalgarno* [1981] but for transitions from level 1, the values are ∼30% smaller than *Fox and Dalgarno* values. For Wu-Benesch ($W - B$) band the calculated values are smaller than those of *Fox and Dalgarno* [1981] by factor of 2 to 4. These differences are mainly due to updated transition probabilities used in the model which are taken from *Gilmore et al.* [1992]. *Piper* [1993] has also reported the transition probabilities of the VK bands, which are consistent with those of *Gilmore et al.* [1992].

5.5 N_2 VK band emissions on Titan

The Saturnian satellite Titan, the second biggest satellite in the solar system, is in many ways the closest analogue to Earth. Like Earth, Titan's atmosphere is dominated by N_2. Hence, it is natural to expect that Titan's airglow will be dominated by emissions of N_2 and its dissociation product N. In addition to N_2, Titan also contains a few percent CH_4 in its atmosphere, with a mixing ratio of about 3% near 1000 km altitude [*De La Haye et al.*, 2007; *Strobel et al.*, 2009].

The Voyager 1 Ultraviolet Spectrometer (UVS) provided the first UV airglow observation of Titan in the 53–170 nm band [*Broadfoot et al.*, 1981]. The EUV spectrum was dominated by emissions near 95–99 nm, which were attributed to N_2 Carroll-Yoshino (CY) $c_4'^1\Sigma_u^+ - X^1\Sigma_g^+$ (0, 0) and (0, 1) Rydberg bands [*Strobel and Shemansky*, 1982]. Far ultraviolet emissions present were LBH bands of N_2, and N and N^+ lines [*Broadfoot et al.*, 1981; *Strobel and Shemansky*, 1982]. By employing multiple scattering model for CY band emissions, *Stevens* [2001] showed that CY (0–0) should be weak and undetectable, while CY (0–1) should be prominent emission at 981 nm, and the features at 950 nm are N I lines. Thus, there is no need to invoke magnetospheric electron impact excitation [*Stevens*, 2001].

After Voyager UVS, Cassini UVIS provided the next observation of Titan's airglow in the EUV (56.1–118.2 nm) and FUV (115.5–191.3 nm) wavelengths [*Ajello et al.*, 2007, 2008]. These disk observations of Titan on 13 Dec. 2004 showed the presence of N_2 LBH bands, atomic multiplets of NI and N^+ lines, and features at 156.1 and 165.7 nm reportedly from CI [*Ajello et al.*, 2008]. Recently, limb observation of Titan by UVIS obtained on 22 June 2009 has revealed the presence of N_2 VK ($A^3\Sigma_u^+ - X^1\Sigma_g^+$) bands in the FUV spectrum [*Stevens et al.*, 2011]. Also, no CI emissions are reported to be observed. Model calculation of *Stevens et al.* [2011] showed a agreement in calculated and UVIS observed N_2 VK band emission intensity.

The model developed to calculate N_2 triplet band emissions in the dayglow of Mars and Venus is presented in Sections 5.3 and 5.4, respectively. This model is applied to Titan to calculate the N_2 triplet band dayglow emissions in Titan's atmosphere. On Mars, the model calculation showed that the N_2 density in the atmosphere of Mars should be reduced by a factor of ∼3 to bring the model calculated N_2 VK (0, 6) emission intensity in agreement with the SPICAM observation. The N_2 is a minor species (∼3%) in the atmospheres of Mars and Venus, which makes its measurement difficult in the two planets. Whereas atmosphere of Titan is mainly composed (∼97%) of N_2, which makes the N_2 density measurement on Titan more reliable [*De La Haye et al.*, 2007; *Strobel et al.*, 2009]. The aim of calculating the N_2 triplet band emissions on Titan is two-fold. Firstly, applying the present model to the N_2 dominated atmosphere, e.g., Titan's atmosphere, would help in ascertaining the performance of model. This exercise would consolidate the suggestion on Mars made in Section 5.3 regarding the reduction of N_2 density in Martian model atmosphere. Secondly, present calculation will help in better understanding of N_2 triplet band emissions on Titan.

The model calculation is carried out on Titan and volume emission rate and limb profiles of N_2 VK bands are discussed in following Section.

5.5.1 Results and discussion

To compare the calculated photoelectron flux with Cassini observations the model calculation are carried out by taking the HASI N_2 density and S2K solar EUV flux on 5 January 2008 (F10.7 = 79.7) at SZA = 37°. Figure 5.15 shows the model calculated photoelectron flux at 1100 km along with the photoelectron flux observed by the CAPS instrument (energy resolution $\Delta E/E$ = 16.7%) on-board Cassini taken from *Lavvas et al.* [2011]. Model calculated photoelectron flux agrees well with the observed flux between 7 and ∼20 eV. Above 20 eV model predicted photoelectron flux is slightly higher than the observation. At higher energies (>60 eV) the calculated photoelectron flux starts decreasing sharply compared to the observed flux. *Lavvas et al.* have also observed similar differences in their calculated and the observed photoelectron flux at energies > 60 eV, which they attributed to the instrument artifact [*Lavvas et al.*, 2011; *Arridge et al.*, 2009].

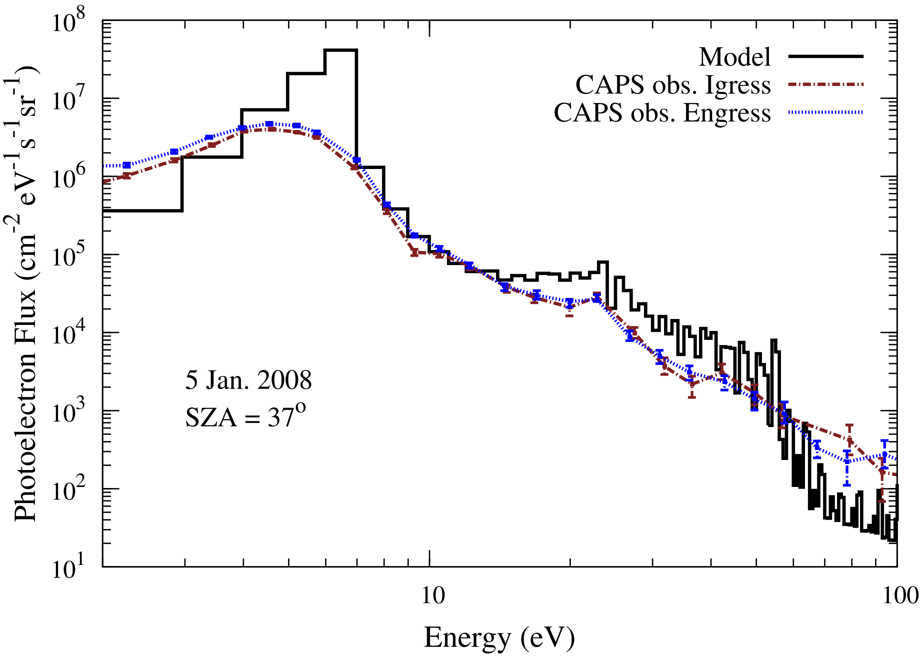

Figure 5.15: Model calculated photoelectron flux on Titan on 5 January 2008 at an altitude of 1100 km obtained by using S2K solar EUV flux compared with the Cassini CAPS observation taken from *Lavvas et al.* [2011] are also shown for comparison.

The calculated band emission rate is integrated along the line of sight at a projected distance from the centre of Titan to obtain limb profile (see Eq. 4.9). As mentioned

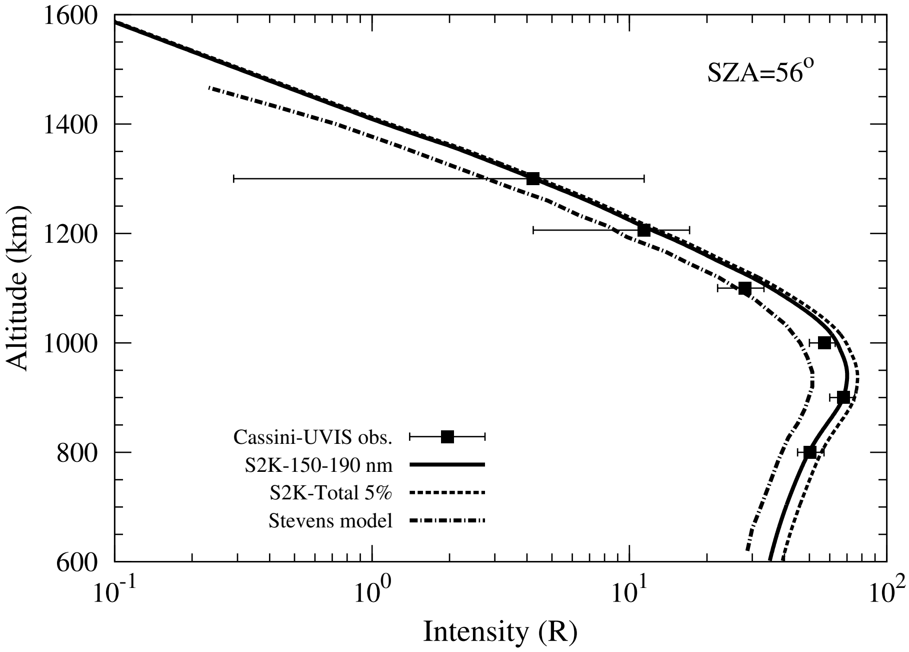

Figure 5.16: Calculated limb profiles of N_2 VK band in 150–190 nm wavelength range on Titan on 23 June 2009 for S2K solar EUV flux models at SZA = 56°, along with the Cassini UVIS observed limb intensity and model profile of *Stevens et al.* [2011]. Limb profile obtained by taking 5% of the total N_2 VK band intensity is also shown.

earlier, N_2 VK bands were observed for the first time in the dayglow of Titan by Cassini UVIS in the 150–190 nm wavelength band [*Stevens et al.*, 2011]. For comparing the calculated limb profiles with UVIS observation the calculations are carried out at the solar zenith angle of 56°. *Stevens et al.* [2011] in their calculation assumed that VK bands in the 150–190 nm range constitutes 5% of the total VK band emission. Figure 5.16 shows the calculated limb intensity of VK bands in the 150–190 nm region by taking 5% of the total VK band intensity, and also by adding the individual bands which lie in the 150–190 nm wavelength region. The calculated limb intensity of *Stevens et al.* [2011] is also shown in Figure 5.16 along with the Cassini–observed limb intensity of VK band in 150–190 nm region taken from *Stevens et al.* [2011]. It is found that VK band emission in the wavelength region 150–190 nm is ∼4.5% of the total VK band intensity. The model calculated limb intensity is in good agreement with the UVIS observation. The model calculated altitude of peak VK emission also agrees well with the observation within the observational uncertainty of 15% [*Stevens et al.*, 2011]. The calculated limb intensities are slightly higher (∼10%) than those calculated by *Stevens et al.* [2011]. Altitude of emission peak is in good agreement in both calculations and is consistent with that of the observed emission peak. Overall good agreement between calculated and observed emission shows that the VK band intensity can be explained by taking the photoelectron impact excitation source alone.

5.6 Summary and conclusions

In this Chapter a model to calculate emission intensities of the N_2 triplet band systems is developed for Mars and Venus. The AYS, which is described in Chapter 3, is used to calculate the steady state photoelectron flux, which in turn is used to calculate volume excitation rates of N_2 VK bands and other triplet states. The populations of various vibrational levels of the triplet states of N_2 have been calculated considering direct excitation as well as cascading from higher triplet states in statistical equilibrium conditions.

Using calculated emission rates, the limb profiles of the VK (0, 5), (0, 6), and (0, 7) bands have been calculated on Mars and are compared with the SPICAM observed limb profiles reported by *Leblanc et al.* [2007]. The observed and calculated limb profiles of the VK (0, 6) band are in good agreement when the N_2 density is reduced by a factor of 3 from those given by the MTGCM model of *Bougher et al.* [1990, 1999, 2000]. Overhead intensities of prominent transitions in VK, First Positive, Second Positive, and $W \rightarrow B$ bands have been calculated. On using the model atmospheres of *Fox* [2004] and *Krasnopolsky* [2002], a decrease in N_2 density in their atmospheric model by a factor of 2.5 and 2.1, respectively, is required to reconcile the calculated VK (0, 6) band limb profile with the observed profile.

The most important parameter that governs the limb intensity of VK band is the N_2/CO_2 ratio. On Mars, Constraining the N_2/CO_2 ratio by SPICAM observations, for different cases of model input parameters, the calculations suggest that the N_2/CO_2 ratio would be in the range of 1.1 to 1.4% at 120 km, 1.8 to 3.2% at 140 km, and 4 to 7% at 170 km. The present study suggests that most of the atmospheric models have N_2 abundances that are larger than the derived values, based on the present calculation, by factors of 2 to 4. Clearly, there is a need for improved understanding of the Martian atmosphere, and the SPICAM observations help to constrain the N_2 relative abundance. A decrease in the N_2 density in the atmospheric models, as suggested by present calculations, would affect the chemistry and other aeronomical processes in the Martian upper atmosphere and ionosphere.

On Venus, the calculated intensities of VK bands are an order of magnitude larger than those on Mars. Hence, the intensities are quite large and can be detected by the SPICAV experiment on board Venus Express. However, very bright sunlit limb due to solar scattering background makes it difficult to observe N_2 VK bands in Venus dayglow by SPICAV. The relative population of vibrational levels is almost constant above 180 km on Venus, while on Mars they attain a constant value above 250 km.

The effect of important model parameters, viz., electron impact N_2 triplet state excitation cross sections, solar flux, solar activity, and model atmosphere (Mars only), on N_2 triplet band emissions have been studied. Changes in the cross section of N_2

triplet states can alter the calculated intensity by a factor of ~2. On the other hand, the calculated intensities are ~15% larger when the S2K v.2.36 solar EUV flux model of *Tobiska* [2004] is used instead of the EUVAC model of *Richards et al.* [1994]. During high solar activity, the calculated intensities are about a factor of 2.5 larger than those calculated for the low solar activity conditions.

The N_2 VK band intensity is also calculated on Titan to explain the recent first observation by Cassini UVIS and to validate the model calculation by applying it to N_2 dominated atmosphere. Model calculated photoelectron flux is in agreement with Cassini-CAPS observations. The calculated intensity of N_2 VK band in wavelength range 1500–1900 Å is in good agreement with the Cassini-UVIS measured limb profile. A good agreement between observed and modelled intensity of N_2 VK band on Titan shows that the model present in this Chapter is able to reproduce the observed profiles. This also justifies the suggestion made in this Chapter regarding the reduction in N_2 density in the atmosphere of Mars.

Chapter 6

Atomic oxygen red, green, and 2972 Å line emissions

6.1 Introduction

Though the UV dayglow measurements on Mars have been carried out extensively [*Barth et al.*, 1971; *Stewart et al.*, 1972; *Stewart*, 1972; *Leblanc et al.*, 2006; *Gronoff et al.*, 2012a], but so far no visible dayglow emissions from Mars are observed by ground, space or spacecraft-based instruments. However, lack of visible emission observation does not rule out the possibility of production of visible dayglow emissions in Martian atmosphere. Similarly, on Venus the observation of ultraviolet dayglow emissions have been carried out by rocket-borne spectrometers, spacecraft flybys, Pioneer Venus Orbiter (PVO), Hopkins Ultraviolet Telescope aboard Space shuttle, and Cassini flyby [*Fox and Bougher*, 1991; *Paxton and Anderson*, 1992; *Feldman et al.*, 2000; *Gérard et al.*, 2008a, 2011a; *Hubert et al.*, 2010] and very recently by SPICAV on-board Venus Express (VEx) [*Chaufray et al.*, 2012]. *Fox and Bougher* [1991] and *Paxton and Anderson* [1992] have given a detailed review on observations and models of ultraviolet dayglow emission on Venus. Though there have been measurements of visible emission from the nightside of Venus [*Krasnopolsky et al.*, 1976; *Lawrence et al.*, 1977; *Slanger et al.*, 2001, 2006a, 2012], so far no observation of visible emission in the dayglow of Venus is reported. The OI 2972 Å line has been observed on Mars and Venus [*Stewart*, 1972; *Leblanc et al.*, 2006; *LeCompte et al.*, 1989]. SPICAV could not clearly detect OI 2972 Å emission on Venus because of coarse (10 nm) resolution [*Chaufray et al.*, 2012]. This line comes from the metastable state O(^{1}S) and only about 5–10% of O(^{1}S) decays through O(^{1}S $\rightarrow$ ^{3}P) transition producing OI 2972 Å emission, while the rest decays through O(^{1}S $\rightarrow$ ^{1}D) transition emitting 5577 Å green line. This implies that if OI 2972 Å is observed on Mars and Venus then the OI 5577 Å emission should also be present with intensity about 10 times more than that of OI 2972 Å line.

Theoretical calculations of visible dayglow emission on Mars have been carried out by *Fox and Dalgarno* [1979a] and *Simon et al.* [2009] and recently by *Gronoff et al.*

[2012a] and on Venus by *Fox and Dalgarno* [1981], *Fox and Bougher* [1991], and *Gronoff et al.* [2008]. Main production mechanism of O(^{1}S) is photodissociative (PD) excitation of CO_2, which is the dominant gas in the atmospheres of Mars and Venus [*Fox and Dalgarno*, 1979a, 1981; *Fox and Bougher*, 1991; *Gronoff et al.*, 2008; *Simon et al.*, 2009; *Gronoff et al.*, 2012a]. Recently, *Huestis et al.* [2010] concluded that the OI 2972 Å emission on Mars is mainly produced by the dissociative recombination of O_2^+, and thus the OI 2972 Å emission can be used to monitor Martian ionosphere and not its ambient neutral atmosphere. *Gronoff et al.* [2012a] analysed the SPICAM data and found that the scale height derived from OI 2972 Å emission profile is in agreement with that deduced from CO_2^+(B–X) emission showing same origin for both the emissions. *Gronoff et al.* [2012a] have found good agreement between their calculated OI 2972 Å emission profile and SPICAM-observation and showed that the PD of CO_2 is the major source of O(^{1}S) production.

In view of recent measurements of OI 2972 Å emission by SPICAM, and revised chemical reaction rates and other molecular parameters, there is a need to revisit the atomic oxygen emission in the dayglow of Mars and Venus. The aim of the present study is to develop a model to understand the role of various processes in governing the atomic oxygen visible emissions in the dayglow of Mars and Venus. The model is applied for both solar minimum and maximum conditions to study the effect of change in solar activity on various processes governing the atomic oxygen emissions. Since the direct comparison of calculated OI 6300 and 5577 Å line emissions with measurement is not possible due to the lack of visible observation on Venus and Mars, the model calculations are compared with the OI 2972 Å emission since both oxygen 5577 and 2972 Å emissions originate from the same upper ^{1}S state. A detailed description of major production processes of O(^{1}S) and O(^{1}D) is given followed by the calculated O(^{1}S) and O(^{1}D) densities in solar minimum and maximum conditions. The limb intensities of OI 6300, 5577, and 2972 Å emissions are computed. The calculated OI 2972 Å brightness profiles are compared with the observations.

6.2 ^{1}S and ^{1}D states of O

Figure 6.1 shows the energy level diagram of atomic oxygen. The metastable ^{1}S and ^{1}D excited states of atomic oxygen lie 1.98 and 4.19 eV, respectively, above the ground ^{3}P state. The O(^{1}S) decays to the O(^{1}D) by emitting green line at 5577 Å. The transition from O(^{1}D) to O(^{3}P) produces red doublet (6300 and 6364 Å) lines. Both OI 5577 Å (green) O(^{1}S $\rightarrow ^1$D) and 6300 Å (red) O(^{1}D $\rightarrow$ ^{3}P) line emissions are strong features in the terrestrial airglow [*Ångström*, 1869; *Witasse et al.*, 1999; *Zhang and Shepherd*, 2008; *Singh et al.*, 1996, 2010]. The O(^{1}S) and O(^{1}D) have a lifetime of 0.8 and 110 seconds, respectively [*Baluja and Zeippen*, 1988; *Froese-Fischer and Tachiev*, 2004]. The 6300 Å emission from O(^{1}D) is used as a diagnostic tool to estimate the relative abundance and distribution of H_2O in the coma of comets [cf. *Bhardwaj and Raghuram*, 2012, and references there in]. Photon impact on oxygen atom cannot populate these states because the transition to ^1S and ^1D states from the ground ^3P state is spin-forbidden due to the selection rule (triplet to singlet transition). Major mechanisms for the production of O(^1S) and O(^1D) are photon and electron impact dissociation of molecules containing atomic oxygen (e.g., CO_2, CO, O_2), dissociative recombination (DR) of O-bearing ions (e.g., CO_2^+, O_2^+, and CO^+), electron impact on atomic oxygen, and three body collision. The later process is known to be one of the dominant mechanisms for the production of O in ^1S state in terrestrial mesosphere-lower thermosphere [*Witasse et al.*, 1999].

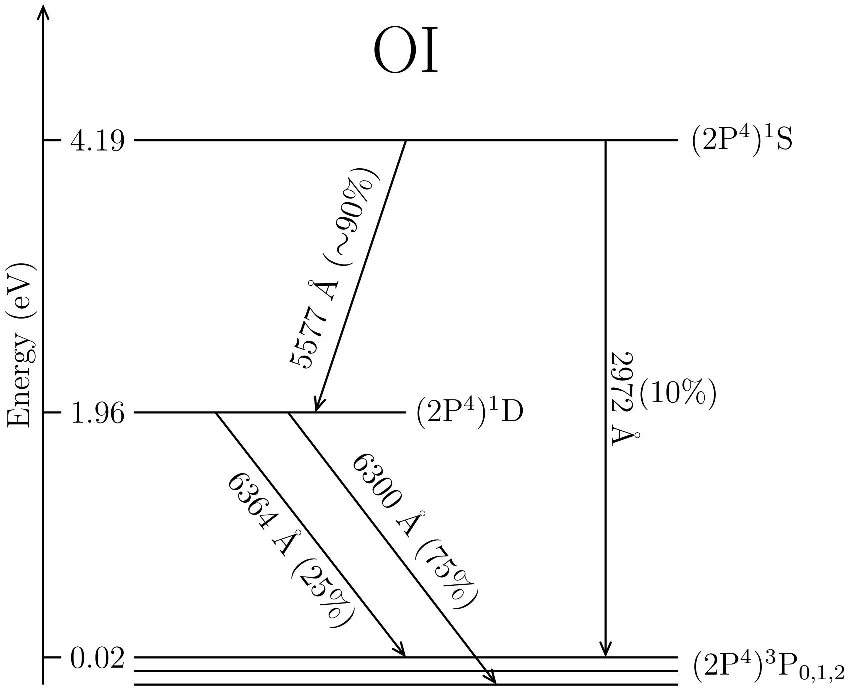

Figure 6.1: Schematic of energy level diagram of atomic oxygen showing different spectroscopic transitions related to ^1S and ^1D states.

Since, both optically forbidden lines O($^1S \rightarrow {}^1D$) at 5577 Å and O($^1S \rightarrow {}^3P$) at 2972 Å originate from the same upper ^1S state of atomic oxygen, their branching ratio is constant. However, there is an uncertainty regarding the branching ratio of the two emissions. Theoretical calculations, laboratory measurements, and atmospheric observations differ substantially regarding the intensity ratio of 5577 and 2972 Å emissions (I_{5577}/I_{2972}) [*Witasse et al.*, 1999; *Slanger et al.*, 2006b, a; *Gattinger et al.*, 2009; *Slanger et al.*, 2011]. While most of the theoretical values for this ratio are close to 16, the laboratory measured value is higher (~22), and the value determined by atmospheric observations is close to 10 [*Slanger et al.*, 2006b; *Gattinger et al.*, 2009; *Slanger et al.*, 2011]. Based on compilation of *Wiese et al.* [1996], NIST recommended a value of 16.7 for the I_{5577}/I_{2972} ratio. Recently, *Slanger et al.* [2011] have recommended a value of 9.4 for the I_{5577}/I_{2972} ratio based on atmospheric observations [*Slanger et al.*, 2006a, b;

Gattinger et al., 2009]. A value of 9.4 for the ratio suggests that either the transition probability of O(^{1}S – ^{1}D) should be lower or that of O(^{1}S – ^{3}P) should be higher. However, a good agreement is found among various studies regarding the lifetime (∼0.8 s) of O(^{1}S) atom [*Baluja and Zeippen*, 1988; *Froese-Fischer and Tachiev*, 2004; *Slanger et al.*, 2006b], and around 90–95% of this lifetime value is determined by the transition probability of O(^{1}S – ^{1}D) emission, which is known to a good degree of accuracy [*Slanger et al.*, 2006b]. Hence, an increase in the transition probability (A-factor) associated with the O(^{1}S–^{3}P) emission may be required to make the I_{5577}/I_{2972} ratio compatible with the recommended value of 9.4 [*Slanger et al.*, 2011; *Slanger et al.*, 2006b]. In the present study the I_{5577}/I_{2972} ratio is taken as 9.4 by increasing the A-factor for O(^{1}S – ^{3}P) transition (see Table 6.1). The effect of a higher value of 16.7 for the I_{5577}/I_{2972} ratio, as recommended by NIST, on the emission intensity of OI 2972 Å is also discussed.

Similarly, the red doublet (6300 and 6364 Å) emissions originate from the same upper ^{1}D state of atomic oxygen; however, unlike the ratio of OI 5577 and 2972 Å emissions, there is good agreement among theory and observations regarding the ratio of OI 6300 and 6364 Å emissions [*Froese-Fischer and Tachiev*, 2004; *Capria et al.*, 2008; *Sharpee and Slanger*, 2006]. The transition probabilities of *Froese-Fischer and Tachiev* [2004] for the emission O(^{1}D – ^{3}P$_2$) at 6300 Å and O(^{1}D – ^{3}P$_1$) at 6364 Å are used in the present study (see Table 6.2).

6.3 Development of model

The model atmospheres for solar minimum and maximum conditions is same as given in Figure 4.2. One of the mechanisms for O(^{1}S) and O(^{1}D) production is Photodissociation (PD) of CO_2 due to photons at wavelength >1200 Å. The 37-bin solar EUV flux used in the earlier chapters is limited to photon flux up to 1150 Å, hence in the current chapter the solar EUV-FUV flux is taken at 10 Å bin (from 5 to 1800 Å) from SOLAR2000 (S2K) v2.36 model of *Tobiska* [2004] at 1 AU for both solar maximum (30 January 2002, F10.7 = 256) and minimum (23 June 2009, F10.7 = 68) conditions. The solar flux is scaled to the heliocentric distance of Mars (1.5 AU). Figure 6.2 shows the solar EUV-FUV flux for solar minimum and maximum conditions at 1 AU. At wavelengths greater than 1230 Å, the solar fluxes for the two conditions are same. Below 1230 Å the flux in solar maximum condition is higher by about a factor of 2 or more than that in solar minimum condition. Below 400 Å, at few wavelength bands the flux in solar maximum is as high as a factor of 6 compared to that in solar minimum. At wavelengths below 100 Å, the difference between the fluxes for high and low solar activities is more than a factor of 6.

Details of photoabsorption and photoionization, and electron impact cross sections are given in Chapter 2. Electron, ion, and neutral temperatures for solar minimum and maximum conditions on Mars and Venus are based on the studies of *Fox and Hac* [2009]

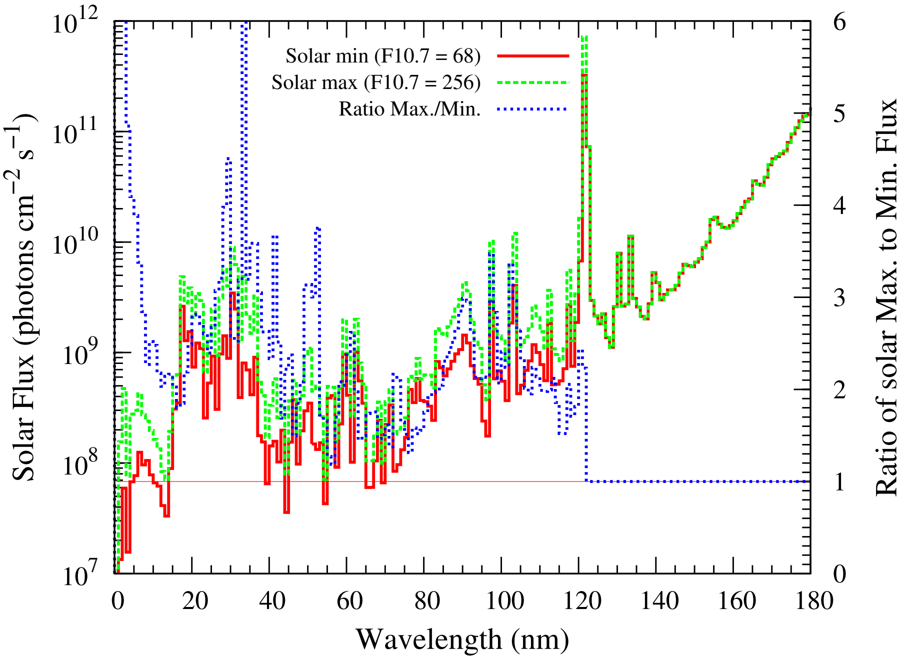

Figure 6.2: Solar EUV-FUV flux at 1 AU for minimum and maximum conditions taken from S2K model. Ratio of solar flux in maximum to minimum conditions is shown by thin dotted curve with values on the right side Y-axis; horizontal line denotes the value of 1.

and *Fox and Sung* [2001], respectively. Chemical reactions for various production and loss mechanisms of O(^{1}S) and O(^{1}D) are given in Tables 6.1 and 6.2, respectively. The details of photoelectron production and calculations of photoelectron flux and volume excitation rates have been given in Chapter 4.

6.3.1 O(^{1}S) and O(^{1}D) production processes

6.3.1.1 Photodissociation of CO_2, CO, and O_2

The thresholds of O(^{1}S) and O(^{1}D) production in dissociative excitation of CO_2 are 1286 and 1671 Å, respectively [*Huebner et al.*, 1992]. The yield of O(^{1}S) in PD of CO_2 has been measured by different workers [*Lawrence*, 1972b; *Slanger et al.*, 1977; *Bibinov et al.*, 1979]. *Slanger et al.* [1977] have measured the quantum yield of O(^{1}S) in the wavelength range 1060–1175 Å; the measured yield is unity between 1100 and 1150 Å. Below 1100 Å, *Slanger et al.* [1977] found an abrupt dip at 1089 Å (yield <0.15), which is the location of very strong rydberg transition in CO_2. According to *Slanger et al.* [1977], the maximum yield of O(^{1}S) at 1089 Å cannot be more than 0.2 and that the minimum yield could be zero. *Lawrence* [1972b] measured the O(^{1}S) yield at wavelengths between 812 and 1216 Å. The measured O(^{1}S) yield of *Lawrence* [1972b] is unity in the range 1080–1150 Å, but the yield measured by *Lawrence* [1972b] did not show sudden dip around 1089 Å. Since the width of absorption feature at 1089 Å is very small (less than 1 Å), and *Lawrence* [1972b] conducted the measurements at a resolution of 8 Å, it might have escaped the detection in his measurement. *Bibinov et al.* [1979] measured the O(^{1}S) quantum yield in wavelength range 1020–1280 Å. They reported a non zero O(^{1}S) yield for wavelengths ≤1286 Å, but the reliability of their measurement for the wavelengths >1150 Å was very poor and *Bibinov et al.* estimated an uncertainty of ~50%. At H Lyman-α line (1216 Å), the yield of O(^{1}S) in the PD of CO$_2$ is important, because it determines the magnitude of O(^{1}S) production at altitudes below 100 km in Martian atmosphere (below 120 km in Venusian atmosphere) [*Fox and Dalgarno*, 1979a; *Fox and Bougher*, 1991; *Simon et al.*, 2009; *Gronoff et al.*, 2012a]. However, at 1216 Å the measurement of O(^{1}S) yield is difficult due to very low absorption coefficient of CO$_2$. The O(^{1}S) yield at 1216 Å measured by *Lawrence* [1972b] is ~13%.

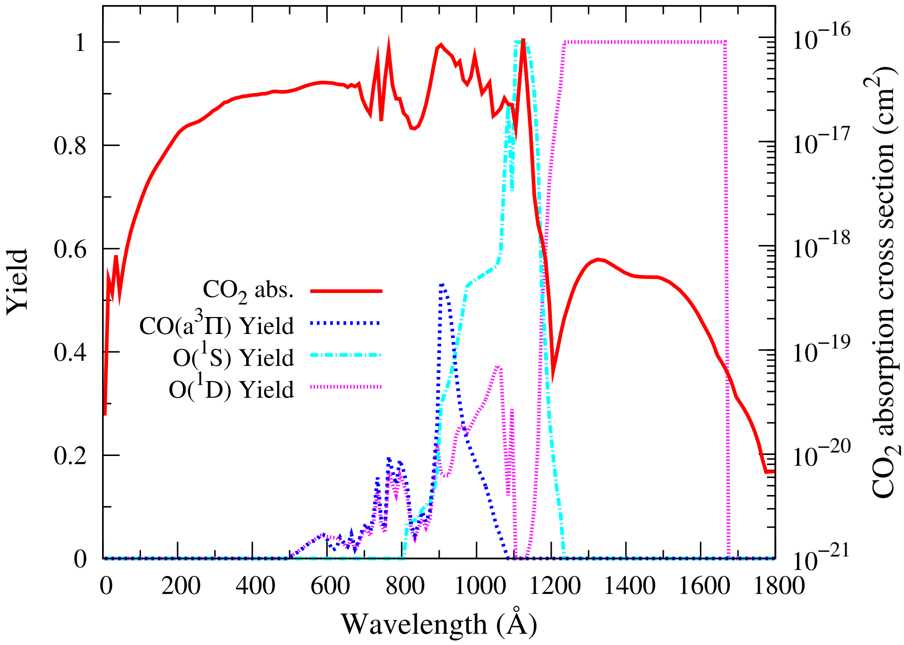

Figure 6.3: Yield of O(^{1}S), O(^{1}D), and CO(a$^3\Pi$) in the photodissociation of CO$_2$. Magnitude of photoabsorption cross section of CO$_2$ is shown on the right side Y-axis. CO$_2$ abs. stands for total absorption cross section of CO$_2$.

In the present study, the O(^{1}S) yield is taken from the studies of *Lawrence* [1972b] and *Slanger et al.* [1977]. Between 1060 and 1160 Å, the O(^{1}S) yield is based on the measurement of *Slanger et al.* [1977]. The O(^{1}S) yield above 1160 and below 1060 Å is based on the measurement of *Lawrence* [1972b]. Figure 6.3 shows the O(^{1}S) yield used in the model.

There is no direct measurement of O(^{1}D) yield in PD of CO$_2$. This is because of the long lifetime (~110 s) of O(^{1}D) and hence it is difficult to measure O(^{1}D) yield in the laboratory. *Slanger and Black* [1978], in the study of photolysis of CO$_2$ at wavelengths below 1670 Å. They concluded that the total PD yield of CO$_2$ would be unity between 1067 and 1670 Å. Based on indirect method of estimating the O(^{1}D) yield in the PD of CO_2, *Slanger and Black* [1978] have concluded that the $O(^1D)$ would be the main product in the PD of CO_2 between 1250 and 1670 Å with unit yield. Below 1250 Å, the $O(^1D)$ yield starts decreasing because another PD channel ($O(^1S)$ + CO(X)) opens up. Between 1150 and 1100 Å the $O(^1D)$ yield becomes zero since the $O(^1S)$ yield is unity in this region. Below 1100 Å, the $O(^1D)$ + CO(X) channel again opens up with a $O(^1D)$ yield of 0.65±0.1. At 1089 Å, as stated earlier, there is a sudden reduction in the $O(^1S)$ yield (<0.15), and according to *Slanger et al.* [1977] the $O(^1D)$ yield can reach a maximum value of unity at 1089 Å. *Slanger and Black* [1978] stated that the $O(^1S)$ and $O(^1D)$ yields at 1067 Å would be 0.6 and 0.35, respectively; with a value of 0.05 for $CO(a^3\Pi)$ yield [*Lawrence*, 1972a]. The yield of $O(^1D)$ in the PD of CO_2 in the present study is based on the work of *Slanger et al.* [1977] and *Slanger and Black* [1978]. Figure 6.3 shows the total $O(^1D)$ yield in the PD of CO_2.

The $O(^1S)$ and $O(^1D)$ yield in the photodissociative excitation of O_2 is taken from *Lawrence and McEwan* [1973] and *Huebner et al.* [1992], respectively. *Huebner et al.* [1992] have calculated the $O(^1D)$ cross section in the PD of CO based on the branching ratios from *McElroy and McConnell* [1971], which is used in the present model calculation.

6.3.1.2 Electron impact on CO_2, CO, O_2, and O

Cross sections for $O(^1S)$ production due to electron impact on CO_2, O_2, and CO are taken from compilation of *McConkey et al.* [2008]. The cross section of $O(^1D)$ production in electron impact on CO_2 is taken from *Jackman et al.* [1977] (cf. Table 2.8). The cross

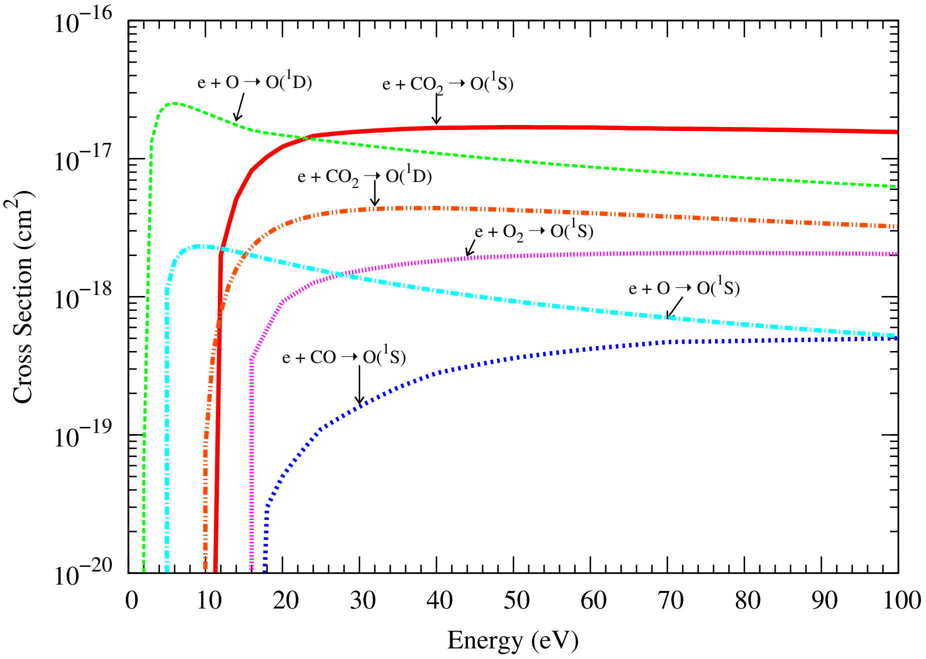

Figure 6.4: Cross sections for $O(^1S)$ and $O(^1D)$ production due to electron impact on CO_2, CO, O_2, and O.

Table 6.1: Reactions for the production and loss of $O(^1S)$.

Reaction	Rate ($cm^3\ s^{-1}$ or s^{-1})	Reference
$CO_2 + h\nu \rightarrow O(^1S) + CO$	2.8×10^{-7} $(7.3 \times 10^{-7})^*$	This work
$O_2 + h\nu \rightarrow O(^1S) + O$	4.4×10^{-9} (1.2×10^{-8})	This work
$CO_2 + e_{ph} \rightarrow O(^1S)$ + others	see text	This work
$CO + e_{ph} \rightarrow O(^1S)$ + others	see text	This work
$O_2 + e_{ph} \rightarrow O(^1S)$ + other	see text	This work
$O + e_{ph} \rightarrow O(^1S)$	see text	This work
$CO_2^+ + e_{th} \rightarrow O(^1S)$ + others	$2.5 \times 10^{-8}(300/T_e)^{0.75}$	*Viggiano et al.* [2005]†
$O_2^+ + e_{th} \rightarrow O(^1S) + O(^1D)$	$9.75 \times 10^{-9}(300/T_e)^{0.7}$ for $T_e \leq 1200K$ $3.7 \times 10^{-9}(1200/T_e)^{0.56}$ for $T_e \geq 1200K$	*Mehr and Biondi* [1969]‡ and *Alge et al.* [1983]
$N_2(A^3\Sigma_u^+) + O \rightarrow O(^1S) + N_2$	$2.1 \times 10^{-11}(T/298)^{0.5}$	*Hill et al.* [2000]§
$O(^1S) \longrightarrow O(^3P) + h\nu_{2972}$	$0.134\ (0.075)^¶$	*Slanger et al.* [2006b]
$O(^1S) \longrightarrow O(^1D) + h\nu_{5577}$	1.26	*Wiese et al.* [1996]
$O(^1S) + CO_2 \rightarrow O(^3P) + CO_2$	$1.2 \times 10^{-11} \exp(-1327/T)$	*Capetanakis et al.* [1993]
$\rightarrow O(^1D) + CO_2$	$2 \times 10^{-11} \exp(-1327/T)$	
$O(^1S) + CO \rightarrow O(^1D) + CO$	$7.4 \times 10^{-14} \exp(-961/T)$	*Capetanakis et al.* [1993]
$O(^1S) + N_2 \rightarrow O(^1D) + N_2$	5×10^{-17}	*Atkinson and Welge* [1972]
$O(^1S) + O_2 \rightarrow O(^1D) + O_2$	$1.4 \times 10^{-12} \exp(-815/T)$	*Capetanakis et al.* [1993]
$\rightarrow O(^3P) + O_2$	$3 \times 10^{-12} \exp(-815/T)$	
$O(^1S) + e_{th} \rightarrow O(^1D) + e$	8.6×10^{-9}	*Berrington and Burke* [1981]
$\rightarrow O(^3P) + e$	1.6×10^{-9} $(T_e/300)^{0.94}$	*Berrington and Burke* [1981]
$O(^1S) + O \rightarrow 2\ O(^1D)$	2×10^{-14}	*Krauss and Neumann* [1975]
$O(^1S) + O_2(a^1\Delta_g) \rightarrow O$ or $O(^1D)$	1.7×10^{-10}	*Slanger and Black* [1981]‖

e_{ph} = photoelectron; e_{th} = thermal electron; $h\nu$ = solar photon; T_e = electron temperature; T = neutral temperature

*Value in parenthesis is for solar maximum. †Rate of *Viggiano et al.* [2005] has been multiplied by 0.06 (see text for detail). ‡Branching ratios are from *Kella et al.* [1997] as used in study of *Fox and Sung* [2001]. §Rate coefficient is the average value of $N_2(A)$ vibrational levels 0, 1, and 2. The quantum yield of 0.47 is taken for $O(^1S)$ production. ¶Value in parenthesis is the NIST recommended value. ‖The $O(^1D)$ yield is 17%.

Table 6.2: Reactions for the production and loss of O(^{1}D).

Reaction	Rate (cm^3 s^{-1} or s^{-1})	Reference
$CO_2 + h\nu \rightarrow O(^1D) + CO$	1.8×10^{-7} $(4 \times 10^{-7})^*$	This work
$CO + h\nu \rightarrow O(^1D) + C$	2.2×10^{-8} (3.5×10^{-8})	This work
$O_2 + h\nu \rightarrow O(^1D) + O$	1.2×10^{-6} (1.4×10^{-6})	This work
$CO_2 + e_{ph} \rightarrow O(^1D) + CO + e$	see text	This work
$CO + e_{ph} \rightarrow O(^1D) + C(^1D) + e$	see text	This work
$O + e_{ph} \rightarrow O(^1D)$	see text	This work
$CO_2^+ + e_{th} \rightarrow O(^1D)$ + others	$2.5 \times 10^{-7}(300/T_e)^{0.75}$	*Viggiano et al.* [2005]†
$CO^+ + e_{th} \rightarrow O(^1D) + C(^1D)$	2.5×10^{-8} $(300/T_e)^{0.55}$	*Rosén et al.* [1998]
$O_2^+ + e_{th} \rightarrow O(^1D)$	$1.56 \times 10^{-7}(300/T_e)^{0.7}$ for $T_e \leq 1200K$ $5.91 \times 10^{-8}(1200/T_e)^{0.56}$ for $T_e \geq 1200K$	*Mehr and Biondi* [1969] and *Alge et al.* [1983]
$O(^1S) \rightarrow O(^1D) + h\nu_{5577}$	1.26	*Wiese et al.* [1996]
$O(^1S) + e_{th} \rightarrow O(^1D) + e$	8.6×10^{-9}	*Berrington and Burke* [1981]
$O(^1S) + CO_2 \rightarrow O(^1D) + CO_2$	$2 \times 10^{-11} \exp(-1327/T)$	*Capetanakis et al.* [1993]
$O(^1S) + CO \rightarrow O(^1D) + CO$	$7.4 \times 10^{-14} \exp(-961/T)$	*Capetanakis et al.* [1993]
$O(^1S) + N_2 \rightarrow O(^1D) + N_2$	5×10^{-17}	*Atkinson and Welge* [1972]
$O(^1S) + O_2 \rightarrow O(^1D) + O_2$	$1.4 \times 10^{-12} \exp(-815/T)$	*Capetanakis et al.* [1993]
$O(^1S) + O \rightarrow 2\, O(^1D)$	2×10^{-14}	*Krauss and Neumann* [1975]
$O(^1S) + O_2(a^1\Delta_g) \rightarrow O(^1D)$	$2.9 \times 10^{-11\ddagger}$	*Slanger and Black* [1981]
$O(^1D) \longrightarrow O(^3P) + h\nu_{6300}$	6.478×10^{-3}	*Froese-Fischer and Tachiev* [2004]
$O(^1D) \longrightarrow O(^3P) + h\nu_{6364}$	2.097×10^{-3}	*Froese-Fischer and Tachiev* [2004]
$O(^1D) + e_{th} \rightarrow O(^3P) + e$	2.9×10^{-10} $(T_e/300)^{0.91}$	*Berrington and Burke* [1981]
$O(^1D) + CO_2 \rightarrow O(^3P) + CO_2$	6.8×10^{-11} $\exp(117/T)$	*Streit et al.* [1976]
$O(^1D) + CO \rightarrow O(^3P) + CO$	3.6×10^{-11}	*Schofield* [1978]
$O(^1D) + N_2 \rightarrow O(^3P) + N_2$	$1.8 \times 10^{-11} \exp(107/T)$	*Atkinson et al.* [1997]
$O(^1D) + O_2 \rightarrow O(^3P) + O_2$	$3.2 \times 10^{-11} \exp(67/T)$	*Atkinson et al.* [1997]
$O(^1D) + O \rightarrow O(^3P) + O$	$6.47 \times 10^{-12}(T/300)^{0.14}$	*Jamieson et al.* [1992]

e_{ph} = photoelectron; e_{th} = thermal electron; hν = solar photon; T_e = electron temperature; T = neutral temperature

*Value in parenthesis is for solar maximum. †Rate of *Viggiano et al.* [2005] has been multiplied by 0.59 (see text for detail). ‡Total rate of O(^{1}S) quenching by $O_2(a^1\Delta_g)$ is multiplied by O(^{1}D) yield of 17%.

sections of $O(^1S)$ and $O(^1D)$ production in electron impact on O are from *Jackman et al.* [1977] (see Table 2.11). Figure 6.4 shows the electron impact cross sections for producing excited oxygen atom in $O(^1D)$ and $O(^1S)$ states for various O-bearing species.

6.3.1.3 Dissociative recombination (DR)

Electron recombination of O-bearing ions is an important process for the $O(^1S)$ and $O(^1D)$ production. The recombination of O_2^+ with electron can lead to the following dissociation channels [*Guberman*, 1987; *Kella et al.*, 1997; *Peverall et al.*, 2001; *Petrignani et al.*, 2005a, b]:

$$O_2^+ + e^- \rightarrow \begin{cases} O(^3P) + O(^3P) + 6.99\ \text{eV} & (a) \\ O(^1D) + O(^3P) + 5.02\ \text{eV} & (b) \\ O(^1S) + O(^3P) + 2.80\ \text{eV} & (c) \\ O(^1D) + O(^1D) + 3.06\ \text{eV} & (d) \\ O(^1D) + O(^1S) + 0.83\ \text{eV} & (e) \end{cases}$$

The branching ratio of channel (c) is zero. The DR of O_2^+ is one of the major sources of oxygen green and red line emissions in terrestrial airglow [*Singh et al.*, 1996; *Zhang and Shepherd*, 2008; *Singh et al.*, 2010]. In the ionospheres of Mars and Venus, O_2^+ production depends on the ion-molecular chemistry [*Fox and Bougher*, 1991; *Fox and Sung*, 2001; *Fox and Hac*, 2009].

Despite having uncertainty regarding the vibrational distribution of O_2^+, the thermal rate coefficients of O_2^+ recombination measured in several experiments are in good agreement [*Petrignani et al.*, 2005a, b; *Fox and Hac*, 2009]. In the present study, total rate coefficient of $1.95 \times 10^{-7}(300/T_e)^{0.7}$ cm^3 s^{-1} for $T_e < 1200$ K [*Alge et al.*, 1983] and $7.39 \times 10^{-8}(1200/T_e)^{0.56}$ cm^3 s^{-1} for $T_e > 1200$ K [*Mehr and Biondi*, 1969] are used (see Tables 6.1 and 6.2). The yield of $O(^1S)$ and $O(^1D)$ depends strongly on the vibrational distribution of O_2^+. *Guberman* [1987] has shown that the yield of $O(^1S)$ in DR of O_2^+ in the ground vibrational level is very small (less than 1%) and that the maximum rate coefficient is that for O_2^+ ($\nu = 2$). The detailed discussion on the branching ratios and $O_2^+(\nu)$ vibrational distribution is available in *Fox and Hac* [2009]. The branching ratios reported by *Kella et al.* [1997] for channels (a), (b), (d), and (e) are 0.22, 0.42, 0.31, and 0.05, respectively, for ground vibrational level, and 0.25, 0.39, 0.27, and 0.09, respectively, for extended vibrational levels. The branching ratios measured by *Kella et al.* [1997] are used to calculate the $O(^1S)$ and $O(^1D)$ production in O_2^+ vibrational levels 0, 1, 2, and 3. The altitudinal profiles of vibrational distribution of $O_2^+(\nu)$ are calculated using the method described by *Fox and Hac* [2009]. Six vibrational levels ($\nu = 0$ to 5) of the $O_2^+(X^2\Pi_g)$ ground state are taken in the model with rate coefficient *Fox* [1985] and *Fox and Hac* [2009].

The DR of CO_2^+ can produce CO and O atom in the excited state. *Seiersen et al.*

[2003] have mentioned three possible exothermic channels for the CO_2^+ + e process, which are

$$CO_2^+ + e^- \rightarrow \begin{cases} CO_2 + 13.8 \text{ eV}, \\ C + O_2 + 2.3 \text{ eV}, \\ CO + O + 8.3 \text{ eV} \end{cases}$$

Seiersen et al. [2003] have reported a total recombination rate of $6.5 \times 10^{-7}(300/T_e)^{0.8}$ $cm^3\,s^{-1}$. *Viggiano et al.* [2005] have concluded that out of three possible dissociation channels of CO_2^+ only one is most probable, i.e., CO + O. Based on their CRYING storage ring experiment they measured recombination rate of $4.2 \times 10^{-7}(300/T_e)^{0.75}$ $cm^3\,s^{-1}$ for CO_2^+, with an uncertainty of ∼20%. The rate of CO_2^+ DR in model calculation is from *Viggiano et al.* [2005] with 100% branching ratio to CO + O channel.

Skrzypkowski et al. [1998] and *Rosati et al.* [2003] have concluded that the yield of CO in excited triplet state ($a^3\Pi$) in the DR of CO_2^+ is around 30%. *Gutchek and Zipf* [1973] have given the yield of CO Fourth Positive (4P) band in the DR of CO_2^+ and concluded that total yield of CO (4P) would not be more than 5%. Thus, apart from 35% yield of singlet and triplet states of CO in DR of CO_2^+, the remainder (65%) might go to $CO(X^1\Sigma^+)$ + $O(^3P, {}^1D, {}^1S)$ [*Skrzypkowski et al.*, 1998]. There is no consensus on the $O(^1S)$ and $O(^1D)$ production in the DR of CO_2^+.

Schmidt et al. [1988], in their compilation, have shown two channels in DR of CO_2^+, viz., $CO(a^3\Pi)$ + O and CO + $O(^1D)$, and estimated the branching ratio of ∼23 and 76%, respectively. They have not reported any channel leading to the production of $O(^1S)$ in dissociation recombination of CO_2. In the present study, it is assumed that ∼60% of CO_2^+ dissociative recombination would result in $O(^1D)$ production and rest 5% leads to the $O(^1S)$ production. Rate coefficients for $O(^1S)$ and $O(^1D)$ production in DR of CO_2^+ are presented in Tables 6.1 and 6.2. The $O(^1D)$ yield in DR of CO is taken from *Rosén et al.* [1998] (see Table 6.2).

6.4 Atomic oxygen emissions on Mars

6.4.1 Production and loss of $O(^1S)$

Figure 6.5 shows the calculated volume productions rates of $O(^1S)$ for various processes for the solar minimum condition. The PD of CO_2 is by far the dominant mechanism for the production of $O(^1S)$ on Mars. Two distinct peaks are clearly seen in the $O(^1S)$ production rate profile. The upper peak at ∼134 km coincides with the ionization peak and is due to the absorption of solar photons in 860–1150 Å wavelength range. A prominent lower peak is seen about 88 km. The PD of CO_2 by solar H Lyman-α is the main source of $O(^1S)$ production below 100 km. Figure 6.6 shows the contribution of different wavelength bands to the $O(^1S)$ production along with the total

$O(^1S)$ production in PD of CO_2 for solar minimum condition. The upper peak at 136 km is mainly due to the photons in wavelength ranges 1100–1150 and 910–1010 Å, contributing about 16 and 24%, respectively. Overall, photons in the wavelength range 860–1160 Å account for more than 90% of the total $O(^1S)$ production at the upper peak. The lower peak is mainly produced by the solar H Lyman-α photons (1216 Å) which penetrate deeper in the atmosphere due to less absorption by CO_2 near this wavelength (cf. Figure 6.3).

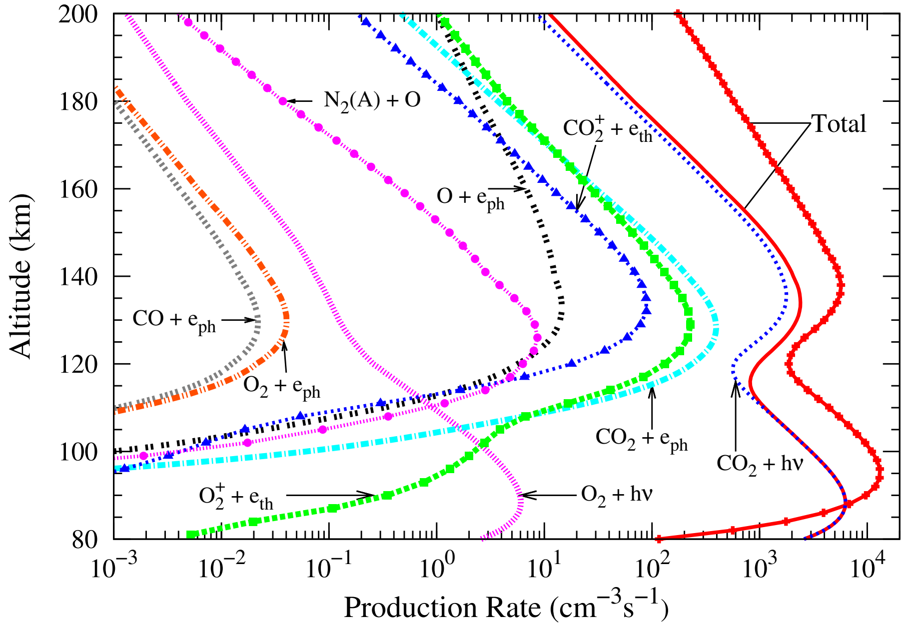

Figure 6.5: Calculated volume production rates of $O(^1S)$ on Mars for various processes during solar minimum condition. Solid curve with symbols shows the total $O(^1S)$ production rate during solar maximum condition. e_{th} = thermal electron; e_{ph} = photoelectron.

Table 6.3 shows the contribution of various processes in $O(^1S)$ production at different altitudes for solar minimum condition. Above 120 km, besides PD of CO_2, the other minor processes for $O(^1S)$ production are photoelectron impact on CO_2, and electron recombination of O_2^+ and CO_2^+. Around the upper peak of $O(^1S)$ production, the contribution of e-CO_2 process is around a factor of 1.8 higher than that of O_2^+ recombination. In the calculation of *Fox and Dalgarno* [1979a], the $O(^1S)$ production at the upper peak due to the O_2^+ DR is larger than that of e-CO_2 process. The reason for this difference might be the use of different set of e-CO_2 cross sections and the yield of $O(^1S)$ in the DR of O_2^+ in two studies. The DR of CO_2^+ contributes around 4% to the $O(^1S)$ production at upper peak; however, the role of this process in $O(^1S)$ production is uncertain due to the non availability of branching ratio. At the upper peak, the $O(^1S)$ production due to electron impact on atomic oxygen and quenching of $N_2(A)$ state by oxygen atom are negligible (<1%), though in Earth's atmosphere both of these processes are very

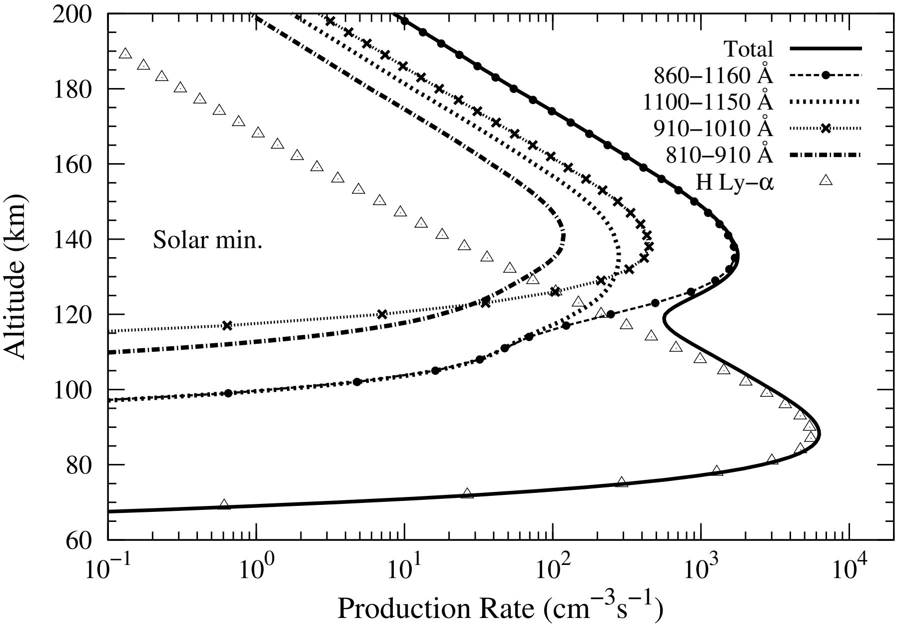

Figure 6.6: Volume production rates of O(^{1}S) due to PD of CO_2 at different wavelengths for solar minimum condition.

important in the production of O(^{1}S) at higher ($\geq$150 km) altitudes [*Witasse et al.*, 1999; *Zhang and Shepherd*, 2008; *Singh et al.*, 2010]. At higher altitudes (>160 km) the O(^{1}S) production due to electron impact on O increases, however, photon and electron impact on CO_2 still accounts for the bulk of O(^{1}S) production (~85%). Three body collision (Barth mechanism) can also contribute to the O(^{1}S) production, but its role during daytime is small and is uncertain as shown by *Gronoff et al.* [2008] in their modelling of Venusian dayglow.

Table 6.3: Contribution of various processes in the production of O(^{1}S) atom on Mars at lower and upper peaks and at a higher altitude (180 km).

Process	Production Rate (cm^{-3} s^{-1})					
	Solar Minimum			Solar Maximum		
	88 km	134 km	180 km	95 km	138 km	180 km
CO_2 + hν	6276 (99)*	1753 (73)	55.4 (82)	13137 (99)	4072 (71)	476 (83)
CO_2 + e_{ph}	-	333 (14)	3.7 (5)	-	857 (15)	36 (6)
O_2^+ + e_{th}	-	202 (8)	4.5 (6)	-	464 (8)	32 (5)
CO_2^+ + e_{th}	-	90 (4)	1.6 (2)	-	251 (4)	20 (3)
O + e_{ph}	-	14.5 (0.6)	2.5 (4)	-	39 (0.6)	10 (2)
N_2(A) + O	-	6 (0.2)	-	-	15 (0.2)	0.6
Total	6282	2398	68	13180	5698	574

*Value in parentheses shows the percentage contribution in total production rate.

The calculated total O(^{1}S) production rate for solar maximum condition is also shown in Figure 6.5. Below 140 km, the total O(^{1}S) production is around a factor of 2 higher compared to that during solar minimum condition. Above 140 km, the O(^{1}S) production rates calculated for solar minimum and maximum conditions differ by more than a factor of 2, and this difference increases with altitude; around 180 km they differ by a factor 7 or more. The change in scale height of O(^{1}S) production from solar minimum to maximum conditions reflects the changes in neutral atmosphere scale height. For solar maximum condition, the contributions of various processes to the total O(^{1}S) production at different altitudes are presented in Table 6.3. In solar maximum condition, both lower and upper peak shifts upward by ∼5 km compared to that in solar minimum condition. Similar to solar minimum condition, the lower peak is predominantly (99%) due to the PD of CO_2. Photon (71%) and electron (15%) impact on CO_2 are two major processes of O(^{1}S) production at upper (138 km) peak. At 180 km, the PD of CO_2 is still the dominant O(^{1}S) production mechanism with 83% contribution, while the DR of O_2^+ contributes around 5%. At 180 km, e-O process contribution is around 2%, which is 50% smaller than the contribution of e-O process in solar minimum condition. During solar minimum condition, above 200 km atomic oxygen becomes the major species, while in solar maximum condition atomic oxygen takes over CO_2 around 230 km. Since the crossing point of atomic oxygen taking over CO_2 density is situated around 30 km higher in solar maximum condition compared to that in solar minimum condition, the contribution of e-O process to the total O(^{1}D) production is more in solar minimum compared to that in solar maximum condition. Overall, the present calculations show that at altitudes up to 200 km, the PD of CO_2 is the dominant mechanism of O(^{1}S) production and together with electron impact dissociation of CO_2, it contributes more than 85% to the total O(^{1}S) production.

As mentioned earlier, *Huestis et al.* [2010] have concluded that scale of height of CO($a^3\Pi \rightarrow X^1\Sigma^+$) and $CO_2^+(B^2\Sigma_u^+ \rightarrow X^2\Pi_g)$ emissions follows the neutral CO_2 scale height, while O(^{1}S $\rightarrow^3$P) 2972 Å emission scale height is best explained if the source mechanism is DR of O_2^+. Recently, *Gronoff et al.* [2012a] have re-analysed the SPICAM data for 37 orbits used in the study of *Simon et al.* [2009], and determined the scale height using a linear regression method. They found that the variation in the altitude of emission peak of O(^{1}S) is same as in CO_2^+(B–X) and CO Cameron bands, which is correlated with the electron density peak, and thus suggested a common source of production. The model calculations have demonstrated that PD of CO_2 is the dominant mechanism of O(^{1}S) production at all altitudes irrespective of the solar activity (see Table 6.3), which is also in agreement with the recent study of *Gronoff et al.* [2012a].

As stated earlier in Section 6.3, the yield of O(^{1}S) in DR of O_2^+, depends upon the vibrational distribution of O_2^+. The effect of O_2^+ vibration distribution on the O(^{1}S) production is evaluated by calculating the population of $O_2^+(X^2\Pi_g)$ ground state vibrational levels. Below 200 km, $\nu = 0$ is the most populated vibrational level in the ground state. At 180 km, fractional populations of $O_2^+(\nu)$ vibrational levels 0, 1, 2, and

3 are 91, 4, 2, and 0.5%, respectively, of the total O_2^+ density. The calculated fractional population of $O_2^+(\nu)$ is in agreement with that of *Fox and Hac* [2009]. It shows that most of the O_2^+ in the Martian ionosphere is produced in the ground state, for which $O(^1S)$ quantum yield in DR is very less (~0.05). Thus, $O_2^+(\nu)$ vibrational distribution would not affect the production of $O(^1S)$ in the Martian atmosphere. Moreover, *Gronoff et al.* [2012a] estimated that if all the O_2^+ in Martian ionosphere is in higher ($\nu = 2$) vibrational level with 41% branching for $O(^1S)$ production, then the contribution of DR of O_2^+ in $O(^1S)$ production becomes equal to that of PD of CO_2. But such a situation is quite extreme and unrealistic [*Gronoff et al.*, 2012a]. Hence, for DR of O_2^+ to become the dominant process for $O(^1S)$ production, the density of O_2^+ in the ionosphere of Mars has to be much higher than that calculated by the models.

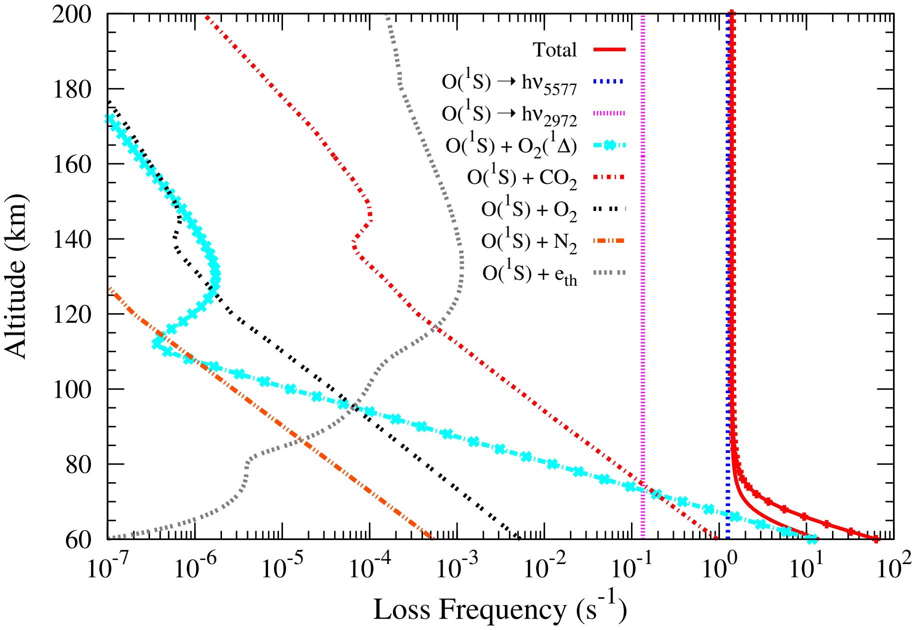

Figure 6.7: Calculated altitudinal profiles of loss mechanisms of $O(^1S)$ for solar minimum conditions. Solid curve with symbols shows the total loss frequency of $O(^1S)$ for solar maximum condition.

Figure 6.7 shows the altitude profiles of various loss mechanisms of $O(^1S)$. Radiative decay to $O(^1D)$ and $O(^3P)$ are the dominant loss mechanisms at all the altitudes. At lower altitude (<80 km) collisional quenching by $O_2(a^1\Delta_g)$ is the most important loss process with an order of magnitude more quenching than that by CO_2. But the effect of this loss process is limited to the altitudes below 80 km. The $O_2(a^1\Delta_g)$ is the source of O_2 1.27 μm dayglow emission in lower and middle atmosphere in Mars, where photolysis of O_3 is the main production mechanism of $O_2(a^1\Delta_g)$ [*Noxon et al.*, 1976; *Fedorova et al.*, 2006]. At higher altitudes it is produced mainly by three body collision process namely, O + O + CO_2 with rate coefficient of $1.2 \times 10^{-32}(300/T)^2$ and yield of 0.66 for the production of O_2 in $^1\Delta_g$ state [*Krasnopolsky*, 2006]. It is evident from various loss profiles that due to its short lifetime of ∼0.8 s, at 80 km and above, most of the O(^{1}S) produced in the Martian atmosphere decay by emitting photon rather than getting quenched by atmospheric molecules.

6.4.2 Production and loss of O(^{1}D)

The altitude profiles of various production processes of O(^{1}D) for solar minimum condition are shown in Figure 6.8, while Table 6.4 shows the contribution of various processes at three different altitudes. The production rate profile of O(^{1}D) shows a double-peak structure; however, the upper peak is not as well defined as O(^{1}S) production peak. Below 120 km, the PD of CO_2 is the major O(^{1}D) production mechanism contributing about 92% at the peak (∼91 km). The O(^{1}S) radiative decay (5%) and PD of O_2 (3%) are minor sources of O(^{1}D). At 130 km, DR of O_2^+ (43%) becomes the dominant O(^{1}D) production process followed closely by PD of CO_2 (29%), O(^{1}S) radiative decay (17%), DR of CO_2^+ (7%), and electron impact on O (2%). At higher altitudes the contribution of electron impact on atomic oxygen starts increasing due to relatively larger density of atomic oxygen; at 180 km, its contribution is around 16%. The contribution of CO_2^+ DR process in O(^{1}D) production was not considered in calculations of *Fox and Dalgarno* [1979a], *Simon et al.* [2009], and *Gronoff et al.* [2012a]. Based on assumptions made in this study (see Section 6.3), this process would also be a significant source mechanism for O(^{1}D) production above 120 km with maximum contribution of ∼7%.

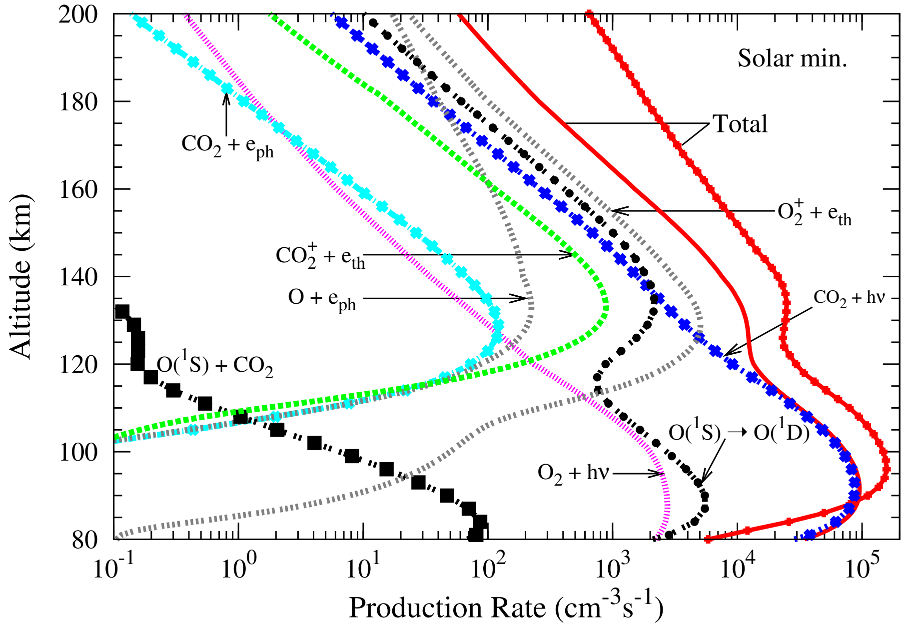

Figure 6.8: Calculated volume production rates of O(^{1}D) for various processes on Mars for solar minimum condition. Red solid curve with symbols shows the total O(^{1}D) production rate for solar maximum condition.

Table 6.4: Contribution of various processes in the production of O(^{1}D) atom on Mars at lower and upper peaks and at a higher altitude (180 km).

Process	Production Rate (cm^{-3} s^{-1})					
	Solar Minimum			Solar Maximum		
	91 km	130 km	180 km	96 km	134 km	180 km
CO_2 + hν	87641 (92)*	3474 (29)	36.7 (14)	135060 (86)	5038 (20)	264 (14)
O(^{1}S $\rightarrow$ ^{1}D)	5314 (5)	2000 (17)	61.2 (24)	11671 (7)	4721 (19)	519 (28)
CO_2^+ + e_{th}	-	820 (7)	16 (6)	-	2351 (9)	197 (10)
O_2^+ + e_{th}	10.5	5035 (43)	100 (39)	39.4	11593 (47)	704 (37)
O + e_{ph}	-	215 (2)	40.5 (16)	-	552 (2)	160 (8)
CO_2 + e_{ph}	-	120 (1)	1.1	-	304 (1)	11
O_2 + hν	2683 (3)	90.3 (0.7)	1.4	10567 (7)	249 (1)	9
CO + hν	-	1.9	-	-	6	2.4
O(^{1}S) + CO_2	40	0.1	-	109	2	-
Total	95508	11759	257	157449	24824	1865

*Value in parentheses shows the percentage contribution in total production rate.

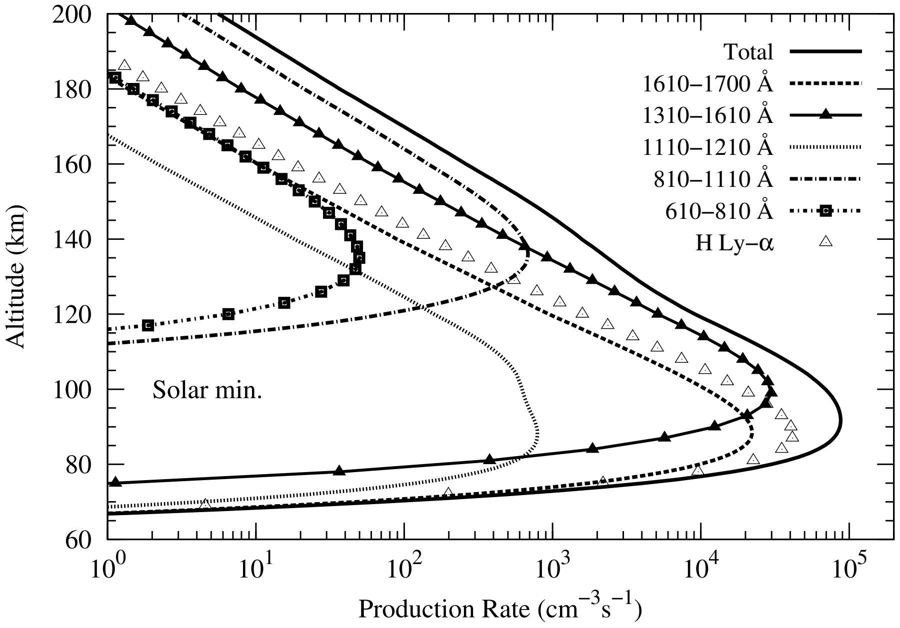

Figure 6.9: Volume production rates of O(^{1}D) due to PD of CO_2 at different wavelengths on Mars for solar minimum condition. The contribution of different wavelengths in solar maximum condition remains same as in the solar minimum condition.

The O(^{1}D) volume production rate for solar maximum condition is also shown in Figure 6.8, depicting that the altitude of peak production rate rises by ∼5 km and the magnitude at peak increases by a factor of 1.6 compared to that during the solar minimum condition. At higher altitudes this difference increases, e.g., at 140 km, the O(^{1}D) production rate is a factor of ∼3 higher. The O(^{1}D) production at the peak is mainly governed by the absorption of higher wavelength photons (1250–1700 Å) by CO_2,

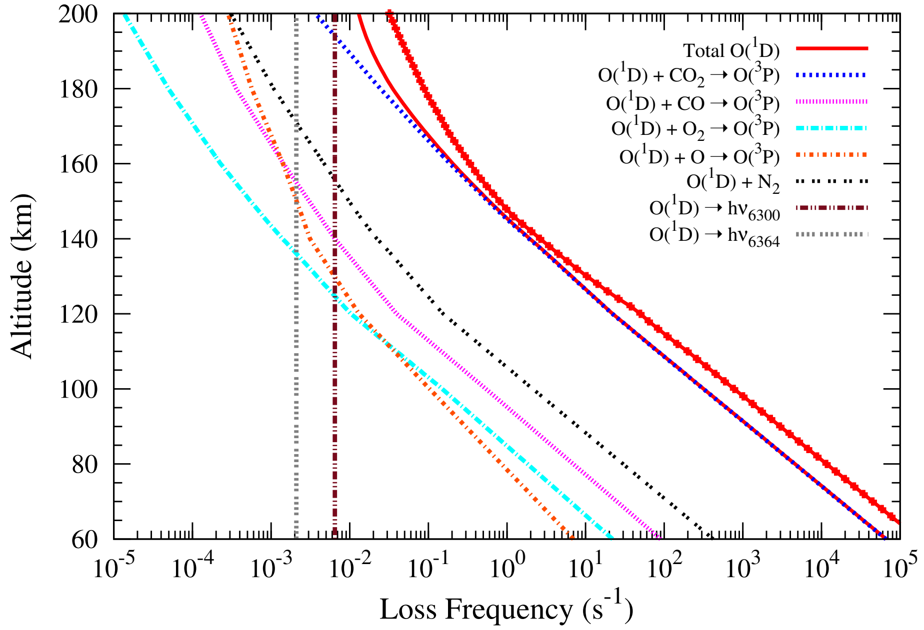

Figure 6.10: Calculated altitudinal profiles of loss mechanisms of O(^{1}D) on Mars for solar minimum condition. Solid red curve with symbols shows the total loss frequency of O(^{1}D) for solar maximum condition.

which do not vary much from solar minimum to maximum condition. Table 6.4 shows the production rates of O(^{1}D) due to various processes at three different altitudes. At peak altitude of 96 km, the PD of CO$_2$ contributes 86% to the total O(^{1}D) production followed by the contributions of O(^{1}S → ^{1}D) (7%) and PD of O$_2$ (7%). At 134 km, the contributions of PD of CO$_2$, DR of O$_2^+$ and CO$_2^+$ and O(^{1}S) radiative decay to the total O(^{1}D) production are 20, 47, 9, and 19%, respectively.

Figure 6.9 shows the calculated altitude profiles of O(^{1}D) volume production rate in the PD of CO$_2$ due to various wavelength bands during solar lines for solar minimum condition. More than 90% of O(^{1}D) production is due to the solar photons at wavelengths higher than 1200 Å, because the O(^{1}D) yield tends to be unity at these wavelengths (cf. Figure 6.3). The O(^{1}D) production due to H Lyman-α peaks at ∼88 (95) km, contributing around 51% (69%), followed by photons in the wavelength range 1610–1700 Å, accounting for about 23% (16%) O(^{1}D) production in low (high) solar activity condition.

Due to its long lifetime of about 110 seconds, the O(^{1}D) can get quenched effectively by atmospheric constituents before it can emit photon. Figure 6.10 shows the altitude profiles of various loss processes of O(^{1}D) for low and high solar activities. Below 180 km, most of the O(^{1}D) is quenched by CO$_2$, which is more than 2 orders of magnitude higher than the quenching by N$_2$. At lower altitudes (<100 km), radiative decay O(^{1}D → ^{3}P) is six orders of magnitude smaller than the quenching by CO$_2$. During solar minimum (maximum) condition, above 200 km (220 km) the radiative decay becomes the dominant loss process.

6.4.3 Density and volume emission rate of O(^{1}S) and O(^{1}D)

The densities of O(^{1}S) and O(^{1}D) atoms are calculated under photochemical equilibrium by using the production and loss rates discussed earlier. Figure 6.11 shows the calculated density profiles of O(^{1}S) and O(^{1}D) for solar minimum and maximum conditions. At lower altitudes (<130 km) most of the O(^{1}D) is quenched, so its density does not vary much with change in solar activity from minimum to maximum. Though the production rate of O(^{1}D) peaks below 100 km (cf. Figure 6.8), its density profile in the solar minimum (maximum) shows a broad peak in the 150–180 (160–200) km region. Since the O(^{1}S) does not get quenched as effectively as O(^{1}D) in Martian atmosphere, the density profile of O(^{1}S) is similar to that of its production rate. Two peaks—one around 90 (95) km and another around 134 (137) km—are seen in the O(^{1}S) density profiles for solar minimum (maximum) condition. The O(^{1}S) density at the lower (upper) peak increases by a factor of 2 (2.3) due to the change in solar activity.

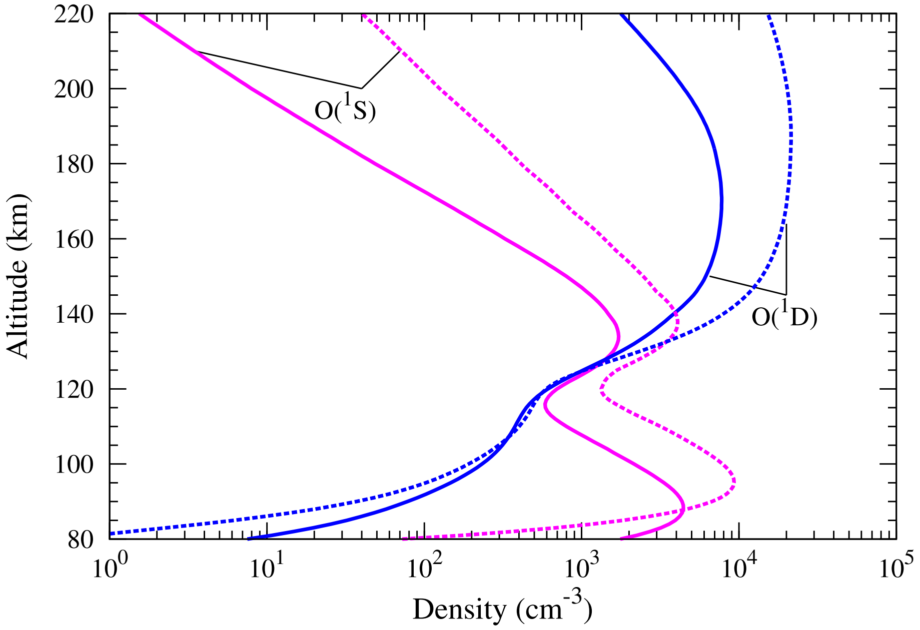

Figure 6.11: Calculated altitude profile of O(^{1}S) and O(^{1}D) densities on Mars in solar minimum (solid curves) and maximum (dashed curves) conditions.

Having calculated the densities of O(^{1}S) and O(^{1}D), the emission rates of OI 2972, 5577 Å, and red doublet (6300, 6364 Å) are computed by using the following equation

$$\mathrm{V_X(Z) = A_X[O(^1S)\,or\,O(^1D)]_Z} \tag{6.1}$$

where $V(Z)$ is the volume emission rate (in cm^{-3} s^{-1}) at altitude Z; A is the transition probability (in s^{-1}) which is given in Tables 6.1 and 6.2; X refers to 2972 or 5577 Å emission in case of $[O(^1S)]_Z$ and to the red doublet (6300, 6364 Å) in case of $[O(^1D)]_Z$ at the altitude Z.

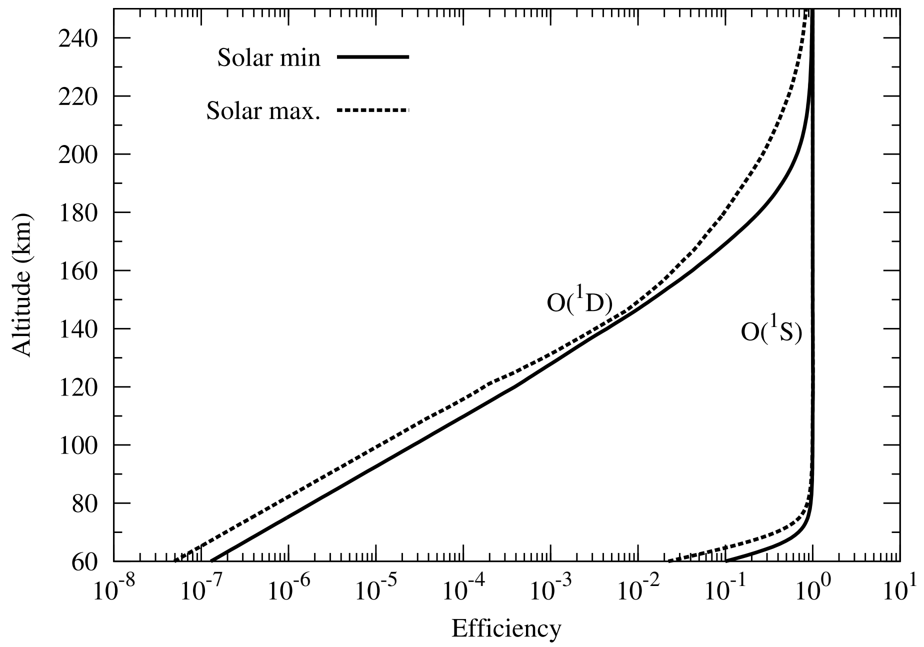

Figure 6.12: Calculated radiative efficiencies of $O(^1S)$ and $O(^1D)$ on Mars during high (maximum) and low (minimum) solar activities.

Figure 6.12 shows the radiative efficiencies of $O(^1S)$ and $O(^1D)$ in the Martian upper atmosphere. The radiative efficiency is the ratio of emission rate to the production rate. Above 80 km, the $O(^1S)$ emission efficiency is unity in both solar minimum and maximum conditions, which clearly shows that above 80 km most of the $O(^1S)$ decay by emitting a photon (either 5577 or 2972 Å). Below 80 km $O(^1S)$ gets rapidly quenched by $O_2(a^1\Delta_g)$; at 70 km its radiative efficiency reduces to 68% (37%) in solar minimum (maximum) condition. Radiative efficiency of the $O(^1D)$ in solar minimum and maximum conditions are very small and they also differ by a factor of 2 or more. Around 140 km, only 0.5 (0.35)% of the total $O(^1D)$ gives off 6300 or 6364 Å emission during solar minimum (maximum) condition. The $O(^1D)$ radiative efficiency increases with altitude because of decrease in density of quenching species (mainly CO_2) at higher altitude. At 200 km, the radiative efficiency of $O(^1D)$ is around 70% (30%) in solar minimum (maximum) condition and it becomes unity at altitude of around 220 (250) km.

Table 6.5 shows the height-integrated column excitation and emission rates of $O(^1S)$ and $O(^1D)$ for both low and high solar activity. The excitation rate of $O(^1D)$ is a factor of 6 (4.7) higher for solar minimum (maximum) condition compared to that of $O(^1S)$. In spite of having large excitation rate, only a very small fraction (0.2 to 0.4%) of $O(^1D)$ gives off photon because of heavy quenching, while ∼99% of $O(^1S)$ decays to ground state via emitting a photon.

Table 6.5: Height-integrated column excitation and emission rates of O(^{1}S) and O(^{1}D) in Martian dayglow for solar minimum and maximum conditions.

Species/Emission	Solar minimum	Solar maximum
Excitation Rates (10^9 cm^{-3} s^{-1})		
O(^{1}S)	20	44
O(^{1}D)	275	441
Emission Rates (kR)		
5577 Å	18	39
2972 Å	1.9	4
Red doublet (6300, 6364 Å)	0.5	1.9

The volume production rate of O(^{1}S) mostly depends on the solar flux in wavelength range 850–1215 Å (cf. Figure 6.5 and Table 6.3), which changes by a factor of 2 during a solar cycle. Due to the lack of quenching above 80 km, the O(^{1}S) production rate directly converts into its emission rate. Hence, a factor of 2 variation is found both in production and emission rates of O(^{1}S) due to change in solar activity. In the case of red doublet emission, the contribution of PD of CO$_2$ in height-integrated column excitation rate of O(^{1}D) is very large and most of it is from the altitudes below 120 km. The O(^{1}D) production in PD of CO$_2$ depends on the solar photons in wavelength range 1250–1670 Å, which does not vary significantly from solar minimum to maximum condition. Hence, a factor of 1.6 variation is observed in the column excitation rate of O(^{1}D) for change from low to high solar activity. However, due to heavy quenching of O(^{1}D), its emission rate peak is found at higher altitudes (>150 km; see Figure 6.11), where O(^{1}D) production is mainly governed by the electron impact and electron recombination processes (cf. Table 6.4). These processes are controlled by the solar ionizing flux at wavelengths below 900 Å that changes by a factor of 3 or more during a solar cycle. Hence, the emission rates of red doublet changes by more than a factor of 3 with solar cycle.

6.4.4 Limb intensities of OI 2972, 5577, and 6300 Å emission

The calculated volume emission rates of 2972, 5577 Å, and red doublet (6300, 6364 Å) are integrated along the line of sight at a projected distance from the centre of Mars to obtain limb profiles (see equation 4.9 for detail). Figure 6.13 shows the calculated limb intensity profiles of OI 2972, 5577, and 6300 Å emissions for solar minimum and maximum conditions. Limb profiles of 2972 and 5577 Å have two peaks; one near 90 km and another near 130 km. The OI 5577 Å emission has maximum intensity of around ∼434 kR (930 kR) at 84 (91) km and intensity of about 164 (400) at 127 (131) km during solar minimum (maximum) condition; a change of more than a factor of 2 due to change in solar activity. At higher altitudes this difference increases, e.g., at 200 km, the calculated OI 5577 Å limb intensity for solar minimum (0.5 kR) differ by more than an order of magnitude from that calculated for solar maximum (10 kR) condition. This difference with increasing altitude is because of the change in scale height of neutral atmosphere from solar minimum to maximum condition. Limb profiles of OI 2972 Å for both solar minimum and maximum conditions are similar to that of respective OI 5577 Å limb profiles but smaller by a factor of 9.4, which is the ratio of OI 5577 and 2972 Å emissions taken in the present study.

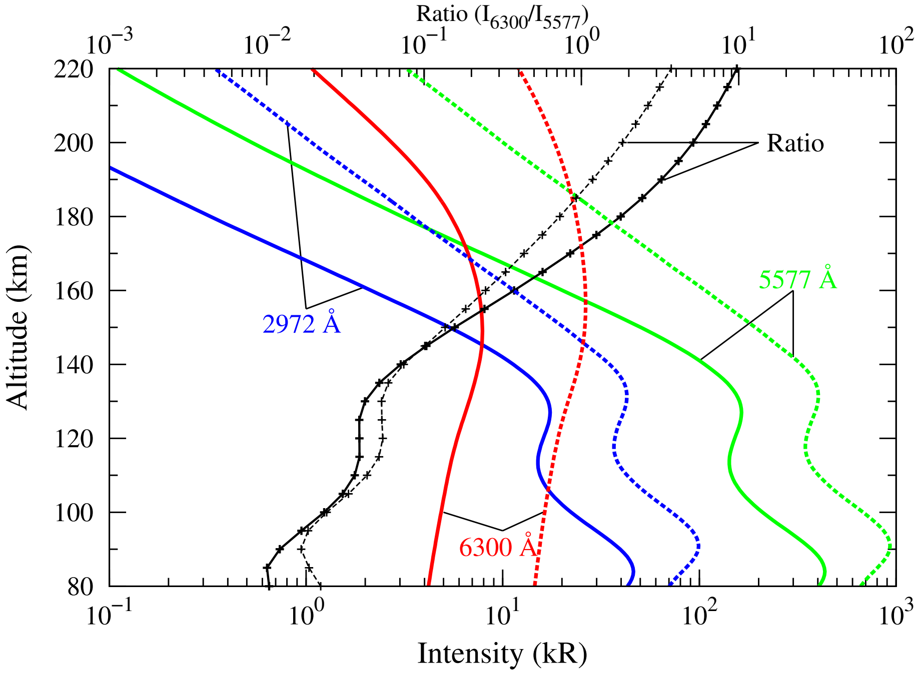

Figure 6.13: Calculated limb intensities of OI 2972, 5577, and 6300 Å on Mars in solar minimum (solid curves) and maximum (dashed curves) conditions at solar zenith angle of 45°. Ratio of intensity of OI 6300 and 5577 Å emissions for solar minimum and maximum conditions is also plotted with scale shown on top X-axis.

Huestis et al. [2010] did not report any double peak structure in OI 2972 Å emission profile. Though *Simon et al.* [2009] did not report any calculated altitude profile of OI 2972 Å limb intensities, they stated that SPICAM-observed OI 2972 Å limb profile has two peaks, one around 80 km and another around 125 km. *Simon et al.* [2009] also stated that comparison of their modelled OI 2972 Å limb profile with SPICAM-observed profile shows similar behaviour but intensities differ by around a factor of 2. *Huestis et al.* [2010] used Mars Express (MEx) data for orbit 941 in their analysis. According to *Gronoff et al.* [2012a], SPICAM data for MEx orbit 947 is having solar contamination and low signal to noise level for the OI 2972 Å emission and might also be contaminated by the N_2 VK (0, 7) emission. Also, according to *Gronoff et al.* [2012a], when the different orbits are analysed separately a peak is seen around 120 km in OI 2972 Å profile, which varies in altitude up to 20 km for different orbit. *Gronoff et al.* [2012a] have shown the OI 2972 Å emission profile for MEx orbit 1298 which depicts a peak around 120 km.

The calculated limb profiles of OI 6300 Å for solar minimum and maximum conditions are shown in Figure 6.13, depicting a broad peak centred around 150 km with a maximum intensity of around 8 and 26 kR, respectively. The ratio of intensity of red (6300 Å) to green (5577 Å) atomic oxygen lines is also shown in Figure 6.13. At lower altitudes calculated ratio is very small (<0.1, but increase with altitude), reflecting higher intensity of green line compared to that of red line. Around 170 (180) km, the intensity ratio becomes unity, and above this altitude it is more than unity due to the higher intensity of the red line compared to that of the green line. It clearly shows that on Mars the most preferable altitudes to observe red line emission would be above 150 km.

6.4.5 Comparison with observation

Observations of OI 2972 Å emission by Mariner 6 and 7 during solar maximum condition was reported by *Stewart* [1972]. We run the model for the condition similar to that during Mariner observations (F10.7 = 180, Mars heliocentric distance = 1.42 AU). Figure 6.14 shows the calculated limb intensity of OI 2972 Å emission at solar zenith angle of 20° along with the intensities observed by Mariner 6 and 7. Intensity of OI 2972 Å emission is also calculated by using the NIST recommended value of 16.7 for the OI 5577 and 2972 Å emission intensity ratio. Below 170 km, the model calculated intensity is in agreement with the Mariner observations when the NIST recommended ratio value is used. It is difficult to determined the ratio of OI 5577 and 2972 Å emission based on agreement between calculated and observed profile due to calibration problems in Mariner Ultraviolet Spectrometer Experiment [*Stewart et al.*, 1972]. Above 170 km, the observed values are more scattered. This may be due to the lower signal to noise ratio at higher altitudes. The model calculated OI 2972 Å emission peak lies around 130 km. Mariner observations did not provide data below 120 km so the lower prominent peak is not visible in the observed OI 2972 Å profiles.

Recently, *Gronoff et al.* [2012a] have provided the OI 2972 Å emission profile measured by SPICAM/MEx for the orbit 1298 (21 January 2005; SZA = 39; Ls = 148; Sun-Mars distance = 1.54 AU; F10.7 = 115). The model calculations are carried out for the similar lighting condition and the day of observation as reported by *Gronoff et al.* [2012a]. Figure 6.14 shows SPICAM-observed profile taken from *Gronoff et al.* [2012a] (after dividing it by a factor of 4π) along with the calculated intensity. The OI 2972 Å emission profile calculated by taking I_{5577}/I_{2972} ratio as 9.4 is in good agreement with the SPICAM observation. Above 160 km, SPICAM-observed data points have large uncertainty due to lower signal to noise ratio. The upper peak is situated near 125 km. The lower peak is not seen in the observed profile; however, an increasing trend is present in the observed profile near 100 km. The OI 2972 Å emission profile (for I_{5577}/I_{2972}=10) modelled by *Gronoff et al.* [2012a] is also shown in Figure 6.14. The shape and magnitude of the calculated OI 2972 Å intensity in the present calculation

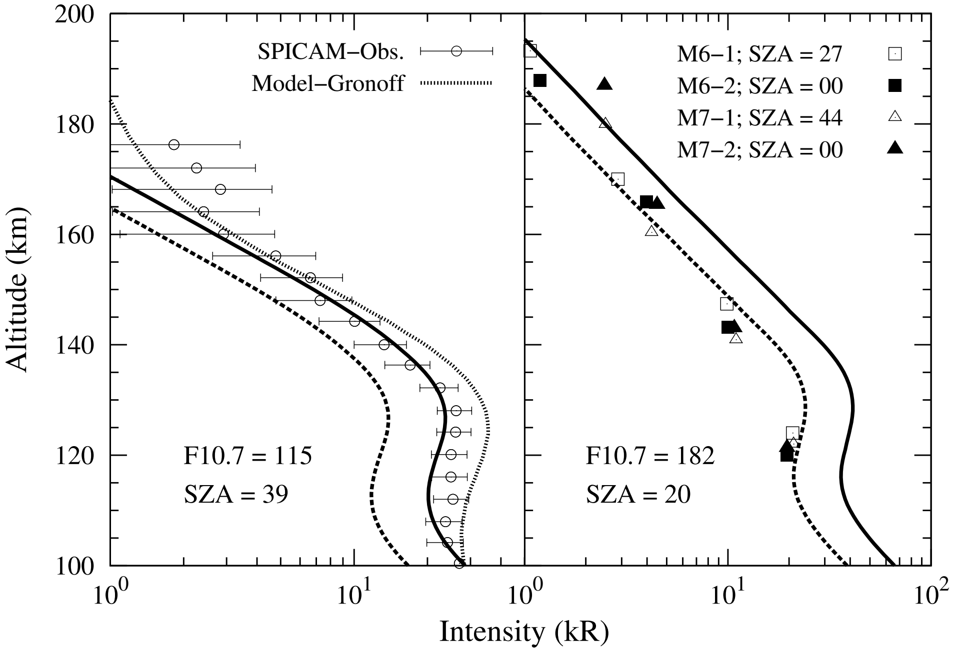

Figure 6.14: Calculated limb intensity of OI 2972 Å on Mars for the condition similar to SPICAM (left panel; SZA = 39°) and Mariner 6 and 7 (right panel; SZA = 20°) observations. OI 2972 Å intensities observed by Mariner 6 and 7 are shown with symbols; M6-1, M7-1, M6-2, and M7-2 refer to Mariner 6 and 7 first and second limb crossing, and SZA refers to the solar zenith angle at which measurements were made. Solid and dashed curves show the calculated OI 2972 Å emission profile by taking the I_{5577}/I_{2972} values of 9.4 and 16, respectively. Calculated limb intensity of OI 2972 Å (for I_{5577}/I_{2972}=10) by *Gronoff et al.* [2012a] is also shown in the figure (left panel).

differs from that of *Gronoff et al.* [2012a]. The difference in shape of emission profile can be attributed to different PD yield of O(^{1}S) used in the two calculations. The calculated profile of *Gronoff et al.* [2012a] could not reproduce the increase in observed profile below 110 km, whereas the calculated profile in the present study depicts an increase in emission intensity near 100 km. However, the two model calculations could reproduce the observed OI 2972 Å profile with PD of CO_2 as the major production source of O(^{1}S). The contribution of DR of O_2^+ is very small in the O(^{1}S) production, contrary to the suggestion of *Huestis et al.* [2010].

6.5 Atomic oxygen emissions on Venus

6.5.1 Production and loss of O(^{1}S)

Figure 6.15 shows the volume production rate of O(^{1}S) for solar minimum and maximum conditions. Two distinct peaks, the lower peak at 117 (114) km and the upper peak at 141 (138) km, is clearly seen in the O(^{1}S) production rate for solar minimum (maximum) condition. Table 6.6 shows the contribution of various processes in the O(^{1}S) production at three altitudes for both low and high solar activity conditions. The lower

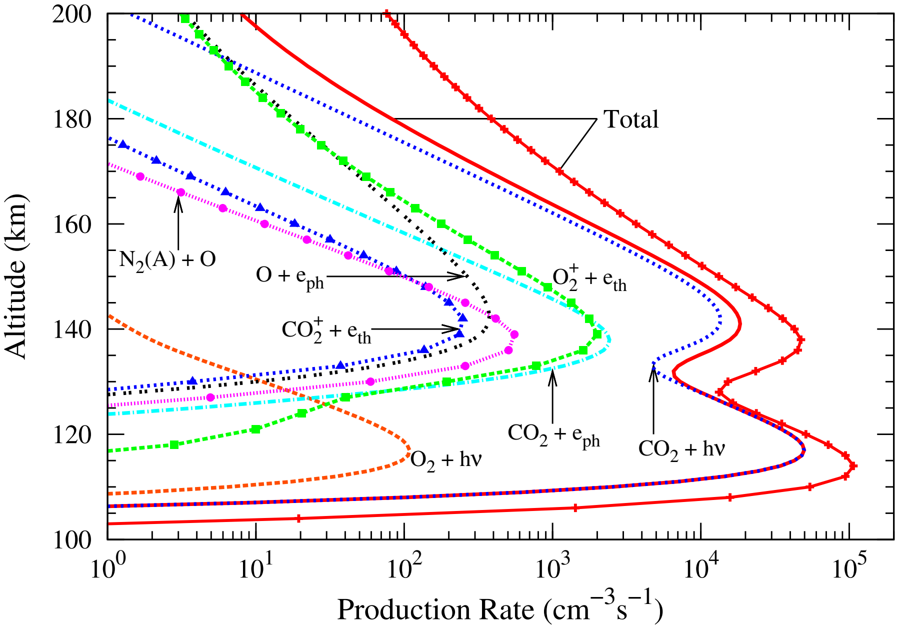

Figure 6.15: Calculated volume production rates of O(^{1}S) on Venus for various processes in solar minimum condition. Solid red curve with symbols shows the total O(^{1}S) production rate in solar maximum condition.

peak is produced solely by the PD of CO_2. At the upper peak, PD of CO_2 remains the major contributor with ∼73% contribution, followed by a 10% contribution each from dissociative recombination (DR) of O_2^+ and electron impact dissociative excitation of CO_2. At higher altitude (∼180 km), PD of CO_2 contributes around 55 (42)%, while DR of O_2^+ and electron impact on O contribute ∼20 (26)% and 21.5 (29)%, respectively, in solar minimum (maximum) condition. Above 180 km, the contribution from DR of O_2^+ and electron impact on O become higher than that from PD of CO_2, which is different from that on Mars, where up to 200 km the PD of CO_2 remains the major source of O(^{1}S) production with contribution of about 80% (see Section 6.4). The calculated O(^{1}S) production rate for solar maximum condition is more than a factor of 2 higher compared to that during solar minimum condition. Both the lower and upper peaks of O(^{1}S) production is situated at higher altitudes in the atmosphere of Venus compared to that in the atmosphere of Mars (cf. Figure 6.5), which is due to the denser atmosphere of Venus.

The contribution of PD of CO_2 at different wavelengths on Venus is similar to that on Mars (see Figure 6.6). The lower peak at 117 km (114 km for high solar activity) is due to the solar photons at 1216 Å. The photons in the wavelength range 860–1160 Å is responsible for the upper peak of O(^{1}S) peak in which 21 (24%) and 15 (13%) contributions are from photons in the wavelength ranges 910–1010 Å and 1100–1150 Å, respectively, during solar minimum (maximum) condition.

Figure 6.16 shows the various loss frequencies of O(^{1}S) in the atmosphere of Venus

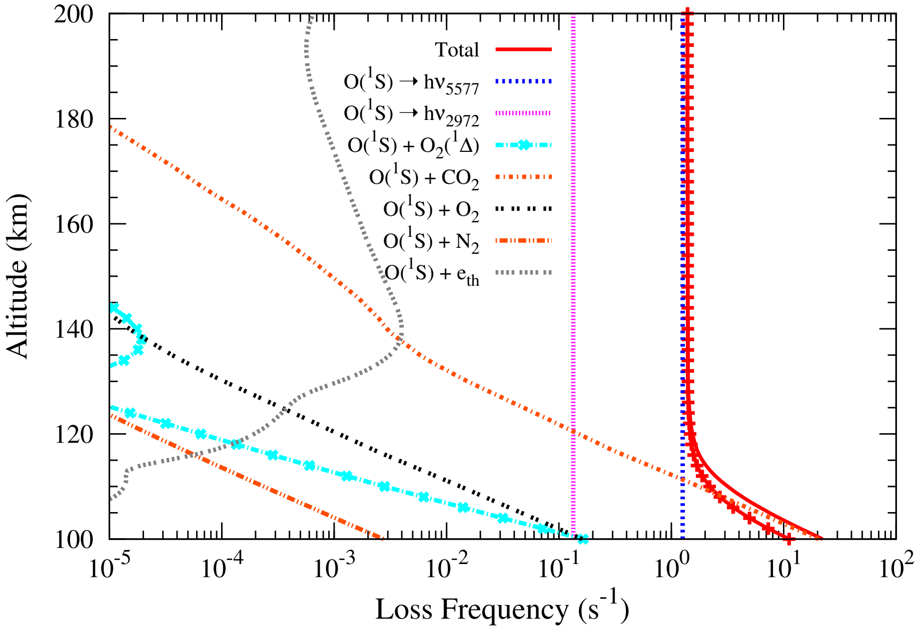

Figure 6.16: Calculated altitudinal profiles of loss rates of O(^{1}S) on Venus for solar minimum condition. Solid red curve with symbols shows the calculated total O(^{1}S) loss frequency for solar maximum condition.

Table 6.6: Contribution of various processes in the production of O(^{1}S) atom at lower and upper peaks and at a higher altitude (180 km) on Venus.

Process	Production Rate (cm^{-3} s^{-1})					
	Solar Minimum			Solar Maximum		
	117 km	141 km	180 km	114 km	138 km	180 km
CO_2 + hν	49625 (99)*	13423 (73)	45.5 (55)	106570 (99)	35090 (74)	163 (42)
CO_2 + e_{ph}	-	1982 (11)	1.9 (2)	-	4120 (9)	7 (2)
O_2^+ + e_{th}	-	1890 (10)	16.3 (20)	-	4574 (10)	100 (26)
CO_2^+ + e_{th}	-	253 (1)	-	-	453 (1)	-
O + e_{ph}	-	367 (2)	17.7 (21.5)	-	1670(3.5)	112 (29)
N_2(A) + O	-	469 (2.5)	-	-	1378 (3)	-
Total	49735	18388	82	106824	47293	387

*Value in parentheses shows the percentage contribution in total production rate.

for low and high solar activity condition. Major loss of O(^{1}S) in Venusian atmosphere is radiative decay via emissions at 5577 and 2972 Å wavelengths. Below 120 km, O(^{1}S) is mainly quenched by CO_2, which is an order higher than the radiative decay.

6.5.2 Production and loss of O(^{1}D)

Figure 6.17 shows the major production rates of O(^{1}D) atom in the atmosphere of Venus along with the total production rate for solar minimum and maximum condition. The production rate peaks at 119 (115) km for solar minimum (maximum) condition.

During the solar maximum condition the O(^{1}D) production rate is about a factor of

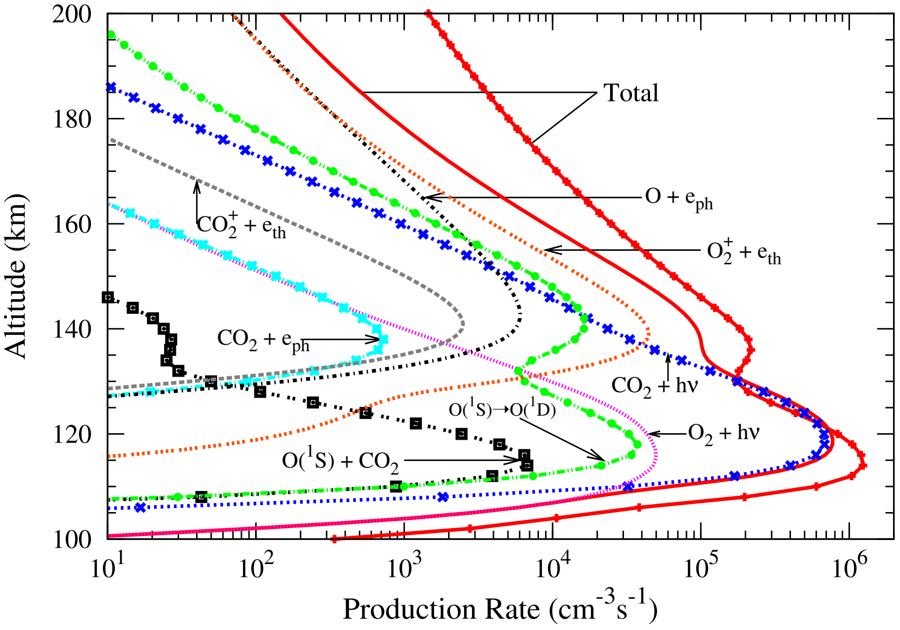

Figure 6.17: Calculated volume production rates of O(^{1}D) on Venus for various processes for solar minimum condition. Solid red curve with symbols shows the total O(^{1}D) production rate in solar maximum condition.

1.6 higher than during the solar minimum condition. Around 140 km a small increase in the O(^{1}D) production rate is seen which is more prominent during solar maximum condition. Table 6.7 shows the contribution of various processes in O(^{1}D) production at different altitudes. At the peak altitude of O(^{1}D) production, the major contribution is from PD of CO_2 (90%), followed by minor contributions (∼5%) from O(^{1}S) radiative decay and PD of O_2. During the solar minimum condition, at 140 km, the contribution of PD of CO_2 reduces to just only 25%. The maximum contribution at this altitude comes from DR of O_2^+ (47%) followed by O(^{1}S) radiative decay (17%). The contribution of electron impact on atomic oxygen increases at 140 km and it amounts to around 6%. During the solar maximum condition, at 136 km, the PD of CO_2 contributes around 18%, against 25% during solar minimum condition. Though the contribution of DR of O_2^+ remains same (49%), the contribution from electron impact on O increases by 5%, which reflects the higher abundance of atomic oxygen in the atmosphere during the solar maximum condition.

At 180 km, the majority of O(^{1}D) production is from DR of O_2^+ and electron impact on O, with a combined contribution of more than 80% (90% in solar maximum). The O(^{1}S) radiative decay contributes <9% in the O(^{1}D) production. Similar situation occurs on Mars where at higher altitudes the contribution of PD of CO_2 in the O(^{1}D) production decreases and that of DR of O_2^+ (40% in both low and high solar activity conditions) and electron impact on O (16% and 8% during low and high solar activity, respectively) increases, but the combined contribution of both these processes is about

50% only (Section 6.4). On Venus, above 160 km atomic oxygen is the dominant species, which causes the increase in contribution of e-O process in O(^{1}S) and O(^{1}D) production at higher altitudes.

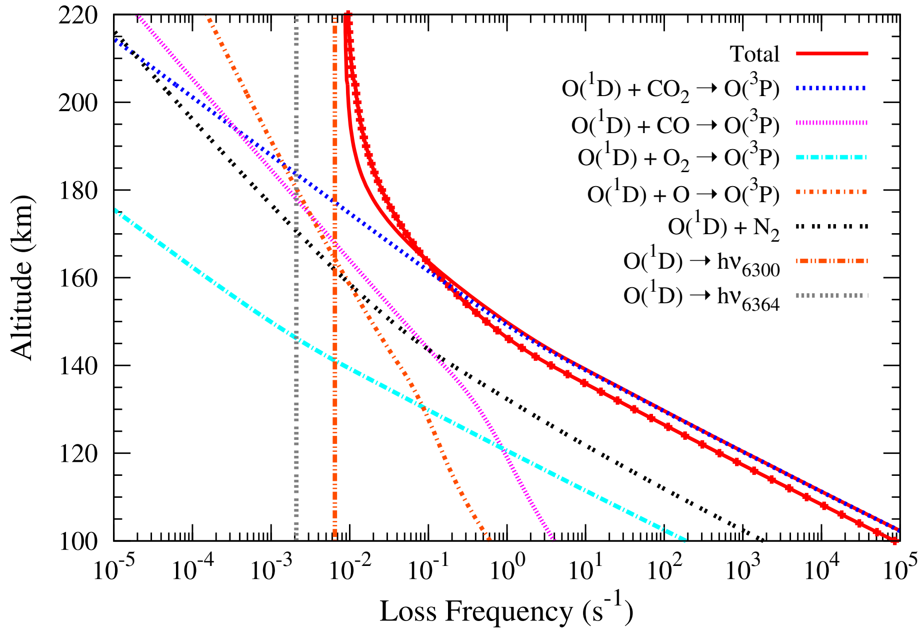

Figure 6.18: Calculated altitudinal profiles of major loss mechanism of O(^{1}D) on Venus for solar minimum condition. Solid curve with symbols shows the total O(^{1}D) loss frequency for solar maximum condition.

Table 6.8 shows the height-integrated total production rate of O(^{1}S) and O(^{1}D) in the atmosphere of Venus. The excitation rate of O(^{1}D) is higher by a factor of 14 (10) than that of O(^{1}S) in low (high) solar activity condition. Similar ratio for both solar minimum and maximum conditions is found on Mars (Section 6.4). Compared to that on Mars, the O(^{1}S) and O(^{1}D) production rate on Venus is higher by a factor of 4.4, which reflects the higher solar flux received at the Venus due to small heliocentric distance.

Figure 6.18 shows the calculated altitudinal profiles of various loss frequencies of O(^{1}D) on Venus for solar minimum (top panel) and maximum (bottom panel) conditions. The CO$_2$ is the largest quencher of O(^{1}D) atom and below 160 km, most of the O(^{1}D) atoms produced in the Venus atmosphere get quenched and do not emit photons. Above 180 km radiative loss via 6300 and 6364 Å photons becomes dominant. It is clear from Figure 6.18 that despite having large production rate very few percentage of O(^{1}D) atoms emit photons at altitudes below 160 km, and most of them get quenched.

6.5.3 Densities of O(^{1}S) and O(^{1}D) atoms on Venus

Figure 6.19 shows the altitudinal profiles of calculated density of O(^{1}S) and O(^{1}D) for solar minimum and maximum condition. The shape of density profiles of O(^{1}S) and O(^{1}D) on Venus is similar to than on Mars (cf. Figure 6.11). The O(^{1}S) density

Table 6.7: Contribution of various processes in the production of O(^{1}D) atom at lower and upper peaks and at a higher altitude on Venus.

Process/Alt	Production Rate (cm^{-3} s^{-1})					
	Solar Minimum			Solar Maximum		
	119 km	140 km	180 km	115 km	136 km	180 km
CO_2 + hν	690090 (89)*	23561 (25)	30 (4)	1092500 (88)	38603 (18)	89 (2)
O(^{1}S → ^{1}D)	35773 (5)	16290 (17)	74 (9)	79514 (6)	40461 (19)	349 (7)
CO_2^+ + e_{th}	-	2455 (3)	5.5	-	4337 (2)	17
O_2^+ + e_{th}	106	43829 (47)	361 (43)	374	106977 (49)	2229 (44)
O + e_{ph}	-	5625 (6)	355 (43)	-	23693 (11)	2333 (46)
CO_2 + e_{ph}	-	653	-	-	1467	2
O_2 + hν	45940 (6)	991 (1)	-	61602 (5)	1285	1
CO + hν	-	83	4.3	-	185	18
O(^{1}S) + CO_2	3356	24	-	9236	53.5	-
Total	775283	93565	832	1243284	217256	5042

*Value in parentheses shows the percentage contribution in total production rate.

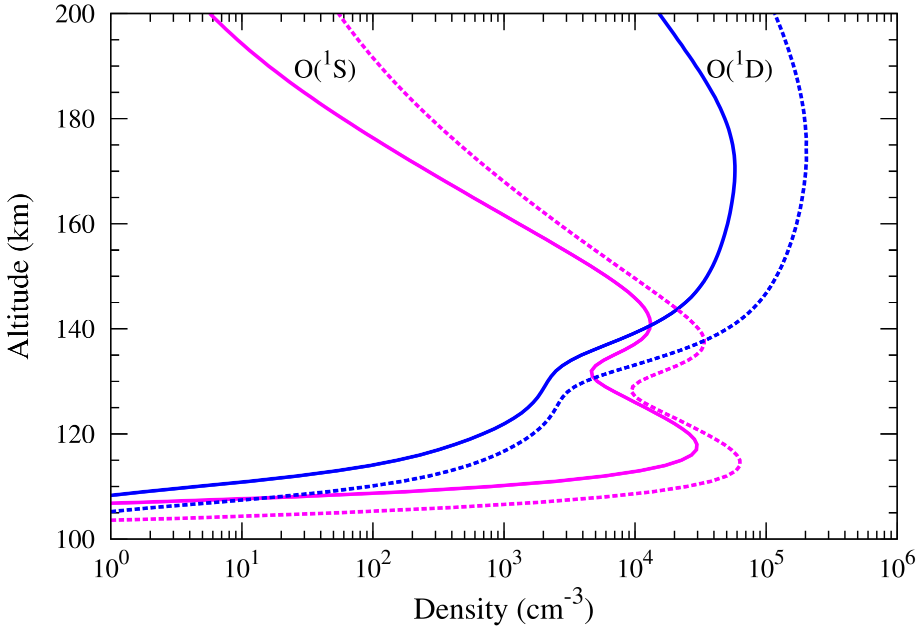

Figure 6.19: Calculated altitude profile of densities of O(^{1}S) and O(^{1}D) on Venus for solar minimum (solid curves) and maximum (dashed curves) conditions.

Table 6.8: Height-integrated column excitation and emission rates of O(^{1}S) and O(^{1}D) in dayglow of Venus for solar minimum and maximum conditions.

Species/Emission	Solar minimum	Solar maximum
Excitation Rates (10^9 cm^{-3} s^{-1})		
O(^{1}S)	84	190
O(^{1}D)	1214	1962
Emission Rates (kR)		
5577 Å	68	155
2972 Å	7	16
Red doublet (6300, 6364 Å)	2.3	10

shows two distinct peaks, one below 120 km and another around 140 km. During solar minimum, the lower peak of O(^{1}S) density peaks at 118 km which is about 4 km higher than O(^{1}S) density peak during solar maximum condition. The magnitude of O(^{1}S) density at lower peak during high solar activity is a factor of ∼2 larger compared to that during low solar activity condition. This difference of a factor of 2 is due to a change in solar H Ly-α flux from low to high solar activity condition. However, the O(^{1}S) density at upper peak (141 km for low and 138 for high solar activity) is a factor of 2.6 larger during solar maximum compared to that during solar minimum condition.

Having calculated the densities of O(^{1}S) and O(^{1}D) atom in Venusian atmosphere, the volume emission rates of OI 2972, green (5577 Å), and red doublet (6300, 6364 Å) are calculated using equation 6.1. Table 6.8 shows the height-integrated emission rates of OI 2972, 5577 Å, and red doublet (6300, 6364 Å) lines. Total excitation rates of O(^{1}S) and O(^{1}D) are also presented in Table 6.8. Variation in the emissions rate of O(^{1}S) and O(^{1}D) from low to high solar activity condition shows trend similar to that on Mars (see Table 6.5).

6.5.4 Limb intensities of OI 2972, 5577, and 6300 Å emission

Figure 6.20 shows the calculated altitudinal limb profiles of OI 2972, 5577, and 6300 Å emission in the atmosphere of Venus for low and high solar activity condition. The limb intensity 5577 Å emission peaks at 115 (112) km and 137 (134) km with a peak value of 2900 (6400) kR and 1230 (3130) kR, respectively, during solar minimum (maximum) condition. The limb intensity of OI 2972 Å is similar in shape to OI 5577 Å but a factor of 9.4 smaller compared to that of OI 5577 Å, which is the ratio I_{5577}/I_{2972} used in the present study (see Table 6.1). Below 140 km, the calculated OI 2972 and 5577 Å emissions are higher by a factor of ∼2.4 during high solar activity compared to that in low solar activity condition. The limb intensity of OI 6300 Å shows a broad peak with a maximum value of about 62 (256) kR at an altitude of ∼154 (157) km in solar minimum (maximum) condition; a difference of more than a factor of 4 in the calculated intensities between low and high solar activity. As discussed earlier, this variation in OI 6300 Å emission intensity from solar minimum to maximum condition is due to the involvement of solar photon at wavelengths >900 Å, which govern the major sources

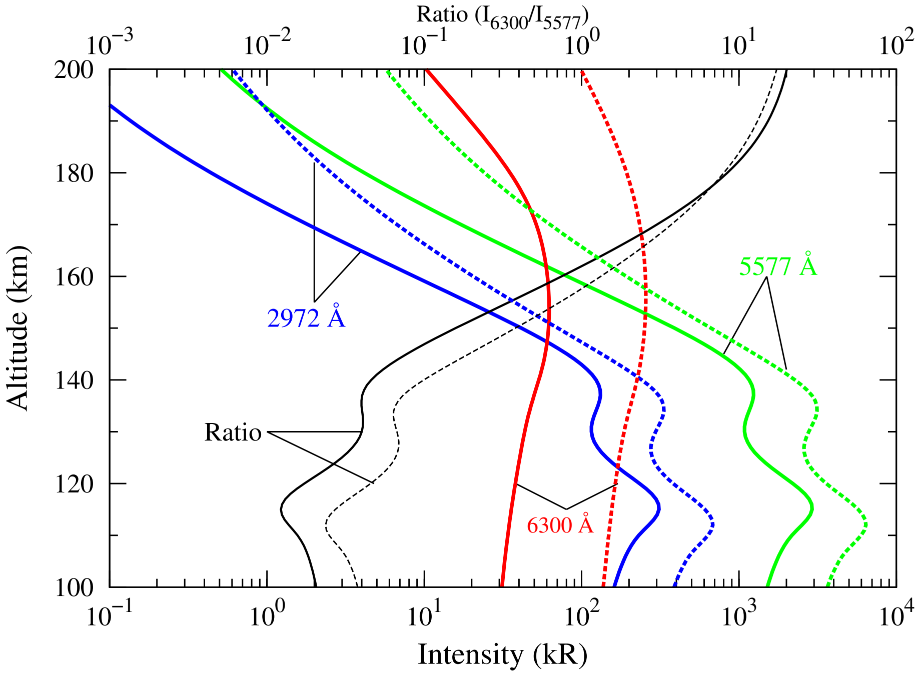

Figure 6.20: Calculated limb intensities of OI 2972, 5577, and 6300 Å on Venus for solar minimum (solid curves) and maximum (dashed curves) conditions at solar zenith angle of 45°. Ratio of intensity of OI 6300 and 5577 Å emissions for solar minimum and maximum conditions is also plotted with scale shown on top X-axis.

(DR of O_2^+ and electron impact on O) of O(^{1}D) production at higher altitudes. The ratio of red to green line is also shown in Figure 6.20. Below 150 km, the ratio I_{6300}/I_{5577} is about 0.1 but above that altitude value of I_{6300}/I_{5577} is larger than 1, which shows that at higher altitudes red line is more stronger than green line.

Due to backscattered radiation from clouds of Venus, it is very difficult to extract useful dayglow emission data but at higher altitudes it is easier to look for dayglow emission without solar contamination. At 160–180 km, OI red line emission intensity is about 20–30 kR, which makes it easier to detect at those altitudes.

LeCompte et al. [1989] have reported the PVOUVS observations of OI 2972 Å dayglow emission from Venus for orbit 187 and 208, which were taken during the initial phase of solar maximum. *LeCompte et al.* [1989] have also modelled the limb profile of OI 2972 Å emission. They showed that the PD of CO_2 is the major of source of 2972 Å emission below 170 km, above that altitude DR of O_2^+ and contribution from CI 2967 Å (^{5}S $\rightarrow ^3$P) made most of the the observed signal. Their calculated limb profiles were in good agreement with the observation at higher altitudes but below 120 km model intensity are about a factor of 2 larger than the observation. *LeCompte et al.* [1989] attributed this difference in observed and modelled intensity below 130 km to the temperature profile used in their model calculation (taken from VTS3 model). The quenching rate of O(^{1}S) by CO_2 is sensitive to the temperature structure and several instruments on-board PVO inferred the presence of oscillating temperature profiles based on the measured neutral densities [see the review of *Fox and Bougher*, 1991, and references therein].

In the present study, calculation are carried out for the condition similar to PVOUVS orbit 187 (9 June 1987). Model atmosphere is taken from VTS3 model (for local time of 1200; SZA = 0°; F10.7 = 240). The calculated overhead intensity of OI 2972 Å is $\sim$17 kR, which is more than a factor of 2 higher than 7 kR reported by *LeCompte et al.* [1989] based on PVOUVS observations, and also higher than the value of 9 kR calculated by *LeCompte et al.* [1989]. We also carried out model calculation by taking I_{5577}/I_{2972} value of 16 (see Section 6.3). For I_{5577}/I_{2972}=16, the calculated height-integrated overhead intensity of OI 2972 Å emission is $\sim$10 kR. This value is in agreement with the model calculated value of *LeCompte et al.* [1989].

Recently, first observations of CO Cameron band and CO_2^+ UV doublet emissions by SPICAV/VEx have been reported by *Chaufray et al.* [2012]. They presented SPICAV observations at spectral resolution of 10 nm, which is rather poor to separate OI 2972 Å emission from bright CO_2^+ UV doublet emission at 2890 Å. Detection of OI 2972 Å emission by SPICAV-UV narrow slit (resolution of 1.5 nm) would be really useful to understand the role of various processes governing this emission on Venus, and also to constrain the I_{5577}/I_{2972} ratio.

6.6 Summary and conclusions

In this chapter a detailed model for the atomic oxygen ultraviolet (2972 Å), green line (5577 Å), and red doublet (6300, 6364 Å) emissions in the dayglow of Mars and Venus is presented. All the possible production and loss reactions of O(^{1}S) and O(^{1}D) in the atmospheres of Mars and Venus have been considered in the present calculation. Based on earlier measurements, the yield of O(^{1}D) in PD of CO_2 is recommended.

Below 120 km, on Mars and Venus, the main production source of O(^{1}D) is photodissociation of CO_2, while at higher altitudes dissociative recombination of O_2^+, O(^{1}S) radiative decay, and photodissociation of CO_2 are the major sources. On Mars, during both solar minimum and maximum conditions, the main production mechanism of O(^{1}S) is photodissociation of CO_2, while on Venus photodissociation of CO_2 is the major source of O(^{1}S) production below 160 km only. Above that altitude, the contributions of dissociative recombination of O_2^+ and electron impact on O increases significantly. Contrary to the recent suggestion of *Huestis et al.* [2010], the present calculation shows that dissociative recombination of O_2^+ is not the major source mechanism for O(^{1}S) production in the 80–170 km region on Mars. Thus, the O(^{1}S) emission cannot be used as a monitor of Martian ionosphere, unlike that mentioned by *Huestis et al.* [2010]. The major loss process for O(^{1}S) is radiative decay and for O(^{1}D), quenching by CO_2. The effect of $O_2^+(\nu)$ vibrational distribution on O(^{1}S) and O(^{1}D) production is found to be negligible. On Mars, the calculated OI 2972 Å emission profiles are in agreement with the Mariner and Mars Express observations.

Calculations carried out in the present study would lead to a better understanding of the photochemical processes governing the O(^{1}S) and O(^{1}D) production in the atmospheres of Mars and Venus. Improved laboratory measurements of O(^{1}D) yield in the PD of CO_2, and branching ratios of O(^{1}S) and O(^{1}D) in DR of O_2^+ and CO_2^+ are needed to constrain the production sources of atomic oxygen emission in the dayglow of Mars and Venus. The OI emission intensities calculated in the present study will also be helpful in the interpretation of OI 2972 Å dayglow measurement of SPICAV-VEx and future visible OI dayglow emission from Venus. Based on the model calculated limb intensity profiles of OI emissions and ratio of 6300 and 5577 Å, it is suggested that in future Mars missions the search for red doublet emissions should focus at altitudes above 160 km, whereas for observing of OI 2972 and 5577 Å emissions the altitude region below 150 km is more suitable.

Chapter 7

Summary and future scope

Summary

Atmospheres of Mars and Venus have been studied extensively by several space missions. The wealth of information acquired by these missions have not only helped in understanding the atmospheric evolution of the two planets, but raised many questions as well. In the present thesis an attempt has been made to understand some of the physical processes that are governed by solar radiation interaction with the upper atmospheres of Mars and Venus. Energetic photons emanating from Sun deposit their energy in planetary upper atmosphere and initiate many physical and chemical processes. Molecular and atomic emissions coming from the sunlit atmosphere (dayglow) are manifestations of such an interaction. These emissions provide useful information about atmospheric structure, composition, temperature, and energetics of the atmosphere. Modelling of dayglow emissions is not only crucial for understanding physical processes governing these emission, also to determine and constrain the input parameters, such as cross sections and model atmosphere. In this thesis, the ultraviolet and visible dayglow emissions (viz., CO Cameron band, CO_2^+ ultraviolet doublet, N_2 VK band, and OI green (5577 Å), red doublet (6300, 6364 Å), and ultraviolet 2972 Å emissions) in atmospheres of Mars and Venus are modelled. The effect of various input parameters on the dayglow emission intensity is also studied. Modelling of these emissions is also important in context of current observations being carried out by SPICAM/Mars Express (MEx) on Mars and SPICAV/Venus Express (VEx) on Venus. Model calculation of emissions other than those mentioned above will be carried out in future and is discussed in the following section.

Photoelectron—generated due to photoionization—is an important source of upper atmospheric emissions. Degradation of an electron in an atmosphere requires a technique for electron energy apportionment. Since atmospheres of both Mars and Venus are predominately CO_2 (95% by volume), a Monte Carlo model is developed in this thesis for electron energy degradation in an atmosphere of CO_2. A detailed compilation of cross sections of electron impact on CO_2 is presented which is used as an input in the

Monte Carlo model and also used in the modelling of dayglow emissions. The output of Monte Carlo simulation is used to generate the "yield spectra", which embodied all the information related to electron degradation process, and can be used to calculate the "yield" or (population) for any inelastic process. The numerical yield spectra have been fitted analytically resulting in an "Analytical Yield Spectra (AYS)". The mean energy per ion pair and efficiencies for different inelastic processes have been calculated using AYS, which compares well with those obtained by using numerical yield spectra. The mean energy per ion pair for neutral CO_2 is found to be 37.5 (35.8) eV at input energy of 200 (1000) eV. Ionization is the dominant loss process due to its higher cross section at higher energies. At energies above 100 eV, ∼50% energy goes into the ionization loss channel. Among the excitation processes, 13.6 eV and 12.4 eV states are dominant loss processes consuming ∼28% energy above 200 eV. The AYS is used to calculate steady state photoelectron fluxes in the atmosphere of Mars and Venus.

The intensity of CO Cameron band and CO_2^+ doublet emissions is calculated in the atmospheres of Mars and Venus. The effect of two solar EUV flux model namely, EUV flux model for Aeronomic Calculation (EUVAC) and SOLAR2000 (S2K) on emission intensity is calculated for different solar activity conditions. The emission rates of $CO(a^3\Pi)$ and $CO_2^+(B^2\Sigma_u^+)$ are height-integrated to calculate the overhead intensity and along the line of sight to obtain the limb intensities. The intensities of $CO(a', d, e)$ triplet band emissions on Mars and Venus are predicted. Calculated limb intensities on Mars are compared with the SPICAM/MEx and UV spectrometer/Mariner observed intensities. The calculated brightness profiles of CO Cameron band and CO_2^+ doublet emissions are in agreement with the SPICAM observation; however, in solar maximum condition the calculated intensities are lower than those observed by Mariner 6 and 7 ultraviolet spectrometers.

On Venus, the calculated brightness of CO Cameron band and CO_2^+ doublet emissions is compared with recent SPICAV observation. The calculated intensities of CO Cameron band and CO_2^+ doublet emissions at the peak altitude are about 50% and 30%, respectively, higher than the observation. The model calculated peak altitude of CO Cameron band and CO_2^+ UV doublet emission profiles is lower by ∼3 km than that observed by SPICAV: indicating lower neutral density in the VTS3 model atmosphere of Venus, which is used in the present calculations. The calculated overhead intensities of CO Cameron and CO_2^+ UV doublet band emissions are about a factor of 2 higher in the solar maximum condition than those during the solar minimum condition. This variation in intensity from low to high solar activity depends upon the solar EUV flux model used in the calculation, e.g., when the S2K model is used instead of EUVAC, the emission intensities of CO Cameron band and CO_2^+ UV doublet vary by less than a factor of 2. Overall, the effect of solar EUV flux models on the emission intensity is 30-40% in solar minimum condition and ∼2-10% in solar maximum condition.

Present study has clearly demonstrated that the cross section of a$^3\Pi$ state in e-CO process is important in modelling CO Cameron band emission on Mars and Venus. The contribution of e-CO process in CO Cameron band also depends on the density of CO in the atmosphere; hence, it is difficult to constrain the former without fixing the later.

For the first time, the SPICAM/MEx observed N_2 Vegard-Kaplan band emission on Mars. Since N_2 is the second most abundant gas on Venus, the N_2 triplet band features are expected on Venus also. In this context, the application of AYS to the calculation of N_2 triplet band dayglow emissions on Mars and Venus has been carried out in the present work. The impact of solar activity, solar EUV flux model, and N_2 triplet state cross sections on the N_2 triplet band emissions are studied. On Mars, the calculated brightness profile is about a factor of 3 smaller than the SPICAM observation. Constraining the N_2/CO_2 ratio on Mars by SPICAM observations, the present calculations suggest that the N_2/CO_2 ratio on Mars would be in the range of 1.1 to 1.4% at 120 km, 1.8 to 3.2% at 140 km, and 4 to 7% at 170 km. The present study also suggests that most of the atmospheric models of Mars have N_2 abundances that are larger than the model-derived values, based on the present calculation, by a factors of 2 to 4. Clearly, there is a need for improved understanding of the Martian atmosphere, and the SPICAM observations help to constrain the N_2 relative abundance.

On Venus, the calculated intensities of VK bands are an order of magnitude larger than those on Mars. Hence, the intensities are quite large and can be detected by the SPICAV experiment on board the Venus Express. The N_2 VK band intensities are also calculated on Titan to explain the recent observations by Cassini spacecraft and to validate the model calculations by applying it to a N_2-dominated atmosphere. A good agreement is found between observed and modelled intensity of N_2 VK band on Titan.

The effects of important model input parameters, viz., electron impact N_2 triplet state excitation cross sections, solar activity, and model atmosphere, on the N_2 triplet band emissions have been studied. Changes in the cross section of N_2 triplet states can alter the calculated intensity by a factor of $\sim$2. During high solar activity, the calculated intensities are about a factor of 2.5 larger than those calculated for the low solar activity conditions.

Recently, the OI 2972 Å emission has been observed on Mars by SPICAM. The presence of this emission on Mars indicates that the OI 5577 Å (green) must also be present on Mars. In view of this a model of atomic oxygen visible emissions on Mars has been developed in this thesis. Since similar atomic oxygen emissions are expected on Venus, this model is also applied to Venus.

The present calculation showed that photodissociation of CO_2 is the major source of O(^{1}S) production on Mars and Venus. Contrary to the recent suggestion of *Huestis et al.* [2010], the present calculation showed that dissociative recombination of O_2^+ is not the main mechanism of O(^{1}S) production in the 80–170 km region on Mars. Thus, the O(^{1}S) emission cannot be used as a monitor of Martian ionosphere, unlike that recommended by *Huestis et al.* [2010]. On Mars and Venus, the main production source of O(^{1}D) is photodissociation of CO_2, while at higher altitudes dissociative recombination of O_2^+, O(^{1}S) radiative decay, and photodissociation of CO_2 are the major sources. The calculated brightness profile of OI 2972 Å on Mars is in good agreement with the SPICAM observation. Calculations carried out in the present study would lead to a better understanding of the photochemical processes governing the O(^{1}S) and O(^{1}D) production in the atmospheres of Mars and Venus. Based on the model calculated limb intensity profiles of OI emissions and ratio of 6300 and 5577 Å, it is suggested that in future Mars mission the search for red doublet emissions should focus at altitudes above 160 km, whereas for observing of OI 2972 and 5577 Å emissions the altitude region below 150 km is more suitable.

The information derived from the present work is useful for dayglow observations on Mars and Venus currently being carried out by Mars Express and Venus Express, respectively, and will be helpful for future planetary missions e.g, MAVEN and Indian Mars orbiter mission.

Scope for future work

The work presented in this thesis demonstrated the importance of modelling studies on Mars and Venus. Some important results are brought out in this work, based on which more in depth studies would be carried out in near future.

The Monte Carlo model developed for electron degradation in a CO_2 atmosphere in this thesis, does not include spatial information of electron degradation. However, based on the present technique, a model for altitudinal degradation of electrons in CO_2 atmosphere can be developed, which would be useful in understanding the electron energy deposition over the magnetic anomalies on Mars, thus help in modelling the aurora processes on Mars.

One of the important results presented in this thesis showed the importance of e-CO process in Cameron band emissions in the atmospheres of Mars and Venus. On Venus, the present study showed that CO Cameron band intensity calculated by using VTS3 model is inadequate in explaining the very recent measurement by SPICAV. In this context, it becomes important to further study the production of CO Cameron band on Venus with different model atmosphere such as Venus Thermospheric General Circulation Model (VTGCM).

The model of N_2 triplet band emissions has been successfully applied to calculated these emissions on Titan. There is further scope for application of this model to calculate N_2 triplet band emissions on Triton, biggest moon of planet Neptune, and Pluto. This study would provide useful for future missions and on-route New Horizons mission.

In this thesis, CO Cameron band, $CO_2^+(B^2\Sigma_u^+)$ doublet, N_2 triplet band, and atomic oxygen visible (5577, 6300, and 6364 Å) and UV (2972 Å) emissions on Mars and Venus have been studied. There is scope for further studies of other emissions (e.g., CO Fourth Positive, atomic Carbon emission lines, OI 1356 Å etc.) emanating from sunlit atmospheres of Mars and Venus by modifying the existing dayglow model.

References

Ångström, J. A. (1869), Spectrum des Nordlichts, *Annalen der Physik*, *213*, 161 – 163, doi:10.1002/andp.18692130510.

Ajello, J. M. (1971a), Emission cross sections of CO_2 by electron impact in the interval 1260-4500 Å, *J. Chem. Phys.*, *55*, 3169 – 3177, doi:10.1063/1.1676564.

Ajello, J. M. (1971b), Emission cross section of CO by electron impact in the interval 1260-5000 Å, *J. Chem. Phys.*, *55*, 3158 – 3168, doi:10.1063/1.1676563.

Ajello, J. M., et al. (2007), Titan airglow spectra from Cassini Ultraviolet Imaging Spectrograph (UVIS): EUV analysis, *Geophys. Res. Lett.*, *34*, L24,204, doi:10.1029/2007GL031555.

Ajello, J. M., et al. (2008), Titan airglow spectra from the Cassini Ultraviolet Imaging Spectrograph: FUV disk analysis, *Geophys. Res. Lett.*, *35*, L06,102, doi:10.1029/2007GL032315.

Alge, E., N. G. Adams, and D. Smith (1983), Measurements of the dissociative recombination coefficients of O_2^+, NO_2^+ , and NH_4^+ in the temperature range 200–600 K, *J. Phys. B*, *16*, 1433 – 1444, doi:10.1088/0022-3700/16/8/017.

Anderson, D. E. (1974), Mariner 6, 7, and 9 ultraviolet spectrometer experiment: Analysis of hydrogen Lyman alpha data, *J. Geophys. Res.*, *79*, 1513 – 1518, doi:10.1029/JA079i010p01513.

Arridge, C. S., L. K. Gilbert, G. R. Lewis, E. C. Sittler, G. H. Jones, D. O. Kataria, A. J. Coates, and D. T. Young (2009), The effect of spacecraft radiation sources on the electron moments from the Cassini CAPS electron spectrometer, *Planet. Space Sci.*, *57*, 854 – 869, doi:10.1016/j.pss.2009.02.011.

Ashihara, O. (1978), Photoelectron fluxes in the cometary atmosphere,, *Icarus*, *35*, 369.

Atkinson, R., and K. H. Welge (1972), Temperature Dependence of O(^{1}S) Deactivation by CO_2, O_2, N_2, and Ar, *J. Chem. Phys.*, *57*, 3689–3693, doi:10.1063/1.1678829.

Atkinson, R., D. L. Baulch, R. A. Cox, R. F. Hampson, Jr., J. A. Kerr, M. J. Rossi, and J. Troe (1997), Evaluated Kinetic and Photochemical Data for Atmospheric Chemistry: Supplement VI. IUPAC Subcommittee on Gas Kinetic Data Evaluation for Atmospheric Chemistry, *J. Phys. Chem. Ref. Data*, *26*, 1329 – 1499, doi:10.1063/1.556010.

Avakyan, S. V., R. N. II'in, V. M. Lavrov, and G. N. Ogurtsov (1998), in *Collision Processes and Excitation of UV Emission from Planetary Atmospheric Gases: A*

Handbook of Cross Sections, edited by S. V. Avakyan, Gordon and Breach science publishers.

Baluja, K. L., and C. J. Zeippen (1988), The photoionisation of the O+(4S 0) ground state, *J. Phys. B: At. Mol. Opt. Phys.*, *21*, 2411 – 2454, doi:10.1088/0953-4075/21/13/011.

Banks, P. M., and A. F. Nagy (1970), Concerning the influence of elastic scattering upon photoelectron transport and escape, *J. Geophys. Res.*, *75*, 1902–1910, doi:10.1029/JA075i010p01902.

Barth, C. A., J. B. Pearce, K. K. Kelly, L. Wallace, and W. G. Fastie (1967), Ultraviolet Emissions Observed near Venus from Mariner V, *Science*, *158*, 1675 – 1678, doi:10.1126/science.158.3809.1675.

Barth, C. A., W. G. Fastie, C. W. Hord, J. B. Pearce, K. K. Kelly, A. I. Stewart, G. E. Thomas, G. P. Anderson, and O. F. Raper (1969), Mariner 6 and 7: Ultraviolet spectrum of Mars upper atmosphere, *Science*, *165*, 1004 – 1005.

Barth, C. A., C. W. Hord, J. B. Pearce, K. K. Kelly, G. P. Anderson, and A. I. Stewart (1971), Mariner 6 and 7 ultraviolet spectrometer experiment: Upper atmosphere data, *J. Geophys. Res.*, *76*, 2213 – 2227, doi:10.1029/JA076i010p02213.

Barth, C. A., A. I. Stewart, C. W. Hord, and A. L. Lane (1972), Mariner 9 Ultraviolet Spectrometer Experiment: Mars airglow spectroscopy and variations in Lyman Alpha, *Icarus*, *17*, 457 – 462, doi:10.1016/0019-1035(72)90011-5.

Berger, M. J., S. M. Seltzer, and K. Maeda (1970), Energy deposition by auroral electrons in the atmosphere., *J. Atmos. Terr. Phys.*, *32*, 1015–1045.

Berkowitz, J. (2002), *Atomic and molecule photoabsorption: Absolute total cross sections*, Academic Press, New York.

Berrington, K. A., and P. G. Burke (1981), Effective collision strengths for forbidden transitions in e-N and e-O scattering, *Planet. Spece. Sci.*, *29*(3), 377 – 381, doi:10.1016/0032-0633(81)90026-X.

Bertaux, J.-L., J. Blamont, S. I. Babichenko, N. N. Dement'eva, A. V. D'yachov, V. G. Kurt, V. A. Sklyankin, A. S. Smirnov, and S. D. Chuvakhin (1975), Measurement of the intensity and spectral characteristics of the radiation in the Lyman alpha line the upper atmosphere of Mars, *Cosm. Res.*, *13*, 35.

Bertaux, J. L., J. E. Blamont, V. M. Lepine, V. G. Kurt, N. N. Romanova, and A. S. Smirnov (1981), Venera 11 and Venera 12 observations of EUV Emissions from the upper atmosphere of Venus, *Planet. Space Sci.*, *29*(2), 149 – 166.

Bertaux, J.-L., et al. (2000), The study of the martian atmosphere from top to bottom with SPICAM light on Mars Express, *Planet. Space Sci.*, *48*, 1303 – 1320, doi:10.1016/S0032-0633(00)00111-2.

Bertaux, J.-L., et al. (2006), SPICAM on Mars Express: Observing modes and overview of UV spectrometer data and scientific results, *J. Geophys. Res.*, *111 - E10*, 10, doi:10.1029/2006JE002690.

Bertaux, J.-L., et al. (2007), SPICAV on Venus Express: Three spectrometers to study the global structure and composition of the Venus atmosphere, *Planet. Spece. Sci.*, *55*, 1673 – 1700, doi:10.1016/j.pss.2007.01.016.

Bhardwaj, A. (1997), Ring current H Atom Precipitation on the Outer Planets, *Adv. Space Res.*, *20*(2), 233 – 237.

Bhardwaj, A. (1999), On the role of solar EUV, photoelectrons, and auroral electrons in the chemistry of C(^{1}D) and the production of CI 1931 Å in the inner cometary coma: A case for comet P/Halley, *J. Geophys. Res.*, *104*, 1929 – 1942, doi:10.1029/1998JE900004.

Bhardwaj, A. (2003), On the solar EUV deposition in the inner comae of comets with large gas production rates, *Geophys. Res. Lett.*, *30*(24), 2244, doi:10.1029/2003GL018495.

Bhardwaj, A., and S. A. Haider (1999), Modeling of metastable carbon atoms in comets: implications for ROSETTA, *Adv. Space Res.*, *23*(7), 1325 – 1328.

Bhardwaj, A., and S. K. Jain (2009), Monte Carlo model of electron energy degradation in a CO_2 atmosphere, *J. Geophys. Res.*, *114*, A11309, doi:10.1029/2009JA014298.

Bhardwaj, A., and S. K. Jain (2012a), Calculations of N_2 triplet states vibrational populations and band emissions in venusian dayglow, *Icarus*, *217*, 752 – 758, doi: 10.1016/j.icarus.2011.05.026.

Bhardwaj, A., and S. K. Jain (2012b), Production of N_2 Vegard-Kaplan and other triplet band emissions in the dayglow of Titan, *Icarus*, *218*(2), 989 – 1005, doi:10.1016/j.icarus.2012.01.019.

Bhardwaj, A., and M. Michael (1999a), Monte Carlo model for electron degradation in SO_2 gas: cross sections, yield spectra and efficiencies, *J. Geophys. Res.*, *104*(10), 24,713 – 24,728, doi:10.1029/1999JA900283.

Bhardwaj, A., and M. Michael (1999b), On the excitation of Io's atmosphere by the photoelectrons: Application of the analytical yield spectrum of SO_2, *Geophys. Res. Lett.*, *26*, 393 – 396, doi:10.1029/1998GL900320.

Bhardwaj, A., and S. Raghuram (2011), Model for Cameron-band emission in comets: A case for the EPOXI mission target comet 103P/Hartley 2, *Mon. Not. R. Astron. Soc. Lett.*, *412*, L25 – L29, doi:10.1111/j.1745-3933.2010.00998.x.

Bhardwaj, A., and S. Raghuram (2012), Coupled Chemistry-Emission Model for Atomic Oxygen Green and Red-doublet Emissions in Comet C/1996 B2 Hyakutake, *Astrophys. J.*, *748*(1), 13, doi:10.1088/0004-637X/748/1/13.

Bhardwaj, A., and R. P. Singhal (1990), Auroral and dayglow processes on Neptune, *Indian Journal of Radio and Space Physics*, *19*, 171 – 176.

Bhardwaj, A., and R. P. Singhal (1993), Optically thin H Lyman alpha production on outer planets: Low-energy proton acceleration in parallel electric fields and neutral H atom precipitation from ring current, *J. Geophys. Res.*, *98*(A6), 9473 – 9481, doi: 10.1029/92JA02400.

Bhardwaj, A., S. A. Haider, and R. P. Singhal (1990), Auroral and photoelectron fluxes in cometary ionospheres, *Icarus*, *85*, 216 – 228, doi:10.1016/0019-1035(90)90112-M.

Bhardwaj, A., S. A. Haider, and R. P. Singhal (1995), Consequences of cometary aurora on the carbon chemistry at comet P/Halley., *Adv. Space Res.*, *16 (2)*, 31 – 36.

Bhardwaj, A., S. A. Haider, and R. P. Singhal (1996), Production and emissions of atomic carbon and oxygen in the inner coma of comet 1P/Halley: Role of electron impact, *Icarus*, *120*, 412 – 430, doi:10.1006/icar.1996.0061.

Bibinov, N. K., F. I. Vilesov, I. P. Vinogradov, L. D. Mikheev, and A. M. Pravilov (1979), Determination of the spectral dependences of the absolute quantum yields of O(^{1}S) by the XeO* luminescence method. I. Photolysis of CO_2 and N_2O, *Sov. J. Quant. Electron.*, *9*(7), 838 – 844, doi:10.1070/QE1979v009n07ABEH009192.

Bougher, S. W. (1995), Comparative thermosphere: Venus and Mars, *Adv. Space Res.*, *15*, 21 – 45.

Bougher, S. W., R. G. Roble, E. C. Ridley, and R. E. Dickinson (1990), The Mars thermosphere: 2. General circulation with coupled dynamics and composition, *J. Geophys. Res.*, *95*, 14,811 – 14,827, doi:10.1029/JB095iB09p14811.

Bougher, S. W., S. Engel, R. G. Roble, and B. Foster (1999), Comparative terrestrial planet thermospheres: 2. Solar cycle variation of global structure and winds at equinox, *J. Geophys. Res.*, *104*, 16,591 – 16,611, doi:10.1029/1998JE001019.

Bougher, S. W., S. Engel, R. G. Roble, and B. Foster (2000), Comparative terrestrial planet thermospheres: 3. Solar cycle variation of global structure and winds at solstices, *J. Geophys. Res.*, *105*, 17,669 – 17,692, doi:10.1029/1999JE001232.

Bougher, S. W., S. Engel, D. P. Hinson, and J. R. Murphy (2004), MGS Radio Science electron density profiles: Interannual variability and implications for the Martian neutral atmosphere, *J. Geophys. Res.*, *109*, E03,010, doi:10.1029/2003JE002154.

Brecht, A. S., and S. W. Bougher (2012), Dayside thermal structure of Venus' upper atmosphere characterized by a global model, *J. Geophys. Res.*, *117*, E08002, doi: 10.1029/2012JE004079.

Broadfoot, A., et al. (1997), N_2 triplet band systems and atomic oxygen in the dayglow, *J. Geophys. Res.*, *102*(A6), 11,567 – 11,584, doi:10.1029/97JA00771.

Broadfoot, A. L., S. Kumar, M. J. S. Belton, and M. B. McElroy (1974), Ultraviolet observations of Venus from Mariner 10: Perliminary results, *Science*, *183*, 1315 – 1318.

Broadfoot, A. L., S. S. Clapp, and F. E. Stuart (1977), Mariner 10 ultraviolet spectrometer: airglow experiment, *Space Sci. Instrum.*, *3*, 199.

Broadfoot, A. L., et al. (1981), Extreme ultraviolet observations from Voyager 1 encounter with Saturn, *Science*, *212*, 206 – 211, doi:10.1126/science.212.4491.206.

Brown, R. H., et al. (2004), The Cassini Visual and Infrared Mapping Spectrometer (VIMS) Investigation, *Space Sci. Rev.*, *115*, 111–168, doi:10.1007/s11214-004-1453-x.

Brunger, M. J., S. J. Buckman, and M. T. Elford (2003), Photon and Electron Interaction with Atoms, Molecules and Ions, in *Landolt-Bornstein Group 1: Elementary Particles, Nuclei, and Atoms, Molecules and Ions*, vol. I/17, edited by Y. Itikawa, chap. Integral elastic cross sections, pp. 6052 – 6084, Springer, New York.

Buckman, S. J., M. T. Elford, and D. S. Newman (1987), Electron scattering from vibrationally excited CO_2, *J. Phys. B*, *20*, 5175.

Buckman, S. J., M. J. Brunger, and M. T. Elford (2002), Photon and Electron Interaction with Atoms, Molecules and Ions, in *Landolt-Bornstein Group 1: Elementary Particles, Nuclei, and Atoms, Molecules and Ions*, vol. I - 17, edited by Y. Itikawa, landolt-börnstein ed., Springer, Berlin.

Buenker, R. J., M. Honigmann, H.-P. Liebermann, and M. Kimura (2000), Theoretical study of the electronic structure of carbon dioxide: Bending potential curves and generalized oscillator strengths, *J. Chem. Phys.*, *113*, 1046.

Buonsanto, M. J., P. G. Richards, W. K. Tobiska, S. C. Solomon, Y. .-K. Tung, and J. A. Fennelly (1995), Ionospheric Electron Densities Calculated Using Different EUV Flux Models and Cross Sections: Comparison with Radar Data, *J. Geophys. Res.*, *100*(A8), 14,569 – 14,580, doi:10.1029/95JA00680.

Campbell, L., M. J. Brunger, A. M. Nolan, L. J. Kelly, A. B. Wedding, J. Harrison, P. J. O. Teubner, D. C. Cartwright, and B. McLaughlin (2001), Integral cross sections for electron impact excitation of electronic states of N_2, *J. Phys. B: At. Mol. Opt. Phys.*, *34*(7), 1185 – 1199, doi:10.1088/0953-4075/34/7/303.

Campbell, L., D. C. Cartwright, M. J. Brunger, and P. J. O. Teubner (2006), Role of electronic excited N_2 in vibrational excitation of the N_2 ground state at high latitudes, *J. Geophys. Res.*, *111*, A09317, doi:10.1029/2005JA011292.

Capetanakis, F. P., F. Sondermann, S. Höser, and F. Stuhl (1993), Temperature dependence of the quenching of $O(^1S)$ by simple inorganic molecules, *J. Chem. Phys.*, *98*, 7883, doi:10.1063/1.464596.

Capria, M. T., G. Cremonese, A. Bhardwaj, M. C. D. Sanctis, and E. M. Epifani (2008), Oxygen emission lines in the high resolution spectra of 9P/Tempel 1 following the Deep Impact event, *Astron. Astrophys.*, *479*(1), 257–263.

Carbary, J. F., S. M. Krimigis, D. G. Mitchell, C. Paranicas, and P. Brandt (2009), Energetic neutral atom (ENA) and charged particle periodicities in Saturns magnetosphere, *Adv. Space Res.*, *44*, 483 – 493, doi:10.1016/j.asr.2009.04.019.

Cartwright, D., S. Trajmar, and W. Williams (1971), Vibrational population of the $A^3\Sigma_u^+$ and $B^3\Pi_g$ states of N_2 in normal auroras, *J. Geophys. Res.*, *76*(34), 8368 – 8377, doi:10.1029/JA076i034p08368.

Cartwright, D. C. (1978), Vibrational populations of the excited state of N_2 under auroral condition, *J. Geophys. Res.*, *83*(A2), 517 – 321, doi:10.1029/JA083iA02p00517.

Cartwright, D. C., S. Trajmar, A. Chutjian, and W. Williams (1977), Electron-impact excitation of electronic states of N_2: 2. Integral cross-sections at incident energies from 10 to 50 eV, *Phys. Rev. A*, *16*(3), 1041 – 1051, doi:10.1103/PhysRevA.16.1041.

Chamberlin, P. C., T. N. Woods, D. A. Crotser, F. G. Eparvier, R. A. Hock, and D. L. Woodraska (2009), Solar cycle minimum measurements of the solar extreme ultraviolet spectral irradiance on 14 April 2008, *Geophys. Res. Lett.*, *36*, L05102, doi:10.1029/2008GL037145.

Chan, W., G. Cooper, and C. Brion (1993), The electronic spectrum of carbon dioxide. discrete and continuum photoabsorption oscillator strengths (6-203 ev), *Chemical Physics*, *178*(13), 401 – 413, doi:10.1016/0301-0104(93)85079-N.

Chaufray, J., J. Bertaux, F. Leblanc, E. Quemerais, and E. Villard (2008a), Study of the Venusian hydrogen corona with SPICAV on Venus Express, *AGU Spring Meeting Abstracts*, p. A2.

Chaufray, J. Y., J. L. Bertaux, F. Leblanc, and E. Quémerais (2008b), Observation of the hydrogen corona with SPICAM on Mars Express, *Icarus*, *195*(2), 598 – 613, doi:10.1016/j.icarus.2008.01.009.

Chaufray, J.-Y., J.-L. Bertaux, and F. Leblanc (2012), First observation of the Venus UV dayglow at limb from SPICAV/VEX, *Geophys. Res. Lett.*, *39*, L20201, doi:10.1029/2012GL053626.

Cheng, A. F. (1986), Energetic neutral particles from Jupiter and Saturn, *J. Geophys. Res.*, *91*, 4524 – 4530, doi:10.1029/JA091iA04p04524.

Cicerone, R., and S. A. Bowhill (1970), Photoelectron escape fluxes obtained by a Monte Carlo technique, *Radio Science*, *5*, 49, doi:10.1029/RS005i001p00049.

Cicerone, R., and S. A. Bowhill (1971), Photoelectron fluxes in the ionosphere computed by a Monte Carlo method, *J. Geophys. Res.*, *76*(34), 8299 – 8317.

Cicerone, R. J., W. E. Swartz, R. S. Stolarski, A. F. Nagy, and J. S. Nisbet (1973), Thermalization and transport of photoelectrons: A comparison of theoretical approaches, *J. Geophys. Res.*, *78*, 6709–6728, doi:10.1029/JA078i028p06709.

Coates, A. J., S. M. E. Tsang, A. Wellbrock, R. A. Frahm, J. D. Winningham, S. Barabash, R. Lundin, D. T. Young, and F. J. Crary (2010), Ionospheric photoelectrons: Comparing Venus, Earth, Mars and Titan, *Planet. Spece. Sci.*, doi:10.1016/j.pss.2010.07.016.

Conway, R., and A. Christensen (1985), The Ultraviolet dayglow at solar maximum, 2. Photometer observations of N_2 Second Positive (0, 0) band emission, *J. Geophys. Res.*, *90*(A7), 6601 – 6607, doi:10.1029/JA090iA07p06601.

Conway, R. R. (1981), Spectroscopy of the Cameron bands in the Mars airglow, *J. Geophys. Res.*, *86*, 4767 – 4775, doi:10.1029/JA086iA06p04767.

Cook, G. R., P. H. Metzger, and M. Ogawa (1966), Absorption, Photoionization, and Fluorescence of CO_2, *J. Chem. Phys.*, *44*, 2935–2942, doi:10.1063/1.1727158.

Cox, C., J. C. Gérard, B. Hubert, J. L. Bertaux, and S. W. Bougher (2010), Mars ultraviolet dayglow variability: SPICAM observations and comparison with airglow model, *J. Geophys. Res.*, *115*, E04,010, doi:10.1029/2009JE003504.

Cravens, T. E., A. F. Nagy, R. H. Chen, and A. I. Stewart (1978), The ionosphere and airglow of Venus: Prospects for Pioneer Venus, *Geophys. Res. Lett.*, *5*(7), 613–616, doi:10.1029/GL005i007p00613.

Dalgarno, A., and T. C. Degges (1971), CO_2^+ Dayglow on Mars and Venus, in *Planetary Atmospheres*, *IAU Symposium*, vol. 40, edited by C. Sagan, T. C. Owen, and H. J. Smith, p. 337.

Dalgarno, A., and M. B. McElroy (1970), Mars: Is Nitrogen present?, *Science*, *170*, 167 – 168, doi:10.1126/science.170.3954.167.

Daniell, R., and D. Strickland (1986), Dependence of auroral middle UV emissions on the incident electron spectrum and neutral atmosphere, *J. Geophys. Res.*, *91*(A1), 321 – 327, doi:10.1029/JA091iA01p00321.

De La Haye, V., et al. (2007), Cassini Ion and Neutral Mass Spectrometer data in Titan's upper atmosphere and exosphere: Observation of a suprathermal corona, *J. Geophys. Res.*, *112*, A07,309, doi:10.1029/2006JA012222.

Dement'eva, N. N., V. G. Kurt, A. S. Smirnov, L. G. Titarchuk, and S. D. Chuvahin (1972), *Icarus*, *17*, 475.

Douthat, D. A. (1975), Electron degradation spectra in helium, *Radiat. Res.*, *61*, 1.

Dreyer, J. W., D. Perner, and C. R. Roy (1974), Rate constants for the quenching of N_2 ($A^3\Sigma_u^+, \nu_A = 0 - 8$) by CO, CO_2, NH_3, NO, and O_2, *J. Chem. Phys.*, *61*(8), 3164 – 3169, doi:10.1063/1.1682472.

Dudok de Wit, T., M. Kretzschmar, J. Aboudarham, O. P. Amblard, F. Auchere, and J. Lilensten (2007), Which solar EUV indices are best for reconstructing the solar EUV irradiance?, *Adv. Space Res.*, in press.

Durrance, S. (1981), The Carbon Monoxide Fourth Positive Bands in the Venus Dayglow, 1. Synthetic Spectra, *J. Geophys. Res.*, *86*(A11), 9115 – 9124.

Erdman, P. W., and E. C. Zipf (1983), Electron-impact excitation of the Cameron system ($a^3\Pi \rightarrow X^1\Sigma$) of CO, *Planet. Spece. Sci.*, *31*, 317 – 321, doi:10.1016/0032-0633(83) 90082-X.

Fano, U., and L. Spencer (1975), Quasi-scaling of electron degradation spectra, *International Journal for Radiation Physics and Chemistry*, *7*, 63–76, doi:10.1016/0020-7055(75)90050-9.

Fedorova, A., O. Korablev, S. Perrier, J.-L. Bertaux, F. Lefevre, and A. Rodin (2006), Observation of O_2 1.27 μm dayglow by SPICAM IR: Seasonal distribution for the first Martian year of Mars Express, *111*, E09S07, doi:10.1029/2006JE002694.

Feldman, P. D., E. B. Burgh, S. T. Durrance, and A. F. Davidsen (2000), Far-ultraviolet spectroscopy of Venus and Mars at 4Å resolution with the Hopkins Ultraviolet Telescope on Astro-2, *Astrophys J.*, *538*, 395 – 400, doi:10.1086/309125.

Ferch, J., C. Masche, and W. Raith (1981), Total cross section measurement for e-CO_2 scattering down to 0.07, *J. Phys. B*, *14*, L97.

Forget, F., F. Montmessin, J. L. Bertaux, F. G. Galindo, S. Lebonnois, E. Quémerais, A. Reberac, E. Dimarellis, and M. A. L. Valverde (2009), Density and temperatures of the upper Martian atmosphere measured by stellar occultations with Mars Express SPICAM, *J. Geophys. Res.*, *114*, E01004, doi:10.1029/2008JE003086.

Fox, J. L. (1982), The Chemistry of Metastable Species in the Venusian Ionosphere, *Icarus*, *51*, 248 – 260.

Fox, J. L. (1985), The O_2^+ vibrational distribution in the venusian ionosphere, *Adv. Space Res.*, *5*, 165 – 169.

Fox, J. L. (1992), Airglow and Aurora in the atmospheres of Venus and Mars, in *Venus and Mars: Atmospheres, Ionospheres, and Solar Wind Interactions*, *Geophys. Monogr. Ser.*, vol. 66, edited by J. G. Luhmann, M. Tatrallyay, and R. O. Pepin, pp. 191 – 222, AGU, Washington, D. C.

Fox, J. L. (2004), Response of the Martian thermosphere/ionosphere to enhanced fluxes of solar soft X rays, *J. Geophys. Res.*, *109*, A11310, doi:10.1029/2004JA010380.

Fox, J. L. (2009), Morphology of the dayside ionosphere of Mars: Implications for ion outflows, *J. Geophys. Res.*, *114*, E12005, doi:10.1029/2009JE003432.

Fox, J. L., and S. W. Bougher (1991), Structure, luminosity, and dynamics of the Venus thermosphere, *Space Sci. Rev.*, *55*, 357 – 489, doi:10.1007/BF00177141.

Fox, J. L., and A. Dalgarno (1979a), Ionization, luminosity, and heating of the upper atmosphere of Mars, *J. Geophys. Res.*, *84*, 7315 – 7333, doi:10.1029/JA084iA12p07315.

Fox, J. L., and A. Dalgarno (1979b), Electron energy deposition in carbon dioxide, *Planet. Space Sci.*, *27*, 491 – 502.

Fox, J. L., and A. Dalgarno (1981), Ionization, luminosity and heating of upper atmosphere of Venus, *J. Geophys. Res.*, *86*, 629 – 639, doi:10.1029/JA086iA02p00629.

Fox, J. L., and A. B. Hac (2009), Photochemical escape of oxygen from Mars: A comparison of the exobase approximation to a Monte Carlo method, *Icarus*, *204*, 527 – 544, doi:10.1016/j.icarus.2009.07.005.

Fox, J. L., and K. Sung (2001), Solar activity variations of the Venus thermosphere/ionosphere, *J. Geophys. Res.*, *106*(A10), 21,305 – 21,335, doi:10.1029/2001JA000069.

Fox, J. L., A. Dalgarno, E. R. Constantinides, and G. A. Victor (1977), The nitrogen dayglow on Mars, *J. Geophys. Res.*, *82*, 1615 – 1616, doi:10.1029/JA082i010p01615.

Fox, J. L., P. Zhou, and S. W. Bougher (1996), The Martian thermosphere/ionosphere at high and low solar activities, *Adv. Space Res.*, *17*(11), 203 – 218, doi:10.1016/0273-1177(95)00751-Y.

Freund, R. S. (1971), Dissociation of CO_2 by electron impact with the formation of metastable $CO(a^3\Pi)$ and $O(^5S)$, *J. Chem. Phys.*, *55*, 3569 – 3577, doi:10.1063/1.1676615.

Froese-Fischer, C., and G. Tachiev (2004), Breit-Pauli energy levels, lifetimes, and transition probabilities for beryllium-like and neon-like sequences, *At. Data Nucl. Data Tables*, *87*, 1 – 184.

Furlong, J. M., and W. R. Newell (1996), Total cross section measurement for the metastable $a^3\Pi$ state in CO, *J. Phys. B*, *29*, 331 – 338, doi:10.1088/0953-4075/29/2/020.

Futaana, Y., J.-Y. Chaufray, H. T. Smith, P. Garnier, H. Lichtenegger, M. Delva, H. Gröller, and A. Mura (2012), Exospheres and Energetic Neutral Atoms of Mars, Venus and Titan, in *The Plasma Environment of Venus, Mars, and Titan*, *Space Sciences Series of ISSI*, vol. 37, edited by K. Szego, pp. 213 – 266, Springer US, doi:10.1007/978-1-4614-3290-6_7.

Garcia, G., and F. Manero (1996), Total cross sections for electron scattering by CO_2 molecules in the energy range 400-5000 eV, *Phys. Rev. A*, *53*, 250.

Gattinger, R. L., N. D. Lloyd, A. E. Bourassa, D. A. Degenstein, I. C. McDade, and E. J. Llewellyn (2009), Observation of the 557.7 nm to 297.2 nm brightness ratio in the auroral spectrum with OSIRIS on Odin, *Can. J. Phys.*, *87*(10), 1133 – 1137, doi:10.1139/P09-102.

Gérard, J. C., B. Hubert, V. I. Shematovich, D. V. Bisikalo, and G. R. Gladstone (2008a), The Venus ultraviolet oxygen dayglow and aurora: Model comparison with observations, *Planet. Space Sci.*, *56*, 542 – 552, doi:10.1016/j.pss.2007.11.008.

Gérard, J.-C., C. Cox, A. Saglam, J.-L. Bertaux, E. Villard, and C. Nehmé (2008b), Limb observations of the ultraviolet nitric oxide nightglow with SPICAV on board Venus Express, *J. Geophys. Res.*, *113*, E00B03, doi:10.1029/2008JE003078.

Gérard, J.-C., B. Hubert, J. Gustin, V. I. Shematovich, D. Bisikalo, G. R. Gladstone, and L. W. Esposito (2011a), EUV spectroscopy of the Venus dayglow with UVIS on Cassini, *Icarus*, *211*(1), 70 – 80, doi:10.1016/j.icarus.2010.09.020.

Gérard, J.-C., J. Gustin, B. Hubert, G. R. Gladstone, and L. W. Esposito (2011b), Measurements of the helium 584 Å airglow during the Cassini flyby of Venus, *Planet. Space Sci.*, *59*, 1524 – 1528, doi:10.1016/j.pss.2011.06.018.

Gibson, J. C., M. A. Green, K. W. Trantham, S. J. Buckman, P. J. O. Teubner, and M. J. Brunger (1999), Elastic electron scattering from CO_2, *J. Phys. B*, *32*, 213.

Gilijamse, J. J., S. Hoekstra, S. A. Meek, M. Metsälä, S. Y. T. van de Meerakker, S. Y. T, G. Meijer, G. C. Groenenboom, and G. C. (2007), The radiative lifetime of metastable CO ($a^3\Pi, \nu{=}0$), *J. Chem. Phys.*, *127*, 221,102–4, doi:10.1063/1.2813888.

Gilmore, F. R., R. R. Laher, and P. J. Espy (1992), Franck-Condon factors, r-centroids, electronic transition moments, and Einstein coefficients for many nitrogen and oxygen band systems, *J. Phys. Chem. Ref. Data*, *21*, 1005 – 1107, doi:10.1063/1.555910.

Green, A. E. S., and C. A. Barth (1965), Calculations of Ultraviolet molecular nitrogen emissions from the Aurora, *J. Geophys. Res.*, *70*(5), 1083 – 1092, doi:10.1029/JZ070i005p01083.

Green, A. E. S., and C. A. Barth (1967), Calculations of the photoelectron excitation of the dayglow, *J. Geophys. Res.*, *72*(15), 3975 – 3986, doi:10.1029/JZ072i015p03975.

Green, A. E. S., and R. P. Sighal (1979), Microplume model of spatialyield spectra, *Geophys. Res. Lett.*, *6*(7), 625 – 628.

Green, A. E. S., C. Jackman, and R. Garvey (1977), Electron impact on atmospheric gases, 2. Yield spectra, *J. Geophys. Res.*, *82*(32), 5104 – 5111.

Green, A. E. S., Dayashankar, and P. F. Schippnick (1985), Yield and concentration microplumes for electron impact on water, *Radiat. Res.*, *104*, 1 – 14.

Green, M. A., et al. (2002), Absolute differential cross sections for electron impact excitation of the 10.8-11.5 EV energy-loss states of CO_2, *J. Phys. B*, *35*, 567.

Gronoff, G., J. Lilensten, C. Simon, M. Barthélemy, F. Leblanc, and O. Dutuit (2008), Modelling the Venusian airglow, *Astron. Astrophys.*, *482*(3), 1015 – 1029, doi:10.1051/0004-6361:20077503.

Gronoff, G., C. S. Wedlund, C. J. Mertens, M. Barthélemy, R. J. Lillis, and O. Witasse (2012a), Computing uncertainties in ionosphere-airglow models. II - The Martian airglow, *J. Geophys. Res.*, *117*, A05309, doi:10.1029/2011JA017308.

Gronoff, G., C. S. Wedlund, C. J. Mertens, and R. J. Lillis (2012b), Computing uncertainties in ionosphere-airglow models: I. Electron flux and species production uncertainties for Mars, *J. Geophys. Res.*, *117*, A04306, doi:10.1029/2011JA016930.

Guberman, S. L. (1987), Production of O(^{1}S) from dissociative recombination of O_2^+, *Nature*, *327*, 408 – 409.

Gutchek, R. A., and E. C. Zipf (1973), Excitation of the CO fourth positive system by the dissociative recombination of CO_2^+ ions, *J. Geophys. Res.*, *78*, 5429 – 5436.

Haider, S. A., and A. Bhardwaj (1997), Chemistry of the ions 40 amu in the inner coma of comet Halley, *Adv. Space Res.*, *20*(2), 291 – 294.

Haider, S. A., and A. Bhardwaj (2005), Radial distribution of production rates, loss rates and densities corresponding to ion masses $\leq$40 amu in the inner coma of Comet Halley: Composition and chemistry, *Icarus*, *177*, 196 – 216, doi:10.1016/j.icarus.2005.02.019.

Haider, S. A., and R. P. Singhal (1983), Analytical yield spectrum approach to electron energy degradation in earth's atmosphere, *J. Geophys. Res.*, *88*, 7185–7189, doi:10.1029/JA088iA09p07185.

Haider, S. A., J. Kim, A. F. Nagy, C. N. Keller, M. I. Verigin, K. I. Gringauz, N. M. Shutte, K. Szego, and P. Kiraly (1992), Calculated ionization rates, ion densities, and airglow emission rates due to precipitating electron in the nightside of Mars, *J. Geophys. Res.*, *97*(A7), 10,639–10,641.

Hall, R. I., A. Chutjian, and S. Trajmar (1973), Electron impact excitation and assignment of the low-lying electronic states of CO_2, *J. Phys. B*, *6*, L264.

Heaps, M. G., and A. E. S. Green (1974), Monte Carlo approach to the spatial deposition of energy by electrons in molecular hydrogen, *J. Appl. Phys.*, *45*, 3183–3188, doi:10.1063/1.1663745.

Hedelt, P., Y. Ito, H. U. Keller, R. Reulke, P. Wurz, H. Lammer, H. Rauer, and L. Esposito (2010), Titan's atomic hydrogen corona, *Icarus*, *210*, 424 – 435, doi:10.1016/j.icarus.2010.06.012.

Hedin, A. E., H. B. Niemann, W. T. Kasprzak, and A. Seiff (1983), Global empirical model of the Venus thermosphere, *J. Geophys. Res.*, *88*(A1), 73 – 83, doi:10.1029/JA088iA01p00073.

Henderson, M. G. (1997), First energetic neutral atom images from Polar, *Geophys. Res. Lett.*, *24*, 1167.

Heroux, L., and H. E. Hinteregger (1978), Aeronomical reference spectrum for solar UV below 2000 Å, *J. Geophys. Res.*, *83*(A11), 5305–5308, doi:10.1029/JA083iA11p05305.

Herzberg, G. (1966), *Molecular Spectra and Molecular Structure, vol. III, Electronic Spectra and Electronic Structure of Polyatomic Molecules*, Van Nostrand Reinhold, New York.

Hill, S. M., S. C. Solomon, D. D. Cleary, and A. L. Broadfoot (2000), Temperature dependence of the reaction $N_2(A^3\Sigma_u^+) + O$ in the terrestrial thermosphere, *J. Geophys. Res.*, *105*, 10,615 – 10,630.

Hinteregger, E. (1976), EUV fluxes in the solar spectrum below 2000 Å, *J. Atmos. Terr. Phys.*, *38*, 791 – 806, doi:10.1016/0021-9169(76)90020-9.

Hinteregger, H. E., K. Fukui, and B. R. Gilson (1981), Observational, reference and model data on solar EUV, from measurements on AE-E, *Geophys. Res. Lett.*, *8*(11), 1147 – 1150, doi:10.1029/GL008i011p01147.

Holmström, M., and E. Kallio (2004), The solar wind interaction with Venus and Mars: energetic neutral atom and X-ray imaging, *Adv. Space Res.*, *33*, 187 – 193, doi:10.1016/j.asr.2003.05.008.

Hord, C. W., C. A. Barth, and J. B. Pearce (1970), Ultraviolet spectroscopy experiment for Mariner Mars, *Icarus*, *12*, 63.

Hubert, B., J. C. Gérard, J. Gustin, V. I. Shematovich, D. V. Bisikalo, A. I. Stewart, and G. R. Gladstone (2010), UVIS observations of the FUV OI and CO 4P Venus dayglow during the Cassini flyby, *Icarus*, *207*(2), 549 – 557, doi:10.1016/j.icarus.2009.12.029.

Hubert, B., J.-C. Gérard, J. Gustin, D. V. Bisikalo, V. I. Shematovich, and G. R.

Gladstone (2012), Cassini-UVIS observation of dayglow FUV emissions of carbon in the thermosphere of Venus, *Icarus*, *220*, 635 – 646, doi:10.1016/j.icarus.2012.06.002.

Huebner, W. F., J. J. Keady, and S. P. Lyon (1992), Solar photorates for planetary atmospheres and atmospheric pollutants, *Astrophys. Space Sci.*, *195*(1), 1 – 289, doi:10.1007/BF00644558.

Huestis, D. L., T. G. Slanger, B. D. Sharpee, and J. L. Fox (2010), Chemical origins of the Mars ultraviolet dayglow, *Faraday Discussions*, *147*, 307 – 322, doi:10.1039/c003456h.

Iga, I., J. C. Nogueira, and M.-T. Lee (1984), Elastic scattering of electrons from CO_2 in the intermediate energy range, *J. Phys. B*, *17*, L185.

Iga, I., M. G. P. Homem, K. T. Mazon, and M.-T. Lee (1999), Elastic and total cross sections for electron-carbon dioxide collisions in the intermediate energy range, *J. Phys. B*, *32*, 4373.

Itikawa, Y. (2002), Cross sections for electron collisions with carbon dioxide, *J. Phys. Chem. Ref. Data*, *31*(3), 749 – 767, doi:10.1063/1.1481879.

Itikawa, Y. (2006), Cross sections for electron collisions with nitrogen molecules, *J. Phys. Chem. Ref. Data*, *35*(1), 31 – 53, doi:10.1063/1.1937426.

Itikawa, Y., and A. Ichimura (1990), Cross sections for collisions of electrons and photons with atomic oxygen, *J. Phys. Chem. Ref. Data*, *19*(3), 637–651.

Itikawa, Y., K. Ichimura, K. Onda, K. Sakimoto, K. Takayanagi, Y. Hatano, M. Hayashi, H. Nishimura, and S. Tsurubuchi (1989), Cross sections for collisions of electrons and photons with oxygen molecules, *J. Phys. Chem. Ref. Data*, *18*(1), 23 – 42.

Jackman, C., R. Garvey, and A. Green (1977), Electron impact on atmospheric gases, I. Updated cross sections, *J. Geophys. Res.*, *82*(32), 5081 – 5090, doi:10.1029/JA082i032p05081.

Jackman, C. H., and A. E. S. Green (1979), Electron impact on atmospheric gases. III - Spatial yield spectra for N_2, *J. Geophys. Res.*, *84*, 2715–2724, doi:10.1029/JA084iA06p02715.

Jain, S. K., and A. Bhardwaj (2011), Model calculation of N_2 Vegard-Kaplan band emissions in Martian dayglow, *J. Geophys. Res.*, *116*, E07005, doi:10.1029/2010JE003778.

Jain, S. K., and A. Bhardwaj (2012), Impact of solar EUV flux on CO Cameron band and CO_2^+ UV doublet emissions in the dayglow of Mars, *Planet. Space Sci.*, *63-64*, 110 – 122, doi:10.1016/j.pss.2011.08.010.

Jamieson, M. J., J. M. Finch, R. S. Friedman, and A. Dalgarno (1992), Collisonal excitation of metastable oxygen $O(^1D)$ atoms through the $^3\Sigma_u^+$ channel of O_2, *Planet. Space Sci.*, *40*, 1719 – 1721.

Johnson, C. E. (1972), Lifetime of $CO(a^3\Pi)$ following electron impact dissociation of CO_2, *J. Chem. Phys.*, *57*(1), 576 – 577, doi:10.1063/1.1678007.

Johnson, P. V., C. P. Malone, I. Kanik, K. Tran, and M. A. Khakoo (2005), Integral cross sections for the direct excitation of the $A^3\Sigma_u^+$, $B^3\Pi_g$, $W^3\Delta_u$, $B'^3\Sigma_u^-$, $a'^1\Sigma_u^-$, $a^1\Pi_g$, $w^1\Delta_u$, and $C^3\Pi_u$ electronic states in N_2 by electron impact, *J. Geophys. Res.*, *110*, A11311, doi:10.1029/2005JA011295.

Johnson, R. E., D. Schnellenberger, and M. C. Wong (2000), The sputtering of an oxygen thermosphere by energetic O^+, *J. Geophys. Res.*, *105*, 1659–1670, doi: 10.1029/1999JE001058.

Johnstone, W. M., P. Akther, and W. R. Newell (1995), Resonant vibrational excitation of carbon dioxide, *J. Phys. B*, *28*, 743.

Kalogerakis, K. S., C. Romanescu, M. Ahmed, K. R. Wilson, and T. G. Slanger (2012), CO prompt emission as a CO_2 marker in comets and planetary atmospheres, *Icarus*, *220*, 205 – 210, doi:10.1016/j.icarus.2012.04.028.

Kanik, I., D. C. McCollum, and J. C. Nickel (1989), Absolute differential elastic scattering cross sections for electron impact on carbon dioxide in the intermediate energy region, *J. Phys. B*, *22*, 1225.

Kanik, I., J. M. Ajello, and G. K. James (1993), Extreme ultraviolet emission spectrum of CO_2 induced by electron impact at 200 eV, *Chem. Phys. Lett.*, *211*, 523.

Karwasz, G. P., S. Brusa, and A. Zecca (2001), One century of experiments on electron-atom and molecule scattering: A critical review of integral cross-sections. II. Polyatomic molecules, *Rivista del Nuovo Cimento*, *24*, 1.

Kawahara, H., H. Kato, M. Hoshino, H. Tanaka, L. Campbell, and M. J. Brunger (2008), Integral cross sections for electron impact excitation of Σ_u^+ and Π_u electronics states in CO_2, *J. Phys. B*, *41*, 85,203.

Kella, D., P. J. Johnson, H. B. Pedersen, L. Vejby-Christenson, and L. H. Andersen (1997), The source of green light emission determined from a heavy-ion storage ring experiment, *Science*, *276*, 1530 – 1533, doi:10.1126/science.276.5318.1530.

Khakoo, M. A., P. V. Johnson, I. Ozkay, P. Yan, S. Trajmar, and I. Kanik (2005), Differential cross sections for the electron impact excitation of the $A^3\Sigma_u^+$, $B^3\Pi_g$, $W^3\Delta_u$, $B'^3\Sigma_u^-$, $a'^1\Sigma_u^-$, $a^1\Pi_g$, $w^1\Delta_u$ and $C^3\Pi_u$ states of N_2, *Phys. Rev. A*, *71*, doi: 10.1103/PhysRevA.71.062703.

Kimura, M., O. Sueoka, A. Hamada, M. Takekawa, Y. Itikawa, H. Tanaka, and L. Boesten (1997), Remark on total and elastic cross sections for the electron and positron scattering from CO_2, *J. Chem. Phys.*, *107*, 6616.

Kitajima, M., S. Watanabe, H. Tanaka, M. Takekawa, M. Kimura, and Y. Itikawa (2001), Differential cross sections for vibrational excitation of CO_2 by 1.5-30 EV electrons, *J. Phys. B*, *34*, 1929.

Kloire, A. J., D. L. Cain, G. S. Levy, V. R. Eshleman, G. Fjeldbo, and F. D. Drake (1965), Occultation experiment: Results of the first direct measurement of Mars atmosphere and ionosphere, *Science*, *149*, 1243 – 1248.

Klots, C. E. (1968), *Energy deposition mechanisms, in Fundamental Processes in Radiation Chemistry*, 40 pp., Inter-science, New York.

Kochem, K.-H., W. Sohn, N. Hebel, K. Jung, and H. Ehrhardt (1985), Elastic electron scattering and vibrational excitation of CO_2 in the threshold energy region, *J. Phys. B*, *18*, 4455.

Krasnopolsky, V. A. (2002), Mars' upper atmosphere and ionosphere at low, medium, and high solar activities: Implications for evolution of water, *J. Geophys. Res.*, *107*(E12), 5128, doi:10.1029/2001JE001809.

Krasnopolsky, V. A. (2006), Photochemistry of the martian atmosphere: Seasonal, latitudinal, and diurnal variations, *Icarus*, *185*, 153 – 170, doi:10.1016/j.icarus.2006.06.003.

Krasnopolsky, V. A. (2007), Long-term spectroscopic observations of Mars using IRTF/CSHELL: Mapping of O_2 dayglow, CO, and search for CH_4, *Icarus*, *190*, 93 – 102, doi:10.1016/j.icarus.2007.02.014.

Krasnopolsky, V. A., and P. D. Feldman (2002), Far Ultraviolet Spectrum of Mars, *Icarus*, *160*, 86 – 94, doi:10.1006/icar.2002.6949.

Krasnopolsky, V. A., and A. A. Krys'ko (1976), On the night airglow of the Martian atmosphere, *Space Res.*, *16*, 1005.

Krasnopolsky, V. A., A. A. Krysko, V. N. Rogachev, and V. A. Parshev (1976), Spectroscopy of the Venus night airglow from the Venera 9 and 10 orbiters, *Cosmic Res.*, *14*, 789 – 795.

Krauss, M., and D. Neumann (1975), On the interaction of O(^{1}S) with O(^{3}P), *Chem. Phys. Lett.*, *36*(3), 372 – 374, doi:10.1016/0009-2614(75)80259-4.

Krimigis, S. M. (1988), Observations of energetic ion enhancements and fast neutrals upstream and downstream of Uranus bow shock by the Voyager 2 spacecraft, *Planet. Space Sci.*, *36*, 311.

Kurt, V. G., S. B. Dostovalow, and E. K. Sheffer (1968), The Venus far ultraviolet observations with Venera 4, *J. Atmos. Sci.*, *25*, 668 – 671.

Kurt, V. G., N. N. Romanova, A. S. Smirnov, J.-L. Bertaux, and J. L. Blamont (1980), Venus ultraviolet radiation in the wavelength region from 300 Å to 1657 Å from Venera 11 and Venera 12 data (preliminary results), *Cosmic Res.*, *17*, 638.

Kwan, C. K., Y.-F. Hsieh, W. E. kauppila, S. J. Smith, T. S. Stein, M. N. Uddin, and M. S. Dababneh (1983), $e^{\pm}$-CO and $e^{\pm}$-CO_2 total cross-section measurements, *Phys. Rev. A*, *27*, 1328.

Lavvas, P., M. Galand, R. V. Yelle, A. N. Heays, B. R. Lewis, G. R. Lewis, and A. J. Coates (2011), Energy deposition and primary chemical products in Titan's upper atmosphere, *Icarus*, *213*, 233 – 251, doi:10.1016/j.icarus.2011.03.001.

Lawrence, G. (1972a), Photodissociation of CO_2 to produce CO(a$^3\Pi$), *J. Chem. Phys.*, *56*, 3435 – 3442, doi:10.1063/1.1677717.

Lawrence, G. (1972b), Production of O(^{1}S) from photodissociation of CO_2, *J. Chem. Phys.*, *57*, 5616 – 5617.

Lawrence, G., and M. J. McEwan (1973), Production of O(^{1}S) from photodissociation of O_2, *J. Geophys. Res.*, *78*(34), 8314 – 8319.

Lawrence, G. M. (1971), Quenching and radiation rates of CO (a$^3\Pi$), *Chem. Phys. Lett.*, *9*, 575 – 577, doi:10.1016/0009-2614(71)85130-8.

Lawrence, G. M., C. A. Barth, and V. Argabright (1977), Excitation of the Venus night airglow, *Science*, *195*, 573 – 574.

Lean, J. (1990), A comparison of models of the Suns extreme ultraviolet irradiance variations, *J. Geophys. Res.*, *95*(A8), 11,933 – 11,944, doi:10.1029/JA095iA08p11933.

Lean, J. L., T. N. Woods, F. G. Eparvier, R. R. Meier, D. J. Strickland, J. T. Correira, and J. S. Evans (2011), Solar extreme ultraviolet irradiance: Present, past, and future, *J. Geophys. Res.*, *116*, A01102, doi:10.1029/2010JA015901.

Leblanc, F., J. Y. Chaufray, J. Lilensten, O. Witasse, and J.-L. Bertaux (2006), Martian dayglow as seen by the SPICAM UV spectrograph on Mars Express, *J. Geophys. Res.*, *111*, E09S11, doi:10.1029/2005JE002664.

Leblanc, F., J. Y. Chaufray, and J. L. Bertaux (2007), On Martian nitrogen dayglow emission observed by SPICAM UV spectrograph/Mars Express, *Geophys. Res. Lett.*, *34*, L02206, doi:10.1029/2006GL0284.

LeClair, L. R., M. D. Brown, and J. W. McConkey (1994), Selective detection of O(^{1}S) and CO(a$^3\Pi$) following electron impact on CO using solid xenon, *Chem. Phys.*, *189*, 769 – 777.

LeCompte, M. A., L. J. Paxton, and A. I. F. Stewart (1989), Analysis and Interpretation of Observations of Airglow at 297 nm in the Venus Thermosphere, *J. Geophys. Res.*, *94*(A1), 208 – 216.

Lee, C.-H., C. Winstead, and V. McKoy (1999), Collisions of low-energy electrons with CO_2, *J. Chem. Phys.*, *111*, 5056.

Lee, M.-T., and V. McKoy (1983), Cross sections for electron impact excitation of the low-lying electronic states of CO_2, *J. Phys. B*, *16*, 657.

Lewis, B. R., and J. H. Carver (1983), Temperature dependence of the carbon dioxide photoabsorption cross sections between 1200 and 1970 Å, *J. Quant. Spectrosc. Radiat. Transfer*, *30*(4), 297 – 309.

Lilensten, J., T. Dudok de Wit, M. Kretzschmar, P.-O. Amblard, S. Moussaoui, J. Aboudarham, and F. Auchère (2008), Review on the solar spectral variability in the EUV for space weather purposes, *Ann. Geophys.*, *26*, 269 – 279.

Lillis, R. J., D. L. Mitchell, R. P. Lin, and M. H. Acuña (2008), Electron reflectometry in the martian atmosphere, *Icarus*, *194*, 544 – 561, doi:10.1016/j.icarus.2007.09.030.

Lillis, R. J., M. O. Fillingim, L. M. Peticolas, D. A. Brain, R. P. Lin, and S. W. Bougher (2009), Nightside ionosphere of Mars: Modeling the effects of crustal magnetic fields and electron pitch angle distributions on electron impact ionization, *J. Geophys. Res.*, *114*, E11009, doi:10.1029/2009JE003379.

Lillis, R. J., M. O. Fillingim, and D. A. Brain (2011), Three-dimensional structure of the Martian nightside ionosphere: Predicted rates of impact ionization from Mars Global Surveyor magnetometer and electron reflectometer measurements of precipitating electrons, *J. Geophys. Res.*, *116*, A12317, doi:10.1029/2011JA016982.

Lindsay, B. G., and M. A. Mangan (2002), Photon and Electron Interaction with Atoms, Molecules and Ions, in *Landolt-Bornstein Group 1: Elementary Particles, Nuclei, and Atoms, Molecules and Ions*, vol. I - 17, edited by Y. Itikawa, landolt-börnstein ed., Springer, Berlin.

Lummerzheim, D., and J. Lilensten (1994), Electron transport and energy degradation in the ionosphere: Evaluation of the numerical solution, comparison with laboratory experiments and auroral observations, *Ann. Geophys.*, *12*, 1039 – 1051, doi:10.1007/s00585-994-1039-7.

Maeda, K. (1965), Diffusion of low energy auroral electrons in the atmosphere, *J. Atmos. Terr. Phys.*, *27*, 259–275, doi:10.1016/0021-9169(65)90121-2.

Mantas, G. P. (1975), Theory of photoelectron thermalization and transport in the ionosphere, *Planet. Space Sci.*, *23*, 337–354, doi:10.1016/0032-0633(75)90139-7.

Mantas, G. P., and S. A. Bowhill (1975), Calculated photoelectron pitch angle and energy spectra, *Planet. Space Sci.*, *24*, 355–375, doi:10.1016/0032-0633(75)90140-3.

Mantas, G. P., and W. B. Hanson (1979), Photoelectron fluxes in the Martian ionosphere, *J. Geophys. Res.*, *84*, 369 – 385, doi:10.1029/JA084iA02p00369.

McConkey, J. W., D. J. Burns, and J. M. Woolsey (1968), Absolute cross sections for ionization and excitation of CO_2 by electron impact, *J. Phys. B*, *1*, 71.

McConkey, J. W., C. P. Malone, P. V. Johnson, C. Winstead, V. McKoy, and I. Kanik (2008), Electron impact dissociation of oxygen-containing molecules-A critical review, *Physics Reports*, *466*, 1.

McConnell, J. C., and M. B. McElroy (1970), Excitation processes for Martian dayglow, *J. Geophys. Res.*, *75*, 7290 – 7293, doi:10.1029/JA075i034p07290.

McElroy, M. B., and J. C. McConnell (1971), Atomic Carbon in the Atmospheres of Mars and Venus,, *J. Geophys. Res.*, *76*(28), 6674 – 6690, doi:10.1029/JA076i028p06674.

Mehr, F. J., and M. A. Biondi (1969), Electron temperature dependence of recombination of O_2^+ and N_2^+ ions with electrons, *Phys. Rev.*, *181*, 264 – 270.

Meier, R. (1991), Ultraviolet spectroscopy and remote sensing of the upper atmosphere, *Space Sci. Rev.*, *58*, 1–185, doi:10.1007/BF01206000.

Michael, M. (2000), Model for electron degradation and production of emissions in the atmosphere of Io, Ph.D. thesis, M. G. University, India.

Michael, M., and A. Bhardwaj (2000), FUV Emissions on Io: Role of Galileo observed field aligned energetic electrons, *Geophys. Res. Lett.*, *27*, 3137 – 3140.

Mitchell, J. B. A., and S. L. Guberman (Eds.) (1989), *Dissociative Recombination: Theory, Experiment, and Application*, World Scientific, NJ.

Morgan, L. A., and J. Tennyson (1993), Electron impact excitation cross sections for CO, *J. Phys. B*, *26*, 2429 – 2441, doi:10.1088/0953-4075/26/15/026.

Morrill, J., and W. Benesch (1996), Auroral N_2 emissions and the effect of collisional processes on N_2 triplet state vibrational populations, *J. Geophys. Res.*, *101*(A1), 261 – 274, doi:10.1029/95JA02835.

Mumma, M. J., E. J. Stone, W. L. Borst, and E. C. Zipf (1972), Dissociative excitation of vacuum ultraviolet emission features by electron impact on molecular gases. III. CO_2, *J. Chem. Phys.*, *57*, 68.

Nagy, A. F., and P. M. Banks (1970), Photoelectron fluxes in the ionosphere, *J. Geophys. Res.*, *75*, 6260–6270, doi:10.1029/JA075i031p06260.

Nakamura, Y. (1995), Drift velocity and longitudinal diffusion coefficient of electron in CO_2-Ar mixtures and electron collision cross sections for CO_2 molecules, *Aust. J. Phys.*, *48*, 357.

Nakata, R. S., K. Watanabe, and F. M. Matsunaga (1965), Absorption and photoionization coefficients of CO_2 in the region 580–1970 Å, *Sci. Light*, *14*, 54.

Nakatsuji, H. (1983), Cluster expansion of the wavefunction, valence and rydberg excitations, ionizations, and inner-valence ionizations of CO_2 and N_2O studied by the sac and sac CI theories, *Chem. Phys.*, *75*, 425.

Nicholson, W. P., G. Gronoff, J. Lilensten, A. D. Aylward, and C. Simon (2009), A fast computation of the secondary ion production in the iono- sphere of Mars, *Mon. Not. R. Astron. Soc.*, *400*, 369 – 382.

Nier, A. O., and M. B. McElroy (1976), Structure of the neutral upper atmosphere of Mars: Results from Viking 1 and Viking 2, *Science*, *194*, 1298 – 1300, doi:10.1126/science.194.4271.1298.

Nisbet, J. S. (1968), Photoelectron escape from the ionosphere, *J. Atmos. Terr. Phys.*, *30*, 1257–1278, doi:10.1016/S0021-9169(68)91090-8.

Noël, S. (1997), Decay of the magnetospheric ring current: A Monte Carlo simulation, *J. Geophys. Res.*, *102*, 2301–2308, doi:10.1029/96JA03275.

Noxon, J. F., W. A. Traub, N. P. Carleton, and P. Connes (1976), Detection of O2 dayglow emission from Mars and the Martian ozone abundance, *Astrophys. J.*, *207*, 1025 – 1035, doi:10.1086/154572.

Onda, K., M. Ejiri, and Y. Itikawa (1999), Analysis of electron auroras based on the Monte Carlo method: Application to active electron arc auroras observed by the sounding rocket at Syowa Station, *J. Geophys. Res.*, *104*, 27,991–28,002, doi:10.1029/1999JA900323.

Oran, E. S., and D. J. Strickland (1978), Photoelectron flux in the Earth's ionosphere, *Planet. Space Sci.*, *26*, 1161–1177, doi:10.1016/0032-0633(78)90056-9.

Orient, O. J., and S. K. Srivastava (1983), Production of O^- from CO_2 by dissociative attachment, *Chem. Phys. Lett.*, *96*, 681.

Orient, O. J., and S. K. Srivastava (1987), Electron impact ionisation of H_2O, CO, CO_2, and CH_4, *J. Phys. B*, *20*, 3923.

Paxton, L. J., and D. E. Anderson (1992), Far ultraviolet remote sensing of Venus and Mars, in *Venus and Mars: Atmospheres, Ionospheres, and Solar Wind Interactions*, *Geophys. Monogr. Ser.*, vol. 66, edited by J. G. Luhmann, M. Tatrallyay, and R. O. Pepin, pp. 113 – 189, AGU, Washington, D. C.

Pearce, J. B., K. A. Gause, E. F. Mackey, K. K. Kelly, W. G. Fastie, and C. A. Barth (1971), The Mariner 6 and 7 ultraviolet spectrometers, *Appl. Opt.*, *10*, 805.

Perry, J. J., Y. H. Kim, J. L. Fox, and H. S. Porter (1999), Chemistry of the Jovian auroral ionosphere, *J. Geophys. Res.*, *104*, 16,541–16,566, doi:10.1029/1999JE900022.

Peterson, L. R. (1969), Discrete deposition of energy by electrons in gases, *Phys. Rev.*, *187*, 105–111, doi:10.1103/PhysRev.187.105.

Petrignani, A., F. Hellberg, R. D. Thomas, M. Larsson, P. C. Cosby, and W. J. van der Zande (2005a), Electron energy-dependent product state distributions in the dissociative recombination of O_2^+, *J. Chem. Phys.*, *122*, 234311, doi:10.1063/1.1937388.

Petrignani, A., W. J. van der Zande, P. C. Cosby, F. Hellberg, R. D. Thomas, and M. Larsson (2005b), Vibrationally resolved rate coefficients and branching fractions in the dissociative recombination of O_2^+, *J. Chem. Phys.*, *122*, 014302, doi:10.1063/1.1825991.

Peverall, R., et al. (2001), Dissociative recombination and excitation of O_2 : Cross sections, product yields and implications for studies of ionospheric airglows, *J. Chem. Phys.*, *114*(15), 6679–6689, doi:10.1063/1.1349079.

Piper, L. G. (1993), Reevaluation of the transition-moment function and Einstein coefficients for the N_2 ($A^3\Sigma_u^+ - X^1\Sigma_g$) transition, *J. Chem. Phys.*, *75*, 3174 – 3181, doi:10.1063/1.465178.

Porco, C. C., et al. (2004), Cassini Imaging Science: Instrument characteristics and anticipated scientific investigations at Saturn, *Space Sci. Rev.*, *115*, 363–497, doi: 10.1007/s11214-004-1456-7.

Pospieszalska, M. K., and R. E. Johnson (1996), Monte Carlo calculations of plasma ion-induced sputtering of an atmosphere: SO_2 ejected from Io, *J. Geophys. Res.*, *101*, 7565, doi:10.1029/95JE03650.

Rabalais, J. W., J. M. McDonald, V. Scherr, and S. P. McGlynn (1971), Electronic spectroscopy of isoelectronic molecules. II. Linear triatomic grouping containing sixteen valence electron, *Chem. Rev.*, *71*, 73.

Raghuram, S., and A. Bhardwaj (2012), Model for the production of CO Cameron band emission in Comet 1P/Halley, *Planet. Space Sci.*, *63-64*, 139 – 149, doi:10.1016/j.pss.2011.11.011.

Rapp, D., and D. D. Briglia (1965), Total cross sections for ionization and attachment in gases by electron impact: II. Negative ion formation, *J. Chem. Phys.*, *43*, 1480.

Rapp, D., and P. Englander-Golden (1965), Total cross sections for ionization and attachment in gases by electron impact: I. Positive ionization, *J. Chem. Phys.*, *43*, 1464.

Register, D. F., H. Nishimura, and S. Trajmar (1980), Elastic scattering and vibrational excitation of CO_2 by 4, 10, 20, and 50 eV electrons, *J. Phys. B*, *13*, 1651.

Richards, P. G., J. A. Fennelly, and D. G. Torr (1994), EUVAC: A solar EUV flux model for aeronomic calculations, *J. Geophys. Res.*, *99*, 8981 – 8992, doi:10.1029/94JA00518.

Richards, P. G., T. N. Woods, and W. K. Peterson (2006), HEUVAC: A new high resolution solar EUV proxy model, *Adv. Space Res.*, *37*(2), 315 – 322, doi:10.1016/j.asr.2005.06.031.

Roelof, E. C., D. G. Mitchell, and D. J. Williams (1985), Energetic neutral atoms ($E{\sim}50$ keV) from the ring current:IMP 7/8 and ISEE-1, *J. Geophys. Res.*, *90*, 10,991.

Rosati, R. E., R. Johnsen, and M. F. Golde (2003), Absolute yields of CO ($a'^3\Sigma^+$, $d^3\Delta_i$, $e^3\Sigma^-$) + O from the dissociative recombination of CO_2^+ ions with electrons, *J. Chem. Phys.*, *119*, 11,630 – 11,635, doi:10.1063/1.1623480.

Rosén, S., et al. (1998), Absolute cross sections and final-state distributions for dissociative recombination and excitation of $CO^+(\nu = 0)$ using an ion storage ring, *Phys. Rev. A*, *57*, 4462 – 4471, doi:10.1103/PhysRevA.57.4462.

Rottman, G. J., and H. W. Moos (1973), The ultraviolet (1200-1900 Angstrom) spectrum of Venus, *J. Geophys. Res.*, *78*, 8033 – 8048, doi:10.1029/JA078i034p08033.

Sakamoto, N., et al. (2010), Oscillator strength spectra and related quantities of 9 atoms and 23 molecules over the entire energy region, *NIFS-DATA*, *109*.

Sawada, T., D. J. Strickland, and A. E. S. Green (1972), Electron energy deposition in CO_2, *J. Geophys. Res.*, *77*, 4812 – 4818.

Schmidt, H. U., R. Wegmann, W. F. Huebner, and D. C. Boice (1988), Cometary gas and plasma flow with detailed chemistry, *Computer Phys. Comm.*, *49*, 17 – 59.

Schofield, K. (1978), Rate constants for the gaseous interactions of $O(2^1D_2)$ and $O(2^1S_0)$: A critical evaluation, *J. Photochem.*, *9*, 55 – 68, doi:10.1016/0047-2670(78)87006-3.

Schroeder, S., and G. W. Proelss (1991), Heating of the upper atmosphere by oxygen ions precipitated from the ring current, *Ann. Geophys.*, *9*, 267–272.

Schunk, R. W., and A. F. Nagy (2000), *Ionospheres: Physics, Plasma Physics, and Chemistry*, Cambridge University Press.

Seiersen, K., A. Al-Khalili, O. Heber, M. J. Jensen, I. B. Nielsen, H. B. Pedersen, C. P. Safvan, and L. H. Andersen (2003), Dissociative recombination of the cation and dication of CO_2, *Phys. Rev. A*, *68*(2), 022,708, doi:10.1103/PhysRevA.68.022708.

Sergienko, T. I., and V. E. Ivanov (1993), A new approach to calculate the excitation of atmospheric gases by auroral electron impact, *Ann. Geophys.*, *11*, 717–727.

Sharp, W. E. (1971), Rocket-borne spectroscopic measurements in the ultraviolet aurora: Nitrogen Vegard-Kaplan bands, *J. Geophys. Res.*, *76*(04), 987 – 1005, doi:10.1029/JA076i004p00987.

Sharpee, B. D., and T. G. Slanger (2006), $O(^1D_2\text{-}^3P_{2,1,0})$ 630.0, 636.4, and 639.2 nm forbidden emission line intensity ratios measured in the terrestrial nightglow, *J. Phys. Chem. A*, *110*, 6707 – 6710, doi:10.1021/jp056163x.

Shaw, D. A., D. M. P. Holland, M. A. Hayes, M. A. MacDonald, A. Hopkirk, and S. M. McSweeney (1995), A study of the absolute photoabsorption, photoionisation and photodissociation cross sections and the photoionisation quantum efficiency of carbon dioxide from the ionisation threshold to 345 Å, *Chem. Phys.*, *198*, 381 – 396.

Shematovich, V. I., D. V. Bisikalo, J.-C. Gérard, C. Cox, S. W. Bougher, and F. Leblanc (2008), Monte Carlo model of electron transport for the calculation of Mars dayglow emissions, *J. Geophys. Res.*, *113*, E02011, doi:10.1029/2007JE002938.

Shirai, T., T. Tabata, and H. Tawara (2001), Analytic cross sections for electron collisions with CO, CO_2, and H_2O relevant to edge plasma impurities, *At. Data Nucl. Data Tables*, *79*(1), 143 – 184, doi:10.1006/adnd.2001.0866.

Shyn, T. W., and W. E. Sharp (1979), Doubly differential cross section of secondary electrons ejected from gases by electron impact: 50-400 EV on CO_2, *Phys. Rev. A*, *20*, 2332.

Simon, C., O. Witasse, F. Leblanc, G. Gronoff, and J.-L. Bertaux (2009), Dayglow on Mars: Kinetic modeling with SPICAM UV limb data, *Planet. Spece. Sci.*, *57*, 1008 – 1021, doi:10.1016/j.pss.2008.08.012.

Singh, V., I. C. Mcdade, G. G. Shepherd, B. H. Solheim, and W. E. Ward (1996), The $O(^1S)$ dayglow emissions as observed by the WIND imaging interferometer on the UARS, *Ann. Geophysicae*, *14*, 637.

Singh, V., A. K. Upadhayaya, and M. V. S. Krishna (2010), Modeling of redline dayglow emission, *Quarterly Journal of the Hungarian Meteorological Service*, *114*(3), 217 – 227.

Singhal, R., and A. Green (1981), Spatial Aspects of Electron Energy Degradation in Atomic Oxygen, *J. Geophys. Res.*, *86*(A6), 4776 – 4780.

Singhal, R. P., and A. Bhardwaj (1991), Monte Carlo simulation of photoelectron energization in parallel electric fields: Electroglow on Uranus, *J. Geophys. Res.*, *96*, 15,963 – 15,972, doi:10.1029/90JA02749.

Singhal, R. P., and S. A. Haider (1984), Analytical Yield Spectrum approach to photoelectron fluxes in the Earth's atmosphere, *J. Geophys. Res.*, *89*(A8), 6847 – 6852, doi:10.1029/JA089iA08p06847.

Singhal, R. P., and S. A. Haider (1986), Some molecular nitrogen emissions from Titan-solar EUV and magnetospheric interaction., *Indian J. Radio Space Sci.*, *15*, 46–52.

Singhal, R. P., C. Jackman, and A. E. S. Green (1980), Spatial aspects of low and medium energy electron degradation in N_2, *J. Geophys. Res.*, *85*(A3), 1246 – 1254, doi:10.1029/JA085iA03p01246.

Singhal, R. P., S. C. Chakravarty, A. Bhardwaj, and B. Prasad (1992), Energetic electron precipitation in Jupiter's upper atmosphere, *J. Geophys. Res.*, *97*(2), 18,245 – 18,256.

Skrzypkowski, M. P., T. Gougousi, R. Johnsen, and M. F. Golde (1998), Measurement of the absolute yield of $CO(a^3\Pi)$+O products in the dissociative recombination of CO_2^+ ions with electrons, *J. Chem. Phys.*, *108*, 8400 – 8407, doi:10.1063/1.476267.

Slanger, T. G., and G. Black (1978), CO_2 photolysis revisited, *J. Chem. Phys.*, *68*, 1844–1849, doi:10.1063/1.435905.

Slanger, T. G., and G. Black (1981), The product channels in the quenching of $O(^1S)$ by $O_2(a^1\Delta_g)$, *J. Chem. Phys.*, *75*, 2247 – 2251, doi:10.1063/1.442284.

Slanger, T. G., R. L. Sharpless, and G. Black (1977), CO_2 photodissociation, 1060-1175 Å, *J. Chem. Phys.*, *67*, 5317–5323, doi:10.1063/1.434710.

Slanger, T. G., P. C. Cosby, D. L. Huestis, and T. A. Bida (2001), Discovery of the Atomic Oxygen Green Line in the Venus, *Science*, *291*, 463 – 465, doi:10.1126/science.291.5503.463.

Slanger, T. G., D. L. Huestis, P. C. Cosby, N. J. Chanover, and T. A. Bida (2006a), The Venus nightglow: Ground-based observations and chemical mechanisms, *Icarus*, *182*, 1 – 9, doi:10.1016/j.icarus.2005.12.007.

Slanger, T. G., P. C. Cosby, B. D. Sharpee, K. R. Minschwaner, and D. E. Siskind (2006b), $O(^1S \rightarrow {}^1D, {}^3P)$ branching ratio as measured in the terrestrial nightglow, *J. Geophys. Res.*, *111*, A12318, doi:10.1029/2006JA011972.

Slanger, T. G., T. E. Cravens, J. Crovisier, S. Miller, and D. F. Strobel (2008), Photoemission phenomena in the solar system, *Space Sci. Rev.*, *139*, doi:10.1007/s11214-008-9387-3.

Slanger, T. G., et al. (2011), Atomic oxygen emission intensity ratio: Observation and theory, *EOS Transactions*, *92*, 291–292, doi:10.1029/2011EO350005.

Slanger, T. G., N. J. Chanover, B. D. Sharpee, and T. A. Bida (2012), O/O_2 emissions in the Venus nightglow, *Icarus*, *217*(2), 845 – 848, doi:10.1016/j.icarus.2011.03.031.

Solomon, S. C. (1993), Auroral electron transport using the Monte Carlo method, *Geophys. Res. Lett.*, *20*, 185–188, doi:10.1029/93GL00081.

Solomon, S. C., P. B. Hays, and V. J. Abreu (1988), The auroral 6300 Å emission: Observations and modeling, *J. Geophys. Res.*, *93*(A9), 9867 – 9882, doi:10.1029/JA093iA09p09867.

Spence, D., and G. J. Schulz (1974), Cross section for the production of O_2^-, and C^- by dissociative electron attachment in CO_2: An observation of Renner-Teller effect, *J. Chem. Phys.*, *60*, 216.

Spencer, L. V., and F. Fano (1954), Energy spectrum resulting from electron slowing down, *Phys. Rev.*, *93*, 1172.

Spenner, K., Z. Dóbé, A. F. Nagy, W. C. Knudsen, and W. Lotze (1997), Photoelectron fluxes in the Venus dayside ionosphere, *J. Geophys. Res.*, *102*(A2), 2577 – 2583, doi:10.1029/96JA03341.

Spielfiedel, A., N. Feautrier, C. Cossart-Magos, G. Chambaud, P. Rosmus, H.-J. Werner, and P. Botschwina (1992), Bent valence excited states of CO_2, *J. Chem. Phys.*, *97*, 8382.

Stevens, M. H. (2001), The EUV airglow of Titan: Production and loss of N_2 $c_4'(0) - X$, *J. Geophys. Res.*, *106*, 3685 – 3689.

Stevens, M. H., et al. (2011), The production of Titan's ultraviolet nitrogen airglow, *J. Geophys. Res.*, *116*, A05304, doi:10.1029/2010JA016284.

Stewart, A. I. (1972), Mariner 6 and 7 ultraviolet spectrometer experiment: Implication of CO_2^+, CO, and O airglow, *J. Geophys. Res.*, *77*, 54 – 68, doi:10.1029/JA077i001p00054.

Stewart, A. I. (1980), Design and operation of the Pioneer Venus orbiter ultraviolet spectrometer, *IEEE Trans. Geosci. Remote Sensing GE*, *18*, 65 – 70.

Stewart, A. I., C. A. Barth, C. W. Hord, and A. L. Lane (1972), Mariner 9 ultraviolet spectrometer experiment: Structure of Mars' upper atmosphere, *Icarus*, *17*(2), 469 – 474, doi:10.1016/0019-1035(72)90012-7.

Stewart, A. I., D. E. Anderson, L. W. Esposito, and C. A. Barth (1979), Ultraviolet spectroscopy of Venus: Initial results from the Pioneer Venus Orbiter, *Science*, *203*, 777 – 779, doi:10.1126/science.203.4382.777.

Stewart, A. I. F., M. J. Alexander, R. R. Meier, L. J. Paxton, S. W. Bougher, and C. G. Fesen (1992), Atomic oxygen in the martian thermosphere, *J. Geophys. Res.*, *97*, 91 – 102.

Stolarski, R. S., and A. E. S. Green (1967), Calculations of Auroral Intensities from Electron Impact, *J. Geophys. Res.*, *72*(15), 3967 – 3974, doi:10.1029/JZ072i015p03967.

Straub, H. C., B. G. Lindsay, K. A. Smith, and R. F. Stebbings (1996), Absolute partial cross sections for electron impact ionization of CO_2 from threshold to 1000 eV, *J. Chem. Phys.*, *105*, 4015.

Streit, G. E., C. J. Howard, A. L. Schmeltekopf, J. A. Davidson, and H. I. Schiff (1976), Temperature dependence of $O(^1D)$ rate constants for reactions with O_2, N_2, CO_2, O_3, and H_2O, *J. Chem. Phys.*, *65*, 4761 – 4764, doi:10.1063/1.432930.

Strobel, D. F., and D. E. Shemansky (1982), EUV emission from Titan's upper atmosphere: Voyager 1 encounter, *J. Geophys. Res.*, *87*, 1361, doi:10.1029/JA087iA03p01361.

Strobel, D. F., S. K. Atreya, B. Bézard, F. Ferri, F. M. Flasar, M. Fulchignoni, E. Lellouch, and I. Müller-Wodarg (2009), Titan from cassini-huygens, chap. Atmospheric Structure and Composition, pp. 235 – 257, Springer, doi:10.1007/978-1-4020-9215-2.

Swartz, W. E. (1972), Electron production, recombination, and heating in the F region of the ionosphere, *Sci. Rep.*, *381.*

Szmytkowski, C., A. Zecca, G. Karwasz, S. Oss, K. Maciag, B. Marinkovic, R. S. Brusa, and R. Grisenti (1987), Absolute total cross sections for electron-CO_2 scattering at energies from 0.5 To 3000 eV, *J. Phys. B*, *20*, 5817.

Tanaka, H., T. Ishikawa, T. Masai, T. Sagara, L. Boesten, M. Takekawa, Y. Itikawa, and M. Kimura (1998), Elastic collisions of low to intermediate energy electrons from carbon dioxide: Experimental and theoretical differential cross sections, *Phys. Rev. A*, *57*, 1798.

Tian, C., and C. R. Vidal (1998), Single to quadruple ionization of CO_2 due to electron impact, *Phys. Rev. A*, *58*, 3783.

Tobiska, W., and C. Barth (1990), A Solar EUV Flux Model, *J. Geophys. Res.*, *95*(A6), 8243 – 8251, doi:10.1029/JA095iA06p08243.

Tobiska, W. K. (1991), Revised Solar Extreme Ultraviolet Flux Model, *J. Atmos. Terr. Phys.*, *53*, 1005 – 1018, doi:10.1016/0021-9169(91)90046-A.

Tobiska, W. K. (1994), Modeled soft X-ray solar irradiances, *Solar Phys.*, *152*, 207 – 215, doi:10.1007/BF01473206.

Tobiska, W. K. (2004), SOLAR2000 irradiances for climate change, aeronomy and space system engineering, *Adv. Space Res.*, *34*, 1736 – 1746, doi:10.1016/j.asr.2003.06.032.

Tobiska, W. K., and S. D. Bouwer (2006), New developments of SOLAR2000 for space research and operations, *Adv. Space Res.*, *37*, 347 – 358, doi:10.1016/j.asr.2005.08.015.

Tobiska, W. K., T. Woods, F. Eparvier, R. Viereck, L. Floyd, D. Bouwer, G. Rottman, and O. R. White (2000), The SOLAR2000 empirical solar irradiance model and forecast tool, *J. Atmos. Sol. Terr. Phys.*, *62*, 1233 – 1250, doi:10.1016/S1364-6826(00)00070-5.

Torr, M. R., and D. G. Torr (1985), Ionization frequencies for solar cycle 21 - revised, *J. Geophys. Res.*, *90*, 6675 – 6678, doi:10.1029/JA090iA07p06675.

Torr, M. R., D. G. T. Torr, and H. E. Hinteregger (1979), Ionization freequencies for major thermospheric constituents as a function of solar cycle 21, *Geophys. Res. Lett.*, *6*, 771 – 774, doi:10.1029/GL006i010p00771.

Trajmar, S., D. F. Register, and A. Chutjian (1983), Electron-scattering by molecules: 2. Experimental methods and data, *Phys. Rep.*, *97*(5), 221 – 356, doi:10.1016/0370-1573(83)90071-6.

Tsurubuchi, S., and T. Iwai (1974), Simultaneous ionization and excitation of CO_2 of by electron impact, *J. Phys. Soc. Jpn.*, *37*, 1077.

van der Burgt, P. J. M., W. B. Westerveld, and J. S. Risley (1989), Photoemission cross sections for atomic transitions in the extreme ultraviolet due to electron collisions with atoms and molecules, *J. Phys. Chem. Ref. Data*, *18*, 1757.

Viggiano, A. A., et al. (2005), Rate constants and branching ratios for the dissociative recombination of CO_2^+, *J. Chem. Phys.*, *122*, 226101, doi:10.1063/1.1926283.

Waite, J. H., T. E. Cravens, J. Kozyra, A. F. Nagy, S. K. Atreya, and R. H. Chen (1983), Electron precipitation and related aeronomy of the Jovian thermosphere and ionosphere, *J. Geophys. Res.*, *88*, 6143–6163, doi:10.1029/JA088iA08p06143.

Walt, M., W. M. McDonald, and W. E. Francis (1969), Penetration of auroral electrons into the atmosphere, in *Physics of the magnetosphere*, edited by R. L. Carovillano, pp. 534–555.

Wells, W. C., W. L. Borst, and E. C. Zipf (1972), Production of CO($a^3\Pi$) and other metastable fragments by electron impact dissociation of CO_2, *J. Geophys. Res.*, *77*(1), 69 – 75, doi:10.1029/JA077i001p00069.

Wiese, W. L., J. R. Fuhr, and T. M. D. (Eds.) (1996), *Atomic transition probabilities of carbon, nitrogen, and oxygen: A critical data compilation*, American Chem. Soc., Washington, D. C.

Witasse, O., J. Lilensten, C. L. re, and P.-L. Blelly (1999), Modelling the OI 630.0 And 557.7 nm thermospheric dayglow during EISCAT-WINDII coordinated measurements, *J. Geophys. Res.*, *104*, 24,639 – 24,656.

Woods, T. N., and G. J. Rottman (2002), Solar ultraviolet variability over time periods of aeronomic interest, in *Atmospheres in the Solar System: Comparative Aeronomy, Geophys. Monogr. Ser.*, vol. 130, edited by M. Mendillo, A. Nagy, and J. H. White, pp. 221 – 233, AGU, Washington, D. C.

Woods, T. N., F. G. Eparvier, S. M. Bailey, P. C. Chamberlin, J. Lean, G. J. Rottman, S. C. Solomon, W. K. Tobiska, and D. L. Woodraska (2005), Solar EUV Experiment (SEE): Mission overview and first results, *J. Geophys. Res.*, *110*, A01,312, doi:10.1029/2004JA010765.

Wysong, I. J. (2000), Measurement of quenching rates of CO($a^3\Pi, \nu = 0$) using laser pump-and-probe technique, *Chem. Phys. Lett.*, *329*(1-2), 42 – 46, doi:10.1016/S0009-2614(00)00967-2.

Yelle, R. V., and B. R. Sandel (1986), Uranian H Ly α emissions: Interstellar wind source, *Geophys. Res. Lett.*, *13*, 89.

Zecca, A., G. Karwasz, and R. S. Bursa (2002), Photon and Electron Interaction with Atoms, Molecules and Ions, in *Landolt-Bornstein Group 1: Elementary Particles, Nuclei, and Atoms, Molecules and Ions*, vol. I - 17, edited by Y. Itikawa, landolt-börnstein ed., Springer, Berlin.

Zhang, S. P., and G. G. Shepherd (2008), Variations of the O(^{1}D) and O(^{1}S) peak volume emission rates without direct solar effects, *Adv. Space Res.*, *42*, 939 – 946, doi:10.1016/j.asr.2007.09.004.